

January 2022

Synthesis And Investigation Of Properties In Ternary Transition Metal Phosphide Nanomaterials For Electrochemical Water Splitting

Tharanga Nisansala Batugedara
Wayne State University

Follow this and additional works at: https://digitalcommons.wayne.edu/oa_dissertations

 Part of the [Chemistry Commons](#)

Recommended Citation

Batugedara, Tharanga Nisansala, "Synthesis And Investigation Of Properties In Ternary Transition Metal Phosphide Nanomaterials For Electrochemical Water Splitting" (2022). *Wayne State University Dissertations*. 3659.

https://digitalcommons.wayne.edu/oa_dissertations/3659

This Open Access Dissertation is brought to you for free and open access by DigitalCommons@WayneState. It has been accepted for inclusion in Wayne State University Dissertations by an authorized administrator of DigitalCommons@WayneState.

**SYNTHESIS AND INVESTIGATION OF PROPERTIES IN TERNARY TRANSITION
METAL PHOSPHIDE NANOMATERIALS FOR ELECTROCHEMICAL WATER
SPLITTING**

by

THARANGA NISANSALA BATUGEDARA

DISSERTATION

Submitted to the Graduate School

of Wayne State University,

Detroit, Michigan

in partial fulfillment of the requirements

for the degree of

DOCTOR OF PHILOSOPHY

2022

MAJOR: CHEMISTRY (Inorganic)

Approved By:

Advisor

Date

DEDICATION

To my beloved parents, Lanka and Premathilaka,

my better half Kelum

and

my precious daughter Linasha

ACKNOWLEDGMENTS

I would like to thank my advisor, Prof. Stephanie L. Brock. I would like to express my heartiest gratitude to her for guiding, listening, encouraging, and supporting me for the past five years. **"A mentor sees more talent and ability within you than you see in yourself and helps bring it out of you."** For me, she was that kind of mentor, my great advisor who raised me up. She became a role model to me. I want to become a wise, kind, and successful woman like her. I would like to thank her for accepting me into her lab. Working with her was a great pleasure, and I am proud to identify myself as a student of Prof. Stephanie Brock.

I would like to extend my heartiest thanks to my committee: Prof. Federico Rabuffetti, Prof. Wen Li, and Prof. Eranda Nikolla, who have been there with me through all of my Ph.D. milestones. I appreciate the thoughtful comments and feedback you provided me, which has helped improve the quality of this dissertation work.

I want to thank my undergraduate advisor, Prof. C.S.K. Rajapakse. She has been encouraging me and celebrating all of my achievements these years. Without her guidance, I couldn't fulfill my dream of pursuing a Ph.D. in the USA.

Thank you to my collaborators, Dr. Samuel Mutinda, Dr. Zhen-Fei Liu, and Olugbenga Adeniran, for their immense expertise in research and help, which have significantly broadened the impact of our research published together.

I am thankful to all the Lumigen Instrument Center staff members, especially Dr. Zhi Mei, Dr. Sameera Perera, Dr. Cassie Ward, and Dr. Johnna Birbeck, for all the technical help they have provided me in the past years. Thank you, Fredricka Morgan, for dedicating her valuable time, without hesitation, to help me with GC analysis any time I needed. I would like to thank all of our

chemistry administrative staff members (Jackie, Melissa, Kimberly), the business office staff, and the staff in science stores.

I would like to thank my wonderful lab mates, especially Dr. Tepora Su'a, Dr. Lakmini Silva, and Lalani Mawella Vithanage, for being my peer mentors and all of the laughter and joy we have shared. They made the lab a second home for me. They became three wonderful sisters to me, and this bond will last forever. Thank you, my colleagues, Vinicius, Fatemeh, Michael, and Sonali. I feel lucky to work and be around them.

I am thankful to my friends Disni Gunasekera, Hasitha Dhanawalavithana, Amali Subasinghe and Jayendra Athukorala for all their encouragement and support. I cherish life with them around.

This dissertation work would not have been possible without the funding support, including the NSF Grants: CHE-1361741 and DMR-1904775, the WSU Rumble Fellowship, and the Summer 2022 Dissertation Award.

Last but not least, I would like to thank my family. I am forever grateful to my loving mother, father, brother, and husband for their endless love, support, and encouragement. Thank you, my precious daughter, for being my happy pill and stress-relieving magic doll. This work is dedicated to them.

TABLE OF CONTENTS

Dedication	ii
Acknowledgments.....	iii
List of Schemes.....	xi
List of Tables	xii
List of Figures	xiv
Chapter 1: Introduction	1
1.1 Hydrogen as a fuel	1
1.2 Hydrogen production via electrocatalytic water splitting.....	4
1.2.1 Hydrogen evolution reaction.....	5
1.2.2 Oxygen evolution reaction.....	7
1.3 Catalysts for electrocatalytic water splitting.....	8
1.4 Electrochemical surface area analysis	9
1.4.1 Redox surface metals method	11
1.4.2 Double-layer capacitance.....	12
1.5 Transition metal phosphides	13
1.6 Nanomaterials and their synthesis	15
1.6.1 Solution-phase arrested precipitation synthesis.....	17
1.4.2 Cation exchange method.....	18
1.7 Transition metal phosphide nanomaterials	22
1.7.1 Nickel iron phosphide	22
1.7.2 Nickel cobalt phosphide.....	23
1.7.3 Cobalt iron phosphide	23

1.7.4 Cobalt manganese phosphide.....	24
1.7.5 Iron manganese phosphide.....	24
1.7.6 Nickel ruthenium phosphide	25
1.7.7 Cobalt rhodium phosphide.....	25
1.7.8 Cu _{3-x} P analogs synthesis by cation exchange method	26
1.8 Transition metal phosphides for water splitting electrocatalysis	27
1.9 Thesis statement.....	31
Chapter 2: Material characterization techniques.....	34
2.1 Materials	34
2.1.1 Metal precursors.....	34
2.1.2 Solvents.....	35
2.2 Experimental techniques	35
2.2.1 Inert atmosphere glove box	35
2.2.2 Schlenk line techniques.....	37
2.2.3 Tube furnace	38
2.3 Material characterization techniques	39
2.3.1 Powder X-ray diffraction (PXRD).....	39
2.3.2 Transmission electron microscopy (TEM)	43
2.3.3 Energy dispersive spectroscopy (EDS).....	46
2.3.4 X-ray photoelectron spectroscopy (XPS)	47
2.3.5 Infrared spectroscopy (IR)	49
2.4 Electrocatalytic testing.....	49
2.4.1 Catalytic ink preparation.....	49

2.4.2 Cyclic voltammetry (CV)	50
Chapter 3: Co _{2-x} Rh _x P nanoparticles as electrocatalysts for the hydrogen production: Catalytic stability and Pt interference	53
3.1 Introduction.....	54
3.2 Experimental section.....	55
3.2.1 Synthesis of Co _{2-x} Rh _x P nanoparticles	55
3.2.2 Synthesis of Co ₂ P nanoparticles	56
3.2.3 Synthesis of Rh ₂ P nanoparticles	56
3.2.4 Characterization	57
3.2.5 Electrocatalytic testing.....	57
3.3 Results and discussion	57
3.3.1 Electrochemical activity in acidic medium.....	59
3.3.2 Long term stability faradaic efficiency and Pt interference in acidic medium	61
3.3.3 Electrochemical activity in basic medium.....	66
3.3.4 Long term stability faradaic efficiency and Pt interference in acidic medium	67
3.4 Conclusions.....	71
Chapter 4: The role of noble and base metal speciation and surface segregation in Ni _{2-x} Rh _x P nanocrystals on electrocatalytic water splitting reactions in alkaline media	73
4.1 Introduction.....	74
4.2 Experimental section.....	76
4.2.1 Synthesis of Ni _{2-x} Rh _x P nanoparticles.....	76
4.2.2 Synthesis of Ni ₂ P nanoparticles	77
4.2.3 Synthesis of Rh ₂ P nanoparticles	78

4.2.4 Characterization	78
4.2.5 Electrochemical measurements.....	78
4.3 Results and discussion	78
4.3.1 Synthetic protocol development	78
4.3.2 Crystal structure and morphology.....	80
4.3.3 Electrocatalytic studies	86
4.3.4 Structural elucidation: STEM-EDS mapping and XPS	96
4.3.5 Assessing the role of noble and base metal components in water-splitting catalysis over bimetallic phosphides.....	102
4.4 Conclusions.....	105
Chapter 5: Ni _{2-x} Rh _x P as a stable electrocatalyst for overall water splitting in acidic media	107
5.1 Introduction.....	108
5.2 Experimental section.....	109
5.2.1 Synthesis of Ni _{2-x} Rh _x P, Ni ₂ P, and Rh ₂ P nanoparticles	109
5.2.2 Characterization	109
5.2.3 Electrochemical measurements.....	109
5.3 Results.....	110
5.3.1 Electrocatalytic studies	110
5.3.1.1 Hydrogen evolution reaction in acid.....	110
5.3.1.2 Oxygen evolution reaction in acid	112
5.3.1.3 Overall water splitting in acid.....	113
5.3.2 Structural elucidation: STEM-EDS mapping and XPS	114
5.4 Discussion.....	119
5.5 Conclusions.....	121

Chapter 6: On the feasibility of Cu-based ternary transition metal phosphide nanoparticle synthesis by cation exchange.....	122
6.1 Introduction.....	123
6.2 Experimental section.....	124
6.2.1 Cu _{3-x} P nanoparticles synthesis	124
6.2.2 Cation exchange of Cu _{3-x} P nanoparticles with In ³⁺	124
6.2.2.1 Cation exchange of Cu _{3-x} P nanoparticles with In ³⁺ protocol 1	124
6.2.2.2 Cation exchange of Cu _{3-x} P nanoparticles with In ³⁺ protocol 2	125
6.2.3 Cation exchange of Cu _{3-x} P nanoparticles with Fe ³⁺	125
6.2.4 Cation exchange of Cu _{3-x} P nanoparticles with Ni ²⁺ and Co ²⁺	126
6.2.5 Characterization	127
6.3 Results and discussion	127
6.3.1 Cu _{3-x} P cation exchange with In ³⁺	127
6.3.2 Cu _{3-x} P cation exchange with Fe ³⁺	130
6.3.3 Cu _{3-x} P cation exchange with Ni ²⁺ and Co ²⁺	134
6.4 Conclusions.....	136
Chapter 7: Conclusions and prospectus	138
7.1 Conclusions.....	138
7.2 Future research directions	142
7.2.1 Studying the intrinsic catalytic activity dependency on material structure	142
7.2.2 Investigating electrochemical water splitting catalytic activities of Cu-based ternary phosphides	143

Appendix A.....	145
Appendix B.....	145
Appendix C.....	147
References.....	150
Abstract.....	182
Autobiographical Statement.....	185

LIST OF SCHEMES

Scheme 1.1 Schematic mechanism of hydrogen evolution reaction (HER) under acidic and alkaline media	7
Scheme 1.2 Schematic mechanism of oxygen evolution reaction (OER) under acidic and alkaline media.....	8

LIST OF TABLES

Table 1.1 Physical properties of selected binary transition metal phosphide nanomaterials ...	14
Table 1.2 Selected summary of some TMP-based nano-catalysts and their HER activities ...	29
Table 1.3 Selected summary of some TMP-based nano-catalysts and their OER activities ...	30
Table 3.1 Quantities of metal precursors employed in synthesis of $\text{Co}_{2-x}\text{Rh}_x\text{P}$ nanoparticles and phosphidation temperature as a function of x	56
Table 3.2 Calculated atomic (Rh, Co, P, Pt) and oxidation state (Rh, P) percentages on the surface of $\text{Co}_{0.75}\text{Rh}_{1.25}\text{P}/\text{C}$ electrocatalysts from XPS data acquired before and after 10 h stability tests with either carbon or platinum counter-electrodes	63
Table 3.3 XPS quantification data for oxidation states for Rh and O elements.....	71
Table 4.1 Quantities of metal precursors employed in the synthesis of $\text{Ni}_{2-x}\text{Rh}_x\text{P}$ (0.21 mmol) nanoparticles	77
Table 4.2 EDS data for samples prepared at different alloying temperatures and with different amounts of TOP	79
Table 4.3 Targeted ratios and TEM-EDS ratios (averaged) for $\text{Ni}_{2-x}\text{Rh}_x\text{P}$ nanoparticle compositions	85
Table 4.4 Electrochemically active surface area values and percentage difference (compared to initial ECSA) for $\text{Ni}_{2-x}\text{Rh}_x\text{P}$ C-NP ink before and after 30 cycles.....	93
Table 4.5 Electrochemically active surface area (ECSA) and ECSA-normalized current densities computed at the indicated applied voltages for $\text{Ni}_{2-x}\text{Rh}_x\text{P}$ C-NP ink on C cloth before and after the 10 h stability test	93
Table 4.6 EDS and XPS elemental ratios before and after the 10 h catalytic stability test (see Table 4.8 for quantified values)	99
Table 4.7 XPS ratios of oxidation states of each element before and after the 10 h catalytic stability test (see Table 4.9 for quantified values)	99
Table 4.8 EDS and XPS elemental quantification before and after catalysis for $\text{Ni}_{1.75}\text{Rh}_{0.25}\text{P}$ (OER) and $\text{Ni}_{0.25}\text{Rh}_{1.75}\text{P}$ (HER).....	99
Table 4.9 XPS quantification of oxidation states for each element for $\text{Ni}_{1.75}\text{Rh}_{0.25}\text{P}$ (OER) and $\text{Ni}_{0.25}\text{Rh}_{1.75}\text{P}$ (HER).....	100
Table 5.1 EDS elemental compositions before and after catalytic testing (P was normalized assuming the metals sum to 2.0).....	115

Table 5.2 XPS elemental ratios and oxidation state ratios before and after catalytic stability tests with $N_{0.25}Rh_{1.75}P/C$ and Rh_2P/C 119

Table 6.1 TEM-EDS atomic percentages of $Cu_{3-x}P$ before and after cation CEx with Fe^{3+} using different Fe^{3+} concentrations, CEx temperatures and times..... 133

Table 6.2 TEM-EDS elemental percentages of $Cu_{3-x}P$ before and after CEx with 1.2 mmol of Ni^{2+} at 180 °C for 30 min and 60 min and after CEx with Co^{2+} at 180 °C for 60 min 136

LIST OF FIGURES

Figure 1.1 Illustration: Production, storage, and utilization of hydrogen fuel.....	2
Figure 1.2 Different methods of industrial hydrogen production	4
Figure 1.3 Model for catalyst surface reflecting different matrices.....	11
Figure 1.4 (a) Model for CV curve showing the integration of the first anodic peak for quantifying the redox-active M; (b and c) Model for determining surface area by the C_{dl} method: (b) CVs at various scan rates (c) Double-layer capacitance calculation	12
Figure 1.5 Structure types of selected binary transition metal phosphides.....	14
Figure 1.6 Selected approaches used for nanoparticle synthesis	16
Figure 1.7 Schematic illustration of La Mer's model: Nucleation and growth stages in nanoparticle formation.....	18
Figure 1.8 Schematic illustration and reaction steps of the cation exchange process	21
Figure 1.9 Cation and ligand pairs are mostly used in cation exchange processes.....	21
Figure 2.1 Schematic diagram of the glove box	37
Figure 2.2 Schematic diagram of the Schlenk line	38
Figure 2.3 Schematic diagram of the horizontal furnace system.....	39
Figure 2.4. Schematic diagram of X-ray generation inside an X-ray tube	40
Figure 2.5. Illustration of Cu $K\alpha$ X-ray generation from electron transition from 2p to 1s	41
Figure 2.6. Illustration of Bragg's law	42
Figure 2.7. Different processes happen when bombarded electrons interact with a specimen	43
Figure 2.8. Schematic diagram of basic components of a TEM instrument.....	45
Figure 2.9. Bright field and dark field imaging modes of TEM	46
Figure 2.10. Basic parts of an EDS system.....	47
Figure 2.11. Schematic illustration of an XPS.....	48

Figure 2.12. a) A standard three-electrode system b) Catalytic ink drop-casting method on a glassy carbon electrode	50
Figure 3.1. PXRD data for Co_2P , Rh_2P and $\text{Co}_{2-x}\text{Rh}_x\text{P}$ nanoparticles with reference stick patterns (powder diffraction files, PDFs) for Co_2P (bottom) and Rh_2P (top).....	58
Figure 3.2. Representative TEM micrographs of different compositions of $\text{Co}_{2-x}\text{Rh}_x\text{P}$ nanoparticles	58
Figure 3.3. (a) HER polarization curves for $\text{Co}_{2-x}\text{Rh}_x\text{P}$ nanoparticles compared to those for Rh_2P and Co_2P end points. (b) Overpotentials at 10 mA/cm^2 (geometrical surface area).....	60
Figure 3.4. Comparison between the HER activity with Pt counter electrode vs. C counter electrode for $\text{Co}_{0.75}\text{Rh}_{1.25}\text{P}$: (a) Polarization curves; (b) Overpotential values at 10 mA/cm^2 geometric.....	61
Figure 3.5 Long term HER stability test for $\text{Co}_{0.75}\text{Rh}_{1.25}\text{P}$ with C and Pt counter electrodes and Rh_2P with C counter electrode.....	62
Figure 3.6 XPS data for the freshly prepared (a-d) and used $\text{Co}_{0.25}\text{Rh}_{1.75}\text{P/C}$ electrocatalysts: after applying constant potential for 1 hour with C counter electrode (e-h), after 1 hour with Pt counter electrode (i-l), after 9 hours run with the C counter electrode (m-p) and after 9 hours with Pt counter electrode (q-t).....	65
Figure 3.7 Faradaic efficiency data of (a) $\text{Co}_{0.25}\text{Rh}_{1.75}\text{P}$ electrocatalyst with Pt counter electrode collected for 30 min, (b) $\text{Co}_{0.75}\text{Rh}_{1.25}\text{P}$ electrocatalyst with C counter electrode collected for an initial 60 min, and (c) $\text{Co}_{0.75}\text{Rh}_{1.25}\text{P}$ electrocatalyst with C counter electrode collected over an additional 60 min relative to Figure 3.7(b)	66
Figure 3.8 (a) HER polarization curves acquired on a glassy carbon support in a rotating disk electrode and (b) Overpotential values for $\text{Co}_{2-x}\text{Rh}_x\text{P/C}$ electrocatalysts at $10 \text{ mA/cm}^2_{\text{geometric}}$	67
Figure 3.9 Faradaic efficiency plot for $\text{Co}_{0.25}\text{Rh}_{1.75}\text{P}$	68
Figure 3.10 Long term stability test data for $\text{Co}_{0.25}\text{Rh}_{1.75}\text{P}$ electrocatalyst in basic media at 60 mV of applied potential.	68
Figure 3.11 XPS data for the freshly prepared (before) and used (after) $\text{Co}_{0.25}\text{Rh}_{1.75}\text{P/C}$ electrocatalysts	70
Figure 3.12 Co 2p XPS spectra for the freshly prepared (before) and used (after) $\text{Co}_{0.25}\text{Rh}_{1.75}\text{P/C}$ electrocatalysts	70
Figure 4.1. PXRD pattern for isolated Ni-Rh alloy after heating metal precursors at $260 \text{ }^\circ\text{C}$ for 3h with 1-octadecene and oleylamine. The stick diagrams correspond to fcc Rh metal (blue) and Ni metal (gold).....	79

Figure 4.2. (a) Structure of hexagonal Ni ₂ P (left) and cubic Rh ₂ P (right) polymorphs. (b) PXRD patterns for targeted compositions of Ni _{2-x} Rh _x P (x=0-2) nanoparticles. Reference patterns for Ni ₂ P and Rh ₂ P are shown with drop lines for major distinguishing peaks. An impurity peak observed for compositions x=0.75-1.5 is indicated with a red asterix.....	81
Figure 4.3 d-spacing change of hexagonal Ni ₂ P with Rh addition (red) and cubic Rh ₂ P with Ni addition (blue).....	82
Figure 4.4 TEM images for Ni _{2-x} Rh _x P (x=0-2) nanoparticles with magnified insets. Targeted compositions are indicated and sizes obtained from the size histograms (depicted in Figure 4.5) are presented in Table 4.3	84
Figure 4.5. Particle size histograms for Ni _{2-x} Rh _x P nanoparticles as a function of x.....	85
Figure 4.6 IR spectra before and after annealing of the Ni _{1.75} Rh _{0.25} P C-NPs composite	87
Figure 4.7 (a) OER polarization curves normalized to geometric area for Ni _{2-x} Rh _x P C-NPs. (b) Overpotentials at 10 mA/cm ² _{geo.} (c) OER polarization curves normalized to ECSA for Ni _{2-x} Rh _x P C-NPs. (d) Overpotentials at 2.0 mA/ cm ² _{ECSA}	89
Figure 4.8 (a) HER polarization curves normalized to geometric area, for Ni _{2-x} Rh _x P C-NPs. (b) Overpotentials at -10 mA/cm ² _{geo.} (c) HER polarization curves normalized to ECSA for Ni _{2-x} Rh _x P C-NPs. (d) Overpotentials at -2.0 mA/cm ² _{ECSA}	91
Figure 4.9 Tafel plots for Ni _{2-x} Rh _x P for (a) OER (b) HER.....	91
Figure 4.10 Activity data for 20%Pt/C catalysts towards (a) OER (b) HER in the 1M KOH medium	92
Figure 4.11 Double-layer capacitance data acquired via RDE on Ni _{2-x} Rh _x P for x = 0, 0.25, 0.50, 1.75 and 2.00). (a) 1 st OER polarization curve (b) 30 th OER polarization curve (c) 1 st HER polarization curve (d) 30 th HER polarization curve.....	92
Figure 4.12 Long-term stability test for (a) Ni _{1.75} Rh _{0.25} P for OER (b) Ni _{0.25} Rh _{1.75} P for HER. The blue squares represent the current normalized to ECSA before and after the stability test.....	94
Figure 4.13 Double-layer capacitance data before and after the long-term (10 h) stability test for (a) Ni _{1.75} Rh _{0.25} P for OER (b) Ni _{0.25} Rh _{1.75} P for HER.....	94
Figure 4.14 Overall water splitting setup.....	95
Figure 4.15 Overall water splitting of the cell Ni _{1.75} Rh _{0.25} P/C Ni _{0.25} Rh _{1.75} P/C (a) activity and (b) stability data.....	96

Figure 4.16 EDS mapping analysis of Ni_{1.75}Rh_{0.25}P C-NPs (a) before and (b) after OER activity and Ni_{0.25}Rh_{1.75}P C-NPs (c) before and (d) after HER activity. (Scale bar is 50 nm in a-c and 100 nm in d).....98

Figure 4.17 EDS mapping analysis of Ni_{1.75}Rh_{0.25}P C-NPs (a) before and (b) after OER activity (arrows indicate areas of Rh segregation after catalysis).....98

Figure 4.18 (a) XPS spectra of Ni_{1.75}Rh_{0.25}P C-NPs before and after 10 h OER activity testing (b) XPS spectra of Ni_{0.25}Rh_{1.75}P C-NPs before and after 10 h HER activity testing.....101

Figure 5.1 (a) HER polarization curves for Ni_{2-x}Rh_xP nanoparticles compared to those for Rh₂P and Ni₂P endmembers and 20% Pt/C (b) Overpotential values at 10 mA/cm²_{geo} (geometrical surface area) (c) corresponding Tafel slopes (d) Long-term stability tests (carried out on C-cloth substrate with a surface area of 1 cm², mass loading 0.285 mg/cm²) at an applied potential of 0.08 V vs. RHE for Ni_{0.25}Rh_{1.75}P nanoparticles compared to Rh₂P and 20% Pt/C in 0.5 M H₂SO₄111

Figure 5.2 (a) OER polarization curves for Ni_{2-x}Rh_xP nanoparticles compared to those for Rh₂P and Ni₂P endpoints and RuO₂ (b) Overpotentials at 10 mA/cm²_{geo}. (c) Tafel slopes (d) Long-term stability tests (carried out on a C-cloth substrate with a surface area of 1 cm², mass loading 0.285 mg/cm²) at 2.0 V vs. RHE applied potential for Ni_{2-x}Rh_xP/C, Rh₂P/C, Ni₂P/C and RuO₂/C towards OER in 0.5 M H₂SO₄113

Figure 5.3 Overall water splitting of the cell Ni_{0.25}Rh_{1.75}P/C || Ni_{0.25}Rh_{1.75}P/C, Rh₂P/C || Rh₂P/C and RuO₂/C || 20% Pt/C (a) activity and (b) stability data.....114

Figure 5.4 EDS mapping analysis of Ni_{0.25}Rh_{1.75}P/C before, after 10h HER activity, and after 1 h OER activity. (Scale bar is 10 nm)115

Figure 5.5 XPS spectra of Ni_{0.25}Rh_{1.75}P/C before and after 10 h HER and 1 h OER stability testing117

Figure 5.6 XPS spectra of Rh₂P/C before and after 10 h HER and 1 h OER stability testing118

Figure 6.1 (a) PXRD patterns (b) TEM image (c) crystal structure of Cu_{3-x}P.....128

Figure 6.2 (a) PXRD pattern/ EDS composition and (b) TEM image of the product of Cu_{3-x}P CEx with In³⁺ via the protocol in section 6.2.2.1.....129

Figure 6.3 (a) PXRD pattern/ EDS composition and (b) TEM image of the product of Cu_{3-x}P CEx with In³⁺ via the protocol in section 6.2.2.2 and (c) crystal structure of WZ InP.....130

Figure 6.4 PXRD patterns for Cu_{3-x}P before and after CEx with Fe³⁺ for different Fe³⁺ amounts, CEx temperatures, and times (Cu₃P PDF #01-074-1067)131

Figure 6.5 TEM images of Cu_{3-x}P after CEx with Fe^{3+} using different amounts of Fe^{3+} , CEx temperatures, and times (image scale bar is 100 nm, inset scale bar is 20 nm).....132

Figure 6.6 STEM/EDS mapping images of Cu_{3-x}P (a) before (scale bar is 20 nm) and (b) after (scale bar is 50 nm) CEx with 0.2 mmol of Fe^{3+} at 200 °C for 30 min134

Figure 6.7 (a) PXRD patterns for Cu_{3-x}P before and after CEx with 1.2 mmol of Ni^{2+} ($\text{Ni}^{2+}/\text{Cu}_{3-x}\text{P}$: 4) at 180 °C for 30 min or 60 min (Cu_3P PDF #01-074-1067 and Ni_2P PDF #03-003-0953) (b) TEM images of Cu_{3-x}P after CEx with Ni^{2+} with different CEx times (scale bar is 100 nm).135

Figure 6.8 (a) PXRD patterns for Cu_{3-x}P before and after CEx with Co^{2+} at 180 °C for 60 min (Cu_3P PDF #01-074-1067) (b) TEM images of Cu_{3-x}P after CEx with Co^{2+} at 180 °C for 60 min (scale bar is 100 nm)136

CHAPTER 1. INTRODUCTION

Due to the growing global energy demand and the increase in environmental pollution that occurs by excessive usage of traditional energy sources, scientists are making a great effort to develop alternative systems with clean and more efficient energy sources. Electrocatalytic hydrogen production from water is a potentially environmentally friendly and appealing pathway. Although rare-earth metals such as Ru, Ir, Pt, etc., show high water splitting and catalytic activity, the scarcity of these metals limits their large-scale industrial applications; therefore, it is essential to develop effective candidate materials for these applications composed of earth-abundant elements. On the nanoscale, transition metal phosphide (TMP) materials exhibit a broad range of unique catalytic properties. Recently bimetallic TMP nanoparticles have shown enhanced catalytic activity, relative to monometallic TMP nanoparticles due to the synergism of the two metals. By combining two earth-abundant transition metals or by diluting a noble-metal with a base-metal, it may be possible to achieve highly active, low-cost TPMs for catalytic applications. In this Chapter, relevant background on water-splitting electrocatalytic processes and TMPs, including their syntheses via solution-phase arrested precipitation (SPAP) and cation exchange (CEX) techniques, and current knowledge of structure-property relationships and electrocatalytic water splitting abilities will be provided. This chapter will conclude with a statement of the dissertation goals and an outline of the rest of the thesis.

1.1. Hydrogen as a fuel

Many energy companies worldwide struggle with balancing natural resource preservation, energy storage, carbon emissions, and customer demands. Therefore, new materials and technologies for energy systems, including power generation and storage, are trending. Hydrogen (H_2) is the key to overcoming these challenges. H_2 can be used as an energy storage medium, in

gas or liquid state. H_2 has a high energy density and will never dissipate until used. In contrast, other energy storage types (batteries and capacitors) can lose the stored energy over time and need to be recharged periodically, even without use.¹ The US Department of Energy, alone, has funded hydrogen and fuel cell research at over \$100 million per year over the last decade.¹ In addition, other countries are also investing heavily in hydrogen.^{1, 2} Still, there is a lack of appropriate and standard hydrogen production methods to enable large-scale commercialization with low carbon emission and a robust, reliable supply chain.^{1, 2} Hence, more research for the development, demonstration, and deployment of hydrogen technologies to improve competitiveness and performance is a necessity.

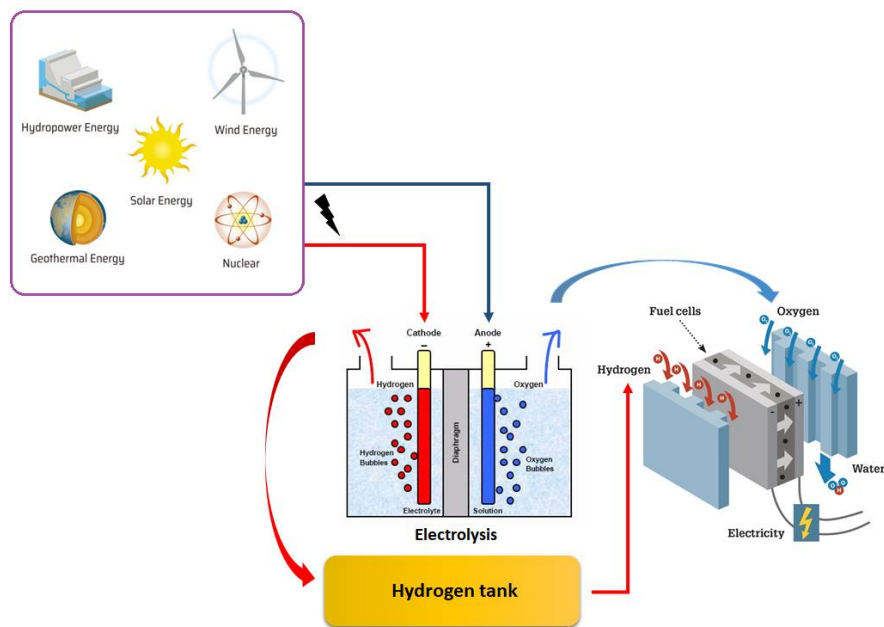


Figure 1.1. Illustration: Production, storage, and utilization of hydrogen fuel (based on references³⁻⁵)

Hydrogen is an effective type of energy carrier that can store and transmit energy. Non-continuous electrical energy from natural sources like solar, wave, wind, hydro etc., can be stored as hydrogen via electrolytic hydrogen production and the stored energy released using hydrogen fuel cells (Figure 1.1).⁶ These types of hydrogen fuel cells are now used as backup power instead

of diesel generators, especially at hospitals, data centers, and telecommunication towers.¹ A fuel cell utilizes hydrogen and oxygen to produce electricity, water, and heat, converting the chemical energy into usable electric power.⁷ Hydrogen fuel cells will produce electricity as long as the fuel (pure hydrogen) is supplied.⁷ Even though hydrogen fuel cells are a promising technology to supply on-site heat and electricity for buildings and electric motor propelling vehicles, obstacles in large-scale pure hydrogen production restrict its versatile applicability.

At present, there are various methods of hydrogen production, as illustrated in Figure 1.2. Among these, photochemical water splitting is potentially the greenest method for hydrogen production as it directly utilizes photons to generate hydrogen, but the reduced quantity of hydrogen production per unit time makes this the least efficient option.^{8,9} Hydrolysis of reactive metals and metal hydrides is a relatively rapid method to produce hydrogen in large quantities.^{10,11} However, this process can be explosive and too violent to control with highly reactive metals/metal hydrides such as for Na, Li, etc. and harsh reaction conditions are needed (high temperature and pressure) for moderately active metals like Fe and Zn.¹² Moreover, the raw metals/metal hydrides are converted into stable metal hydroxides in the process; hence, the effective recycling and reusing of the primary raw metal source is difficult to realize.¹² Steam reforming of hydrocarbons is the currently used method for large scale hydrogen production, but the usage of high pressure, high temperature, and emission of carbonaceous fuels make this process less environmentally friendly.^{10,11} Electrolysis of water is the best method to produce pure hydrogen rapidly on a large scale and in an environmentally friendly way. However, current commercial electrocatalytic water splitting is mainly done with precious and scarce metal-based catalysts such as Pt for HER and RuO₂ and IrO₂ for OER.¹³⁻¹⁵ For this reason, water electrolysis is economically infeasible for large scale industrial hydrogen production. In recent years it was found

that transition metal phosphides can be highly active catalytic materials for hydrogen production via electrocatalytic water splitting.¹⁶⁻²⁵ In this work, transition metal phosphides synthesized based on Ru, Co, Ni, Cu, and Fe metals are evaluated for electrocatalytic water splitting in different electrolytes in terms of geometric and electrochemical surface area.

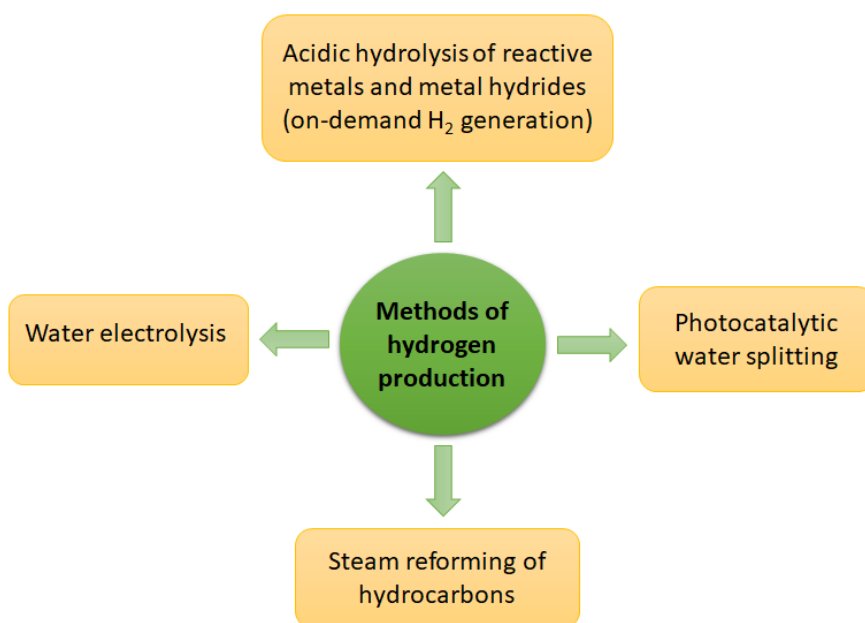


Figure 1.2. Different methods of industrial hydrogen production (based on references^{10, 26-28})

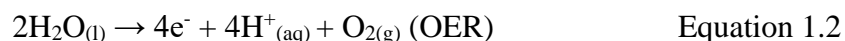
1.2. Hydrogen production via electrocatalytic water splitting

Hydrogen production by electrochemical water splitting was first reported in 1789.²⁹ Troostwijk and Deiman used two gold wires connected to an electrostatic generator and immersed in water and observed gas production (oxygen and hydrogen).²⁹ The electrochemical water splitting is typically carried out in an electrolyzer composed of an anode, cathode, and electrolyte. There are two half-cell reactions in water splitting. They are the hydrogen evolution reaction (HER) and oxygen evolution reaction (OER). HER occurs at the cathode, whereas OER occurs at the anode. Between these two half-cell reactions, HER has been studied more intensively as efficient production of H₂ with low electrical energy outlay is the primary goal of this effort. But

considering the OER process is also significant as OER limits the overall water splitting feasibility due to the higher potential requirement and the sluggish kinetics.³⁰ However, extra energy (overpotential) is required for both HER and OER to overcome the high activation barrier due to the very low conductivity of water, and this applied overpotential can be minimized by employing effective electrocatalysts and by improving the conductivity of water by adding acids, bases, or salts.²⁹

1.2.1. Hydrogen evolution reaction

As stated previously, the overall water splitting reaction consists of two half-cell reactions. The hydrogen evolution reaction (HER) on the cathode (Equation 1.1) and the oxygen evolution reaction (OER) on anode (Equation 1.2).¹⁶



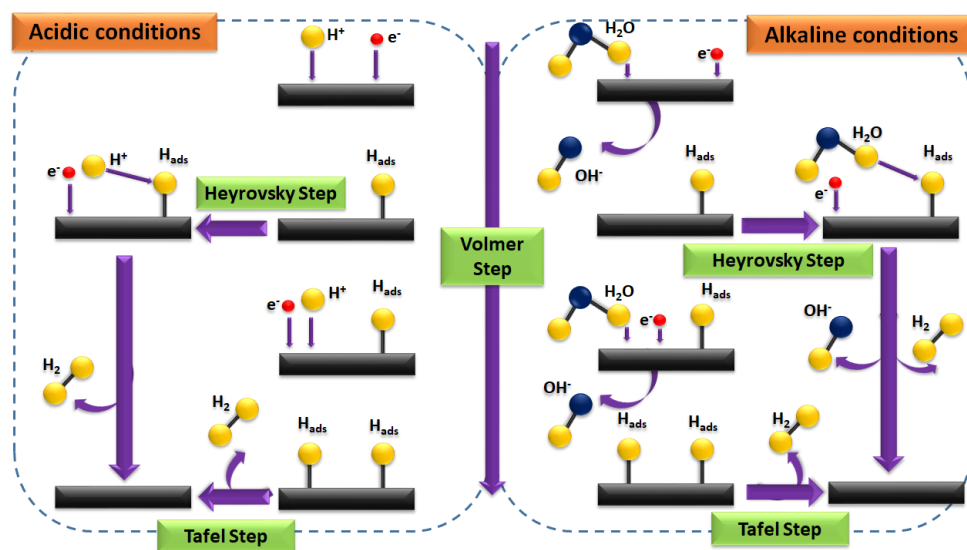
In acidic media, there are two main steps for HER (Scheme 1.1). The first step is $\text{H}^+_{(\text{aq})}$ adsorption/reduction, and the other is the H_2 formation/desorption from the catalyst.³¹ The name of the first step is the Volmer reaction, and it is the discharge process. Here the H^+ ions in the electrolyte are transformed into intermediate states on the active catalytic sites by capturing electrons. After that, it was observed that there are two different mechanisms in the hydrogen desorption process. The favored mechanism is based on the adsorption ability and the coverage of active sites on the catalyst.³² When the concentration of adsorbed hydrogen ions (H_{ads}) is low, H_{ads} combine with another electron and an H^+ from the electrolyte to form H_2 , which then desorbs from the catalyst (Heyrovsky reaction). When the H_{ads} coverage is high, H_{ads} on different active sites couple with each other to form H_2 , which evolves from the catalytic site (Tafel reaction).³²

According to the Sabatier principle, a good catalyst should have a moderate affinity for both adsorption and desorption processes.^{33,34} Thermodynamically, the Gibbs free energy (ΔG_{Hads}) is used to evaluate both hydrogen adsorption and desorption.³⁵ This value can be obtained through density functional theory (DFT) calculations and Equation 1.3.³²

$$\Delta G_{\text{Hads}} = \Delta E_{\text{ZPE}} + \Delta E_{\text{Hads}} - T\Delta S_{\text{H}} \quad \text{Equation 1.3}$$

Where ΔE_{ZPE} is the zero-point energy difference between adsorbed H and isolated H, ΔE_{Hads} is the differential H chemisorption energy, T is the temperature, and ΔS_{H} is the entropy change between the H adsorption and desorption process.³² The Sabatier principle says a catalyst with $\Delta G_{\text{Hads}} = 0$ is the ideal catalyst that can have the maximum rate of HER under acidic conditions.³⁶ Unlike reactions in acidic media, HER in alkaline solution suffers from relatively slow kinetics. This originates from the additional water dissociation step, which does not occur in the acidic medium (Scheme 1.1).³⁷ This step provides protons for the subsequent reactions. Generally, in an alkaline medium, the HER proceeds through two steps. First, the catalyst cleaves a water molecule (H_2O) into a hydrogen ion (H^+) and hydroxyl ion (OH^-), and the adsorption of the hydrogen atom (H_{ads}) occurs (Volmer step).³⁷ Then, a hydrogen molecule detaches via either the Heyrovsky or the Tafel step.

Because of the presence of an additional water breaking step, the H_{ads} coverage is much lower in alkaline than acidic solutions. Hence the Volmer step becomes the rate-controlling step in alkaline solution, which also results in a slower reaction rate.^{38,39} Recently, studies have shown other factors, such as adsorption of the hydroxyl intermediate, also need to be taken into account when determining the rate of the HER in alkaline media, making the process even more complicated.⁴⁰⁻⁴²



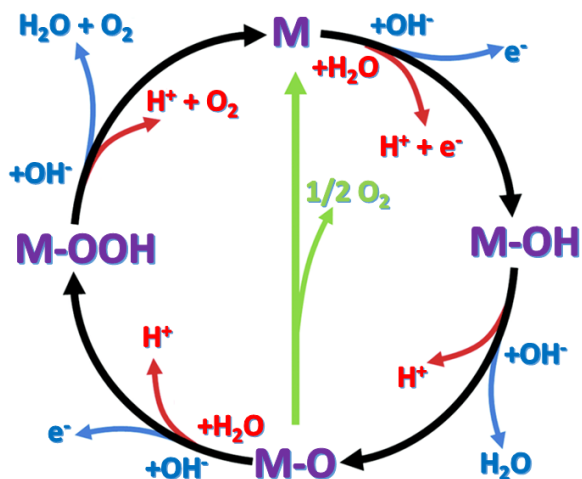
Scheme 1.1. Schematic mechanism of hydrogen evolution reaction (HER) under acidic and alkaline media (adopted from Wei *et al.*)³⁷

1.2.2. Oxygen evolution reaction

In the overall water splitting process, there is a significant efficiency loss due to the slow kinetics of the oxygen evolution reaction (OER). Water oxidation has a high activation barrier (standard water oxidation potential = 1.23 eV) as it transfers four electrons and four protons. Hence OER is the rate-limiting step and the electron supplier for HER in electrocatalytic water splitting.^{35, 43} Therefore developing effective electrocatalysts for OER to reduce the huge activation barrier is crucial in order to carry out successful hydrogen production via water electrolysis.

In the case of heterogeneous electrocatalytic OER, many research groups have proposed possible mechanisms at the anode electrode for either acid or alkaline conditions (Scheme 1.2, red and blue routes, respectively). According to those mechanisms, intermediates such as M-OH, M-O, and M-OOH can be present in the OER.⁴⁴ There are two different possible pathways to form oxygen from an M-O intermediate. One is the green route, illustrated in Scheme 1.2, which combines 2M-O to produce O_{2(g)}, and the other (Scheme 1.2 black route) involves the formation

of the M-OOH intermediate from M-O and subsequent decomposition into $O_{2(g)}$. However, in both cases, the bonding interactions between the metal atom and oxygen (M-O) within intermediates play an essential role in the efficiency of water oxidation, so oxides are inevitable.⁴⁴



Scheme 1.2. Schematic mechanism of oxygen evolution reaction (OER) under acidic (red) and alkaline (blue) media (adopted from Suen *et al.*)⁴⁴

1.3. Catalysts for electrocatalytic water splitting

In order to carry out large-scale hydrogen production via water splitting, low overpotential values and efficient, abundant, stable, and active electrocatalytic materials are essential. The practical considerations for the development of electrocatalysts include special requirements related mainly to their performance in the acid/alkaline environment. Fundamentally, the main requirements for well-performing electrocatalysts can be listed as follows.⁴⁵

1. Low intrinsic overpotential to carry out desired half-cell reaction (HER/OER)
2. High active surface to facilitate fast accessibility and removal of reactant and products, respectively
3. High electrical conductivity to provide pathways for electrons
4. Proper long-term stability

- a. chemically compatible with, and stable in, the electrolyte
 - b. electrochemically stable under applied overpotentials
 - c. mechanically stable if the electrolysis operates under high temperature or pressure
5. Low capital costs to compete with conventional catalysts and other non-renewable energy production methods

Catalysts, including noble-metals such as Pt, Ru, Rh, Ir, and Pd, have been proven as excellent catalysts for water splitting. However, due to their high cost, several strategies have been considered to reduce or eliminate the noble-metal concentration in the catalyst while maintaining reasonable activity and efficiency, such as:⁴⁶

1. Alloying noble-metals with base-metals to increase the site-specific activity
2. Developing efficient non-noble-metal compounds (carbides, sulfides, selenides, phosphides, oxides, etc.) and their composites
3. Increasing the number of reactive sites by fabricating nanostructures
4. Depositing monolayer of active noble-metal material on low-cost materials

Since water electrolysis always occurs on the surface of the catalyst, fabricating nanostructures is an efficient strategy. Nanostructures not only have more active sites per geometric area but also facilitate the diffusion of reactants and produced gases. Over the past decade, different types of nanomaterials with controlled morphology and compositions have been designed and studied for electrochemical water splitting applications.⁴⁶

1.4. Electrochemical surface area analysis

The principal goal of studying half-reactions (HER and OER) of electrocatalytic water splitting is to identify highly active and efficient materials as catalysts. To find the optimal electrocatalytic activity, a prerequisite is the usage of correct, convenient, and reasonable activity

matrices. Currently, the most popular matrices are geometric activity, mass activity, and specific activity (Figure 1.3).⁴⁷ The geometric activity can be used to evaluate device performances. The catalytic community measures this geometric activity as the overpotential to reach a geometric current density of 10 mA cm^{-2} ($\eta@10 \text{ mA cm}_{\text{geo}}^{-2}$).^{48,49} However, this geometric activity does not reflect the participation of active surface sites and is mostly dependent on the loading mass of the catalyst.^{49,50} On the other hand, the mass activity and the current density normalized to the loading mass of the catalyst ($\text{mA mg}_{\text{catalyst}}^{-1}$) largely depend on the particle size of the electrocatalyst.⁶ Mass activity can be used as a reasonable parameter for evaluating intrinsic catalytic properties of bulk materials where ions diffuse into bulk materials with micro-cracks during charge/discharge reactions.⁶ However, for surface reactions, neither the geometric activity nor mass activity reflects the intrinsic activity.⁴⁷ The specific activity is the most reasonable way to measure intrinsic activity. This is measured by normalizing the current density to the electrocatalytic surface area ($\text{mA cm}_{\text{catalyst}}^{-2}$).⁵¹ As this exposed surface area is associated with the real number of active sites, this can reflect the activity per active site.⁵¹ Even though there are a variety of techniques available for surface area measurement, such as Brunauer–Emmett–Teller (BET), electron microscopy, etc., the widely accepted best way is to normalize the catalytic activity to the electrochemically active surface area (ECSA).⁴⁷

There are two main types of methods for ECSA analysis. One is using surface faradaic reactions such as hydrogen underpotential deposition (HUPD),^{52,53} underpotential deposition of metals (UPD),^{54,55} CO stripping,^{52,53} and redox surface metals.^{56,57} The other one is non-faradaic double-layer capacitance (C_{dl}).⁵⁸⁻⁶⁰ In this dissertation work, we used the redox surface metal method and C_{dl} method in order to analyze the ECSA.

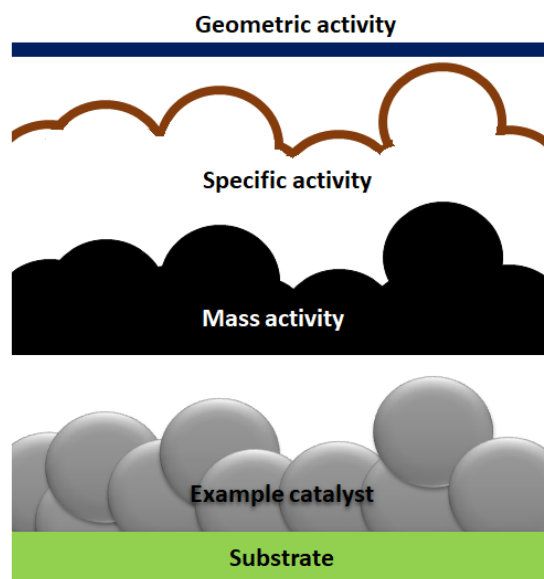


Figure 1.3. Model for catalyst surface reflecting different matrices (adopted from Wei *et al.*)⁴⁷

1.4.1. Redox surface metals method

The redox surface metals method relies on the reaction between the surface metal atoms and oxygen species. Here the cyclic voltammetry (CV) curves are collected under reduction/oxidation conditions, and the peak due to the formation of metal oxide monolayer (Figure 1.4.a) is integrated and converted to the surface area using specific charge values.⁴⁷ Since the coulombic charge under the CV peaks is associated with electrocatalytic surface sites, this method quantitatively tells how many active metal atoms are present on the catalytic surface.⁶¹ However, there are four significant challenges to utilizing this method for measuring ECSA of new materials.^{56-58, 62, 63} Those are;

1. Finding the formation potential of metal oxide monolayer
2. Determining the specific charge values
3. Determining the number of electrons transferred per metal site
4. Determination of the baseline of the CV peak for integration purpose

Despite these challenges, at present, the surface redox method is highly acceptable as a powerful ECSA analysis method for OER due to the capability of approximate quantification of metal sites (active sites) under similar reaction conditions as for OER.⁴⁷

1.4.2. Double-layer capacitance

The double-layer capacitance (C_{dl}) method is widely used for measuring ECSA for new materials. Here CVs are collected at various scan rates under non-faradaic conditions. The double-layer capacitive current difference (Equation 1.4) is taken from the middle of the potential window and is plotted against the scan rate (v).⁶⁰ The linear behavior confirms the ideal capacitor behavior, and according to the relationship in Equation 1.5, the C_{dl} is determined by calculating the slope.⁶⁰ Figure 1.4.b and 1.4.c illustrates the expected observations for the C_{dl} method.

$$(\Delta J = (J_a - J_c)/2)$$

Equation 1.4

$$\Delta J = C_{dl} \cdot v$$

Equation 1.5

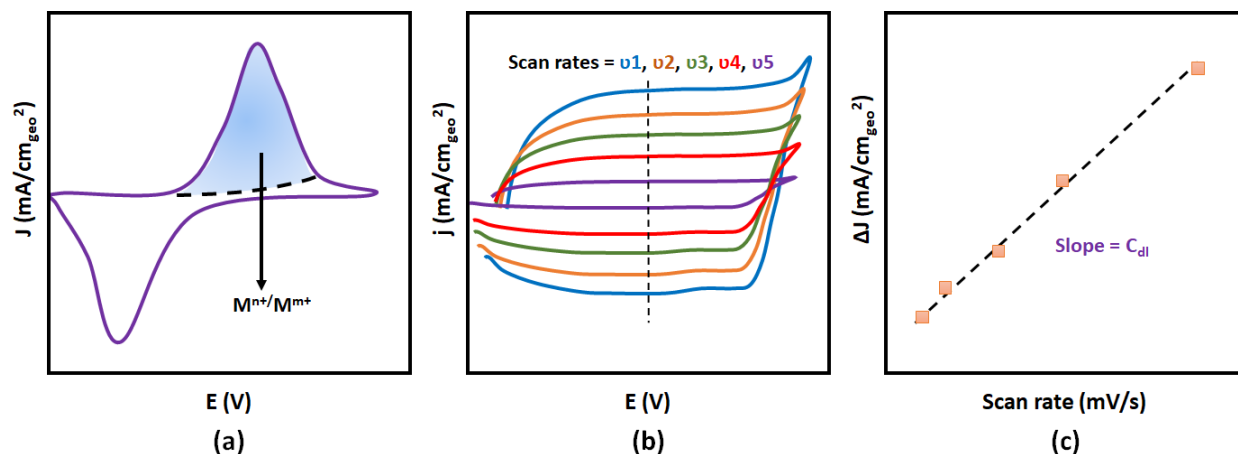


Figure 1.4. (a) Model for CV curve showing the integration of the first anodic peak for quantifying the redox-active M; (b and c) Model for determining surface area by the C_{dl} method: (b) CVs at various scan rates (c) Double-layer capacitance calculation

Note that additives such as carbon black increase the conductivity and ensure the smooth charge transfer at the interface of the electrocatalytic composite material, hence maximizing the

metal site utilization.⁶⁴ This makes it hard to identify the intrinsic activity purely coming from the new material active sites, thus it is hard to define pure intrinsic activity.^{64, 65} Also, the specific capacitance values of new materials are unknown. Therefore, this parameter is mostly determined by referring to primarily used/ related values from the literature. Thus, there is a great possibility for specific capacitance values to vary depending on surface structure, electrolyte concentration, electrode potential, etc.⁵⁹ Additionally, side reactions such as corrosion, specific adsorption, intercalation, etc., also can affect the C_{dl} value.⁶⁶ However, studies carried out using highly conductive materials vs. low conductivity materials to evaluate surface area have shown that, when the conductivity of the catalytic material is high, ECSA from the C_{dl} method vs. Brunauer–Emmett–Teller (BET) method gave similar values (for samples without added carbon).⁴⁷ In contrast, such consistency was not observed in semiconducting and insulating materials with low conductivity, which showed much lower C_{dl} -based ECSAs than BET surface areas. Therefore it is wise to use C_{dl} measurements to evaluate ECSA when the catalyst itself is highly electrically conductive.⁴⁷

1.5. Transition metal phosphides

Transition metal phosphides (TMP) have gained the attention of scientists due to the wide range of unique catalytic optical and magnetic properties. Metal phosphides can be represented by the general formula M_xP_y . They are solid-state compounds formed by a combination of metallic elements with phosphorus.⁶⁷ The bulk-phase synthesis of metal phosphides is done through traditional solid-state methods, which typically employ heating the elements at a high temperature (>800 °C) in an evacuated tube.⁶⁸

Binary transition metal phosphides can exist in different stoichiometries and structures. Phosphorus-rich phases have a covalent character, while metal-rich phases exhibit metallic

characteristics.⁶⁹ X-ray adsorption studies show that the electronic structures of metal-rich phosphides are similar to the corresponding pure metals.⁷⁰ Table 1.1 shows how different properties arise based on composition and structure.

Table 1.1. Physical properties of selected binary transition metal phosphide nanomaterials^{71, 72}

Ferromagnetism	MnP	Fe ₃ P	Fe ₂ P
Semiconductivity	CoP ₃	FeP ₂	NiP ₂
Superconductivity	W ₃ P	Mo ₃ P	
Catalytic activity	WP	MoP	Ni ₂ P

The properties of these binary compounds can be tuned by replacing M or P with other transition metals or main group elements, especially among isostructural series (Figure 1.5), allowing the synthesis of ternary transition metal phosphides.⁶⁸ Various research groups have developed different synthetic methods to prepare TMP materials. Yet, these materials remain a synthetic challenge, as they can adopt a wide range of stoichiometries and structures even within binary formulations.⁷³ Ternary (bimetallic) TMPs are an even more significant challenge due to phase segregation issues.

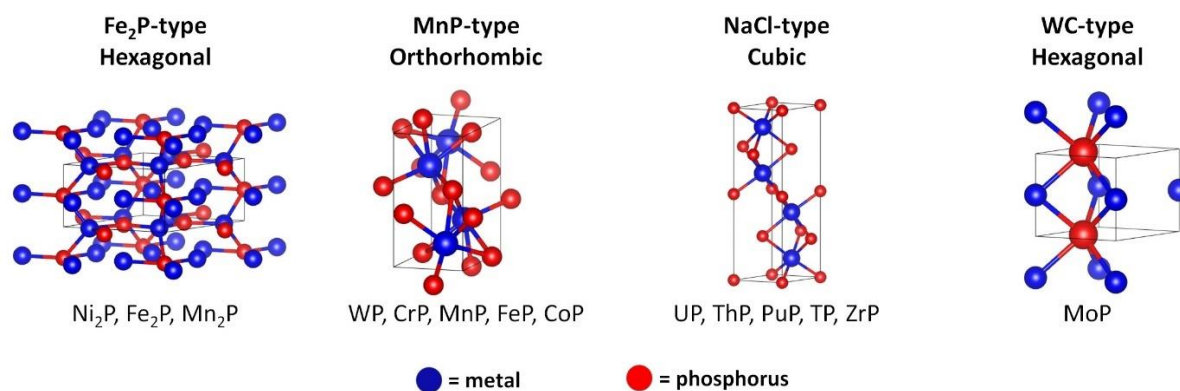


Figure 1.5. Structure types of selected binary transition metal phosphides

For the past 20 years, the Brock group has developed methods to synthesize nanoscale binary and ternary transition metal phosphides with controlled size shape and composition for various applications such as hydrodeoxygenation (HDO), hydrodesulfurization (HDS), thermoelectric devices and magnetic refrigeration. Recently we and others have discovered that ternary TMP nanoparticles exhibit superior catalytic activity relative to their binary end members in water splitting hydrogen production (HER and OER).²²⁻²⁵ Therefore, we elected to study different phase-pure ternary TMPs and their intrinsic properties to evaluate key metrics underscoring activity in catalytic water-splitting applications.

1.6. Nanomaterials and their synthesis

Nanomaterials are solids with sizes less than 100 nm in one or more dimensions. The first concept of nanomaterials was presented by Dr. Richard Feynman in 1959 in his talk "There's plenty of room at the bottom,"⁷⁴ where he described the ability to manipulate and control individual atoms and molecules. In 1974 a Japanese scientist, Norio Taniguchi, defined the term "nanotechnology" as "nanotechnology mainly consists of the processing of separation, consolidation, and deformation of materials by one atom or one molecule".⁷⁵ After that, with the invention of the scanning tunneling microscope, by Gerd Binnig and Heinrich Rohrer and the discovery of fullerene in 1981 by Richard Smalley, Robert Curl and Harold Kroto the development of nanotechnology was established.⁷⁴ The first book on nanotechnology, "Engines of Creation: The Coming Era of Nanotechnology," was published In 1986 by K. Eric Drexler.⁷⁶ With the contribution of thousands of scientists such as Charles Plank, Edward Rosinski, Mark A. Ratner, Arie Aviram, Richard P. Van Duyne, Jacop Sagiv, and so on,⁷⁷ today nanotechnology has become a branch of science and engineering dealing with material creations for a vast range of applications through observing, measuring, assembling and manipulating matter at the nano-scale. Due to the

small size, the surface/volume ratio of the nanomaterial is higher than that of the bulk. Therefore, the percentage of atoms at the surface of the material becomes significant and it starts showing surface properties over bulk properties when the size approaches the nanoscale. Also, the size of a nanoparticle can determine its physical and chemical properties, while bulk materials have constant physical properties regardless of size.⁷⁸⁻⁸¹ This unique behavior of nanomaterials makes them ideal candidates for various technological applications including nanomedicine, nanobiotechnology, energy applications etc.⁸²⁻⁸⁶ However, to exploit the advantages of nanomaterials, they have to be prepared in the right composition, size, and shape.

For nanoparticle synthesis, two main approaches can be used: top-down or bottom-up (Figure 1.6). The top-down process breaks down bulk materials to create nanomaterials, and the bottom-up method uses molecular level precursors and constructs nanomaterials by nucleation.⁸⁷⁻⁸⁹ The advantages of the bottom-up approach are the ability to synthesize small nanoparticles (~2 nm) and control the size and shape by controlling the reaction parameters. Also, surface ligands can be used to functionalize the surface of the nanomaterials and alter the physicochemical properties.⁹⁰

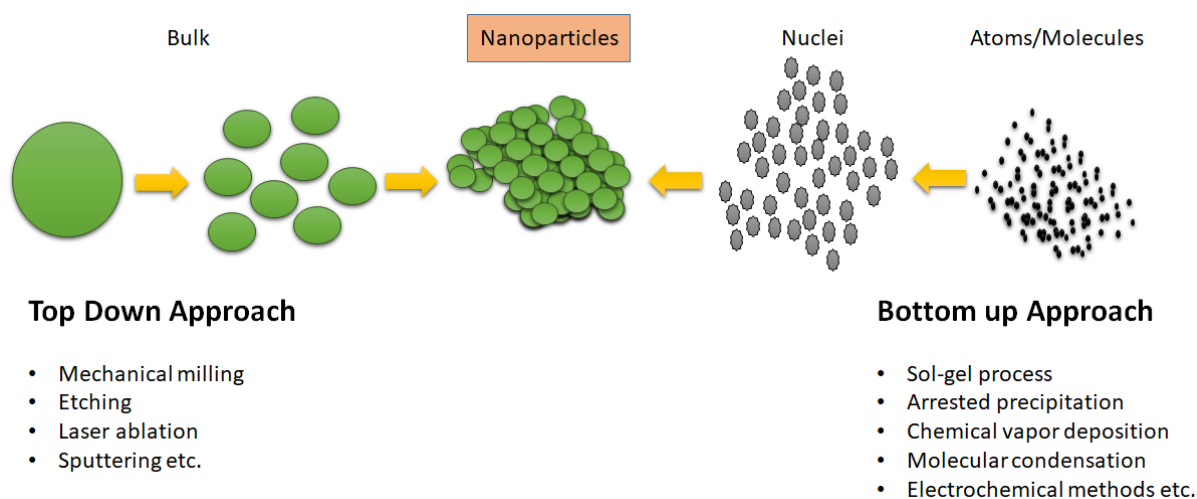


Figure 1.6. Selected approaches used for nanoparticle synthesis

1.6.1. Solution-phase arrested precipitation synthesis

The solution-phase arrested precipitation (SPAP) method is a powerful synthetic technique that produces crystalline nanomaterials with controlled size, shape, composition, and crystal phase, ideally as low poly-dispersity samples.⁹¹ This method involves arresting the growth of nanoparticles by adding inorganic coordinating agents or organic ligands.⁹² Here, the selection of coordinating ligands is critical.⁹³ Ligands with long alkyl carbon chains that have bonding groups (typically Lewis bases) at their tails are useful to control the growth of nanocrystals. Common coordinating ligands include alkyl acids, alkyl amines, alkyl phosphine oxides, alkyl phosphines, etc. In some reactions, more than one kind of ligand can be employed to control the nanoparticle synthesis.⁹⁴ In general, when the alkyl chain is shorter, or the concentration of a ligand is lower, larger nanoparticles will form as a result of the decreased steric stabilization, and vice versa.⁹⁴

There are two key steps for controlling nucleation and growth in nanocrystal formation with a small size distribution.⁹⁵ Figure 1.7 shows La Mer's model of nucleation and growth adapted from Klimov.⁹⁶ First, the injection of the organometallic precursors into the hot solvents results in the immediate decomposition of the precursors. This results in the supersaturation of monomers. The supersaturated monomers then form nuclei. These nuclei act as seeds for the next growth step. The growth rate will be rapid; therefore, it will proceed by consuming additional monomers from the formed seeds. No more nuclei will form when the monomer concentration goes down below the threshold limit. Due to this depletion of the monomers, the growth steps are then governed by the Ostwald ripening process. During this process, small nanoparticles will dissolve due to the higher surface energy and re-deposit onto larger nanocrystals. The supersaturation and nucleation can be optimized by using slow heating rates of the precursors to the reaction temperature. The reaction time, ligand type/concentration, and reaction temperature are the controllable factors that

impact the SPAP process. Generally, higher temperatures, shorter ligands/low concentration of the ligand, and longer Ostwald ripening times will result in larger nanoparticles due to the fast growth rate, low steric stabilization, and long growth time, respectively.

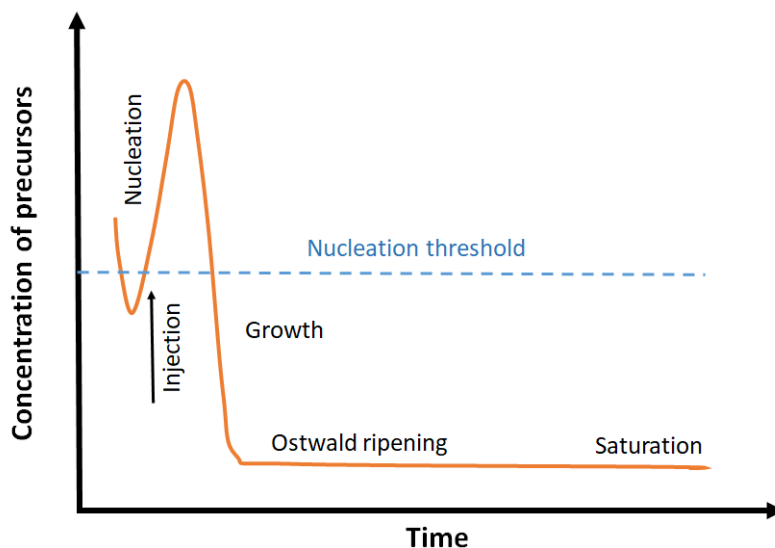


Figure 1.7. Schematic illustration of La Mer's model: Nucleation and growth stages in nanoparticle formation (adopted from Klimov)⁹⁶

1.6.2. Cation exchange method

Ion exchange in which one cation is substituted for one or more others is called cation exchange (CEX). The substitution of cations in a solid with those in solution is an old strategy for modifying the composition of crystalline materials. In recent years, the cation exchange (CEX) method has been increasingly applied as a synthetic tool to develop novel nanomaterials. Nanocrystals, which are prepared by the traditional solution-phase arrested precipitation method, can be used as anion templates for the preparation of diverse phases via CEX that would be inaccessible by direct methods.⁹⁷ The mild reaction conditions attendant to most exchanges allows accessing many nonequilibrium morphologies, crystal phases, and compositions. Control over the reaction can extend the utility of CEX for accessing a wide variety

of heterostructures and doped nanocrystals.⁹⁷ However, there are kinetic and thermodynamic factors that govern the mechanism of CEx reactions. Typically, a CEx reaction proceeds through the inward diffusion of guest ions followed by the outward diffusion of host ions. The exchange of cations often occurs under a nonequilibrium state governed by kinetics.⁹⁸ To understand the related mechanisms, the identification of kinetic factors that influence ion diffusion is important. Reaction zone, lattice structure, and defects in the crystal structure can act as influencing dynamic factors in the CEx process.

The region where substitution reactions take place in the nanoparticle by solid-state diffusion is called the reaction zone.⁹⁸ In the reaction zone, the substitution reaction by diffusion takes place, and the difference in the diffusion rates between two metal ions can control the overall reaction rate.⁹⁸ This determines the reaction region of the nanoparticle: the whole surface or only a specific zone. Also, this reaction zone seems to affect the morphology and the crystal structure of the end product directly.⁹⁹ If the region is the whole surface, inter-diffusion can occur, and a core-shell structure can be formed. If a specific part of the crystal structure serves as the reaction zone, the local lattice distortion of the template can occur.⁹⁹ This should be at a level that is sufficient to maintain the anion sublattice structure. Here, the shape of the template nanostructure can be maintained during the conversion.

The stability of the nanoparticle anion sublattice structure can determine the overall morphology after the CEx process. A volume change in the template lattice structure can be caused by a different size between the host and the guest ions. In contrast, morphology changes can result depending on the degree of strain tolerance that the lattice structure can relieve with the new ions being incorporated.⁹⁸ At a critical point, the stress applied to the lattice structure by the new ions can lead to void formation or shape changes. Defects are one of the most important factors for ion

diffusion during CEx.¹⁰⁰⁻¹⁰⁴ These defects can facilitate an ion diffusion pathway with a low activation barrier for the CEx process. Groeneveld *et al.*¹⁰⁰ introduced a "Frenkel pair" concept for diffusion process modeling in the presence of defects. A Frenkel pair is a defect in the lattice of a crystal where an atom/ion occupies a normally vacant site other than its own and leaves its own lattice site vacant. At high temperatures, a Frenkel pair can form, and that can promote the spontaneous external diffusion of host cations from the lattice. Vacancies and interstitial sites in the nanoparticle template also can accelerate CEx reactions.^{102, 104} These defects also provide a pathway for ion diffusion with low activation energy, hence a more active CEx process.^{102, 104}

In CEx, thermodynamic factors can determine the spontaneity of the reaction. These factors are also important in selecting suitable ligands and solvents for corresponding CEx processes. The CEx reaction has four reaction steps (Figure 1.8).¹⁰⁵ The lattice energies of the template and final crystal structures influence the association and dissociation process. A spontaneous CEx can be predicted if the lattice energy of the product is larger than the template nanoparticle.^{105, 106} In desolvation and solvation steps, the degree of solubility of host and guest cations in the solvent is important.¹⁰⁰ If the solubility of the host cation is greater in the solvent than the guest cation, the CEx process will proceed well.¹⁰⁷ Pearson's hard and soft acid/ base (HSAB) theory can be used as a tool in selecting a suitable solvent. This theory predicts the affinity among solvents, ligands, and ions. According to HSAB, hard acids are preferred by hard bases, while soft acids are preferred by soft bases.¹⁰⁸ Therefore, if the host cation can make a more stable acid-base pair with the solvent/ligand compared to the guest cation, the CEx process will be feasible. Some common cation and ligand pairs are illustrated in Figure 1.9. However, it is a challenge to predict the exact ligand/solvent combination for a particular process as both ligand and solvent are simultaneously

involved in the CEx process. Other than that, the CEx processes can also be influenced by other processes, such as decomposition of the ligand or side reactions.⁹⁸

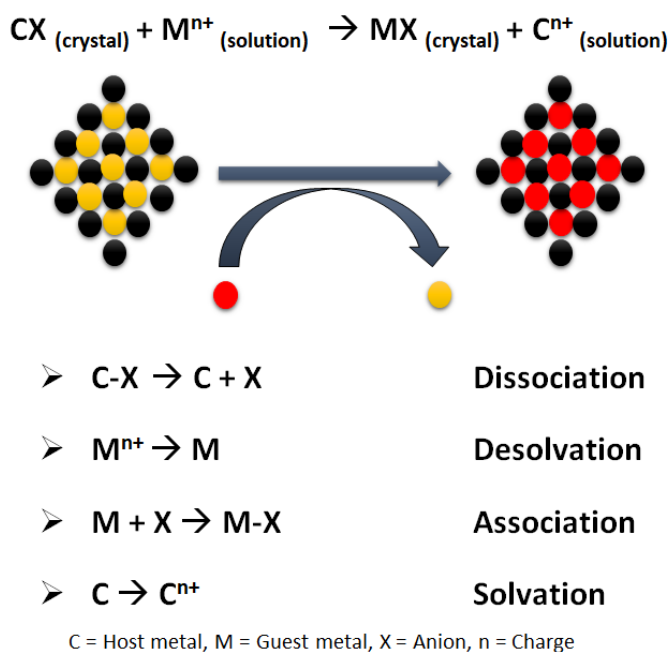


Figure 1.8. Schematic illustration and reaction steps of the cation exchange process (based on references^{102, 104})

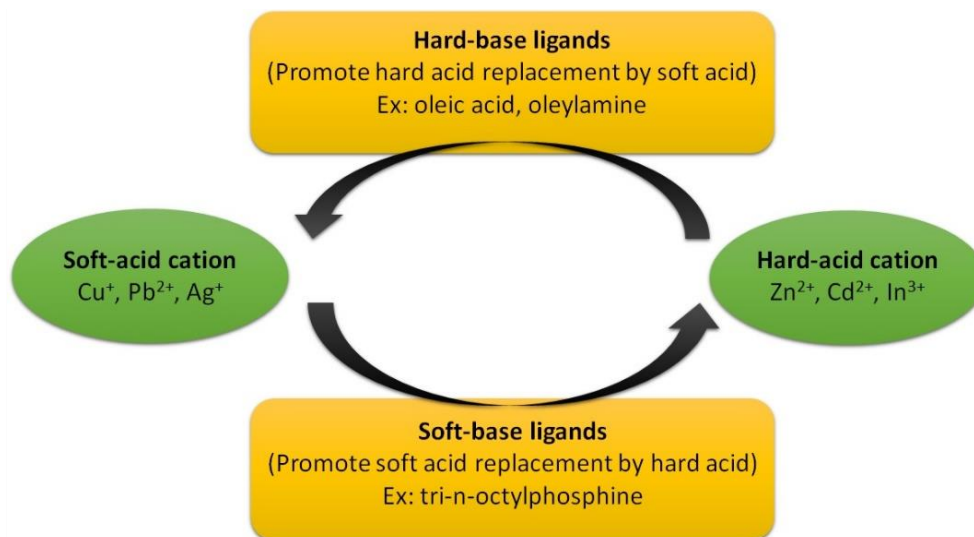


Figure 1.9. Cation and ligand pairs are mostly used in cation exchange processes (based on references^{99, 109-117})

1.7. Transition metal phosphide nanomaterials

Considerable effort has been placed on transition metal phosphide synthesis in the last decade. In these cases, the solution-phase arrested precipitation method has been successfully applied to synthesize nearly monodisperse binary transition metal phosphide nanomaterials, and most of them have well-developed synthetic protocols, and their properties have been studied for different applications.

Even though on the nanoscale, metal phosphide binary phases have been extensively studied, ternary nano phases are still under exploration. Ternary phases are quite important as the synergism present in these bimetallic systems enhances the opportunities to tune the properties. However, while the properties and the phase diagrams for ternary bulk phases with Cr, Co, Fe, Mn, Ni, etc., are well established,¹¹⁸ the study of nano phases of ternary transition metal phosphides has begun only recently. Many research groups have developed different strategies for ternary transition metal phosphide synthesis based on solution-phase arrested precipitation reactions and cation exchange methods, as described below.^{22-25, 119-125}

1.7.1. Nickel iron phosphide

In 2008, the synthesis of $(\text{Fe}_x\text{Ni}_{1-x})_2\text{P}$ ($x = 0-1$) nanorods by the thermal decomposition of metal-TOP complexes was reported by Hyeon and co-workers.¹¹⁹ First, they formed a Fe-TOP solution by the reaction of $\text{Fe}(\text{CO})_5$ with TOP. Then a Ni-TOP complex formed by reacting $\text{Ni}(\text{acac})_2$ and TOP was injected into the Fe-TOP solution. In 2015 the Brock group synthesized $\text{Ni}_{2-x}\text{Fe}_x\text{P}$, with a focus on compositional control and phase formation over all x .¹²⁰ They found that the phase separation and inhomogeneity in ternary phosphide nanoparticles can result due to the different reactivities of the two metal precursors. Thus, since $\text{Ni}(\text{acac})_2$, the (Ni precursor) was considerably less reactive compared to $\text{Fe}(\text{CO})_5$ (the Fe precursor), first $\text{Ni}(\text{acac})_2$ was reacted with

TOP at 230 °C followed by the introduction of $\text{Fe}(\text{CO})_5$ to form the amorphous mixed metal phosphide phase $\text{Ni}_{2-x}\text{Fe}_x\text{P}$. Then the temperature was increased to 350 °C, allowing the conversion of the amorphous phase to the crystalline phase. A composition-dependent morphology was observed for these materials with a spherical morphology for Ni-rich compositions, which then transitions to nanorods with the increment of Fe incorporation.

1.7.2. Nickel cobalt phosphide

The Brock group prepared $\text{Ni}_{2-x}\text{Co}_x\text{P}$ nanoparticles using similarly active metal precursors, $\text{Ni}(\text{acac})_2$ and $\text{Co}(\text{acac})_2$, along with TOP, oleylamine, and octyl ether.¹²¹ The Ni-Co-P alloy precursor particles were formed at intermediate temperatures (230-260 °C), and these were converted to the final crystalline phase at 350 °C. For Ni-rich compositions, a dense spherical morphology was observed, while increasing the amount of Co, hollow particles appeared due to the Kirkendall effect, which arises from their higher mobility of Co metal in the phosphide lattice compared to Ni metal.

1.7.3. Cobalt iron phosphide

In 2011, Han and co-workers reported the synthesis of $\text{Co}_{2-x}\text{Fe}_x\text{P}$ nanostructures.¹²² Metal oleate complexes of Co and Fe were reacted with TOP in the presence of oleylamine. They observed a temperature-dependent composition and morphology change. At 290 °C, $\text{Co}_{1.5}\text{Fe}_{0.5}\text{P}$ adopted rice-shaped nanorods, whereas at 320 °C, split nanostructures were observed for the $\text{Co}_{1.7}\text{Fe}_{0.3}\text{P}$ composition. In 2015, Sun and co-workers synthesized $\text{Co}_{2-x}\text{Fe}_x\text{P}$ nanoparticles by converting Co-Fe-O to the phosphides.¹²³ There, the oxide particles were synthesized by thermal decomposition of metal-acetylacetonate precursors. In the presence of oleylamine and oleic acid as surfactants, by reacting metal oxide nanoparticles with TOP at 300 °C, polyhedral particles of $\text{Co}_{0.94}\text{Fe}_{1.06}\text{P}$ and $\text{Co}_{1.58}\text{Fe}_{0.42}\text{P}$ nanorods were obtained. By adding sodium oleate to the reaction

mixture, they were also able to synthesize $\text{Co}_{0.48}\text{Fe}_{1.52}\text{P}$ and $\text{Co}_{1.08}\text{Fe}_{0.92}\text{P}$ cubic particles with sea-urchin-like structures. In 2016 the Brock group reported an alternate synthesis of $\text{Co}_x\text{Fe}_{2-x}\text{P}$ ($x=0$ to 2) nanoparticles. First, $\text{Co}_x\text{Fe}_{2-x}$ alloy nanoparticles were prepared at 200 °C and converted to the crystalline ternary phosphide phase by reaction with TOP at 330-350 °C.¹²⁴ In this case, due to the Kirkendall effect, the resultant $\text{Co}_x\text{Fe}_{2-x}\text{P}$ particles were hollow.

1.7.4. Cobalt manganese phosphide

In 2016, the Brock group reported the preparation of a new nanoscale phase; $\text{Co}_{2-x}\text{Mn}_x\text{P}$ spherical-shaped nanoparticles.²² In this preparation, CoMn alloy was formed at 200 °C in an oleylamine/1-octadecene solution using $\text{Co}(\text{CO})_8$ and $\text{Mn}(\text{CO})_{10}$ as metal precursors. The CoMn alloy was converted to the phosphide phase by the reaction with TOP at 350 °C. It was possible to prepare phases with x up to 1.4, despite the fact that all attempts by the Brock lab to prepare Mn_2P as a discrete colloidal phase results in MnP or manganese oxides.

1.7.5. Iron manganese phosphide

The first colloidal synthesis of $\text{Fe}_{2-x}\text{Mn}_x\text{P}$ ($x=0.15$ to 0.7) nanoparticles was reported in 2011 by Whitmire and co-workers from the thermal decomposition of $\text{FeMn}(\text{CO})_8(\mu\text{PH}_2)$ in the presence of oleic acid and hexadecyl amine.¹²⁵ Their repeated experiments carried out under identical conditions resulted in different elemental composition of the particles ranging from $\text{Fe}_{1.85}\text{Mn}_{0.15}\text{P}$ to $\text{Fe}_{1.3}\text{Mn}_{0.7}\text{P}$ due to the high sensitivity of the decomposition rate of the single-source precursor to small changes in experimental parameters. Minor temperature fluctuations, hot-spot formation and stirring speed may have resulted in this composition variation. In 2017, the Brock group adopted a new approach for $\text{Fe}_{2-x}\text{Mn}_x\text{P}$ based on their previous $\text{Co}_{2-x}\text{Mn}_x\text{P}$ synthesis.^{22, 23} In this case, the Mn composition ($x=0.2-0.7$) was controlled by varying the reaction time from 1 h to 3 h while using an excess of Mn precursor, instead of varying starting metal ratios, as was

the case for the analogous Co phase.²³ Specifically, the synthesis was carried out by injecting a mixture of $\text{Fe}(\text{CO})_5$ (0.75 mmol), $\text{Mn}_2(\text{CO})_{10}$ (1.25 mmol), and trioctylphosphine (TOP) into a degassed system of OAm at 325 °C. Mn-uptake flattened at $x = 0.7$ after 3 h. To increase Mn loading further, a second injection of manganese precursor were injected after the saturation point (3 h), enabling formation of nanorods with $x = 0.9$.

1.7.6. Nickel ruthenium phosphide

In 2017, the Brock group began to study mixed noble-base metal phosphides. $\text{Ni}_{2-x}\text{Ru}_x\text{P}$ nanoparticles was the first system investigated.²⁴ In this study, it was revealed that the Ru(III) chloride precursor is not susceptible to reduction in the presence of TOP. Consequently, Ru nanoparticles were prepared first, using RuCl_3 as the precursor and oleylamine as the reducing agent at 260 °C, and subsequently, the Ni precursor ($\text{Ni}(\text{acac})_2$) was introduced to the system with TOP. Amorphous Ni-Ru-P particles were prepared as the intermediate phase (260 °C), and the final crystalline phase was obtained at 350 °C. This study showed that, at 350 °C in the solution phase, crystalline $\text{Ni}_{2-x}\text{Ru}_x\text{P}$ materials could be prepared for $x \leq 1$, but the Ru-rich compositions were all amorphous, including Ru_2P .

1.7.7. Cobalt rhodium phosphide

In 2018 the Brock group synthesized another mixed noble-metal and base-metal phase, $\text{Co}_{2-x}\text{Rh}_x\text{P}$.²⁵ In this study, a wide range of $\text{Co}_{2-x}\text{Rh}_x\text{P}$ ($x=0-2$) compositions were synthesized by adjusting the stoichiometric ratios of $\text{Co}(\text{acac})_2$ and $\text{RhCl}_3 \cdot n\text{H}_2\text{O}$ metal precursors. As with Ru, Rh(III) reduction was unsuccessful in the presence of TOP. In this case, the two metal precursors were dissolved in octadecene and oleylamine solvent mixture and allowed to form an amorphous metal alloy at 230 °C for 9 hours. TOP was then injected into the Co-Rh alloy mixture, and the temperature was increased (between 310 °C-350 °C) to form Co-Rh-P phases. The morphology of

nanoparticles can be described as spherical with hollow voids at the Co rich end due to the Kirkendall effect. With increasing Rh incorporation, particles become quasi-spherical with diminished hollow features.

1.7.8. Cu_{3-x}P analogs synthesis by cation exchange method

To date, there are only two reported works on pure phase Cu_{3-x}P nanoparticle cation exchange. For the first time, in 2015, Manna and co-workers reported the use of Cu_{3-x}P nanoparticles as a starting material to probe cation exchange reactions.¹²⁶ They demonstrated that hexagonal Cu_{3-x}P nanoparticles can be cation exchanged easily with In³⁺ to produce hexagonal wurtzite InP nanoparticles. Cu_{3-x}P nanoparticles were synthesized via the solution-phase arrested precipitation method using CuCl as the metal precursor, oleylamine as the reducing agent and TOP as phosphidizing agent. These synthesized hexagonal platelet-like crystalline nanoparticles were cation exchanged with In³⁺ (In:Cu molar ratio 1:1) in a TOP and octadecene solvent mixture at 200 °C. Here the anion framework of Cu_{3-x}P, which is very close to that of wurtzite InP, was preserved after complete cation exchange. The cation exchange process was found to start from the peripheral corners of nanoparticles which gradually evolved toward the center. As a result, an intermediate of the reaction was found to have Cu_{3-x}P/InP heterostructure.

After that, in 2019, Lee and co-workers further evaluated how the Cu_{3-x}P to InP cation exchange process and morphology of nanoparticles are affected by the reaction conditions.¹²⁷ Here, they demonstrated that cation exchanged nanoparticles exhibit morphological changes depending on the ligand composition (TOP/solvent = Ψ = 0.07, 0.14 or 0.5) and cation exchange temperature (200°C vs 250°C) in the cation-exchange reaction. For example, at higher TOP amounts (Ψ = 0.5) or higher cation exchange temperatures (250°C), a high Cu⁺ vacancy density was observed in the Cu_{3-x}P segment that would accumulate and nucleate the Kirkendall voids. By

a quantitative analysis of solvation energetics, they found that higher TOP amounts enhances the solvation of both Cu^+ and In^{3+} during the cation exchange reaction. At higher temperatures, the high mobility of cations might affecting the void formation. This creates an imbalance between solvation of Cu^+ and desolvation of In^{3+} and high Cu^+ vacancy density in the Cu_{3-x}P segment. Finally, annealing of cation exchanged cracked InP nanoparticles at high temperature resulted in crystal ripening, and void coalescence was observed, leading to a hole and resulting in hollow nanoparticles.

Other than that, in 2020, Hong *et al.* reported successful cation exchange of $\text{Cu}_3\text{P}_{1-x}\text{S}_x$ ($x=0.3$) with Co^{2+} and Ni^{2+} . Here $\text{Cu}_3\text{P}_{1-x}\text{S}_x$ was synthesized by colloidal synthesis of $\text{Cu}_{29}\text{S}_{16}$ nanoparticles followed by phosphidation with tris-(diethylamino) phosphine at 220 °C. Then the cation exchange of $\text{Cu}_3\text{P}_{1-x}\text{S}_x$ with Co^{2+} followed by Ni^{2+} was carried out in the presence of oleylamine, benzyl ether, and TOP at 180°C to obtain $\text{Co}_2\text{P}_{1-x}\text{S}_x$ and $\text{Co}_{2-y}\text{Ni}_y\text{P}_{1-x}\text{S}_x$ ($y=0.17$) respectively. In this case, also, the rapid Kirkendall effect and the desulfurization process created numerous ionic vacant sites, which led to the morphological and phase evolution of these phospho-sulfides.

1.8. Transition metal phosphides for water splitting electrocatalysis

TMPs as electrocatalysts for water splitting were first mentioned by Rodriguez's group in 2005.¹²⁸ Their DFT calculation results showed that when the Ni is diluted by introducing P to produce Ni_2P , the Ni_2P (001) plane behaves like hydrogenase instead of the pure metal surface.¹⁶ This was experimentally tested by Lewis and Schaak *et al.* in 2013 on Ni_2P nanoparticles synthesized using TOP as phosphorous precursor.¹²⁹ They observed hollow crystalline structures which showed high catalytic activity and good durability toward HER in 0.5 M H_2SO_4 with an overpotentials of 130 mV at a current density of 20 mA cm^{-2} for Ni_2P . After that they discovered

that Co₂P hollow nanoparticles synthesized using a similar protocol was more active than Ni₂P towards HER in 0.5 M H₂SO₄ with an overpotential of 85 mV required to obtain a current density of 20 mA cm⁻².¹³⁰ Schaak *et al.* also synthesized electrodes with TMPs by reacting commercially available metal foils such as Fe, Co, Ni, Cu, and NiFe with various organophosphine reagents.¹³¹ All of the phosphides showed good HER and OER catalytic activities, while Ni₂P electrodes showed the highest HER activity with overpotentials of 128 mV in acid and 183 mV in base at 10 mA cm⁻² of current density. Since the original report on Ni₂P in 2013, many other non-noble metal phosphide-based materials have been intensively studied for HER. Moreover, recent studies demonstrated that when a secondary metal is introduced into the crystal lattice, it substantially improves its electrocatalytic activity for HER. Examples of select monometallic and bimetallic phosphides evaluated for HER electrocatalysis are shown in Table 1.2.

Early studies on water splitting using TMPs as catalysts were primarily focused on HER. In 2015, Yang *et al.* first reported the OER activity of a porous cobalt phosphide/phosphate thin film.¹³² It showed a low onset overpotential (220 mV) in the alkaline medium. Afterward, many investigations have been reported on the OER performance of a variety of mono-metallic and bimetallic TMPs based on non-noble-metals with closely related structures, as shown in Table 1.3.¹³³

The Brock group was a leading contributor to studying how ternary metal phosphide nanoparticles could enhance the OER activity in alkaline media. Initial studies focused on Co_{2-x}Mn_xP and Fe_{2-x}Mn_xP materials and analyzing their catalytic properties towards OER catalysis in base.^{22, 23} The ternary phosphides showed higher activities than their binary end members. In the course of OER electrocatalysis, the surface of the metal phosphides is oxidized to generate metal phosphate and oxy/hydroxy moieties. The phosphate is liberated, and the oxy/hydroxy species are presumed to be the active catalytic species.^{19, 134}

Liu and co-workers recently systematically investigated the influence of the number of transition metal species and their specific combinations on the OER activity in alkaline media.¹³⁵ They found that the OER activity of bi-metallic TMPs is higher than that of mono-metallic TMPs, while tri-metallic TMPs are even more active than bi-metallic TMPs. Moreover, TMPs containing Fe were the least active for the OER. When Co is present in TMPs, it helps to reduce the overpotential of OER electrocatalysis in the low potential region, while having Ni in TMPs boosts the anodic current in the high potential region. The trend in OER activity was found to be FeP < NiP < CoP < FeNiP < FeCoP < CoNiP < FeCoNiP from both catalytic activities and OER reaction kinetics (Tafel slopes and charge transfer resistance).¹³⁵

Table 1.2. Selected summary of some TMP-based nano-catalysts and their HER activities

Catalyst	$\eta_{\text{HER}} @ 10 \text{ mA cm}^{-2}$ (mV vs. RHE)		Reference
	Acidic	Alkaline	
MoP	83	86	32
Cu ₃ P	62	-	136
FeP	96	194	137
FeP ₂	61	186	137
CoP ₂	56	-	138
CoP ₃	-	76	138
NiCo ₂ P _x	104	58	32
Zn _{0.04} Co _{0.96} P	39	-	138
Fe _{0.1} -doped CoP	-	78	139
Ni _{1.85} Fe _{0.15} P	-	106	140
Cu ₃ P-CoP	59	-	141

Not only non-noble-metal based TMPs, but TMPs containing platinum group metals have also been recently explored to catalyze the OER. According to Luo *et al.*, PdP₂ nanoparticles were

highly active in both alkaline and neutral media (with phosphate buffer) with overpotential values of 270 mV and 277 mV to reach 10 mA cm^{-2} respectively, due to the high active surface area associated with PdP₂.⁵⁸ These values were promising for OER compared to state-of-the-art IrO₂ electrocatalyst, which demands 301 mV of overpotential to drive 10 mA cm^{-2} .⁵⁸ Work done by Duan *et al.* showed that Rh₂P could be an excellent catalyst for OER in an acidic medium with a 510 mV overpotential to reach 5 mA cm^{-2} current density, but the catalytic activity started to drop after 300 test cycles.⁵⁹ As previously mentioned, transition metal phosphides are expected to oxidize and form active sites during *in-situ* OER catalysis.^{19, 134} Due to the high solubility of these *in-situ* prepared oxide active sites in acids, it is challenging to perform OER in low pH media. In 2017, the Brock group found that noble and non-noble mixed ternary metal phosphides (Ni_{2-x}Ru_xP, Co_{2-x}Rh_xP) are more active than non-noble ternary metal phosphide materials toward OER in alkaline medium.^{24, 25} The XPS data analysis suggests the redox properties of the base-metal are modified, making it easier to oxidize as noble-metal is incorporated.

Table 1.3. Selected summary of some TMP-based nano-catalysts and their OER activities

Catalyst	$\eta_{\text{OER}}@10 \text{ mA cm}^{-2}$ (mV vs. RHE) In alkaline medium	Ref.
Co ₂ P	430	123
Fe ₂ P	560	123
Ni ₂ P	350	142
NiP	424	143
CoP	399	143
FeP	347	143
NiCoP	286	143
NiFeP	300	143
NiCoP	280	144
NiCoFeP	200	135

1.9. Thesis statement

The worldwide energy sector struggles with competing demands to preserve natural resources, limit carbon emissions, and provide customers with cheap energy. Renewable hydrogen (H_2) is the key to overcoming these challenges because it has a high energy density and can be stored indefinitely without dissipation. However, commercially viable electrocatalytic H_2 production requires the development of efficient and inexpensive catalysts. Recently, ternary transition metal phosphide (TMP) nanomaterials have been shown to be active towards H_2O electrolysis due to the synergism of the two metals. By combining two earth-abundant transition metals or by diluting a noble metal with a base metal, it is thus possible to achieve highly active, low-cost TPM materials for catalytic applications. However, significant challenges associated with the synthesis of these materials remain, including the need to overcome phase segregation and to control the size, shape, homogeneity, and stoichiometric targeting of the end product. On the other hand, in terms of catalytic activities, the following questions are unresolved: (1) In new ternary transition metal phosphide materials, how does metal synergism affect the catalytic activity and stability? (2) In mixed noble- and non-noble metal phosphides, to what extent can the noble metal can be diluted without impacting overall activity/stability?

Although significant development of TMP nanoparticles for water splitting has been achieved, the fundamental electrocatalytic mechanisms still need to be discovered. It is known that that most electrocatalysts undergo a surface/structural reconstruction during the electrochemical reaction resulting in a change in electrocatalytic activity. In view of this, discovering the surface/structural changes associated with the activity is important to properly evaluate the reaction mechanism. Accordingly, in the dissertation research, the focus is on establishing rational synthetic pathways to ternary transition metal phosphide nanoparticles with controlled size, shape,

and composition via solution phase arrested precipitation methods and cation exchange methods and determining the physicochemical properties that underscore catalyst activity and stability towards electrochemical water splitting applications.

The dissertation is laid out as follows.

Chapter 2 describes the materials, experimental methods, and characterization techniques employed throughout this dissertation research.

Chapter 3 describes HER electrocatalytic studies of $\text{Co}_{2-x}\text{Rh}_x\text{P}$ nanoparticles and Pt interference noted when Pt is used as the counter electrode in acidic media. The hydrogen evolution reaction (HER) activity and stability of $\text{Co}_{2-x}\text{Rh}_x\text{P}$ nanoparticles/carbon black composite ($\text{Co}_{2-x}\text{Rh}_x\text{P}/\text{C}$) in acidic and alkaline medium with a Pt counter electrode vs. a carbon counter electrode is reported under applied potentials below the Pt oxidation potential (<0.6 eV vs. RHE).

Chapter 4 describes the formation of $\text{Ni}_{2-x}\text{Rh}_x\text{P}$ nanocrystals and their activity with respect to electrocatalytic water splitting reactions in alkaline media. The first synthesis of colloidal $\text{Ni}_{2-x}\text{Rh}_x\text{P}$ nanocrystals by arrested precipitation routes is reported in this chapter, along with the composition-dependent activity of carbon composites ($\text{Ni}_{2-x}\text{Rh}_x\text{P}/\text{C}$) for the electrocatalytic hydrogen evolution reaction (HER) and oxygen evolution reaction (OER) in alkaline media. The changes in noble and base-metal speciation and surface segregation over the course of catalytic studies is discussed in terms of the mode of catalyst activation/deactivation.

Chapter 5 describes the activity and stability of Rh-rich $\text{Ni}_{2-x}\text{Rh}_x\text{P}/\text{C}$ catalysts from Chapter 4 towards HER and OER in acidic (0.5 M H_2SO_4) media, including activity towards overall water splitting (OWS). Structural elucidation analysis was conducted to better understand the structure-property relationships related to the enhanced catalytic stabilities of $\text{Ni}_{2-x}\text{Rh}_x\text{P}/\text{C}$ relative to Rh_2P .

Chapter 6 describes efforts towards the synthesis of Cu-based ternary transition metal phosphide nanoparticles for electrocatalytic water splitting applications using a cation exchange approach. We explored protocols to cation exchange Cu^+ in Cu_{3-x}P with Fe^{3+} , Ni^{2+} and Co^{2+} . Preliminary characterization is performed to assess the efficacy of the exchange process and understand the structural and morphological changes that result.

Finally, Chapter 7 summarizes the significant insights gained from new ternary transition metal phosphide synthesis method development and their structure-property relationships towards electrocatalytic water splitting reactions. Future directions to develop highly active and stable new catalytic materials are also discussed based on the knowledge gained.

Portions of the text in this chapter were reprinted with permission from (2021) American Chemical Society, (2021) Wiley-VCH GmbH, and (2022) American Chemical Society.

CHAPTER 2. MATERIAL CHARACTERIZATION TECHNIQUES

This chapter is focused on experimental methodologies and characterization techniques employed in the research study. Ternary transition metal phosphides, $\text{Ni}_{2-x}\text{Rh}_x\text{P}$ and $\text{Co}_{2-x}\text{Rh}_x\text{P}$ were synthesized by the solution-phase arrested precipitation (SPAP) method, and $\text{Cu}_{3-x}\text{M}_x\text{P}$ (M = Fe, Co, Ni) synthesis was carried out using cation exchange (CEX) methods. In both cases, air-sensitive synthetic techniques (glove box and Schlenk line) were used. The synthesized materials were characterized by powder X-ray diffraction (PXRD), transmission electron microscopy (TEM), energy dispersive spectroscopy (EDS), X-ray photoelectron spectroscopy (XPS), inductively coupled plasma-mass spectrometry (ICP-MS) and infrared spectroscopy (IR). Finally, electrochemical surface area analysis and water splitting catalytic activities were evaluated for the synthesized ternary transition metal phosphide/ carbon composite ink catalyst using cyclic voltammetry (CV).

2.1. Materials

2.1.1. Metal precursors

Nickel(II) acetylacetonate ($\text{Ni}(\text{acac})_2$, Alfa Aesar, 95%), rhodium(III) chloride hydrated ($\text{RhCl}_3 \cdot n\text{H}_2\text{O}$, Sigma-Aldrich, 38-40% Rh), cobalt(II) acetylacetonate ($\text{Co}(\text{acac})_2$, Sigma-Aldrich, 99%), cobalt(II) chloride (CoCl_2 , Alfa Aesar, 99.7%), iron(III) acetylacetonate ($\text{Fe}_3(\text{acac})_3$, Sigma-Aldrich, 95%), iron(III) chloride (FeCl_3 , Sigma-Aldrich, 97%), nickel(II) chloride hexahydrate ($\text{NiCl}_2 \cdot 6\text{H}_2\text{O}$, Sigma-Aldrich, $\geq 98\%$), indium(III) bromide (InBr_3 , Sigma-Aldrich, 99%) and copper(I) chloride (CuCl , Alfa Aesar, 99.99%) were used as metal precursors. CuCl was stored in the glove box under an inert atmosphere.

2.1.2. Solvents

Tri-n-octyl phosphine (TOP, STREM Chemicals, 97%), tris(diethylamino)phosphine (TDAP, Sigma-Aldrich, 97%), n-octyl ether (TCI America, 95%), oleylamine (TCI America, >50%), nafion (5%, LQ-1105, Ion Power), chloroform (Fisher Scientific, $\geq 99.8\%$), hexanes (technical grade, Fisher Scientific, 98.5%), ethanol (200 proof, Decon Laboratories), isopropyl alcohol (Sigma-Aldrich, 99.9%), potassium hydroxide (KOH, Sigma-Aldrich, $\geq 85\%$, pellets), sulfuric acid (H_2SO_4 , Fisher Scientific, 93-98%), toluene (Fisher Scientific, 99.5%), benzyl ether (Acros Organics, 99%) were used. All chemicals were used as received.

2.2. Experimental techniques

2.2.1. Inert atmosphere glove box

The glove box is a device that keeps air and moisture-sensitive materials away from atmospheric oxygen and water. It is a fully enclosed "bench top" which contains an inert atmosphere, which a person could reach into with gloves (Figure 2.1). A glove box has four major components:¹⁴⁵

1. The main box: This is a large and tightly sealed steel argon-filled chamber with a plastic front window with two gloves, which is the working area of the glove box.
2. The antechamber: This allows materials to go in and out without letting in air. The main box is connected to the antechamber from outside, and once materials are introduced to the antechamber, it should be degassed. The degassing process is done by using a vacuum pump connected to the chamber for a sufficient time (minimum of 20 minutes). This process removes air/moisture from the antechamber and then can transfer the contents from the antechamber to the box.

3. The copper catalyst and molecular sieves: The argon gas in the box is continuously circulating through this device, and it removes any oxygen or water present. This component can be periodically regenerated in order to maintain the inert atmosphere inside the box. In the regeneration process, the copper catalyst and molecular sieves are heated under a mixture of H_2 and N_2 , followed by evacuation. This removes O_2 adsorbed onto copper, which is eliminated as H_2O , resulting in a fresh copper catalyst surface. The water from the molecular sieves and the catalyst regeneration are removed in the final evacuation process. However, it is important to note that the catalyst can be damaged by certain reactive chemicals such as chlorine, sulfur, etc. Therefore, careful precautions must be taken to eliminate the evaporation of such chemicals into the box atmosphere.
4. Pressure regulator: The glove box needs to regulate the pressure inside to maintain a positive pressure minimizing air diffusing through the rubber gloves, pinholes, or other weak points. This is a photohelic pressure gauge that is set to tolerate only a few millibars of positive and negative pressure. This device automatically pumps argon in/out of the box to maintain the desired pressure inside the glove box. Also, when working in the glove box, one can regulate the pressure manually with a foot pedal.

In this dissertation work, the glove box model HE 493 purchased from the Vacuum Atmosphere was used.

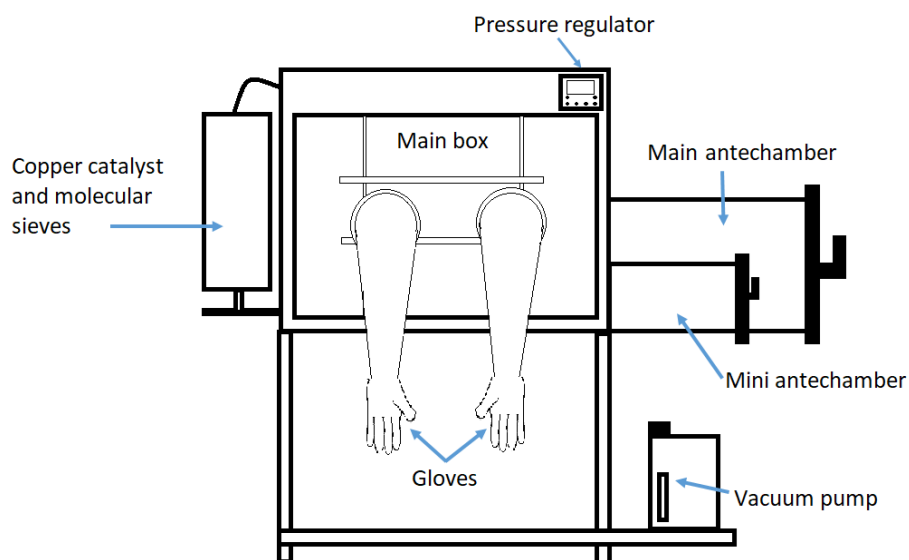


Figure 2.1. Schematic diagram of the glove box

2.2.2. Schlenk line techniques

Schlenk line techniques provide a convenient means of manipulating air and moisture-sensitive materials without the use of a glove box. These lines may have a dual or single manifold design. In a single manifold design, the manifold is attached to a vacuum pump, whereas the dual manifold design is attached to an inert gas (Ar) tank from one side and attached to a vacuum pump via a cold liquid nitrogen trap from the other side (Figure 2.2)

The dual manifold line has several ports with two-way stopcocks connected to the Schlenk flasks through flexible rubber tubes. The Schlenk flask is the reaction vessel. It contains the reaction mixture, which is typically loaded and sealed in the glove box and then attached to the line. After that, it is degassed by opening the sidearm of the flask to the evacuation manifold via a two-way stopcock. Then the flask is filled with inert argon gas by opening the stopcock to the Ar line manifold. Reactions are typically conducted under a positive pressure of Ar.¹⁴⁶

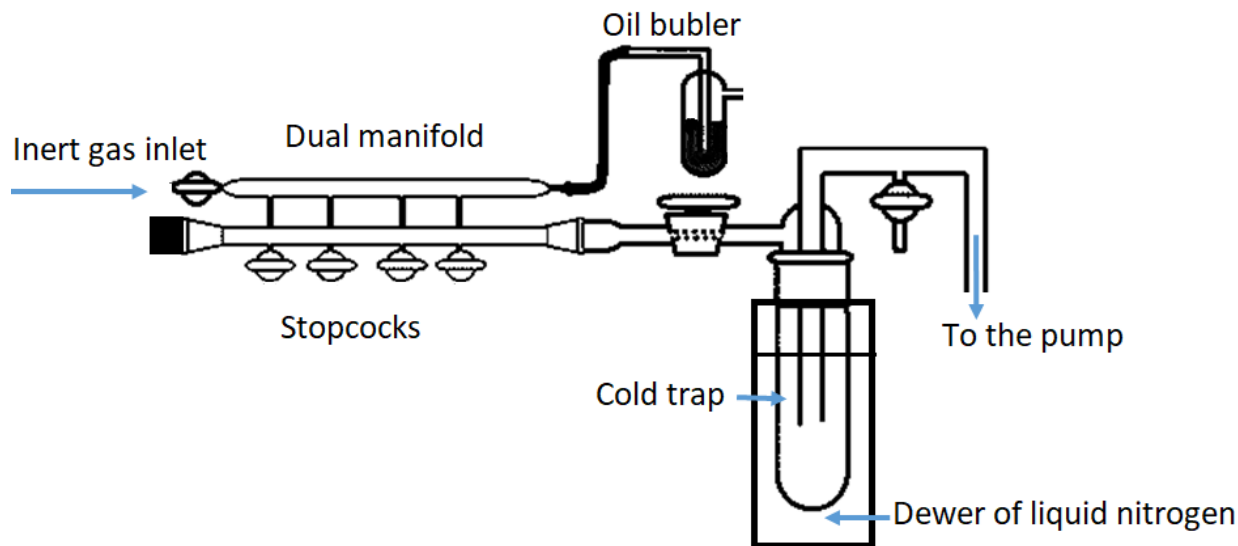


Figure 2.2. Schematic diagram of the Schlenk line (Adopted from ref.¹⁴⁷)

2.2.3. Tube furnace

The tube furnace (Figure 2.3) is an electric heating device consisting of heating coils embedded in a thermally insulating matrix. The temperature of the furnace can be controlled and monitored by a temperature controller and a thermocouple, respectively. The temperature controller is used to control the ramping rate and soaking time. The sample is usually placed on a combustion boat within a fused silica tube and placed in the furnace. The tube can be connected to one or more gas resources. The flow controllers are used to control the flow rate of different gases. This allows the sample to be treated under the required atmosphere.¹⁴⁸ In this dissertation, a tube furnace was used to perform an after-synthesis purification (remove surface-bound ligands) on as-prepared nanoparticles.

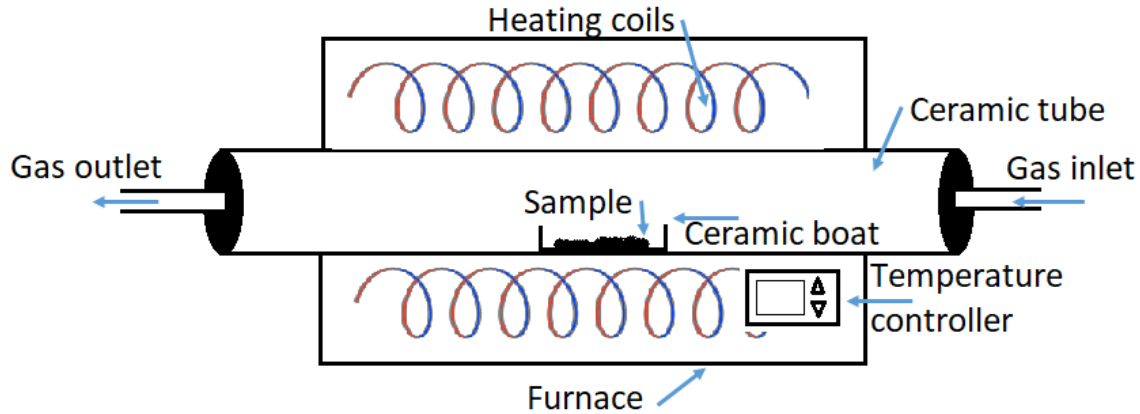


Figure 2.3. Schematic diagram of the horizontal furnace system

2.3. Material characterization techniques

2.3.1. Powder X-ray diffraction (PXRD)

In X-ray diffraction (XRD), X-rays interact with the lattice of a crystalline phase, and a diffraction pattern is created. This X-ray diffraction pattern is unique for different crystalline materials. Therefore, the XRD pattern can be considered as a "fingerprint" of a material. Since there are many XRD patterns of different material crystalline phases that have been collected and stored as standards, this technique can be used to identify the crystalline phases in a newly created sample by reference to standard XRD patterns.

Inside a tube, a metal target (typically Cu or Ni) is struck by a high-energy electron beam to generate X-rays. This is called an X-ray generating tube (Figure 2.4). Electrons are generated by passing a current through a tungsten filament. Then these electrons are accelerated from cathode to anode by applying an acceleration voltage. At the anode collision between the high-energy electron beam and the metal target results in X-ray generation. A transparent beryllium (Be) window enables X-rays to pass through toward the sample. Cold water flow is usually used in cooling the metal target as the heat generated by the high-energy electrons can melt the metal. A

rotating anode provides more surface area of the metal target that is exposed hence, enables the production of a high current via the generation of more significant X-ray flux.

This generated X-ray radiation has white radiation, with a continuous spectrum of wavelengths, and characteristic radiation. White radiation occurs due to the loss of energy of the electrons in the metal-electron collision. When the energy of the accelerated electrons is enough to overcome a particular threshold value, characteristic radiation is emitted. The characteristic radiation consists of monochromatic X-rays arising from the target metal atom ionization. In the case of the Cu ($1s\ 2s\ 2p\ 3s$) metal target, some of the Cu $1s$ electrons (in the K shell) are ionized in the collision event, resulting in a vacant site. An electron from a higher atomic level ($2p$ or $3p$ orbitals) can drop into that vacant inner orbital while emitting an X-ray photon, which is characteristic of the energy difference between the two orbitals (Figure 2.5). A monochromatic filter is used to pass only $K\alpha$ radiation toward the sample to get a better resolution.

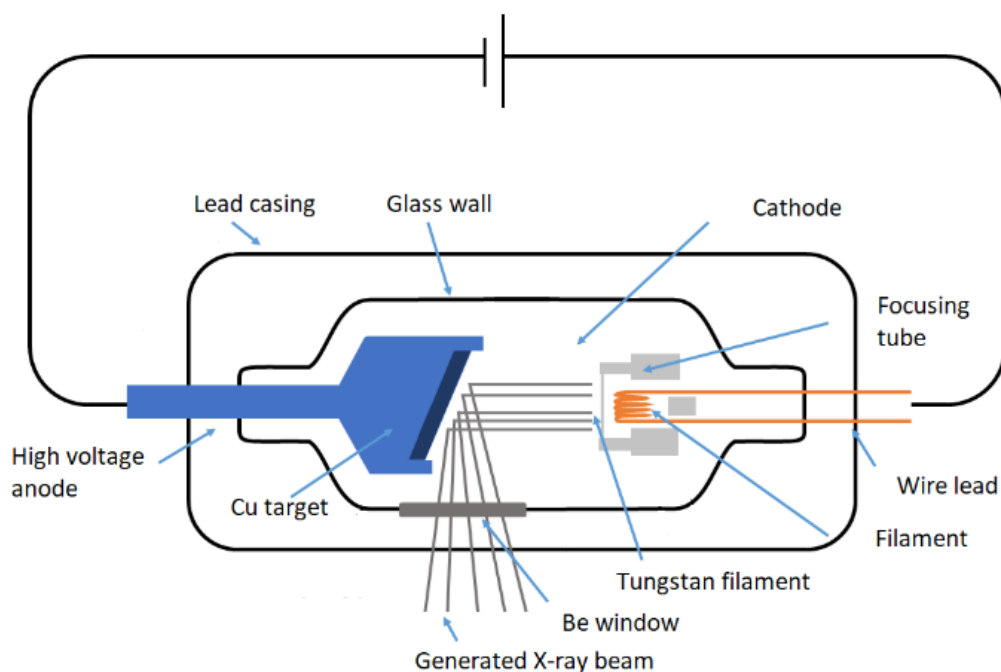


Figure 2.4. Schematic diagram of X-ray generation inside an X-ray tube (adapted from ref.¹⁴⁹)

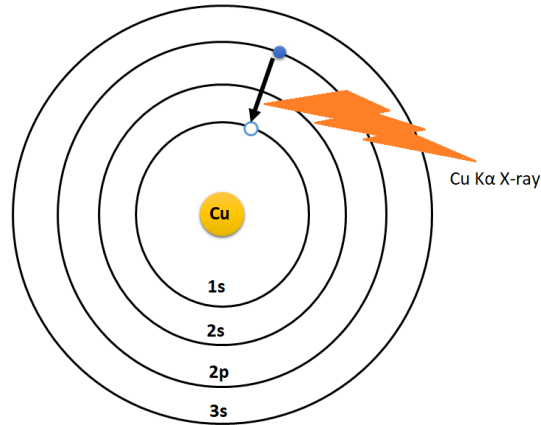


Figure 2.5. Illustration of Cu $K\alpha$ X-ray generation from electron transition from 2p to 1s (adapted from ref.¹⁵⁰)

In crystalline solids, atoms are arranged in a repeating structure. The smallest volume element is called a unit cell, which is repeated in three dimensions. When an X-ray beam hits a sample, electrons around can oscillate with the same frequency as the beam. In most directions, the oscillation interferences are destructive (combining waves are out of phase); therefore, no energy leaves the solid sample. However, due to the regular arrangement of atoms in a crystalline phase, interference could be constructive (waves are in phase) in some directions; hence, there is an X-ray beam leaving the sample in specific directions. Assume an X-ray beam (I_1 , I_2) hits a pair of parallel planes of a crystalline solid, with an interplanar spacing d , there are two parallel X-ray beams (D_1 , D_2) making an angle (θ) with the planes (Figure 2.6). If D_1 and D_2 are in phase, then the reflected beam of maximum intensity results. Thus, the difference between I_1 to D_1 and I_2 to D_2 in the path length is an integer number of wavelengths. This relationship is expressed by Bragg's law (Equation 2.1). Using Bragg's law, we can find the corresponding d value for a crystalline material, which is directly related to the lattice parameters (a , b , c) and the structure plane parameters (h , k , l). The intensity of the reflected beam is determined by the electron distribution in the unit cell, and the peak positions are determined by the size and the shape of the unit cell.

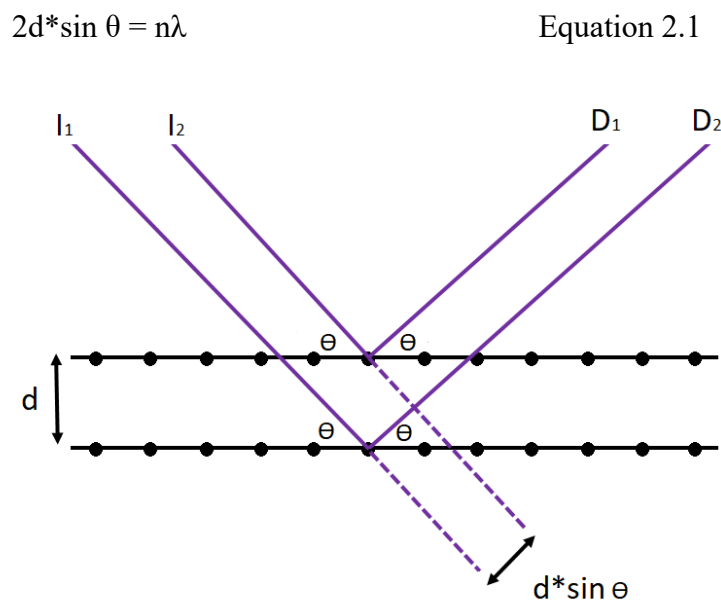


Figure 2.6. Illustration of Bragg's law (adapted from ref.¹⁵⁰)

Compared to bulk crystalline materials, The PXRD patterns of nanoparticles are broader. That is due to a fewer number of planes, and hence, the beams undergo partial interference around the ideal Bragg angle. The size of the nanocrystal can be calculated using the Scherrer equation (Equation 2.2). Where D is the average size of the nanocrystal, λ is the wavelength of X-ray radiation, β is the full width at half maximum (FWHM) in radians and θ is the Bragg angle.

$$\beta = \frac{0.9\lambda}{(\text{FWHM}) \cos \theta} \quad \text{Equation 2.2}$$

In this dissertation study, PXRD patterns were acquired at room temperature on a Bruker Phaser II model X-ray diffractometer equipped with a Cu anode. The X-ray generating voltage is 40 kV, and the current is 150 mA. A zero-background quartz holder was used as the sample holder. The acquired PXRD patterns are identified by comparing them with the phases in the international center for diffraction data (ICDD) powder diffraction file (PDF) database.

2.3.2. Transmission electron microscopy (TEM)

With the invention of transmission electron microscopy (TEM) by Max Knoll and Ernst Ruska in 1931, a tremendous development in the characterization and visualization of materials on the nano level or atomic level has happened. This significantly affected the nanotechnology field, where the TEM became an essential tool for the characterization of nanoparticle size, shape, and morphology. Due to the extremely short de Broglie wavelength of electrons, TEM has a significantly higher resolution than the optical microscope. Compared to light, electrons are preferred to have a high resolution as the wavelength of electrons can be tens of thousand times smaller than a photon at similar energies. The wavelength of the electrons can be easily tuned with an acceleration voltage, and the electron beams can be controlled by a magnetic field, as electrons have a charged nature. Also, electrons scatter strongly as they can interact with both the nucleus and the electrons of the atoms in the specimen. Different processes can take place when a sample is bombarded with a beam of electrons (Figure 2.7). Among these processes, the transmitted electrons are used for transmission electron microscopy (TEM). X-rays can be used for energy dispersive spectroscopy (EDS), which is discussed in detail in section 2.3.3.

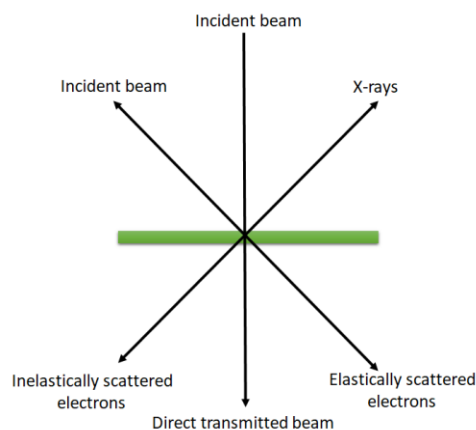


Figure 2.7. Different processes happen when bombarded electrons interact with a specimen (adapted from ref.¹⁵¹)

Figure 2.8 shows a schematic diagram of a typical TEM instrument's basic components. Two types of electron sources are used in TEM. One is called a thermionic source, where a tungsten (W) or lanthanum hexaboride (LaB_6) filament is heated. The other is a field emission source, where fine tungsten needles are used as the field emitters. Although the majority of TEMs use a thermionic source, the electrons generated from thermionic sources are less monochromatic. Also, the W filament or LaB_6 crystals can gradually evaporate or oxidize, making their life more limited. In field-emission sources, a powerful electric field ($\sim 10^9 \text{ Vm}^{-1}$) is used to extract the electrons from the tungsten needles. Therefore, the temperature needed is lower than the thermionic source. Hence, the lifetime of the filament is longer. Also, the electrons generated from the field emission source are monochromatic, and brightness is much higher compared to thermionic sources. These advantages make the field emission source more popular. However, the field emission sources require a rigorous high vacuum environment.

Generally, the electron accelerating voltage in the TEM is between 100 kV and 400 kV. This voltage determines the wavelength of the generated electrons. The relationship between the voltage of the electrons and their wavelength can be expressed as shown in Equation 2.3, where m_0 is the mass of the electron, E is the kinetic energy, h is Planck's constant, and λ is the wavelength. After electron production, the electrons are passed through condenser lenses. This controls the intensity and angular aperture of the electron beam before interacting with the specimen. Objective lenses are present for beam focusing. Then the electron beam that comes through the specimen and the intermediate projective lenses expand the beam on the viewing screen. In TEM, transmitted radiation is used. Therefore, it depends on the atomic number of the elements and the sample thickness. So, in sample preparation, it is important to make sure it is uniformly deposited and suitably thin ($< 1000 \text{ \AA}$) to obtain a high-quality image.

$$\lambda = \frac{h}{(2m_0E)^{0.5}} \quad \text{Equation 2.3}$$

There are two basic imaging modes in TEM (Figure 2.9). The diffracted beams are blocked by an objective aperture in the bright field mode, so only the direct beam reaches the screen. Here the material appears in the dark within a bright background. Whereas in the dark field mode, images of material are bright in a dark background as only the diffracted beams reach the screen while the direct beam is blocked.

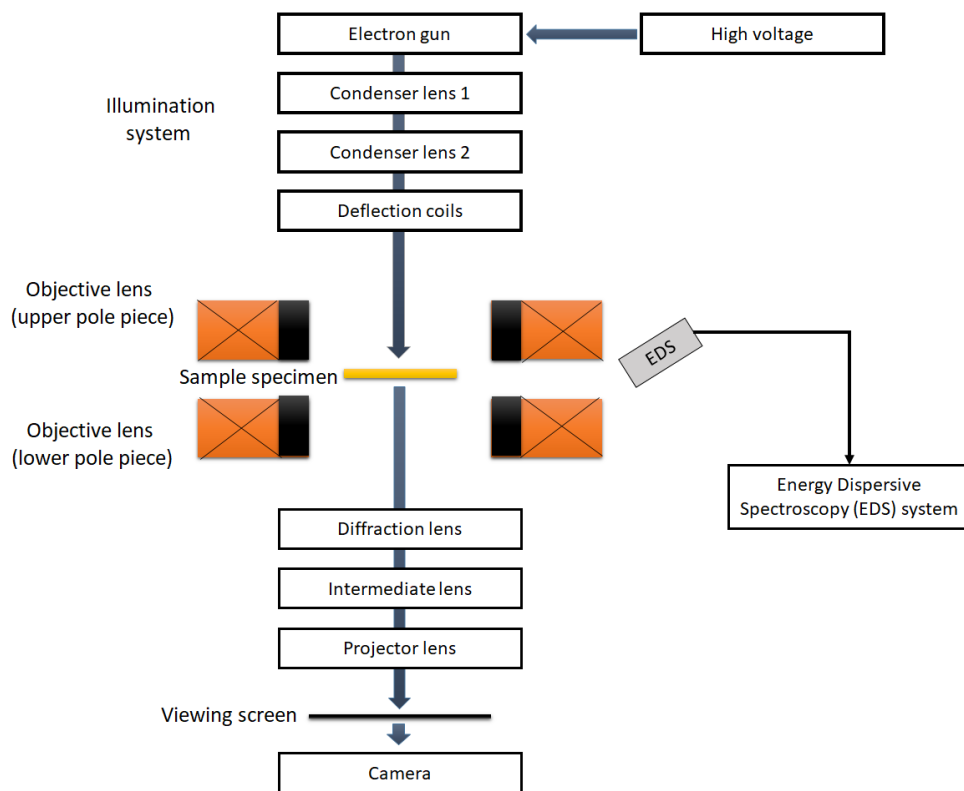


Figure 2.8. Schematic diagram of basic components of a TEM instrument (adapted from ref. ¹⁵²)

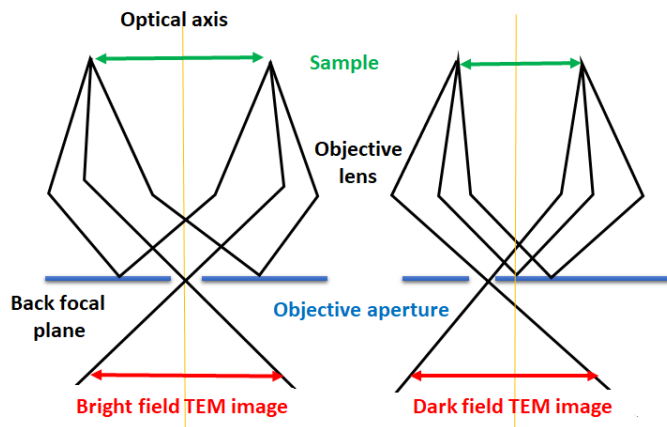


Figure 2.9. Bright field and dark field imaging modes of TEM (adapted from ref.¹⁵¹)

In this dissertation work, TEM images were collected using a JEOL 2010 electron microscope that operates at a voltage of 200 kV. Bright field images were collected via Amtv 600 software. TEM specimens were prepared by dispersion of nanoparticles in the desired solvent and depositing a drop of solution on a carbon-coated 200 mesh grid (Cu, Ni, or Au), followed by drying in air.

2.3.3. Energy dispersive spectroscopy (EDS)

Energy dispersive spectroscopy (EDS) is used to determine the chemical composition of a compound. EDS is typically associated with either a transmission electron microscope (TEM) or a scanning electron microscope (SEM). When an electron beam strikes a specimen, atoms can be ionized hence, generating holes. To fill the holes, electrons from outer shells jump into the holes releasing characteristic X-rays. These energies of these characteristic X-rays depend on the identity of the element and the difference in energy between the hole and source of the outer shell electron.

EDS detectors are usually a semiconductor device (lithium doped silicon or high purity germanium). When released X-rays strike the detector, it generates a charge pulse. This charge pulse is proportional to the X-ray energy. A pulse processor converts these pulses to a voltage, and

elements can be identified relative to the voltage value where a peak appears. Figure 2.10 illustrates the basic components of an EDS system.

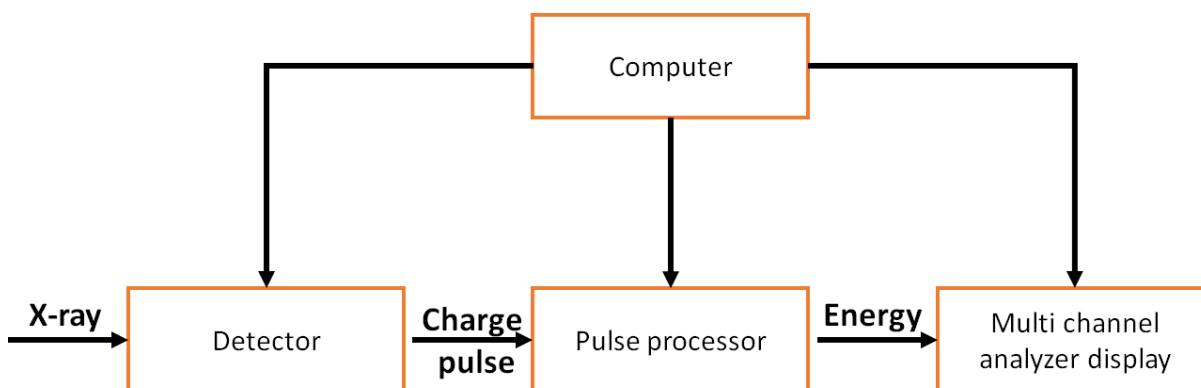


Figure 2.10. Basic parts of an EDS system (adapted from ref.¹⁵²)

In this dissertation study, an EDAX, Inc. detection unit associated with JEOL 2010 TEM was used. EDS was employed to determine the elemental compositions of the synthesized nanoparticles. The atomic weight percentages of nanomaterials were determined using EDAX Genesis software.

2.3.4. X-ray photoelectron spectroscopy (XPS)

X-ray photoelectron spectroscopy (XPS) is a surface analyzing technique that measures the chemical environment and oxidation states of surface elements of materials. The technique uses X-rays, which are usually produced by an Al or Mg source. The sample is irradiated with X-rays, and electrons at core levels absorb the photon energy and are ejected. The kinetic energy (E_K) and the number of ejected electrons are measured by the XPS instrument (Figure 2.12), and using Equation 2.4, it calculates the binding energy (E_B). E_P is the photon energy, which depends on the metal source used for X-ray production, and ϕ represents the work function of the instrument. The binding energy of an ejected electron is specific to an element and varies with the elemental electron configuration. Therefore, it can be used to identify the element as well as their oxidation state or the binding environments.

$$E_B = E_P - (E_K + \phi) \quad \text{Equation 2.4}$$

In this work, A NEXSA Thermo Fisher Scientific instrument was used with a monochromatic Al K α (1486.7 eV) X-ray source operating at 6 mA and 12 kV. The work function was calibrated to give binding energy of 83.98 eV for Au4f7/2. The spot size is 400 μm . The surface charges were neutralized using a focused low-energy electron beam. Spectrometer resolution details: Ag 3d5/2 core line FWHM at 10 eV pass-energy = 0.5 eV; instrumental resolution = 0.38 eV. XPS was conducted for selected pre-catalyst and post-catalyst samples supported on C cloth. Samples were sputtered at 2 keV with Ar $^+$ for 90 seconds before collecting the spectra. The scan details are shown in Appendix A. A Thermo Advantage v5.9922 software was used to analyze the collected high-resolution spectra, and binding energies were calibrated against the C 1s peak at 282.8 eV.

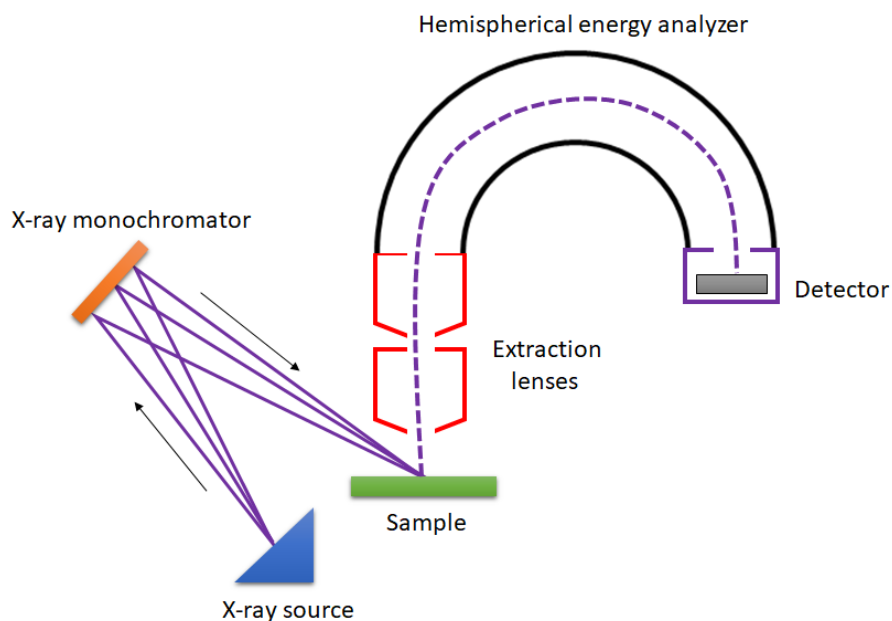


Figure 2.11. Schematic illustration of an XPS (adapted from ref.¹⁵³)

2.3.5. Infrared spectroscopy (IR)

Infrared (IR) spectroscopy is a valuable tool to identify functional groups present by detecting vibrations in a molecule. This technique uses the infrared region of electromagnetic radiation. The vibrational frequency of a chemical bond depends on the vibration mode, bond strength, and atomic masses. To give an IR signal, the dipole moment of a bond should change with the vibration. This technique is commonly used in organic spectroscopy. To evaluate the efficacy of surfactant removal by annealing during ink processing, we collected IR data before and after the heat treatment using a Bruker Tensor 27 FTIR-spectrometer with OPUS 6.5 software version. The samples were prepared by mixing the composite with dry KBr salt, followed by pressing them into transparent pellets using a 13 mm die set and a Carver press. IR data were collected and referenced to a blank KBr pellet.

2.4. Electrocatalytic testing

2.4.1 Catalytic ink preparation

The ink preparation method was adopted from Mutinda et al.²⁵ 10 mg of nanoparticles were mixed with 5 mg of carbon-black powder. Hexane (10 mL) was added to the mixture, followed by sonication for 30 minutes. The nanoparticle/carbon mixture was then precipitated by adding ethanol, followed by centrifugation. The solids were dried under a vacuum, placed on a ceramic boat, and heated in a tube furnace under 5% H₂/Ar gas flow at 400 °C for 1 hour. After the sample had cooled down to room temperature, the boat was removed, and the solid was suspended in ethanol (2 mL) and sonicated for 15 minutes, after which nano-pure H₂O (1 mL) and isopropanol (1 mL) were added and the mixture sonicated for another 15 minutes. Finally, Nafion solution (1 mL) was added, and the mixture sonicated for a final 15 minutes to produce the ink.

2.4.2 Cyclic voltammetry (CV)

Cyclic voltammetry (CV) can be used to study the electrochemical properties of materials. A typical CV is performed with a standard three-electrode system by measuring the current against a cycling potential. A standard three-electrode system has a working electrode (WE), a reference electrode (RE), and a counter electrode (CE) (Figure 2.13a). The WE is made out of the material of interest, and the potential is applied to the WE, which passes to the analyte. The RE is a half-cell where the reduction potential is known. It controls and measures the potential applied to the working electrode. The CE passes the current in the system and balances the current observed at the WE. With such a CV system, both potential and current can be controlled and monitored in order to study the electrochemical behavior of the analyte.

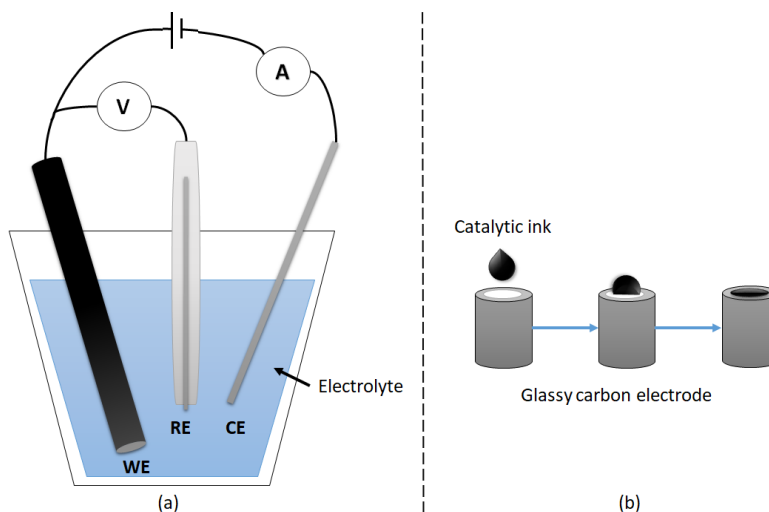


Figure 2.12. a) A standard three-electrode system b) Catalytic ink drop-casting method on a glassy carbon electrode (adapted from ref.⁴⁷)

In this dissertation, CVs were collected using an EC epsilon potentiostat equipped with a rotating disc electrode (RDE) using a standard three-electrode setup. An Ag/AgCl electrode was used as the RE, and the potential was checked against a master Ag/AgCl reference electrode periodically to ensure there was no potential drift from electrode oxidation under strongly acidic/alkaline conditions. A carbon electrode or a Pt wire was used as CE. A glassy carbon electrode

with a surface area of 0.07 cm^2 was modified by drop-casting $10 \text{ }\mu\text{L}$ of nanoparticle/carbon ink onto the surface to get a catalytic loading of 0.285 mg/cm^2 (Figure 3.13b). The electrode was then dried under an infrared heat lamp for 2-3 minutes. Polarization curves were obtained in an electrolyte at a scan rate of 10 mV/s with the RDE operating at 1600 rpm . IR compensation was performed prior to collecting polarization curves by applying IR-COMP using the epsilon software. The potential was measured in reference to the Ag/AgCl electrode and converted to the reversible hydrogen electrode (RHE) scale using Equation 2.5.

$$E_{\text{RHE}} = E_{\text{Ag/AgCl}} + 0.197 + (0.059 \times \text{pH}) \quad \text{Equation 2.5}$$

Double-layer capacitance (C_{dl}) measurements were carried out using the same experimental setup. C_{dl} data were collected pre-catalysis and post-catalysis, and the data were used to calculate the corresponding electrochemically active surface area (ECSA) values. Here forward and reverse CV scans were performed at different scan rates ($20\text{-}100 \text{ mV/s}$) within an energy window of $\pm 50 \text{ mV}$ of the open circuit potential (OCP). Then the double layer capacitance values for each sample were obtained by plotting the current density difference at the OCP against the scan rates. These data were then used to calculate the ECSA for the different samples.

Stability tests were performed in an H-type cell using similar reference electrodes, counter electrodes, and electrolytes as in CV measurements. The working electrode was prepared by drop-casting $140 \text{ }\mu\text{L}$ of selected catalyst ink on a carbon cloth substrate with a geometric surface area of 1 cm^2 and dried under an IR lamp (0.280 mg/cm^2). Before ink drop-casting, the substrate material was cleaned and preheated at $450 \text{ }^\circ\text{C}$ for 2 hours under atmospheric air conditions in a furnace to remove any residual organic material. The fabricated carbon cloth electrode was then used to carry out the long-term stability tests by applying a constant potential on the activated working electrode to get a constant current density.

Cathodic faradaic efficiency measurements were performed in an H-type cell as used for the long-term stability test. Here, the sample was held at a constant potential for a short period of time (~30 min), after which the headspace gas amount was measured using a GOW-MAC series 400 gas chromatograph that was fitted with a TCD detector. Helium gas was utilized as the carrier at a flow rate of 30 mL per minute, whereas nitrogen gas was utilized as an internal standard. In all cases, a blank experiment was carried out with the working electrode without catalytic material and subtracted to produce the reported data.

Overall water splitting activity evaluation was carried out in a two-electrode system, where nanoparticle/carbon composites were utilized as the anode and cathode electrocatalysts,. The electrodes were prepared as described for the long-term stability tests on carbon cloth. CV data were recorded in a single flask with anode and cathode located approximately 1 cm apart. Subsequently, a long-term stability test was carried out at a constant potential.

CHAPTER 3. $\text{Co}_{2-x}\text{Rh}_x\text{P}$ NANOPARTICLES AS ELECTROCATALYSTS FOR THE HYDROGEN PRODUCTION: CATALYTIC STABILITY AND Pt INTERFERENCE

Abstract

Large-scale hydrogen production through electrochemical water splitting is a promising alternative to prevent/limit the usage of traditional fossil fuels, hence mitigating global warming. For the hydrogen evolution reaction (HER), Pt is the most efficient electrocatalyst, but the practical application of Pt is limited due to its skyrocketing prices. Thus, developing alternative electrocatalysts with low/no noble metals content is essential for the widespread adoption of Pt-free HER electrocatalysts with high activity, stability, and efficiency. While many papers have reported testing and evaluation, in some cases, Pt has been employed as a counter electrode without taking the precaution of employing an ion-exchange membrane (PEM) between the working and counter electrodes, it is known that Pt can be oxidized and dissolved under certain chemical or electrochemical conditions such as in acid at applied polarization potentials that are greater than the Pt oxidation potential (>1.2 eV vs. RHE). These oxidized Pt species migrate to the working electrode and deposit, leading to overestimating the working electrode's performance. In this study, we investigated the activity and stability changes of a novel electrocatalyst $\text{Co}_{2-x}\text{Rh}_x\text{P}$ nanoparticles in carbon black composite ($\text{Co}_{2-x}\text{Rh}_x\text{P}$ NP/C) in an acidic and basic medium with a Pt counter electrode vs. a carbon counter electrode under lower applied potentials than the Pt oxidation potential (<0.6 eV vs. RHE). The study revealed that using Pt as a counter electrode for HER even under low applied polarization potentials for an extended time can also affect the working electrode's stability.

3.1. Introduction

Hydrogen gas can be a promising energy carrier to replace traditional fossil fuels, if produced in large quantities through electrochemical water splitting. Up to date Pt is the most efficient electrocatalyst for the water reduction half-reaction, which is hydrogen evolution reaction (HER), but its practical large-scale applications have been greatly limited by its high cost. Thus, developing low-cost water reduction electrocatalyst with comparable catalytic activity to Pt has become extremely important. Different studies done with earth abundant materials based electrocatalytic studies have shown that some materials exhibit comparable activity with Pt based electrocatalysts. For an example, when molybdenum carbide is coupled with reduced graphene oxide (r-GO) it showed almost overlapped HER activity with commercial Pt/C.¹⁵⁴ Also, Ni-C-based catalyst synthesized from carbonization of Ni-based metal-organic frameworks (MOFs) reported a similar HER performance as that of Pt.¹⁵⁵ However, it was noticed that in these studies, Pt was chosen as the counter electrode without applying an ion-exchange membrane across the working and counter electrodes during the electrochemical measurements. A literature study conducted by Chen *et al.* found that around 50% of the published HER studies adopted Pt as the counter electrode without using an ion-exchange membrane.¹⁵⁶ Based on thermodynamics, Pt can be oxidized and dissolved under certain chemical or electrochemical conditions such as the presence of chloride in the acidic solution. Chloride will enhance the chemical and electrochemical dissolution of Pt by forming stable chloride complexes (PtCl_3^- , PtCl_4^{2-} , and PtCl_6^{2-}).^{157, 158}

In 2020 Sang and co-workers carried out a study to find out whether Pt can/cannot be used as the counter electrode during the measurement of HER activity. Their study showed that even under the Pt oxidation potential, Pt counter electrode in acidic or basic electrolyte was subject to cause dissolution and redeposition of Pt on the working electrode, and that significantly improves

the HER activity. Therefore, Pt cannot be a suitable counter electrode for measuring the activity of HER.¹⁵⁹

In our recent studies done with the novel electrocatalyst $\text{Co}_{2-x}\text{Rh}_x\text{P}$ nanoparticles in carbon black composite ($\text{Co}_{2-x}\text{Rh}_x\text{P}$ NP/C), we also employed Pt as the counter electrode for the HER activity evaluation in the acidic medium. However, the external applied potential (>0.6 eV vs RHE) was much less than that of the Pt oxidation potential (1.2 eV vs RHE). Therefore, we hypothesized that the effect of Pt on the working electrode might be insignificant in the HER activity performance of the Co-Rh-P system. In order to confirm our hypothesis, we carried out a detailed comparison study where we investigated the HER activity and stability changes of $\text{Co}_{2-x}\text{Rh}_x\text{P}$ NP/C in acidic and basic medium with a Pt counter electrode vs. a carbon counter electrode under lower applied potentials than the Pt oxidation potential. Results revealed that using Pt as a counter electrode for HER in acidic medium even under low applied polarization potential for an extended time can affect the working electrode's stability, while in the basic medium the effect of Pt is insignificant.

3.2. Experimental section

All materials used in the synthesis of $\text{Co}_{2-x}\text{Rh}_x\text{P}$ nanoparticles are reported in Chapter 2.

3.2.1. Synthesis of $\text{Co}_{2-x}\text{Rh}_x\text{P}$ nanoparticles

$\text{Co}_{2-x}\text{Rh}_x\text{P}$ nanoparticle synthesis was carried out according to the procedure developed by Mutinda *et al.*²⁵ A series of $\text{Co}_{2-x}\text{Rh}_x\text{P}$ nanoparticles was synthesized using stoichiometric amounts of $\text{RhCl}_3 \cdot n\text{H}_2\text{O}$ and $\text{Co}(\text{acac})_2$ metal precursors according to Table 3.1. The metal precursors were dissolved in a mixture of 15 mL of oleylamine and 5 mL 1-octadecene. The mixture was degassed at 110 °C for 30 min, then purged with Ar. The temperature was increased to 230 °C and maintained for 9 hours. Then 6 mL of trioctylphosphine was injected and the mixture was maintained at 230

°C for another 3 hours. Then the reaction temperature was adjusted to 310 °C – 350 °C (temperature selected based on composition targeted, see Table 3.1) and maintained for 3 hours. The product was then purified by sequential dispersion in chloroform and precipitation with ethanol.

Table 3.1. Quantities of metal precursors employed in synthesis of $\text{Co}_{2-x}\text{Rh}_x\text{P}$ nanoparticles and phosphidation temperature as a function of x

Targeted composition	Co(acac) ₂ / mmols	RhCl ₃ .nH ₂ O/ mmols	Phosphidation temperature/ °C
Co _{0.25} Rh _{1.75} P	0.048	0.336	350
Co _{0.50} Rh _{1.50} P	0.096	0.285	350
Co _{0.75} Rh _{1.25} P	0.143	0.240	350
Co _{1.00} Rh _{1.00} P	0.192	0.192	330
Co _{1.50} Rh _{0.50} P	0.285	0.096	330
Co _{1.75} Rh _{0.25} P	0.336	0.048	310

3.2.2. Synthesis of Co₂P nanoparticles

Co₂P nanoparticles were synthesized in a similar manner to that reported by Robinson's group.¹⁶⁰ 0.44 mmol of Co₂(CO)₈ was dissolved in a degassed solvent mixture of 15 mL 1-octadecene and 3 mL oleylamine. Then the mixture was aged at 200 °C for 1.5 hours followed by injection of 0.2 mL of TOP. The temperature was increased to 300 °C and held constant for 1.5 hours. The product was then cooled naturally to room temperature, washed and recovered in the same way as outlined in 3.2.1.

3.2.3. Synthesis of Rh₂P nanoparticles

The synthetic strategy was adopted from the literature reported procedure of Schaak group.¹⁶¹ 0.38 mmol of RhCl₃.nH₂O was dissolved into a mixture of 5 mL 1-octadecene and 15 mL oleylamine. The mixture was degassed at 110 °C for 30 minutes, followed by aging at 230 °C for 90 minutes. 6 mL of TOP was injected into the solution, after that the temperature was increased to 350 °C. The reaction mixture was then held at the same temperature for 3 hours and the product was isolated after cooled down, by purifying as described in 3.2.1.

3.2.4. Characterization

Powder X-ray diffraction (PXRD), Transmission electron microscopy (TEM) equipped with an energy dispersive X-ray spectroscopy (EDS, EDAX, inc.), and X-ray photoelectron spectrometry (XPS) were operated as mentioned in Chapter 2.

3.2.5. Electrocatalytic testing

A catalytic ink was prepared using $\text{Co}_{2-x}\text{Rh}_x\text{P}$ nanoparticles, and electrocatalytic activity, stability, and efficiency tests were performed following protocols in Chapter 2. Here, we used 0.5 H_2SO_4 or 1 M KOH as electrolyte solutions, while a carbon rod/ Pt wire electrode (for comparison) was used as counter electrodes.

3.3. Results and discussion

Different compositions of $\text{Co}_{2-x}\text{Rh}_x\text{P}$ nanoparticles capped with oleylamine/trioctylphosphine ligands were prepared by solution-phase arrested precipitation reactions according to our established protocol.²⁵ Powder X-ray diffraction (PXRD) data confirm our previous findings (Figure 3.1): Rh-rich phases adopt the cubic antiferite structure whereas Co-rich phases adopt the orthorhombic Co_2P structure; diffraction peaks shift systematically with the change in the composition (i. e., change in ionic radius), consistent with solid-solution formation. While we have seen evidence for mild phase segregation in $\text{Co}_{1.00}\text{Rh}_{1.00}\text{P}$ in the past, the samples prepared here reveal discernable diffraction peaks only for antiferite. Transmission electron microscopy (TEM, Figure 3.2) data were also consistent with prior studies, demonstrating a distinct particle size/morphology correlation to the structure. Co-rich phases form relatively large (10–20 nm diameter) irregularly-shaped (in some cases, rod-like) and spherical particles, often with hollow voids at their centers that are consistent with the Kirkendall effect. Rh-rich phases form small, solid spheroids with sizes of 3–5 nm. The $\text{Co}_{1.00}\text{Rh}_{1.00}\text{P}$ phase is morphologically

similar to the Co-rich phases, with spheroids and irregularly shaped/rod-like features ranging in size from 5–20 nm in their largest dimension, with a few voids.

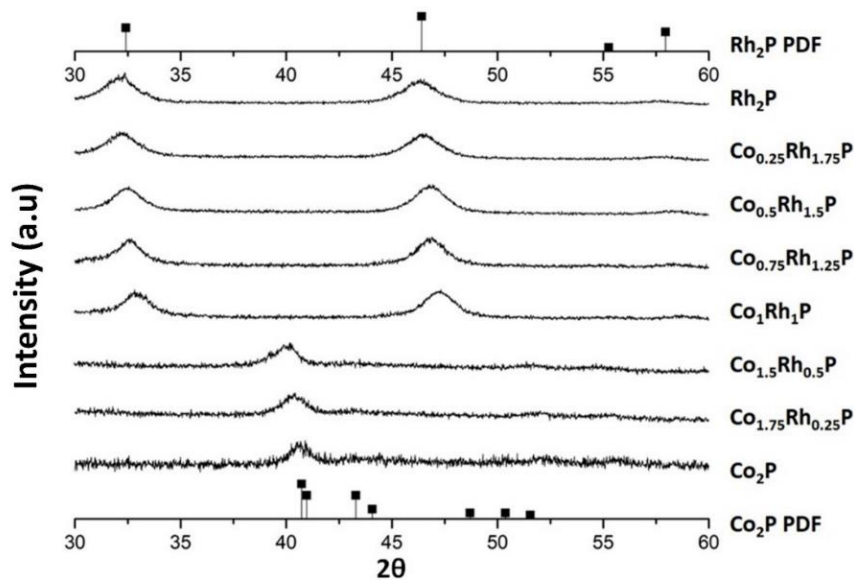


Figure 3.1. PXRD data for Co_2P , Rh_2P and $\text{Co}_{2-x}\text{Rh}_x\text{P}$ nanoparticles with reference stick patterns (powder diffraction files, PDFs) for Co_2P (bottom) and Rh_2P (top)

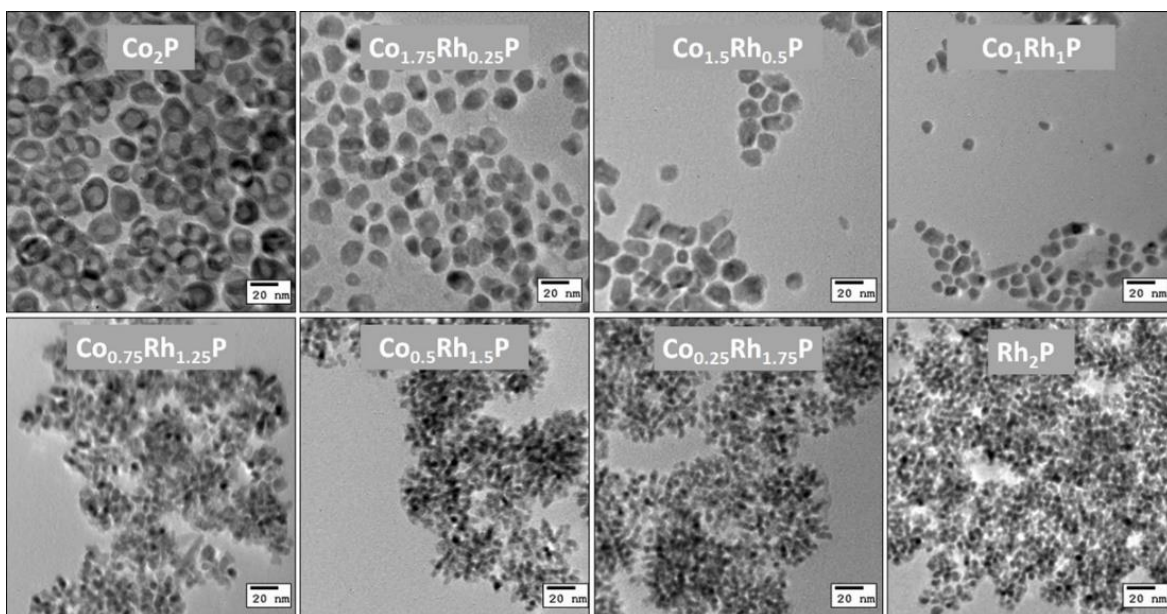


Figure 3.2. Representative TEM micrographs of different compositions of $\text{Co}_{2-x}\text{Rh}_x\text{P}$ nanoparticles.

A nanoparticle ink was prepared by our standard method.²⁵ An ink with a concentration of 2 mg nanoparticles/mL was used in electrocatalytic testing.

3.3.1. Electrochemical activity in acidic medium

To probe the effect of composition on the HER catalytic performance of $\text{Co}_{2-x}\text{Rh}_x\text{P}$ nanoparticles, polarization curves for different compositions were recorded at 10 mV/s under identical conditions for comparison purposes. Figure 3.3a shows a compilation of HER polarization curves for the different compositions that were examined, while Figure 3.3b presents a comparison of the respective overpotentials at 10 mA/cm² (geometrical surface area). Scrutinizing the data clearly reveals that the HER performance of $\text{Co}_{2-x}\text{Rh}_x\text{P}$ nanoparticles in acidic media is composition-dependent, with the Rh-rich phases being the most active (i.e., having the lowest overpotential) as compared to the Co-rich ones. It is interesting to note that samples in which $x \geq 1.25$ have a more or less comparable HER performance to that of Rh_2P nanoparticles. For example, compositions with x values of 1.25, 1.50, and 1.75 correspond to overpotential values of 90.5 ± 3.5 , 88.5 ± 0.7 , and 84.0 ± 2.8 mV, which are not statistically different (within 3σ) from the overpotential of pure Rh_2P , 87.5 ± 0.7 mV. Thus, one can dilute rhodium sites with cobalt, up to a composition of $\text{Co}_{0.75}\text{Rh}_{1.25}\text{P}$, while still retaining the catalytic activity of pure Rh_2P .

On the other hand, samples in which $x \leq 1$ all have overpotentials that are above 100 mV. Our previous work showed that the crystal structure of $\text{Co}_{2-x}\text{Rh}_x\text{P}$ nanoparticles varies with composition, where Rh-rich and Co-rich regimes adopt the (cubic) antiferite and orthorhombic Co_2P structures, respectively, with a sharp phase transition occurring at the $\text{Co}_{1.00}\text{Rh}_{1.00}\text{P}$ composition. We also showed that although the $\text{Co}_{1.00}\text{Rh}_{1.00}\text{P}$ composition was mostly defined by the cubic phase, there exists a subtle phase separation, where impurities of the orthorhombic phase were observed.²⁵ While we do not detect any phase segregation in our PXRD pattern, the

sensitivity of the technique is limited, particularly when characterizing nanomaterials., the somewhat abrupt difference in HER activity between the $\text{Co}_{0.75}\text{Rh}_{1.25}\text{P}$ and the $\text{Co}_{1.00}\text{Rh}_{1.00}\text{P}$ compositions could, therefore, be due to the presence of orthorhombic phase impurity in the $\text{Co}_{1.00}\text{Rh}_{1.00}\text{P}$ composition.

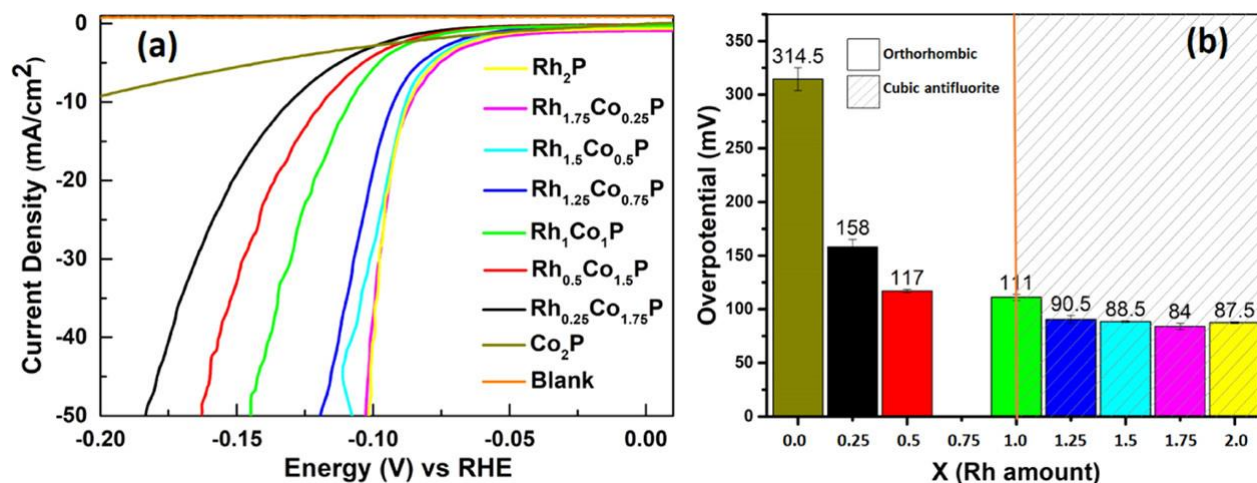


Figure 3.3. (a) HER polarization curves for $\text{Co}_{2-x}\text{Rh}_x\text{P}$ nanoparticles compared to those for Rh_2P and Co_2P end points. (b) Overpotentials at 10 mA/cm^2 (geometrical surface area)

According to Sang *et al.*, when applying potentials in catalytic HER in an acidic medium, there is a possibility of dissolving and depositing platinum from the Pt counter electrode on the working electrode at higher voltages ($1.6\text{--}2.0 V_{\text{RHE}}$).¹⁵⁹ Even though our systems are operating at low potentials, additional experiments replacing the Pt counter electrode with C were performed for the selected composition $\text{Co}_{0.75}\text{Rh}_{1.25}\text{P}$. According to the polarization curves and overpotential values exhibited, there is no significant difference in activity between data collected with the Pt vs the C counter electrode (Figure 3.4).

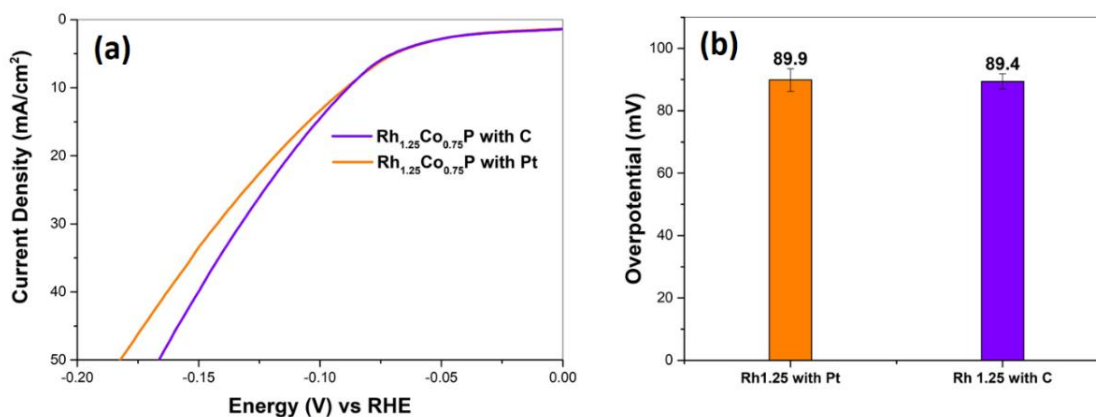


Figure 3.4. Comparison between the HER activity with Pt counter electrode vs. C counter electrode for Co_{0.75}Rh_{1.25}P: (a) Polarization curves; (b) Overpotential values at 10 mA/cm² geometric

3.3.2. Long term stabilityo faradaic efficiency and Pt interference in acidic medium

Long term stability measurements were conducted on the Co_{0.75}Rh_{1.25}P system, as shown in Figure 3.5, by applying a constant potential on the working electrode and recording the resulting current density with both Pt and C counter electrode. The Co_{0.75}Rh_{1.25}P composition was chosen in lieu of Co_{0.25}Rh_{1.75}P as the increased Co concentration makes it easier to assess the speciation of Co in the samples as a function of treatment. As shown in Figure 3.5, when Pt is used as counter electrode, the initial current density of 10mA/cm² is stable over the 9-hour test. However, when C is the counter electrode, the initially high activity falls over the first half-hour, to 5 mA/cm², and then remains steady for the remainder of the test. These data suggest that Pt is playing an active role in stabilizing the electrode.

To better understand the system, the surface chemical state of the electrocatalyst material was analyzed using XPS before and after 1 h and 9 h of stability testing, comparing Pt and C as counter electrodes (Table 3.2, Figure 3.6). Before the catalytic activity tests in the freshly prepared Co_{0.75}Rh_{1.25}P/C ink, cobalt primarily existed in its oxidized forms (Co²⁺ and Co₃O₄, peaks between

779-785 eV) while rhodium was predominantly $\text{Rh}^{\delta+}$ (~ 307 and ~ 312 eV), see Appendix B. for peak assignments and references. The rhodium spectrum also reveals the presence of shoulder peaks at ~ 309 and ~ 314 eV, which confirm the presence of a low concentration of Rh^{3+} ions in the material. The phosphorus spectrum, on the other hand, reveals the coexistence of both zero-valent (~ 130 eV) and oxidized states (P^{5+} , ~ 134 eV), with the oxidized form in excess. The presence of oxidized Rh, Co, and P in the sample can be attributed to surface oxidation, which was also found to occur in the pure Rh_2P electrocatalyst.¹⁶² Intriguingly, before catalysis, we see that the Rh is actually in deficit relative to Co. The ideal Rh/Co ratio should be $1.25/0.75 = 1.67$; however, XPS gives a ratio considerably different: $0.86/1.14 = 0.75$, suggesting the surface is quite Co-rich. Additionally, P is unexpectedly low, with a M/P ratio observed of $2/0.55 = 3.63$ instead of $2/1 = 2$.

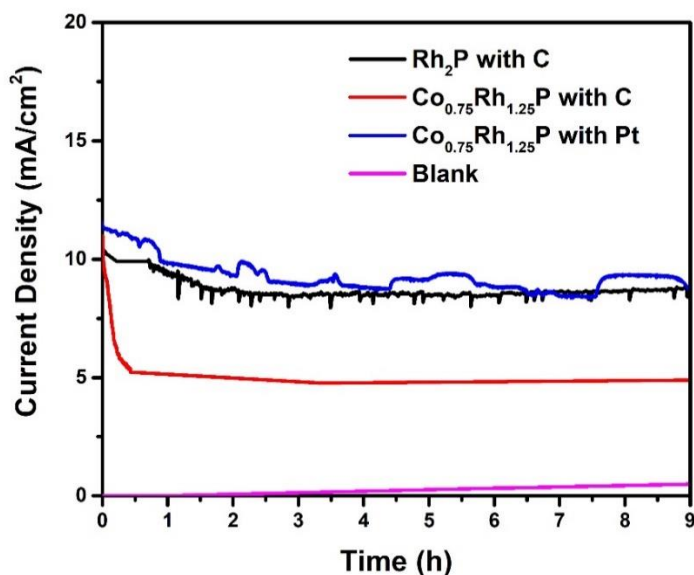


Figure 3.5. Long term HER stability test for $\text{Co}_{0.75}\text{Rh}_{1.25}\text{P}$ with C and Pt counter electrodes and Rh_2P with C counter electrode

Table 3.2. Calculated atomic (Rh, Co, P, Pt) and oxidation state (Rh, P) percentages on the surface of $\text{Co}_{0.75}\text{Rh}_{1.25}\text{P}/\text{C}$ electrocatalysts from XPS data acquired before and after 10 h stability tests with either carbon or platinum counter-electrodes

	Atomic %				% Contribution to elemental signal			
	Rh	Co	P	Pt	Rh ^{δ+}	Rh ³⁺	P ⁰	P ⁵⁺
Before	33.68	44.74	21.58	-	63.72	36.31	17.52	82.48
1h/C	67.94 ±2.77	7.69 ±2.70	24.37 ±0.07	-	70.16 ±12.65	29.89 ±9.04	30.65 ±9.58	69.33 ±9.32
9h/C	69.38 ±3.11	8.63 ±6.65	22.00 ±3.54	-	62.62 ±28.36	37.38 ±28.66	36.96 ±21.73	63.06 ±11.24
1h/Pt	73.07	5.84	19.34	1.75	36.02	63.97	35.94	64.12
9h/Pt	73.66	-	18.52	7.82	36.18	63.82	49.78	50.22

Regardless of counter electrode, XPS data reveal significant depletion of Co at the catalyst surface in all cases (Table 3.2), with the P atomic percentage remaining largely constant ($\text{M}/\text{P} = 3.31$), and the Rh concentration going up to compensate for Co loss ($\text{Rh}/\text{Co} = 8.44$). However, when Pt wire was employed as the counter electrode, Pt deposition on the working electrode can be seen after 1 hour (Figure 6*l*), and the amount has increased after 9 hours (Table 3.2). The speciation of Rh is also sensitive to the presence of Pt, with Rh³⁺ the dominant species when Pt is present, whereas the more reduced Rh^{δ+} associated with the phosphide is dominant in the absence of Pt, and in concentration comparable to that in the pre-catalyst. The speciation of P, on the other hand, is similar regardless of counterelectrode identity, corresponding to a modest increase in the ratio of P⁰/P⁵⁺ relative to the pre-catalyst. Notably, Rh₂P does not deactivate when carbon is the counter-electrode (Figure 3.5). These data suggest that substitution of Co for Rh within the antiferroite structure type does not change the native activity of the catalyst (i.e., initial overpotential at 10mA/cm²), but does set it up for partial deactivation due to Co leaching under catalytic conditions. The use of the Pt counterelectrode masks this activity/composition relationship, as the Pt likely compensates for Co loss and may even be displacing Rh as active catalyst (consistent with Rh³⁺ formation when Pt is present). An interesting take-away from this

study is the notion that activity is more closely tied to the structure than to Rh/Co ratio; i.e., if Co (or possibly another metal) can be incorporated into the antifluorite structure type and mechanisms for base-metal etching can be shut down, Rh₂P activity can be maintained with considerably smaller atomic percentages of Rh. It is worth noting that after Co loss, activity again stabilizes, suggesting that the remaining Rh has not lost its activity.

Faradaic efficiency tests are consistent with an electrochemical process associated with the initial deactivation step. Notably, in the presence of the Pt counter electrode, selectivity to H₂ evolution is ca 100% (See Figure 3.7), whereas for Rh_{1.25}Co_{0.75}P it is 88% over the first hour, where the potential is falling, but 100% over the next hour, after the potential stabilizes. As this time period correlates to the initial deactivation and loss of Co we surmise that some of the current density may be contributing to the Co dissolution process.

Since the acidic medium activity didn't show stable activity with C counter electrode and the stability gained with Pt counter electrode came with overestimated activity due to Pt metal deposition on the working electrode, the electrolyte media was change from 0.5 M H₂SO₄ to 1M KOH and carried out a series of experiments were carried out to evaluate catalytic activity and stability of Co_{2-x}Rh_xP nanomaterial.

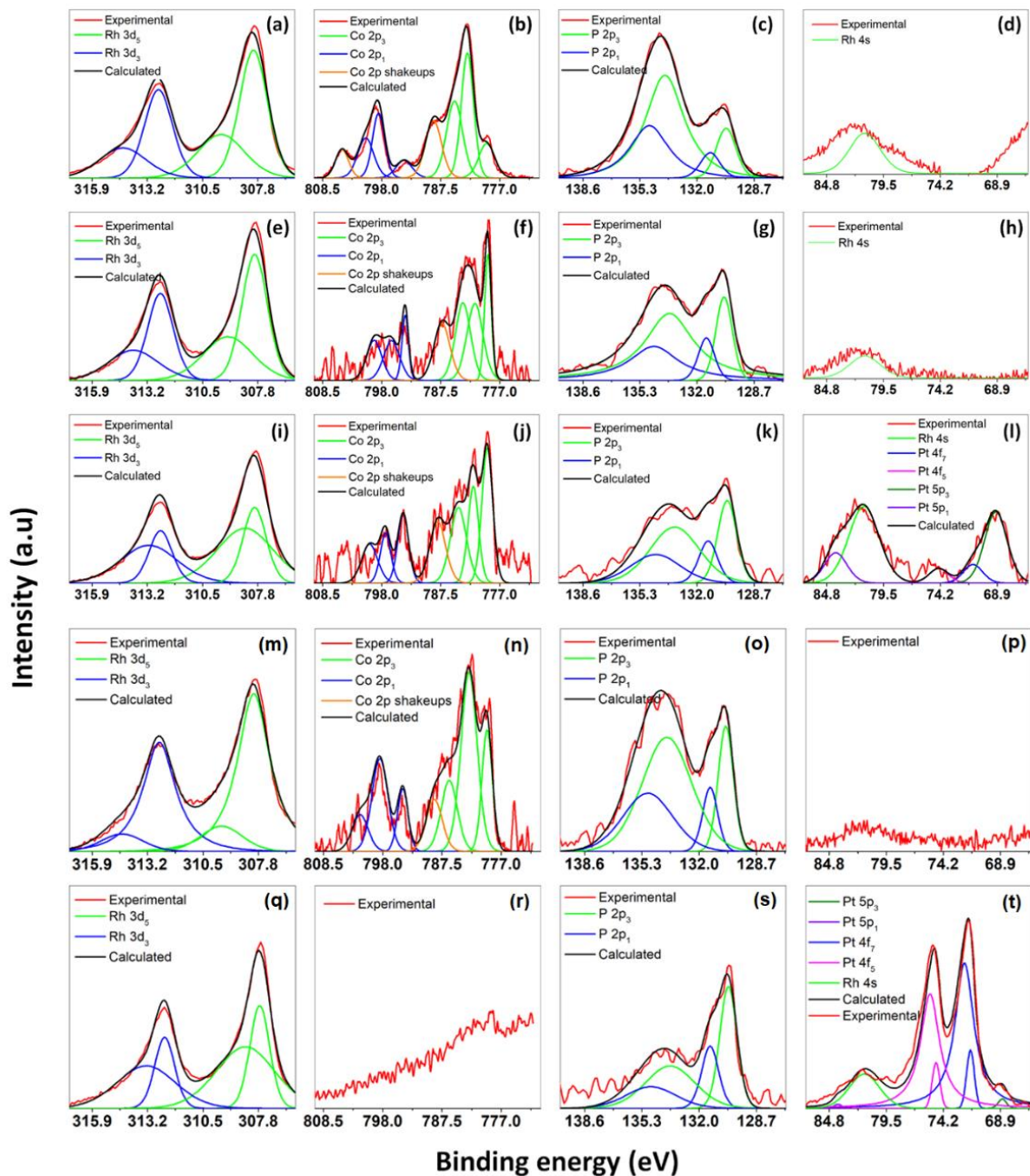


Figure 3.6: XPS data for the freshly prepared (a-d) and used $\text{Co}_{0.25}\text{Rh}_{1.75}\text{P}/\text{C}$ electrocatalysts: after applying constant potential for 1 hour with C counter electrode (e-h), after 1 hour with Pt counter electrode (i-l), after 9 hours run with the C counter electrode (m-p) and after 9 hours with Pt counter electrode (q-t)

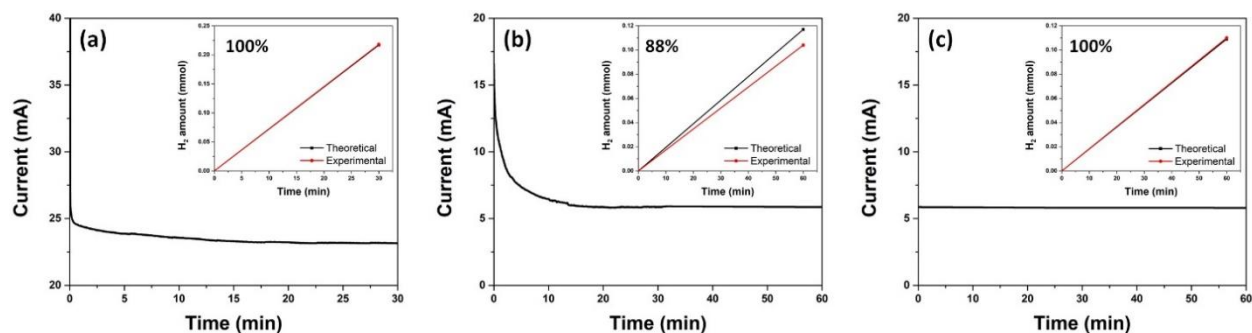


Figure 3.7. Faradaic efficiency data of (a) Co_{0.25}Rh_{1.75}P electrocatalyst with Pt counter electrode collected for 30 min, (b) Co_{0.75}Rh_{1.25}P electrocatalyst with C counter electrode collected for an initial 60 min, and (c) Co_{0.75}Rh_{1.25}P electrocatalyst with C counter electrode collected over an additional 60 min relative to Figure 3.7(b)

3.3.3. Electrochemical activity in basic medium

The HER activity of Co_{2-x}Rh_xP nanoparticles as well as a commercial 20%Pt/C catalyst reference was evaluated on a glassy carbon rotating disk electrode in a 1M KOH electrolyte solution. Figure 3.8 shows the HER polarization curves as a function of x, along with the overpotentials that were required to deliver a current density of 10 mA/cm²_{geometric}. As evidenced from the data, all samples with some degree of Rh incorporation outperformed the 20% Pt/C reference standard, with the Co_{0.25}Rh_{1.75}P composition the most active (overpotential = 58.1 mV), and the Rh-free Co₂P the least active (overpotential = 188.1 mV). The 20% Pt/C reference has an overpotential of 135.1±4.0 mV at 10 mA/cm²_{geometric} which is comparable with literature reported values for samples with similar mass loading on glassy carbon electrode and catalytic ink preparation methods to ours (103 mV and 132 mV at 10 mA/cm² in basic medium).^{163, 164} The general trend in activity is clearly composition-dependent as in the acidic medium, with Rh-rich samples being more active towards HER as compared to their Co-rich counterparts, with an abrupt change for Co_{2-x}Rh_xP, x < 1. This correlates to a change in structure-type from cubic antiferroite to the orthorhombic Co₂P-type. Rh₂P itself has already been found to demonstrate superior HER

activity at pH values from 0-14, outperforming the activity of the state-of-the-art Pt/C electrocatalyst.¹⁶⁵⁻¹⁶⁸ Moreover, while the $\text{Co}_{0.25}\text{Rh}_{1.75}\text{P}$ sample has the lowest overpotential of the systems studied, the standard deviations in the measurements reveal that the activity is not significantly different for compositions $x \geq 1.25$. Thus, even with the basic medium a significant quantity of Rh can be eliminated without sacrificing activity.

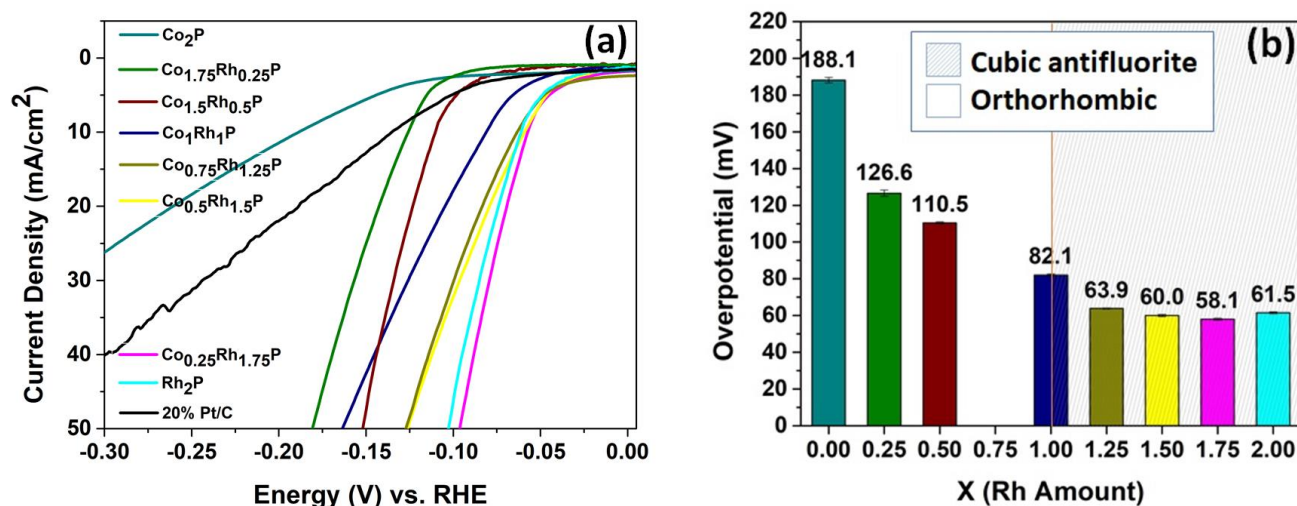


Figure 3.8. (a) HER polarization curves acquired on a glassy carbon support in a rotating disk electrode and (b) Overpotential values for $\text{Co}_{2-x}\text{Rh}_x\text{P}/\text{C}$ electrocatalysts at $10 \text{ mA}/\text{cm}^2_{\text{geometric}}$

3.3.4. Long term stability faradaic efficiency and Pt interference in basic medium

In order to determine whether the cathodic current that was observed during our HER measurements was indeed associated with proton reduction, a cathodic faradaic efficiency measurement was conducted for 30 minutes on a representative sample ($\text{Co}_{0.25}\text{Rh}_{1.75}\text{P}$, Figure 3.9). Data elucidation from the measurement revealed that the sample was 99% efficient, meaning that there were minimal faradaic losses encountered during the measurement and hydrogen is the only product in the basic medium.

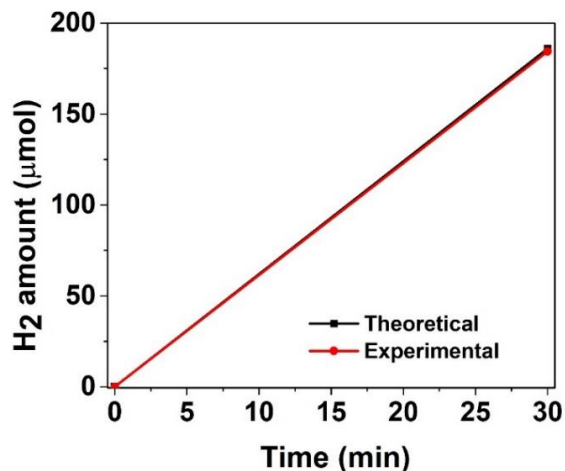


Figure 3.9. Faradaic efficiency plot for $\text{Co}_{0.25}\text{Rh}_{1.75}\text{P}$

A long-term stability measurement was also performed on the same electrocatalyst at an applied potential of 60 mV (current density $\sim 12.5 \text{ mA/cm}^2_{\text{geometric}}$) for 10 hours as shown in Figure 3.10. In distinct contrast to our observations in acid, where the current density dropped by 50% during the first 30 minutes, the reaction in basic media is quite robust, behaving similarly to Rh_2P which maintained HER activity through 1000 cycles in base.¹⁶⁷ These data are in alignment with previous studies of Co_2P , where the cathode undergoes dissolution in acid but is transformed to Co-hydroxide species in base (the putative catalyst).¹⁶⁹

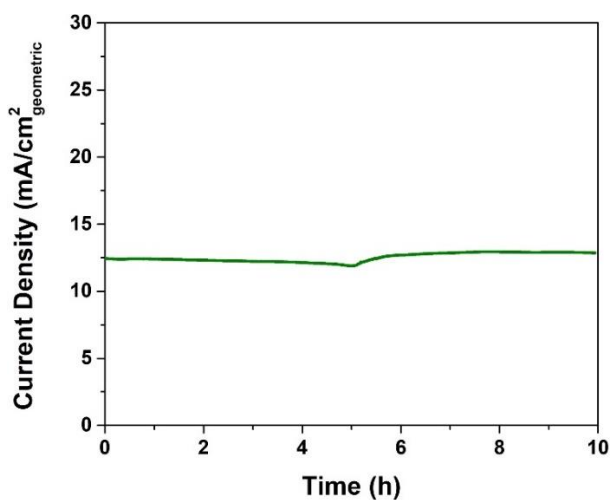


Figure 3.10. Long term stability test data for $\text{Co}_{0.25}\text{Rh}_{1.75}\text{P}$ electrocatalyst in basic media at 60 mV of applied potential

In order to determine the surface changes occurring on the electrocatalytic material upon catalysis in the basic medium, XPS analyses were carried out before and after the 10 h stability test. Figure 3.11 shows XPS spectra of the regions corresponding to Rh 3d, P 2p and O 1s, both before and after a 10 h stability test. Due to low signal-to-noise ratio observed for the Co 2p spectrum, we were unable to assess composition and speciation for this element (Figure 3.12).

For Rh XPS data acquired before catalysis we find that the metal primarily exists in a P bonded matrix (binding energy, BE 306.9 eV and 311.6 eV), with the spectra evidencing a lesser contribution from Rh^{3+} (BE 309.1 eV and 313.7 eV, ca 25%, see Table 3.3). The P 2p spectrum acquired before catalytic testing is dominated by oxidized states (P^{5+} , 133.5 eV), associated with surface oxidation; although a small shoulder at 130 eV is indicative of P^0 associated with metal-bonded P. The O 1s spectrum shows the presence of C bonded oxygen (main peak 533.0 eV) and some S bonded oxygen (535.7 eV), both associated with Nafion, along with a lower binding energy peak (531.9) attributed to metal oxide (~ 30%, See Table 3.3).

After the stability test, XPS data were acquired on the tested sample (Figure 3.11). The Rh spectrum remained essentially unchanged, but the P spectrum was devoid of discernible signal. We attribute the decrease in surface P to (i) formation of phosphate under active electrocatalytic conditions; (ii) displacement of phosphate with oxide/hydroxide species in the highly basic media.¹⁶⁹ This is supported in part by the O 1s spectrum, where the percent of metal-bonded O has doubled to 60% (Table 3.3). These data are consistent with previous work on HER electrocatalyzed by Co_2P in base,¹⁶⁹ and support the hypothesis that the metal phosphide serves as a pre-catalyst, with the phosphide converting to phosphate under electrochemical conditions (solubilized in the aqueous media), and the active catalyst is a surface oxide/hydroxide species.

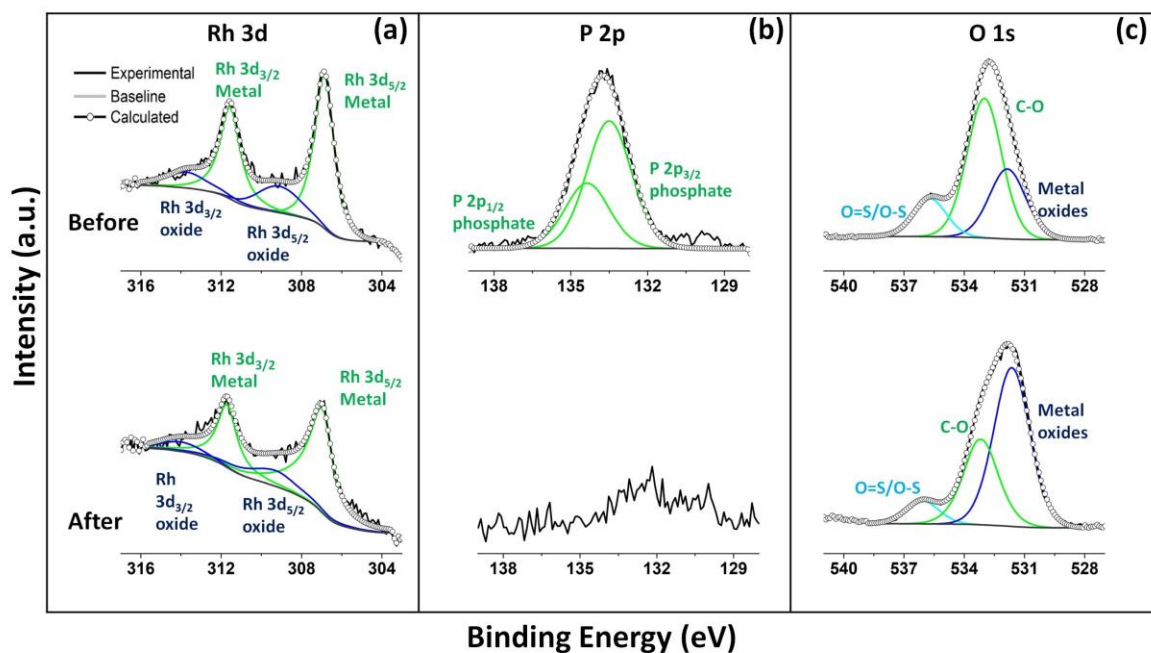


Figure 3.11. XPS data for the freshly prepared (before) and used (after) $\text{Co}_{0.25}\text{Rh}_{1.75}\text{P/C}$ electrocatalysts

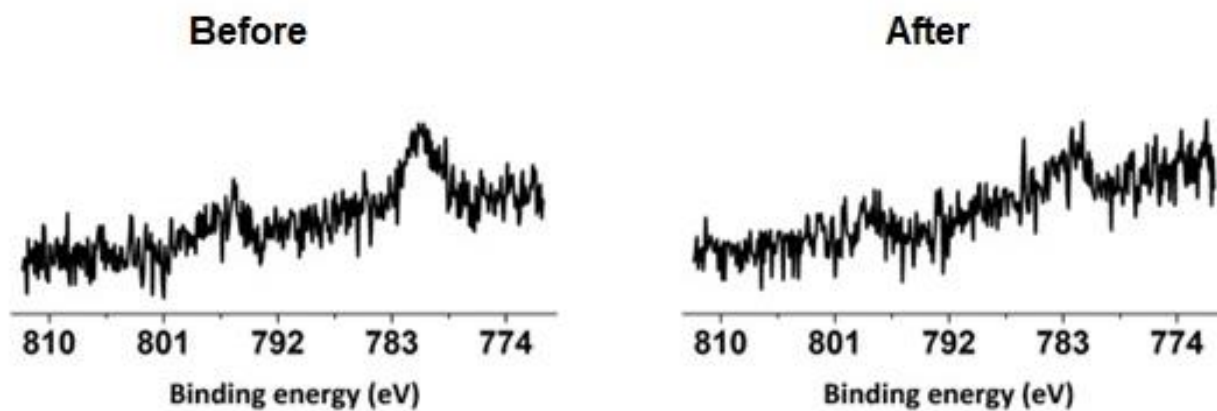


Figure 3.12. Co 2p XPS spectra for the freshly prepared (before) and used (after) $\text{Co}_{0.25}\text{Rh}_{1.75}\text{P/C}$ electrocatalysts

Table 3.3. XPS quantification data for oxidation states for Rh and O elements

	Before catalysis		After catalysis	
	Peak position	% Contribution	Peak position	% Contribution
O1s				
Metal oxides	531.9	29%	531.6	60%
C-O	533.0	56%	533.1	32%
Sulfonic acid oxygen in Nafion	535.7	15%	536.0	8%
Rh 3d				
Rh metal	306.9	75%	307.0	78%
	311.6		311.7	
Rh oxide	309.1	25%	309.3	22%
	313.7		313.9	

3.4. Conclusions

Co_{2-x}Rh_xP nanoparticles are electrocatalytically active toward the HER in acidic and basic media. The activity is composition-dependent, with Rh-rich samples being more active than their Co-rich counterparts. Interestingly, we have also shown that the activities are comparable for compositions in which $x \geq 1.25$, which effectively allows one to dilute rhodium sites with cobalt up to the composition of Co_{0.75}Rh_{1.25}P without losing the initial activity. However, Co is not stable in the acidic medium under electrocatalytic conditions for the long term, depleting from the surface concomitant with a 50% drop in the current density. Then we carefully studied the dissolution behavior of Pt and its interference on the working electrode when used as the counter electrode at lower potentials (<0.6 V vs. RHE). Our results show that the deactivation of Co_{2-x}Rh_xP/C due to Co dissolution in the acidic medium, is masked by redeposition of Pt on the working electrode, which significantly improves the HER stability. As a result, Pt should not be selected as the counter electrode for measuring the activity and stability of HER even under mild applied potentials, especially in the acidic electrolyte. However, in the basic medium, we do not see any Co dissolution, activity deactivation, or Pt redeposition. In that case, the P atom plays a sacrificial

role, and *in-situ*, formed metal oxide/hydroxides act as the catalytic material providing promising activity and stability.

CHAPTER 4. THE ROLE OF NOBLE AND BASE METAL SPECIATION AND SURFACE SEGREGATION IN $\text{Ni}_{2-x}\text{Rh}_x\text{P}$ NANOCRYSTALS ON ELECTROCATALYTIC WATER SPLITTING REACTIONS IN ALKALINE MEDIA

Abstract

Transition metal phosphides have proven to be surprisingly active electrocatalysts for electrochemical water splitting, but the nature of the “active” catalyst depends strongly on the solution pH, the identity of the metals, and whether the reactions are anodic (oxygen evolution reaction, OER) or cathodic (hydrogen evolution reaction, HER). In order to understand the origin of this activity, the synthesis of well-defined, compositionally controlled pre-catalysts is needed, as are detailed catalytic studies and physicochemical characterization/activity assessment of catalysts at different stages. While base metal phosphides of Ni and Co have the advantage of being earth abundant, in alkaline media they are less active and less stable than noble metal phosphides such as Rh_2P . As a means to combine the abundant nature of base metals with the activity and stability of noble metals, the first synthesis of colloidal $\text{Ni}_{2-x}\text{Rh}_x\text{P}$ nanocrystals by arrested precipitation routes is reported along with their composition-dependent activity for electrocatalytic HER and OER. Phase-pure samples of $\text{Ni}_{2-x}\text{Rh}_x\text{P}$ were realized at the Ni-rich (hexagonal, Fe_2P -type) end ($x = 0.00, 0.25, 0.50$) and Rh-rich (cubic, antiferrotype-type) end ($x = 1.75, 2.00$). When assessed in terms of current density normalized to electrochemical surface area (ECSA) at fixed potential, the most active pre-catalyst for OER is $\text{Ni}_{1.75}\text{Rh}_{0.25}\text{P}$ and for HER it is $\text{Rh}_{1.75}\text{Ni}_{0.25}\text{P}$. Evaluation of X-ray photoelectron spectroscopy, transmission electron microscopy/energy dispersive spectroscopy and ECSA data before and after 10 h stability runs were performed. The data reveal surface compositions to be considerably richer in Ni and poorer in Rh and P relative to the bulk composition, particularly for $\text{Ni}_{0.25}\text{Rh}_{1.75}\text{P}$ where the surface ratio of Ni:Rh is nearly 2:1, and increases to 4:1 after HER catalysis. In all cases, surface phosphorus is

completely depleted post-catalysis, suggesting a sacrificial role for phosphide under alkaline conditions. Moreover, the activity of “Rh_{1.75}Ni_{0.25}P” for HER decreases over time, even as the ECSA continues to rise, attributed to a decrease in the more active and stable Rh sites relative to Ni on the surface. In contrast, the enhancement in OER activity of Ni₂P with 12.5% Rh incorporation is attributed to restructuring upon phase-segregation of Rh, suggesting that the noble metal also plays a sacrificial role and does not participate in OER catalysis. The roles of minority noble metals (Rh) in base-metal phosphides for OER and of minority base metals in noble-metal (Rh) phosphides for HER are discussed in light of related data on Co_{2-x}Rh_xP.

4.1. Introduction

A major limiting factor in the widespread adoption of water electrolysis is the absence of inexpensive, highly efficient catalysts for HER and OER that are stable under extreme pH conditions. This need provides a driving force for the discovery of new catalytic materials, and transition metal phosphides have emerged as a promising class of materials in this regard. Phosphides were suggested as suitable catalysts for HER by Rodriguez and co-workers in 2005 based on DFT calculations conducted on Ni₂P that revealed a moderation in bonding of intermediates and products on the (001) plane due the combination of Lewis acidity of the Ni (acting as a hydride acceptor) and Lewis basicity of the phosphide (acting as a proton-acceptor) associated with the ensemble effect (the separation of Ni sites by P).¹²⁸ The activity of Ni₂P was validated experimentally by Schaak and Lewis in 2013, where Ni₂P was found to exhibit a low-overpotential and high-stability (in acid) relative to other earth-abundant catalysts investigated.¹⁷⁰ This spurred widespread investigation of transition metal phosphides for first HER, and subsequently OER, and related reactions.^{16, 171-176}

While very good HER catalysts in acid and alkali, base metal phosphides do not outperform noble metals, prompting the study of noble metal phosphides. Work done by Duan *et al.* showed that Rh₂P nanocubes could be an excellent catalyst for HER, outperforming the activity and stability of Pt and Rh metals in acidic media.¹⁷⁷ Likewise, Yang *et al.* reported quasi spherical Rh₂P nanoparticles (~3 nm in sizes) to be the first Pt-free electrocatalyst that has a higher pH-universal HER performance compared to the state-of-the-art commercial Pt/C.¹⁷⁸ With respect to OER, base metal phosphides are excellent pre-catalysts for OER in alkaline media (where they transform to oxide/hydroxides), but are typically not stable at positive potentials in acid.^{135, 179} In contrast, Rh₂P is an active catalyst for OER in acidic conditions, exhibiting a lower overpotential and enhanced stability relative to Pt/C; the overall stability is improved in alkaline media without sacrificing activity, such that Rh₂P can serve as a bifunctional catalyst for overall water electrolysis generating 200 mA/cm² for 1.7 V applied.¹⁸⁰

As a means to further limit the noble metal content, we sought to determine whether Rh₂P-type HER activity could be retained upon substitution of some of the noble metal content with base metals. Intriguingly, for Rh_{2-x}Co_xP nanocrystals, there was actually an enhancement of activity upon introduction of Co, and more significantly, replacement of up to 40% of Rh produced materials with activities comparable to Rh₂P in both acid and base. The catalysts demonstrated good stability in base, although Co was observed to leach under acidic conditions leading to a decrease and leveling off of activity in this system over time. Likewise, we found that Co₂P, a good base metal catalyst for OER in alkaline media, actually demonstrated an enhancement in activity upon incorporation of small amounts of Rh, despite the fact that Rh₂P prepared similarly is not particularly active. The OER activity was found to increase over time, associated with phase segregation of Rh, suggesting sacrificial depletion of Rh may enhance activity of the Co

oxide/hydroxide formed under oxidative conditions.^{24, 25, 181, 182} As a means to discern how the interplay between the base metal and noble metal governs activity and stability, we seek here to investigate the compositional effects on water splitting catalysis of the nickel analog, $\text{Ni}_{2-x}\text{Rh}_x\text{P}$. Ni was chosen because it is one of the three base metals (along with Co and Fe) known to form layered double hydroxides that are highly active for alkaline OER catalysis, and because of prior reports of high HER activity in a phosphided RhNi phase under alkaline conditions.¹⁸³

Indeed, the prior study on phosphided RhNi supported on graphene oxide underscores the problems with discerning the innate compositional effects on catalysis in the context of surface area, mediators, and phase/phase purity, while at the same time providing a motivation for evaluating this system for HER.¹⁸³ The phosphided RhNi is not crystalline, nor does it appear compositionally to adhere to the classic 2:1 M:P ratio of the crystalline phases, but it does catalyze HER in alkaline hydrazine more efficiently than the metal alloy.¹⁸³ With that study as inspiration, we report here the first synthesis of discrete $\text{Ni}_{2-x}\text{Rh}_x\text{P}$ nanoparticles and evaluate their composition-dependent electrocatalytic activities towards water oxidation and reduction in alkaline media. A systematic comparison to $\text{Co}_{2-x}\text{Rh}_x\text{P}$ enables us to better define the roles of minority noble metals (Rh) in base-metal phosphides for OER and of minority base metals in noble-metal (Rh) phosphides for HER.

4.2. Experimental section

All materials used in the synthesis of $\text{Ni}_{2-x}\text{Rh}_x\text{P}$ nanoparticles are given in Chapter 2.

4.2.1. Synthesis of $\text{Ni}_{2-x}\text{Rh}_x\text{P}$ nanoparticles

All reactions were carried out under an argon atmosphere using standard Schlenk line techniques. To synthesize $\text{Ni}_{2-x}\text{Rh}_x\text{P}$ (Table 4.1), the corresponding amount of Ni precursor and Rh precursor in (0.42-x) mmol Ni to x mmol Rh ratio were combined with 15.0 mL of oleylamine

(reducing agent and coordinating ligand) and 5.0 mL of 1-octadecene (solvent) in a 200 mL Schlenk flask with an attached condenser. Then the flask was placed on a heating mantle which was connected to a temperature controller. The thermocouple was inserted between the flask and the heating mantle, and the mixture was degassed at 120 °C for 30 min to remove moisture and oxygen. Then argon was purged for 20 min at the same temperature. The temperature was then increased up to 260 °C and maintained for 3 h. After 3 h, 8.0 mL of TOP was quickly injected into the mixture from the top of the condenser using a 12" long needle. Next, the temperature was set to 350 °C and was maintained for another 3 h. After naturally cooling the mixture to room temperature, 20 mL of ethanol was added to the solution and centrifuged to isolate the precipitate. The precipitate was dispersed in 5 mL of chloroform, sonicated for 5 min, and reprecipitated, adding ethanol, followed by centrifugation. This sonication and precipitation process was carried out two times.

Table 4.1. Quantities of metal precursors employed in the synthesis of Ni_{2-x}Rh_xP (0.21 mmol) nanoparticles

Targeted composition	Ni(acac) ₂ / mmols	RhCl ₃ ·nH ₂ O / mmols
Ni _{0.25} Rh _{1.75} P	0.06	0.36
Ni _{0.5} Rh _{1.5} P	0.12	0.30
Ni _{0.75} Rh _{1.25} P	0.18	0.24
Ni _{1.0} Rh _{1.0} P	0.21	0.21
Ni _{1.25} Rh _{0.75} P	0.24	0.18
Ni _{1.5} Rh _{0.5} P	0.30	0.12
Ni _{1.75} Rh _{0.25} P	0.36	0.06

4.2.2. Synthesis of Ni₂P nanoparticles

Ni₂P nanoparticles were synthesized using a method developed by Muthuswami *et al.* with minor variations.¹⁸⁴ Ni(acac)₂ (0.59 g), 6.0 mL of oleylamine, 15.0 mL of n-octyl ether and 2.0 mL of TOP was added to a 200 mL Schlenk flask. The mixture was degassed at 120 °C for 30 min, and then argon was purged for 20 min at the same temperature. The temperature was then increased

up to 230 °C and maintained for 90 minutes. After 90 minutes, 3.0 mL of TOP was quickly injected into the mixture. Next, the temperature was set to 350 °C and was maintained for another 3 h. After naturally cooling the mixture to room temperature, the sample was purified three times using chloroform and ethanol, as described in the procedure for the synthesis of Ni_{2-x}Rh_xP.

4.2.3. Synthesis of Rh₂P nanoparticles

Rh₂P nanoparticle synthesis was carried out using the protocol in section 3.2.3.

4.2.4. Characterization

Powder X-ray diffraction (PXRD), Transmission electron microscopy (TEM) equipped with an energy dispersive X-ray spectroscopy (EDS, EDAX, inc.), X-ray photoelectron spectrometry (XPS), and Fourier Transform Infrared Spectroscopy (FT-IR) were operated as mentioned in Chapter 2.

4.2.5. Electrochemical measurements

A catalytic ink was prepared using Ni_{2-x}Rh_xP nanoparticles, and electrocatalytic activity, stability, electrochemically active surface area (ECSA), and overall water splitting tests were performed following protocols as described in Chapter 2. Here, we used 1 M KOH as electrolyte solutions, while a carbon rod counter electrode was used for HER, and a Pt wire counter electrode was used for OER.

4.3. Results and discussion

4.3.1. Synthetic protocol development

Our approach to the synthesis of Ni_{2-x}Rh_xP, is based on our method established for Co_{2-x}Rh_xP,²⁵ where we were able to make a solid-solution over all x. In both cases, we used solution-phase arrested precipitation employing a one-pot two-step process in which the metal precursors, combined in targeted stoichiometric ratios, were allowed to co-reduce in a mixture of oleylamine

(which acts as a reducing agent) and the noncoordinating solvent 1-octadecene to form the alloy at an intermediate temperature, followed by injection of the P precursor, trioctylphosphine (TOP), and an increase in temperature to achieve phosphidation. The temperature conditions and concentration of TOP were varied to identify optimal conditions for phase purity (0.2 mmol total metal precursor; 15 mL oleylamine, 5 mL octadecene), although phase purity was not always possible (*vide infra*). Based on the optimization studies, the targeted metal ratios were obtained with 8 mL of TOP using an alloying temperature of 260 °C and a phosphidation temperature of 350 °C (Table 4.2). The formation of a Rh-Ni alloy at the intermediate phase, was verified by isolation and characterization (see Figure 4.1). For comparison of the activity, binary end members Ni₂P and Rh₂P were also synthesized using a modification of standard procedures.^{25, 184}

Table 4.2. EDS data for samples prepared at different alloying temperatures and with different amounts of TOP

Targeted composition	Alloying temperature (°C)	TOP amount (ml)	EDS ratio
Ni _{1.5} Rh _{0.5} P	230	6.0	Ni _{1.73} Rh _{0.27} P
Ni _{1.5} Rh _{0.5} P	230	8.0	Ni _{1.62} Rh _{0.38} P
Ni _{1.5} Rh _{0.5} P	230	10.0	Ni _{1.65} Rh _{0.35} P
Ni _{1.5} Rh _{0.5} P	260	8.0	Ni _{1.52} Rh _{0.48} P
Ni _{1.75} Rh _{0.25} P	260	8.0	Ni _{1.75} Rh _{0.25} P

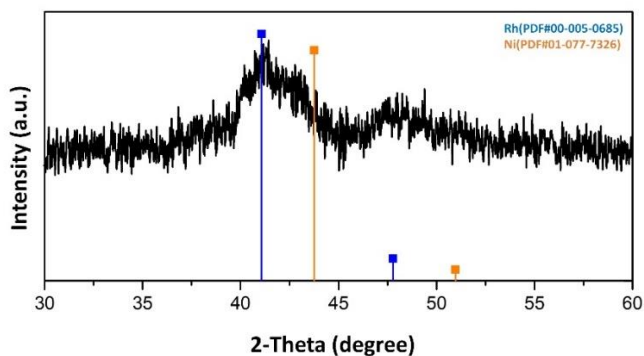


Figure 4.1. PXRD pattern for isolated Ni-Rh alloy after heating metal precursors at 260 °C for 3h with 1-octadecene and oleylamine. The stick diagrams correspond to fcc Rh metal (blue) and Ni metal (gold)

4.3.2. Crystal structure and morphology

Synthesized $\text{Ni}_{2-x}\text{Rh}_x\text{P}$ nanoparticles with different compositions were characterized for phase purity using PXRD, morphology by TEM, and composition using EDS. Figure 4.2 shows the PXRD patterns of the targeted phases and Ni_2P and Rh_2P endmembers. Ni_2P and Rh_2P adopt fundamentally different structures: hexagonal (Fe_2P -type) and cubic antiferite, respectively. Thus, Ni_2P has two metal sites, one with tetrahedral geometry and one with square pyramidal geometry (equally populated) and P occupies the tricapped trigonal prismatic geometry defined by the metal atoms (Figure 4.2). In contrast, Rh_2P , has only one metal site: tetrahedral holes inside the face-centered-cubic P anionic lattice (Figure 4.2). $\text{Ni}_{2-x}\text{Rh}_x\text{P}$ nanoparticles are found to adopt the Fe_2P hexagonal structure-type up to $x = 1.5$, where a mixture of hexagonal and antiferite form; more Rh-rich phases are exclusively antiferite. The incorporation of the second metal is manifest in peak shifts associated with expansion of the hexagonal lattice upon Rh incorporation (to lower 2θ), or compression of the antiferite structure upon Ni incorporation (to higher 2θ), as shown in Figure 4.3. Intriguingly, while initial incorporation of Rh into Ni_2P results in a quasi linear increase in the d-spacing of the (111) reflection, suggestive of adherence to Vegard's Law, for $0.75 < x < 1.5$, the increase in lattice parameters is significantly dampened. At $x = 1.5$, where two distinct phases are present, the hexagonal (111) lattice parameter decreases to a value intermediate between those recorded for $x = 0.25$ and $x = 0.5$. On the other side, as Ni is added to the antiferite structure type, there is a significant drop in the d-spacing of the (200) reflection upon incorporation of 0.25 Ni ($x = 1.75$), but hardly any additional compression noted for 0.50 Ni ($x = 1.5$), where the phase segregation occurs. Clearly, at $x = 1.5$, the Rh is being partitioned between the two structure types. Nevertheless, the minimal change in lattice parameters between $x = 0.75$ and $x = 1.5$ suggests the incorporation of Rh into the hexagonal structure is limited. We also noted a subtle

enhancement in the intensity of the Ni₂P 110 peak, which is barely discernable in the native structure, upon incorporation of Rh, likely due to the difference in scattering factor between Rh and Ni. An unidentified peak near 37.5° 2 θ is also noted for these phases and marked with a red asterisk. This peak could be attributed to more P-rich phases, as both RhP₂ and Rh₄P₃ have a peak in that area, but in the absence of other peaks, phase identification is speculative.

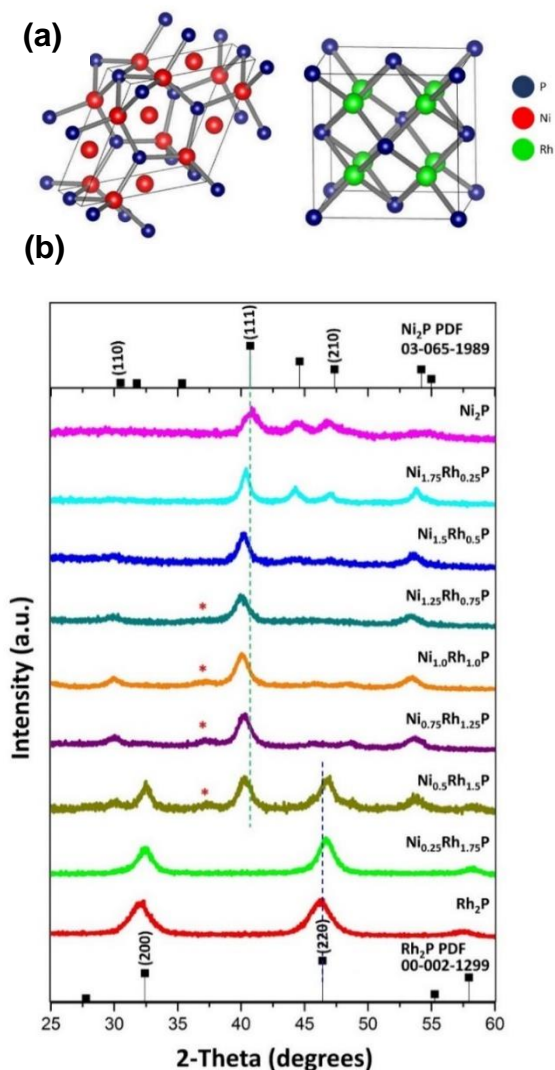


Figure 4.2. (a) Structure of hexagonal Ni₂P (left) and cubic Rh₂P (right) polymorphs. (b) PXRD patterns for targeted compositions of Ni_{2-x}Rh_xP (x=0-2) nanoparticles. Reference patterns for Ni₂P and Rh₂P are shown with drop lines for major distinguishing peaks. An impurity peak observed for compositions x=0.75-1.5 is indicated with a red asterisk

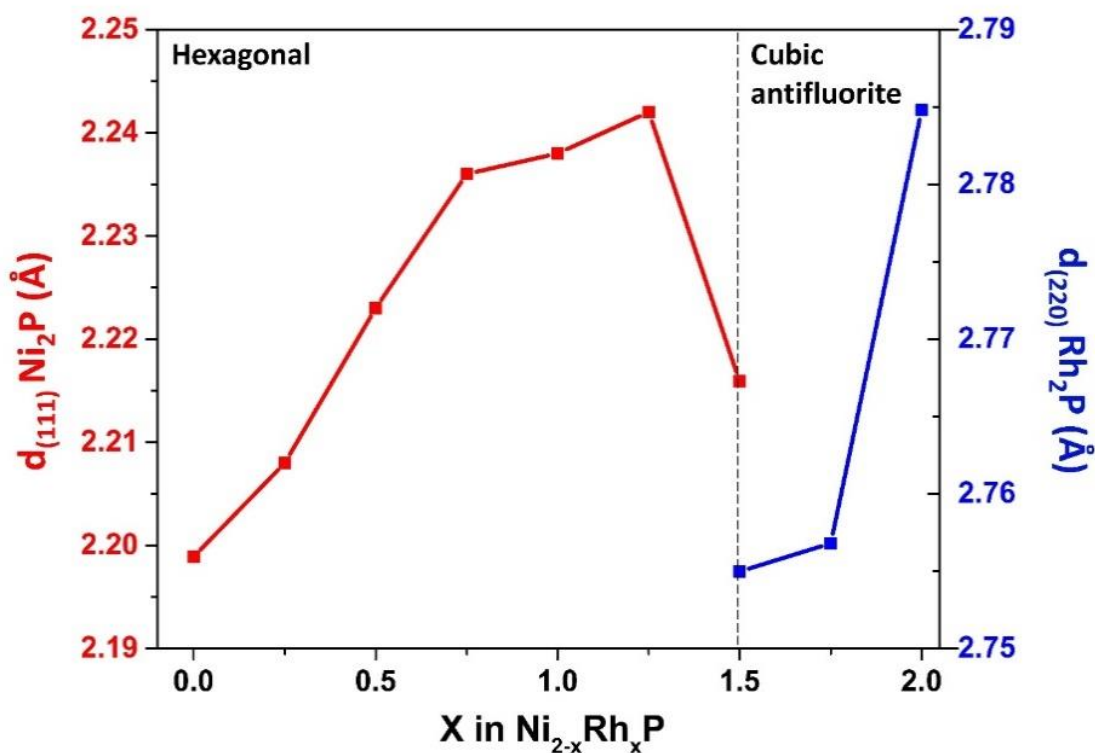


Figure 4.3. d-spacing change of hexagonal Ni_2P with Rh addition (red) and cubic Rh_2P with Ni addition (blue)

The observation of phase segregation in $\text{Ni}_{2-x}\text{Rh}_x\text{P}$ came as a surprise, as we were able to prepare $\text{Co}_{2-x}\text{Rh}_x\text{P}$ over all x , with the Co_2P -type structure adopted for $x \leq 0.75$ and the Rh_2P (antiferite) type adopted for $x \geq 1$, suggesting a sharp phase transition is occurring for $0.75 > x < 1.0$. However, while the structures of Ni_2P and Co_2P are similar in that they have a square pyramidal and tetrahedral site, the arrangement of the polyhedra is not the same, such that Ni_2P is hexagonal (Fe_2P -type) and Co_2P is orthorhombic (Co_2P -type).¹⁸⁵ It is possible that these subtle structural differences facilitate miscibility between Co_2P - Rh_2P but inhibit miscibility between Ni_2P - Rh_2P . Alternatively, there may be a competing ternary phase that is more stable, a possibility hinted at by the unidentified peak at near $37.5^\circ 2\theta$. We also considered the possibility that incorporation was limited for intermediate compositions, an effect we have previously observed

in $\text{MnAs}_{1-x}\text{Sb}_x$ nanoparticles.¹⁸⁶ In the case of $\text{MnAs}_{1-x}\text{Sb}_x$, we noted that As incorporation in MnSb was significantly limited, leading to observed compositions that were considerably As-poor relative to the targeted compositions. This was attributed to differences in relative reactivity. However, EDS data conducted in the TEM for $\text{Ni}_{2-x}\text{Rh}_x\text{P}$ revealed a close agreement between the targeted composition, and the observed composition (see Table 4.3).

Figure 4.4 shows the TEM images for $\text{Ni}_{2-x}\text{Rh}_x\text{P}$, Ni_2P , and Rh_2P nanoparticles. According to the images, Ni_2P nanoparticles have a spherical structure with an average size of 6 ± 1 nm. This value is very close to the crystallite size (6.2 nm) calculated by application of the Scherrer Equation to the (111) reflection, Rh_2P on the other hand has a quasi spherical morphology with an average TEM size of 3 ± 1 and corresponding crystallite size (based on the (220) reflection) of 3.1 nm. As is evident in Figure 4.4, incorporation of Rh into Ni_2P results in void formation due to the Kirkendall effect, resulting in a larger (more than double) overall particle size (ca 15 nm, Table 1).^{160, 187} This increase is not wholly attributed to void formation, since the crystallite size computed from the Scherrer equation also increases, albeit by a smaller amount (ca 1.5x). At the other end of the compositional space, incorporation of 12.5% Ni to Rh_2P also results in an increase in particle size of ca 1.5x but without apparent void formation; the crystallite size for the (220) reflection increases proportionally. The phase segregated $x=1.5$ sample has irregular particles of ca. 14 nm in diameter; some voids are still seen, but otherwise differentiation of particles adopting hexagonal vs. cubic structure is not obvious. Likewise, computed crystallite sizes for hexagonal and cubic are similar (ca 8 nm).

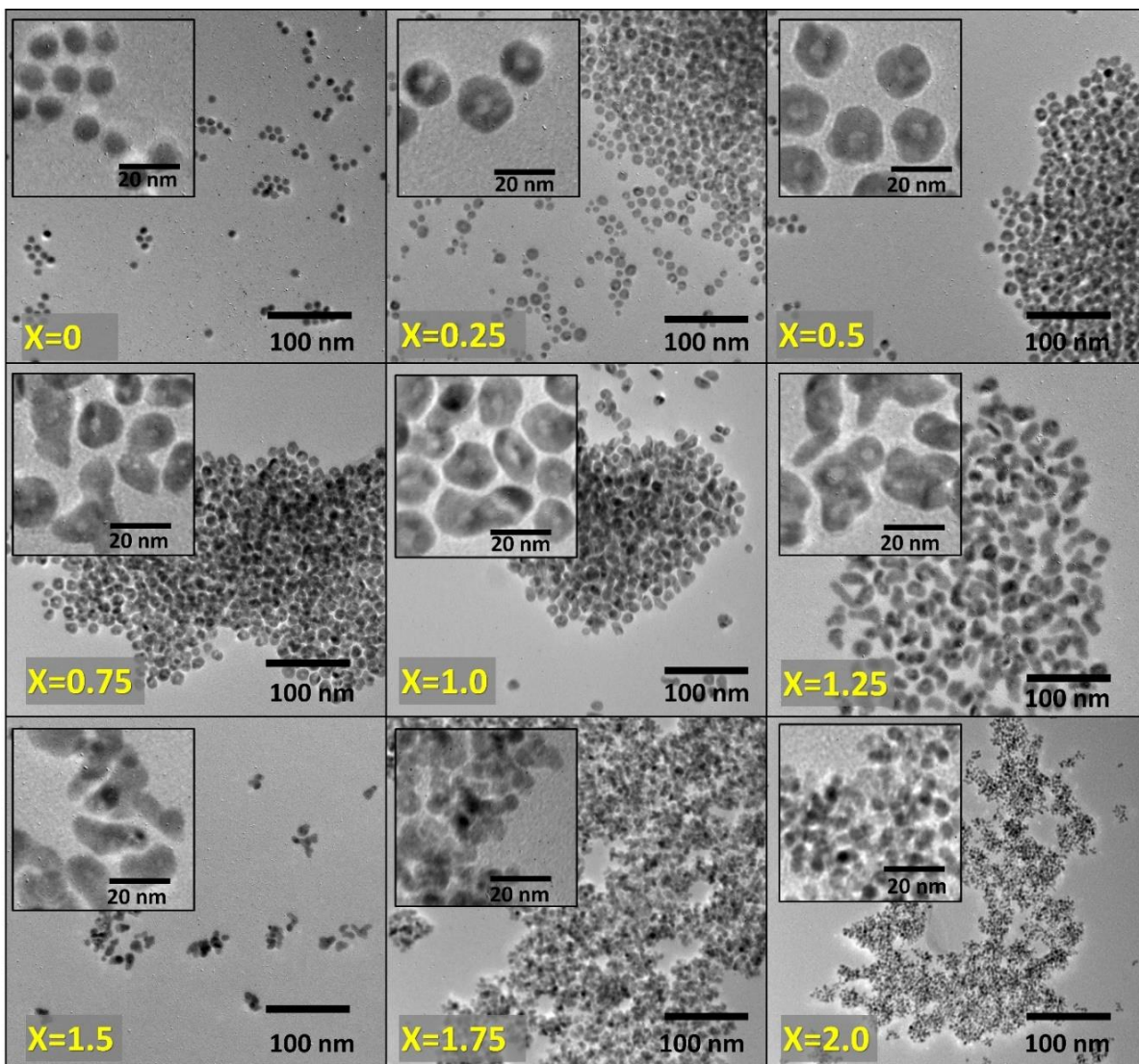


Figure 4.4. TEM images for $\text{Ni}_{2-x}\text{Rh}_x\text{P}$ ($x=0-2$) nanoparticles with magnified insets. Targeted compositions are indicated and sizes obtained from the size histograms (depicted in Figure 4.5) are presented in Table 4.3

Table 4.3. Targeted ratios and TEM-EDS ratios (averaged) for $\text{Ni}_{2-x}\text{Rh}_x\text{P}$ nanoparticle compositions. TEM particle size histograms are plotted in Figure 4.5

Targeted composition	Average EDS composition	TEM particle size (nm)	Scherrer crystallite size (nm)
Ni_2P	$\text{Ni}_{2.00(0)}\text{P}_{1.07(7)}$	6 ± 1	6.2
$\text{Ni}_{1.75}\text{Rh}_{0.25}\text{P}$	$\text{Ni}_{1.74(2)}\text{Rh}_{0.26(2)}\text{P}_{0.94(8)}$	15 ± 2	10.7
$\text{Ni}_{1.50}\text{Rh}_{0.50}\text{P}$	$\text{Ni}_{1.51(2)}\text{Rh}_{0.49(2)}\text{P}_{0.88(9)}$	14 ± 2	9.8
$\text{Ni}_{1.25}\text{Rh}_{0.75}\text{P}$	$\text{Ni}_{1.22(3)}\text{Rh}_{0.78(3)}\text{P}_{1.21(12)}$	14 ± 2	8.4
$\text{Ni}_{1.00}\text{Rh}_{1.00}\text{P}$	$\text{Ni}_{1.11(7)}\text{Rh}_{0.89(7)}\text{P}_{1.27(44)}$	15 ± 3	8.3
$\text{Ni}_{0.75}\text{Rh}_{1.25}\text{P}$	$\text{Ni}_{0.75(6)}\text{Rh}_{1.25(6)}\text{P}_{1.35(45)}$	19 ± 5	8.1
$\text{Ni}_{0.50}\text{Rh}_{1.50}\text{P}$	$\text{Ni}_{0.52(2)}\text{Rh}_{1.48(2)}\text{P}_{1.33(37)}$	14 ± 5	8.5 and 7.9
$\text{Ni}_{0.25}\text{Rh}_{1.75}\text{P}$	$\text{Ni}_{0.26(4)}\text{Rh}_{1.74(4)}\text{P}_{1.03(15)}$	5 ± 1	4.4
Rh_2P	$\text{Rh}_{2.00(1)}\text{P}_{0.98(1)}$	3 ± 1	3.1

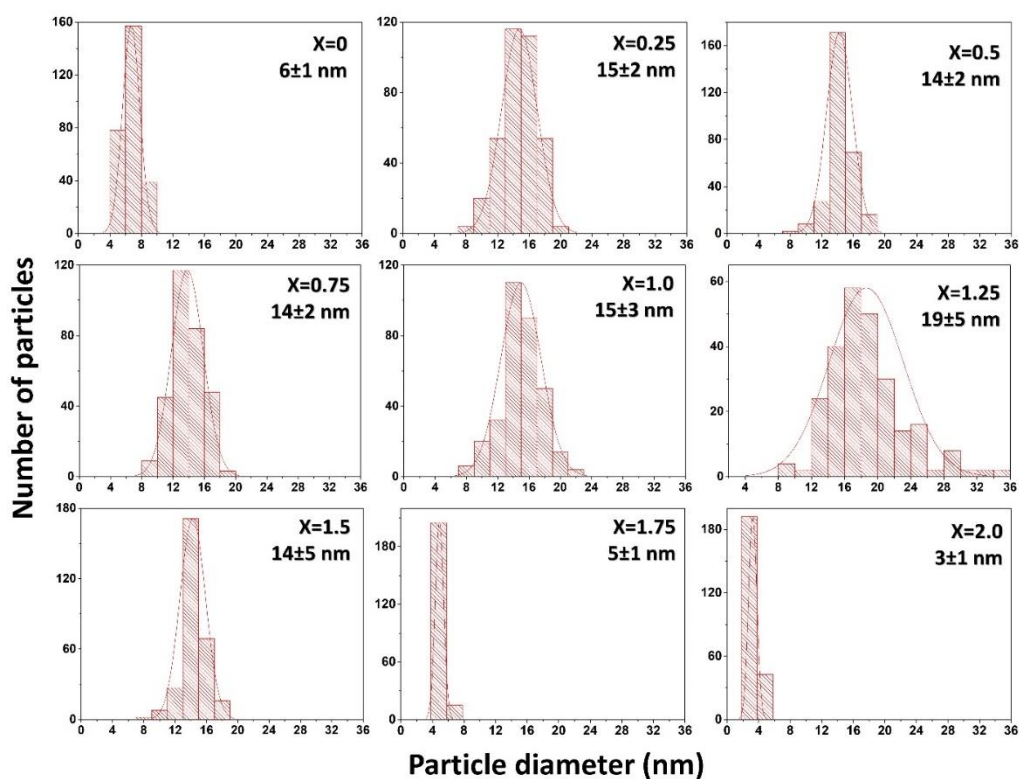


Figure 4.5. Particle size histograms for $\text{Ni}_{2-x}\text{Rh}_x\text{P}$ nanoparticles as a function of x

4.3.3. Electrocatalytic studies

Generally, there is a growing consensus that HER and OER conducted in strongly alkaline media transforms the phosphide precatalysts into oxide/hydroxides. It is an intriguing aspect of these materials that, upon activation, the phosphides outperform deliberately prepared oxide/hydroxide materials.¹⁸⁸⁻¹⁹² It is possible that the differences reflect the reduced “core” of the catalysts produced from phosphides, which may facilitate electron transport to and from the reactive surface.

To evaluate the composition-dependent electrocatalytic activity of $\text{Ni}_{2-x}\text{Rh}_x\text{P}$, samples deemed to be phase-pure by PXRD (i.e., those on the extreme Ni-rich end and Rh-rich end: $x = 0, 0.25, 0.50, 1.75,$ and 2.0) along with the $\text{Ni}_{1.0}\text{Rh}_{1.0}\text{P}$ composition as a representative of phase segregated and intermediate composition sample, were incorporated into a carbon ink to form $\text{Ni}_{2-x}\text{Rh}_x\text{P}$ C-NPs inks. Before the ink preparation, we annealed $\text{Ni}_{2-x}\text{Rh}_x\text{P}$ C-NPs composite under reducing conditions. We collected IR data before and after the heat treatment (Figure 4.6). We observed the disappearance of native peaks at 3300-3500 due to N-H (oleylamine) and C-H (oleylamine, TOP, octylether) stretching. The peak at 1120 due to C-O stretching (octylether) is significantly attenuated after annealing, suggesting the bulk of the surface ligands have been removed by this process. The prepared $\text{Ni}_{2-x}\text{Rh}_x\text{P}$ C-NPs inks were drop cast onto a glassy carbon rotating disk electrode (mass loading: 0.285 mg/cm^2 , surface area 0.07 cm^2). The electrocatalytic OER and HER activity of $\text{Ni}_{2-x}\text{Rh}_x\text{P}$ C-NPs were evaluated in 1M KOH using a three-electrode system.

Figure 4.7 shows the OER catalytic activity data for $\text{Ni}_{2-x}\text{Rh}_x\text{P}$ C-NPs. A clear oxidation peak that corresponds to NiII to NiIII/IV formation can be observed in our polarization curves at $\sim 1.40 \text{ V}$ for Ni-rich phases (Figure 4.7a), shifted from $\sim 1.44 \text{ V}$ in Ni_2P .^{21, 24, 193} This suggests that

Rh incorporation facilitates oxidation of Ni, an unexpected result. The Ni_{1.0}Rh_{1.0}P sample has an excessively broad (>200 mV) peak that is shifted to higher potential ~1.48 V, demonstrating unique behavior that may be associated with impurity phase observed by PXRD. From the literature, it is known that *in-situ* formed metal oxides comprise the catalytic surface of phosphide catalysts in alkaline media.¹⁹³ According to our data, when normalized to geometric surface area the Ni_{1.75}Rh_{0.25}P catalyst exhibits the highest OER activity among the investigated electrocatalysts, with an overpotential (η) of 273.1 mV @ 10 mA/cm²_{geo}, (Figure 4.7b). Unsurprisingly, this composition also exhibits the lowest Tafel slope (30 mV/dec, Figure 4.9). The slope is consistent with the oxidation of surface metal hydroxide to oxide as the rate-determining step at low surface coverage. All Ni_{2-x}Rh_xP samples outperform a commercial Pt/C catalyst when performed under identical conditions (η = 720 mV @ 10mA/cm²_{geo}, Figure 4.10).

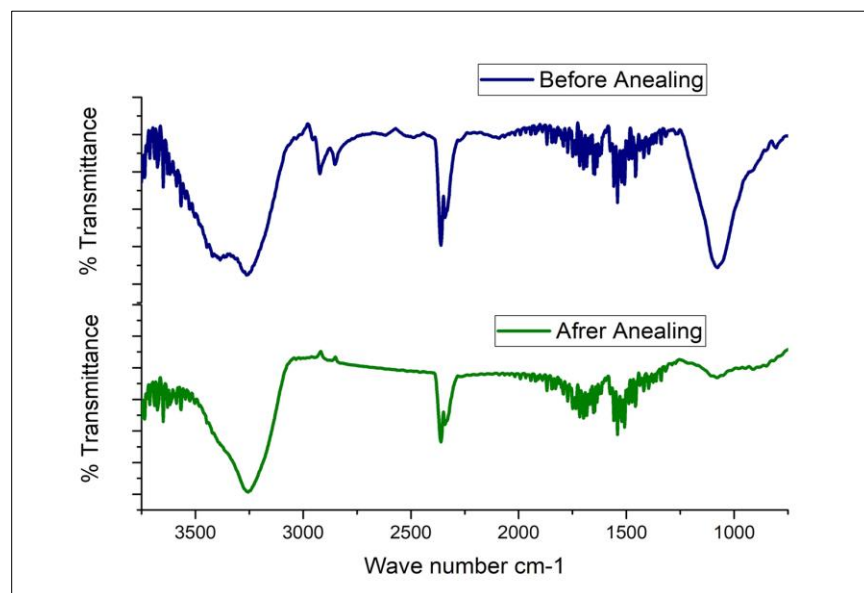


Figure 4.6. IR spectra before and after annealing of the Ni_{1.75}Rh_{0.25}P C-NPs composite

While the geometry-normalized activity is useful for evaluating device performance, it does not reflect the intrinsic activity because it assumes an equivalent number of available active sites per unit area (or per mg, since we have the same mass loading in each case).^{47, 49} Thus,

geometric normalized data fails to account for surface roughness associated with sample preparation, composition-dependent variations of particle size (see Figure 4.3) and sample-to-sample variations in active site density within a specific composition. Accordingly, we measured the electrochemical surface area (ECSA) as a means to assess the average activity per active site.⁴⁷ ⁵¹ ECSA values were calculated from double-layer capacitance measurements (C_{dl})⁵⁸⁻⁶⁰ conducted at different scan rates in the non-faradaic region (see Figure 4.11 for C_{dl} plots).⁵¹ Because our inks incorporate carbon black, which contributes to the overall conductivity and capacitive behavior,^{64, 65} and because side reactions such as corrosion, specific adsorption, intercalation, etc., also can affect these C_{dl} values,⁶⁶ we do not purport to report the absolute intrinsic activity and use ECSA only for direct comparison of samples prepared in the same way. We also employ ECSA as a means to probe the stability of the relevant catalysts and understand how they are changed in the catalytic process. We further note that the calculated ECSA values (Table 4.4) are much higher than the geometric surface area; hence, we evaluated the overpotential at $2.0 \text{ mA/cm}^2_{\text{ECSA}}$ to compare the catalytic activity.

According to the ECSA normalized data (Figure 4.7c,d) again, $\text{Ni}_{1.75}\text{Rh}_{0.25}\text{P}$ shows the highest activity, but the activity difference between this phase and the other Ni-rich (hexagonal) phases is enhanced, suggesting a significant intrinsic activity difference not reflected in the geometric surface area normalized data. When we compared the ECSA for the 1st polarization curve vs. the 30th polarization curve, a moderate increment is noted for all of the Ni-rich phases (< 20%). In contrast a significant difference between ECSA (>75% increment after 30 cycles) was observed with Rh-rich cubic $\text{Ni}_{2-x}\text{Rh}_x\text{P}$ compounds (Table 4.4), reflecting the instability and evident continuous restructuring with oxidation of the Rh rich end.

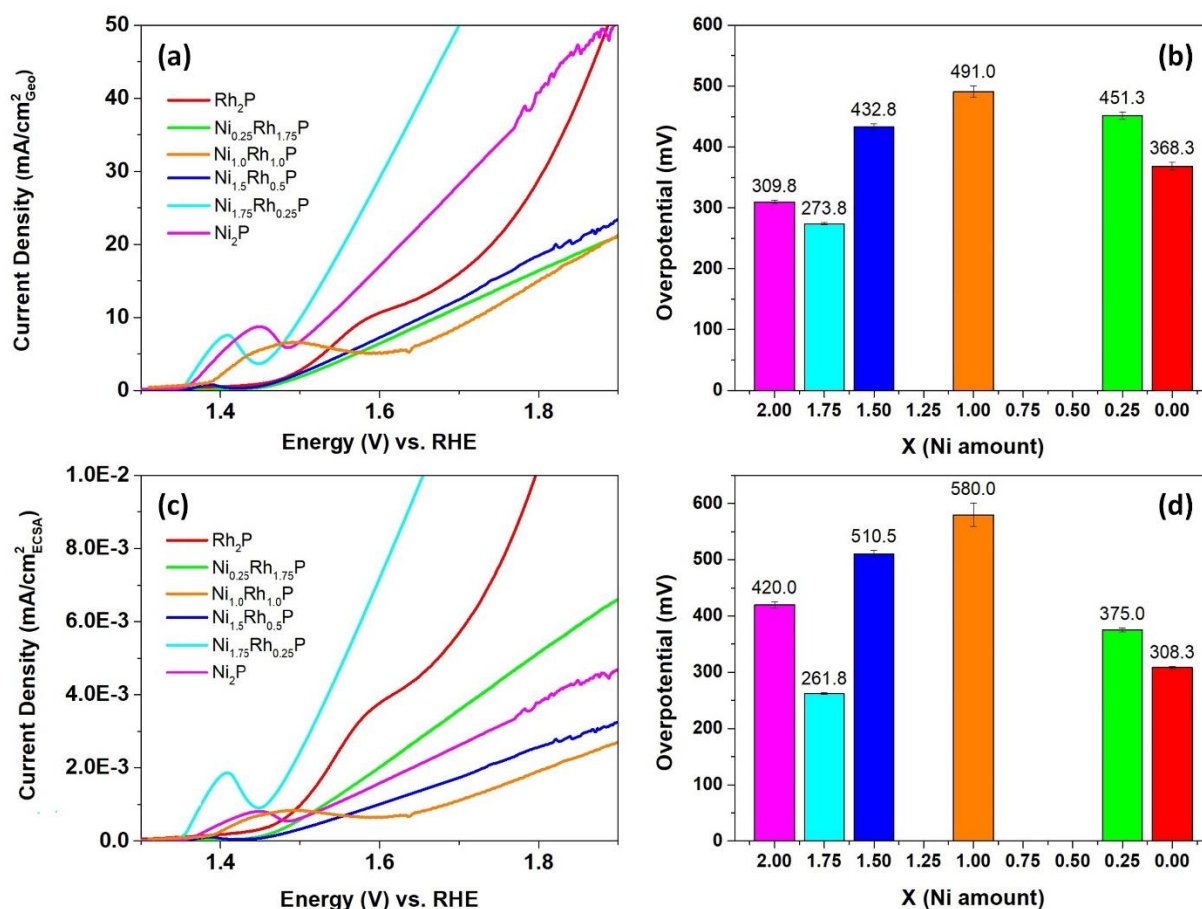


Figure 4.7. (a) OER polarization curves normalized to geometric area for Ni_{2-x}Rh_xP C-NPs. (b) Overpotentials at 10 mA/cm²_{geo}. (c) OER polarization curves normalized to ECSA for Ni_{2-x}Rh_xP C-NPs. (d) Overpotentials at 2.0 mA/cm²_{ECSA}

HER catalytic activity data are presented in Figure 5. As expected, the Rh-rich phases are more active, with Rh₂P ($\eta = 66.2$ mV @ 10 mA/cm²_{geo}) outperforming the modestly doped ternary phase Ni_{0.25}Rh_{1.75}P ($\eta = 82.1$ mV @ 10 mA/cm²_{geo}). With the exception of Ni₂P and Ni_{1.75}Rh_{0.25}P, all compositions outperform the commercial Pt/C standard ($\eta = 135$ mA @ 10 mA/cm²_{geo}, Figure S5). The Tafel slopes of Rh₂P (56 mV/dec) and Ni_{0.25}Rh_{1.75}P (63 mV/dec) are close to the expected value for a rate-limiting chemical step preceded by electron transfer (59 mV/dec),¹⁹⁴ whereas the slopes of the more Ni-rich phases are considerably higher, ranging from 84–112 mV/dec. However, when normalized to ECSA, the overpotential of the Ni_{0.25}Rh_{1.75}P phase is half that of Rh₂P (44.5

vs. 88.0 mV @ 2 mA/cm²_{ECSA}). According to the literature, the water dissociation step associated with HER in alkaline media can occur on Ni(OH)₂ and then facilitate the production of hydrogen intermediates adsorbed to the surface of neighboring noble metal active sites to yield molecular hydrogen.¹⁹⁵ A similar phenomenon might be happening on the Ni_{0.25}Rh_{1.75}P surface. Thus, even though the ternary phase necessarily has a lower number of Rh sites than Rh₂P, the overall higher site activity suggested by the ECSA might be a consequence of a lowering of the energy barrier in the water dissociation step. We also noted an increment in ECSA after 30 cycles of HER, but the changes are moderate for the most active Rh-rich phases (<20%, Table S4). Alternatively, it is possible that the large ECSA obtained upon Ni incorporation reflects sites that are electrochemically active, but not catalytically active.

The targeted 1:1 metal composition phase was also evaluated for both OER and HER activity (Figure 5 and 6) to establish whether phase-segregation positively effects the activity, which would motivate a more detailed evaluation of the fellow intermediate composition phase-segregated samples. However, for both geometric activity and the ECSA normalized activity, the observed overpotential values were not competitive with the more active phases. Therefore, further evaluation of phase-segregated samples was not carried out.

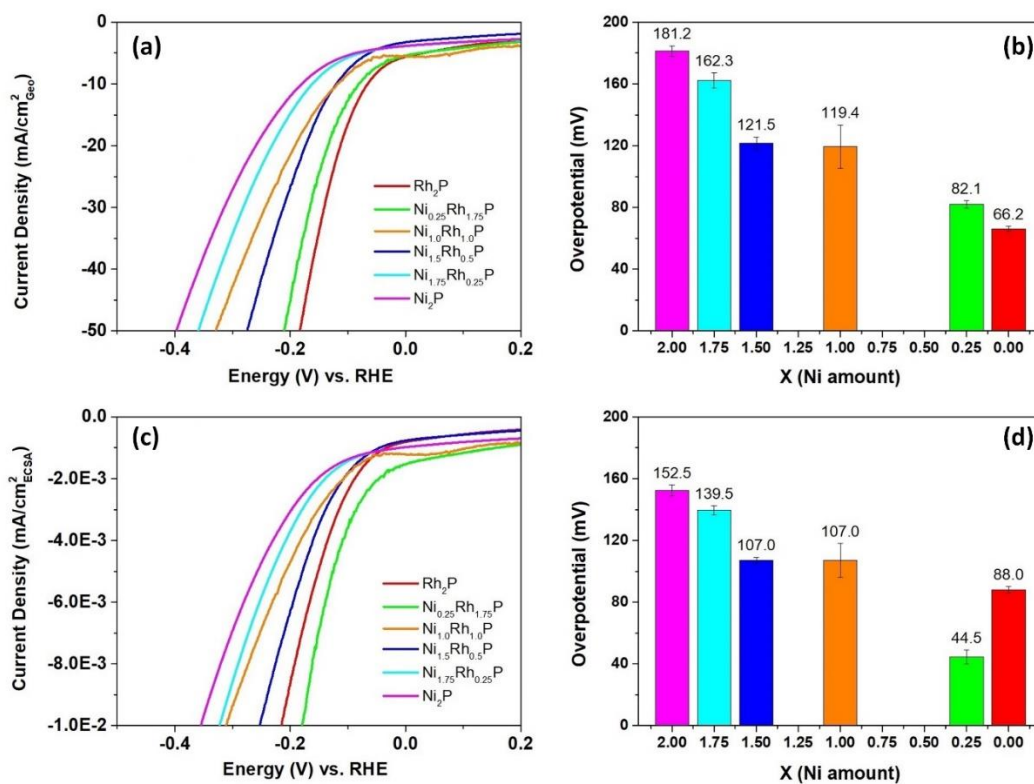


Figure 4.8. (a) HER polarization curves normalized to geometric area, for Ni_{2-x}Rh_xP C-NPs. (b) Overpotentials at $-10 \text{ mA}/\text{cm}^2_{\text{geo}}$. (c) HER polarization curves normalized to ECSA for Ni_{2-x}Rh_xP C-NPs. (d) Overpotentials at $-2.0 \text{ mA}/\text{cm}^2_{\text{ECSA}}$

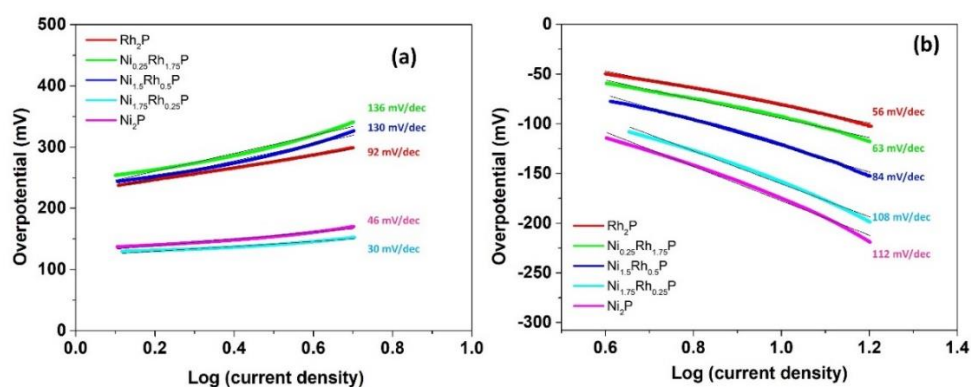


Figure 4.9. Tafel plots for Ni_{2-x}Rh_xP for (a) OER (b) HER

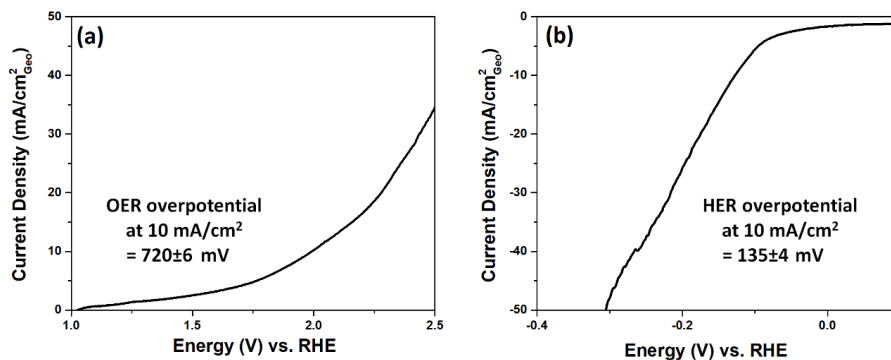


Figure 4.10. Activity data for 20%Pt/C catalysts towards (a) OER (b) HER in the 1M KOH medium. (Note: Observed data are comparable with literature reported values with similar mass loadings on GCE^{163, 164})

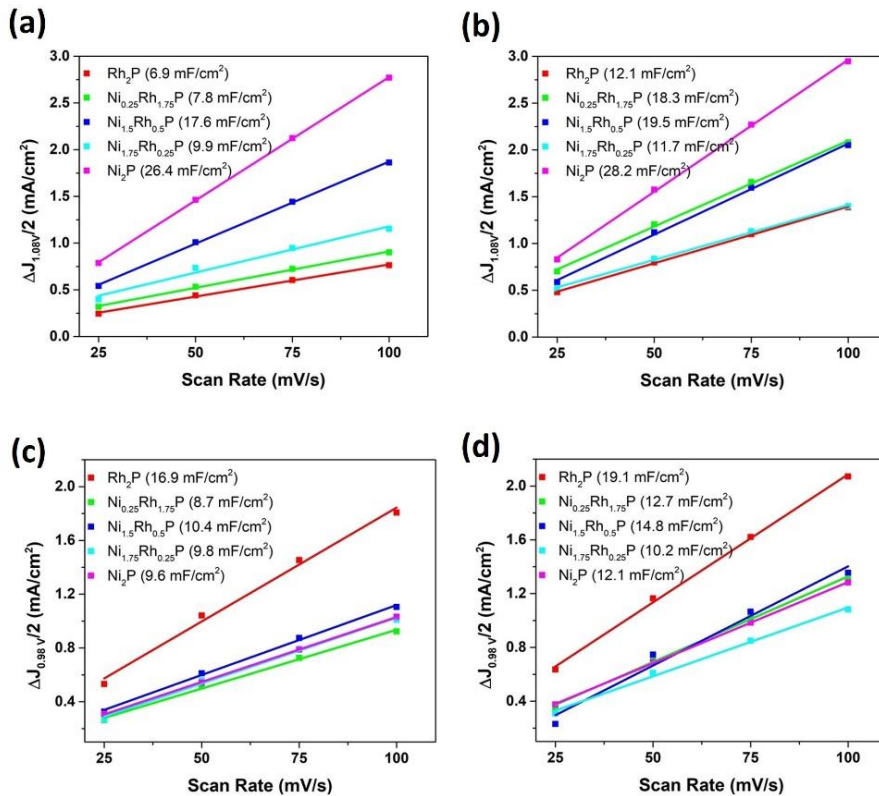


Figure 4.11. Double-layer capacitance data acquired via RDE on Ni_{2-x}Rh_xP for x = 0, 0.25, 0.50, 1.75 and 2.00). (a) 1st OER polarization curve (b) 30th OER polarization curve (c) 1st HER polarization curve (d) 30th HER polarization curve

Table 4.4. Electrochemically active surface area values and percentage difference (compared to initial ECSA) for Ni_{2-x}Rh_xP C-NP ink before and after 30 cycles

Catalyst	Initial ECSA for OER (cm ²)	ECSA after 30 cycles of OER (cm ²)	ECSA difference for OER (%)	Initial ECSA for HER (cm ²)	ECSA after 30 cycles of HER (cm ²)	ECSA difference for HER (%)
Ni ₂ P	754	806	7	274	346	26
Ni _{1.75} Rh _{0.25} P	283	334	18	280	291	4
Ni _{1.5} Rh _{0.5} P	503	557	11	297	423	42
Ni _{0.25} Rh _{1.75} P	223	523	135	248	263	6
Rh ₂ P	197	346	76	483	546	13

Table 4.5. Electrochemically active surface area (ECSA) and ECSA-normalized current densities computed at the indicated applied voltages for Ni_{2-x}Rh_xP C-NP ink on C cloth before and after the 10 h stability test

Catalyst	Initial ECSA (cm ²)	Initial current density, normalized to ECSA (μA/cm ² _{ECSA} @ V)	ECSA after 10 h stability test (cm ²)	Current density after 10 h, normalized to ECSA (μA/cm ² _{ECSA} @ V)
Ni _{1.75} Rh _{0.25} P for OER	263	3.1 @ 1.505 V	180	4.9 @ 1.505 V
Ni _{0.25} Rh _{1.75} P for HER	211	3.9 @ 0.850 V	306	2.5 @ 0.850 V

To evaluate the stability of the catalysts, long-term stability measurements were collected on the composition with the highest intrinsic activity for OER and HER. As shown in Figure 4.12, the geometric activity of Ni_{1.75}Rh_{0.25}P shows a 6% increase after 10 h in the basic medium for OER while Ni_{0.25}Rh_{1.75}P shows a 22% activity decrease after 10h for HER. To better understand how restructuring might be affecting the intrinsic properties, we also compared the ECSA values (Figure 4.13, Table 4.5) and ECSA normalized current density data (Figure 4.12) before and after the 10 h runs. We observed that the changes in device performance (geometrical) are reflecting intrinsic changes in the catalyst; i.e., a decrease (OER, 0.7x) or increase (HER, 1.5x) in ESCA over the course of the 10 h catalytic study. To discern the nature of these changes, we probed

localized and surface compositional/speciation changes using STEM-EDS mapping and XPS before and after the 10 h stability cycles.

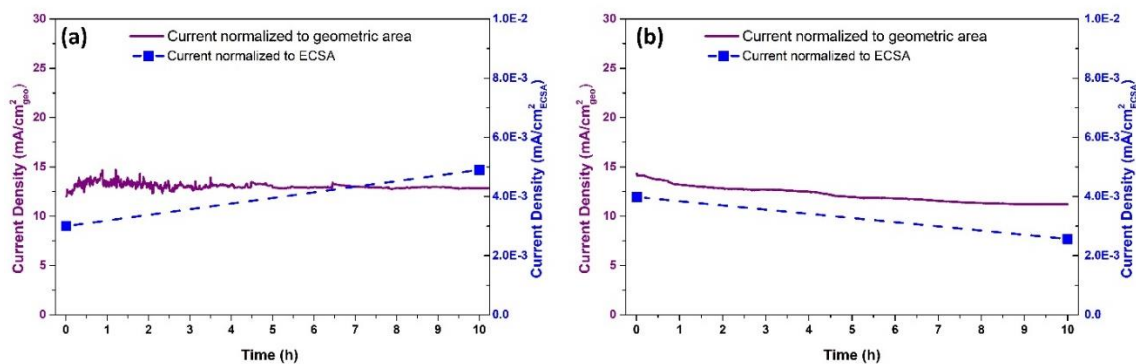


Figure 4.12. Long-term stability test for (a) $\text{Ni}_{1.75}\text{Rh}_{0.25}\text{P}$ for OER (b) $\text{Ni}_{0.25}\text{Rh}_{1.75}\text{P}$ for HER. The blue squares represent the current normalized to ECSA before and after the stability test. The blue dotted lines are a guide for the eye

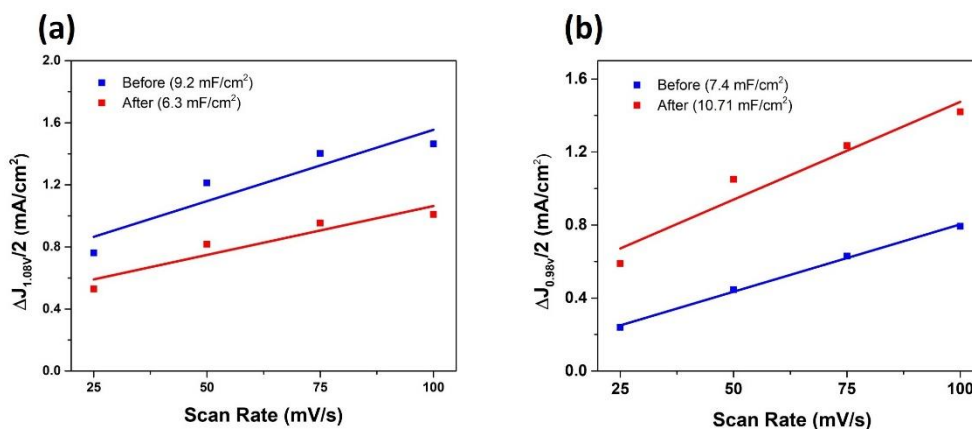


Figure 4.13. Double-layer capacitance data before and after the long-term (10 h) stability test for (a) $\text{Ni}_{1.75}\text{Rh}_{0.25}\text{P}$ for OER (b) $\text{Ni}_{0.25}\text{Rh}_{1.75}\text{P}$ for HER

We also tested the electrolytic performance of $\text{Ni}_{2-x}\text{Rh}_x\text{P}$ C-NPs composite towards overall water splitting, an overall water electrolyzer was prepared in a two-electrode configuration. $\text{Ni}_{1.75}\text{Rh}_{0.25}\text{P}$ and $\text{Ni}_{0.25}\text{Rh}_{1.75}\text{P}$ C-NPs ink were used to prepare the anode and cathode, respectively. In order to lower the overall cell resistance, the anode and cathode electrodes were kept close to each other with no membrane separator (Figure 4.14). The electrolytic activity of the overall cell was evaluated by collecting a cyclic voltammogram to determine the potential required to achieve

a current density of $20 \text{ mA/cm}^2_{\text{geometric}}$ (Figure 4.15a). The overall cell potential to deliver $20 \text{ mA/cm}^2_{\text{geometric}}$ was 1.78 V (without IR correction). This value was slightly higher than the sum of the HER and OER half-cell reactions values to achieve $20 \text{ mA/cm}^2_{\text{geometric}}$ (1.69 V , with IR correction). This difference might be due to the cell resistance.

As shown in Figure 4.15b, the electrochemical stability of the overall cell was also evaluated at a constant potential of 1.85 V for 10 hours. The current density was found to decrease by 19.6% over time, which we attribute to deactivation of the cathode as observed in the HER stability test (Figure 4.12b).

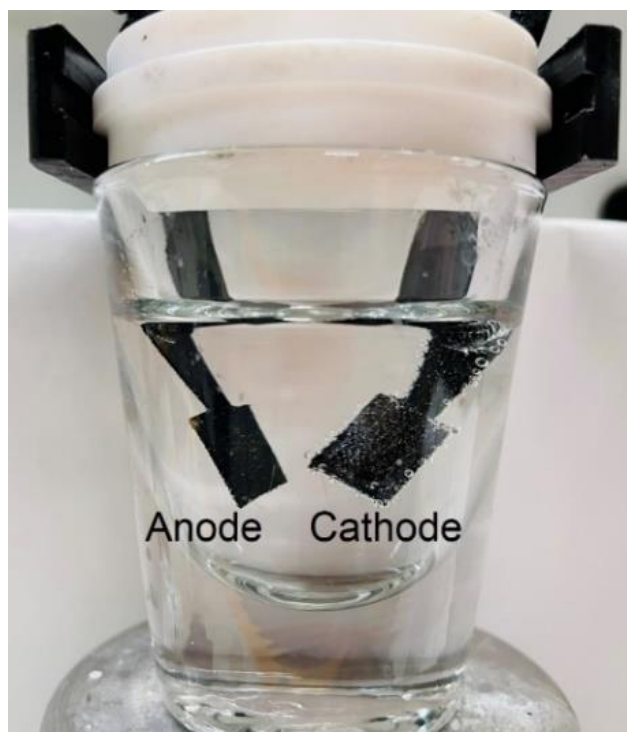


Figure 4.14. Overall water splitting setup

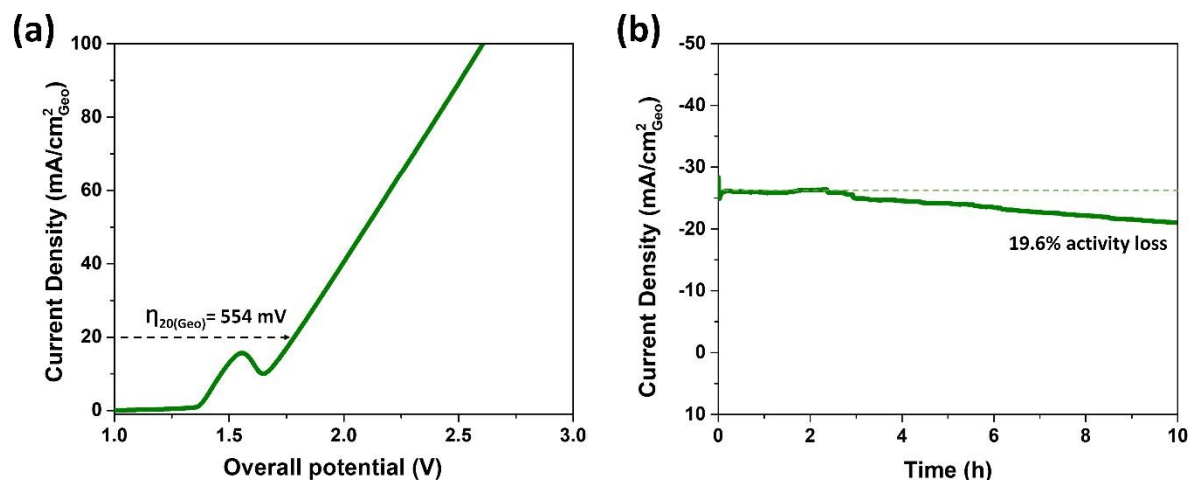


Figure 4.15. Overall water splitting of the cell $\text{Ni}_{1.75}\text{Rh}_{0.25}\text{P}/\text{C} \parallel \text{Ni}_{0.25}\text{Rh}_{1.75}\text{P}/\text{C}$ (a) activity and (b) stability data

4.3.4. Structural elucidation: STEM-EDS mapping and XPS

According to STEM-EDS mapping images in both compositions, Ni, Rh, and P were uniformly distributed in the structure of the nanoparticles before catalysis (Figure 4.16a,c). After 10 h of catalytic activity, the channel for oxygen, which displayed uniform intensity before catalysis (See Figure 4.16a,c) now shows O to be co-localized on the nanoparticles (Figure 4.16b,d). Intriguingly, the $\text{Ni}_{1.75}\text{Rh}_{0.25}\text{P}$ sample showed evidence of Rh segregation in high resolution images conducted after OER (Figure 4.17), whereas the elemental components in the $\text{Ni}_{0.25}\text{Rh}_{1.75}\text{P}$ sample were still uniformly distributed after HER (Figure 4.16d).

To better understand how the active surfaces are changing upon OER and HER catalysis, and aid in contextualizing the STEM-EDS data, XPS analyses were also carried out before and after the 10 h stability test using $\text{Ni}_{1.75}\text{Rh}_{0.25}\text{P}$ and $\text{Ni}_{0.25}\text{Rh}_{1.75}\text{P}$ containing inks, respectively. Figure 4.18a summarizes the XPS spectra of Ni 2p, Rh 3d, P 2p, and O 1s, before and after the 10 h OER stability test for $\text{Ni}_{1.75}\text{Rh}_{0.25}\text{P}$. According to the EDS elemental analysis (in TEM) of the fresh ink, the nanoparticles have a bulk composition of $\text{Ni}_{1.74}\text{Rh}_{0.26}\text{P}_{0.94}$ (Table 4.6). However, the surface composition elicited from XPS is quite different, with M/P = 5.3 vs. 2.0 ideal, and only a

trace of Rh (not quantified). The pre-catalyst has Ni 2p_{3/2} peaks at 853.5 eV and 856.3 eV, attributed to metallic nickel bound to phosphorous and Ni²⁺ from oxides/hydroxides, respectively.¹⁹⁶ Satellite peaks of the Ni spectrum can be seen at 860.4 eV and 863.5 eV.¹⁹⁷ The surface signals for Rh 3d were very weak as there is a low amount of Rh in the composition and, possibly, Rh is underrepresented on the surface. The Ni₂P surface is known to be readily oxidized and moisture adsorbing, forming NiO and Ni(OH)₂ when exposed to the atmosphere.¹⁹⁸⁻²⁰⁰ Our data also suggest that the surface of Ni_{2-x}Rh_xP is susceptible to air oxidation and atmospheric moisture adsorption resulting in an Ni⁰/Ni²⁺ ratio of 0.79 (Table 4.7). Likewise, the P spectrum shows two doublet peaks at 129.9 eV and 133.6 eV for reduced phosphorus (in the metal phosphide) and phosphate,^{197, 201} respectively, and the O1s spectrum confirms metal oxides at 531.8 eV. An additional peak at 533.8 eV in the O1s spectrum is attributed to C-O due to Nafion in the ink and/or surface hydroxide groups.^{197, 202, 203}

After catalysis, the overall bulk composition by EDS (TEM) reveals minimal changes in the Ni:Rh ratio, but a significant depletion (~48%) in P (Ni_{1.73}Rh_{0.27}P_{0.45}). However, the surface XPS data shows the presence of 2% Rh, and 98% Ni, with no detectable P. Leaching of phosphorus as phosphate is expected as the surface becomes oxidized. Likewise, the presence of metallic Ni on the surface is significantly depleted due to oxidation (Ni⁰/Ni²⁺ = 0.05, Table 4.7). Another new peak at 858.4 eV is visible in the spectrum, which we attribute to Ni³⁺ resulting from electrochemical oxidation of Ni²⁺.^{204, 205} Interestingly, after catalysis the Rh spectrum is better resolved, enabling clear fitting. This may be a consequence of the segregation noted in the STEM-EDS (see Figure 4.17). In contrast to Ni, the Rh appears unoxidized post OER.

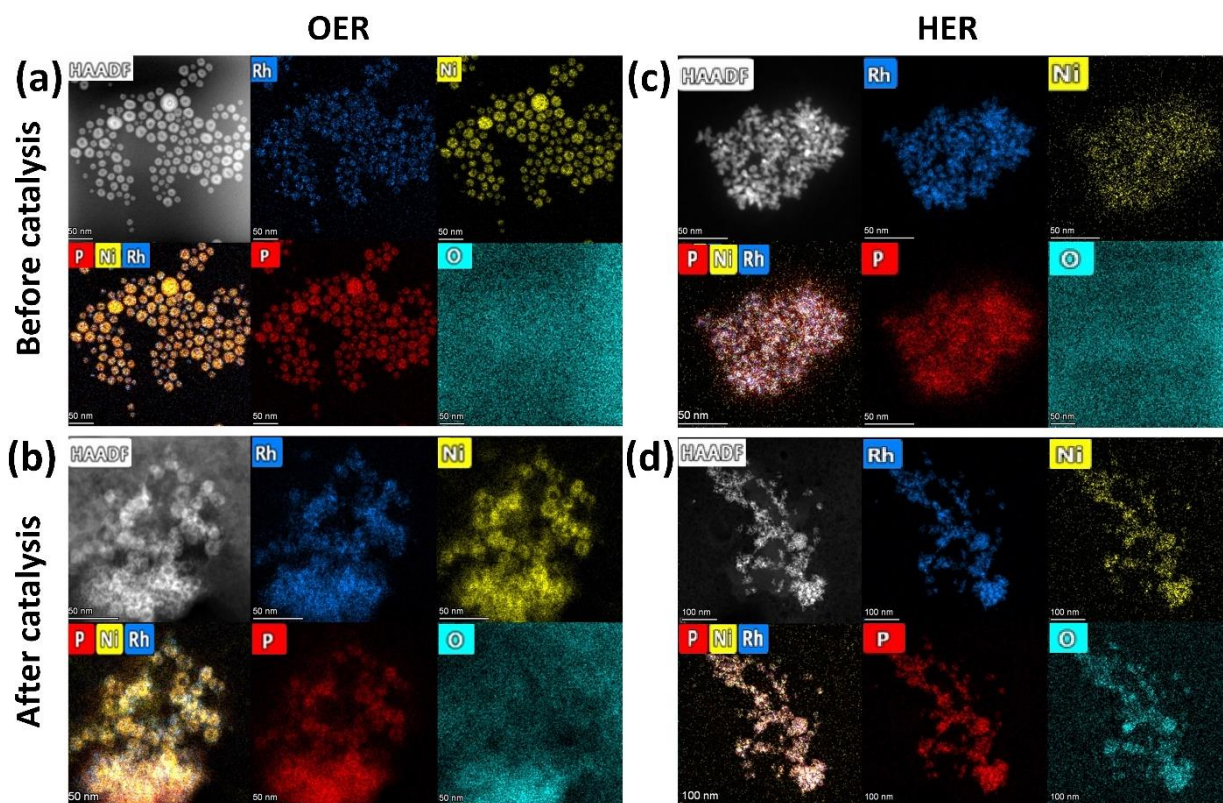


Figure 4.16. EDS mapping analysis of $\text{Ni}_{1.75}\text{Rh}_{0.25}\text{P}$ C-NPs (a) before and (b) after OER activity and $\text{Ni}_{0.25}\text{Rh}_{1.75}\text{P}$ C-NPs (c) before and (d) after HER activity. (Scale bar is 50 nm in a-c and 100 nm in d)

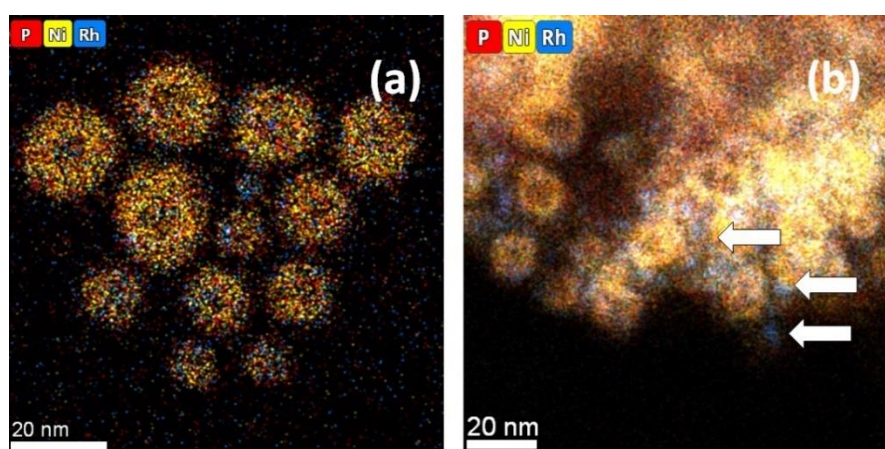


Figure 4.17. EDS mapping analysis of $\text{Ni}_{1.75}\text{Rh}_{0.25}\text{P}$ C-NPs (a) before and (b) after OER activity (arrows indicate areas of Rh segregation after catalysis)

Table 4.6. EDS and XPS elemental ratios before and after the 10 h catalytic stability test (see Table 4.8 for quantified values)

Composition	Status	EDS (bulk)		XPS (surface)	
		Ni:Rh	M:P	Ni:Rh	M:P
Ni _{1.75} Rh _{0.25} P	Before OER	87:13	68:32	100:0	84:16
	After OER	87:13	82:18	98:2	100:0
Ni _{0.25} Rh _{1.75} P	Before HER	13:87	66:34	66:34	88:12
	After HER	15:85	70:30	81:19	100:0

Table 4.7. XPS ratios of oxidation states of each element before and after the 10 h catalytic stability test (see Table 4.9 for quantified values)

Composition	Status	Ni: Ni ^{2+/3+}	Rh:Rh ³⁺	P:PO ₄ ³⁻
Ni _{1.75} Rh _{0.25} P	Before OER	44:56	ND	25:75
	After OER	5:95	100:0	ND
Ni _{0.25} Rh _{1.75} P	Before HER	12:88	39:61	15:85
	After HER	6:94	14:86	ND

Table 4.8. EDS and XPS elemental quantification before and after catalysis for Ni_{1.75}Rh_{0.25}P (OER) and Ni_{0.25}Rh_{1.75}P (HER)

	EDS (bulk)			XPS (surface)		
	Ni%	Rh%	P%	Ni%	Rh%	P%
Before OER	59.3	8.8	31.9	84	ND	16
After OER	70.7	11.0	18.3	98	2	ND
Before HER	8.6	57.4	34.0	58	30	12
After HER	10.1	59.4	30.5	81	19	ND

Table 4.9. XPS quantification of oxidation states for each element for Ni_{1.75}Rh_{0.25}P (OER) and Ni_{0.25}Rh_{1.75}P (HER)

	Ni			Rh			P		O		
	Ni-P	Ni ²⁺	Ni ³⁺	Rh-P	Rh (III) oxide	Undefined Rh peak, 310.7 eV*	M-P	Phosphate	C-O	M-O	H ₂ O
Before OER	44%	56%	ND	ND	ND	ND	25%	75%	50%	50%	ND
After OER	5%	70%	25%	100%	ND	ND	ND	ND	22%	78%	ND
Before HER	12%	45%	43%	39%	42%	19%	15%	85%	40%	60%	ND
After HER	6%	55%	39%	14%	49%	37%	ND	ND	35%	57%	8%

* This peak has been variously attributed to satellites from Rh(III) oxide, Rh(OH)₃, RhX₃ (X = Cl or F) or Rh⁴⁺ ^{206, 207}

Figure 4.18b summarizes the XPS data before and after the 10 h stability test for HER activity. XPS analysis of the fresh catalyst reveals Ni 2p_{3/2} peaks at 853.8 eV and 856.5 eV for Ni-P and Ni²⁺ respectively.¹⁹⁷ There is also an intense peak at 858.7 eV for Ni³⁺, distinctly different from the Ni-rich phase studied for OER where Ni³⁺ is only observed post-catalysis (see Table 4.9). This Ni³⁺ peak is reminiscent of those reported for Pd bonded Ni surfaces (862.0 eV) and Fe-Ni-S (858.5 eV) surfaces, wherein the Ni electron density is appropriated in bonding to Pd or Fe-S.^{204, 208} In our case, we attribute it to Ni bonded to both Rh and P as the sample is Rh rich. The Rh 3d_{5/2} spectrum has peaks at 307.6 eV and 308.8 eV attributed to Rh⁰ (in the phosphide) and Rh³⁺(Rh₂O₃), respectively, as well as an additional peak at 310.7 eV that cannot be definitively interpreted, but may be a satellite peak associated with Rh₂O₃.^{197, 209} The P spectrum peaks at 129.6 eV and 133.9 eV indicate reduced phosphorus (in the metal phosphide) and phosphate, respectively. The O1s spectrum confirms the presence of metal oxides (531.6 eV).

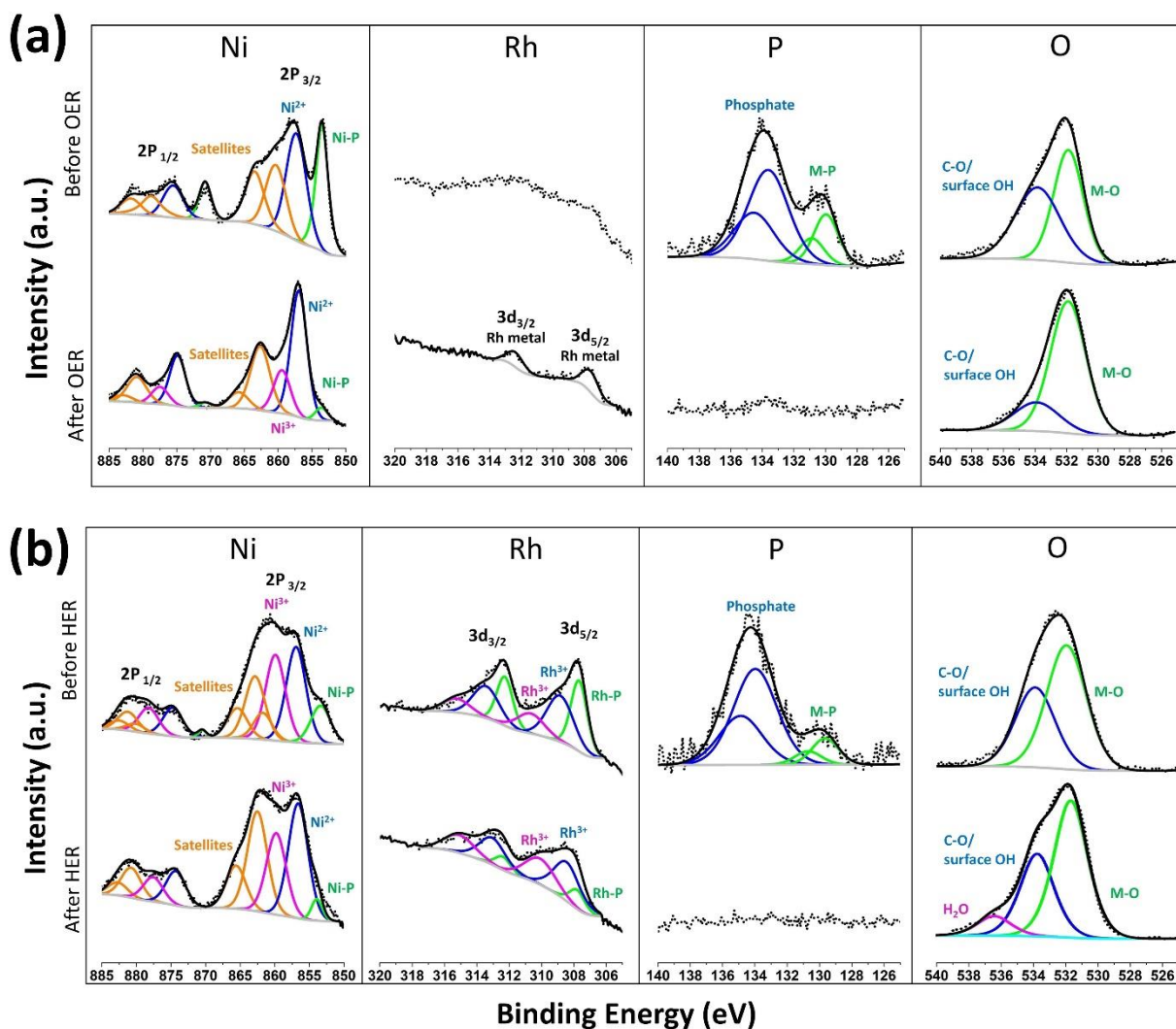


Figure 4.18. (a) XPS spectra of Ni_{1.75}Rh_{0.25}P C-NPs before and after 10 h OER activity testing (b) XPS spectra of Ni_{0.25}Rh_{1.75}P C-NPs before and after 10 h HER activity testing

Even though the bulk composition of the catalyst according to TEM/EDS elemental analysis is Ni_{0.26}Rh_{1.74}P_{1.03}, the XPS analysis shows the surface is surprisingly Ni-rich (Ni/Rh = 1.9 vs. 0.15 ideal), and, as with the Ni_{1.75}Rh_{0.25}P sample, phosphorus deficient (M/P = 7.3). The origin of the Ni-enhancement at the surface noted for both phases may be a function of differing diffusion energies, surface energies (due to preferred faceting and/or dictated by surface ligands used in the synthesis), and/or defects, etc.²¹⁰ We note that a similar trend was observed for

Co_{0.75}Rh_{1.25}P: Rh and P are deficient at the surface relative to the base metal, Co, although the differences are less pronounced than for Ni (Co/Rh = 1.3 vs. 0.6 ideal; M/P = 3.6 vs. 2.0 ideal).¹⁸¹

After HER catalysis, the only significant change in bulk composition is a decrease of P by 15%, (Ni_{0.29}Rh_{1.71}P_{0.88}), suggesting overall P losses are not as great for HER relative to OER. However, according to the XPS data, the surface P is completely depleted, as it was for Ni_{1.75}Rh_{0.25}P post OER, consistent with phosphate displacement by hydroxide species during electrochemical cycling in alkaline media.¹⁶⁹ Intriguingly, the surface has become even more Ni-rich (Ni/Rh = 4.3), and both Ni and Rh are present mostly in oxidized form (Ni⁰/Ni^{2+/3+} = 0.06; Rh⁰/Rh³⁺ = 0.16, Table 4.7).

4.3.5. Assessing the role of noble and base metal components in water-splitting catalysis over bimetallic phosphides

The combined STEM/EDS and XPS data suggest that (1) the surface composition of Ni_{2-x}Rh_xP is quite different from the bulk (targeted) composition with Ni exhibiting a superabundance relative to Rh and P; and (2) Ni_{2-x}Rh_xP undergoes dramatic *in-situ* chemical modifications during both HER and OER processes. In both cases, the initial phosphide/phosphate on the pre-catalytic surface readily oxidizes and then dissolves in the basic electrolyte solution as metal oxides/hydroxide species are formed, as evidenced by the complete disappearance of a P signal in the XPS combined with losses of 15% (HER) to 48% (OER) of P relative to Rh+Ni in STEM/EDS bulk analysis. This loss of phosphide (as phosphate) is by now a generally recognized characteristic of phosphide catalysts for water-splitting reactions in alkaline media.^{169, 211-213} However, the nature of the *in-situ* changes depends significantly on the native metal composition, surface characteristics, and electrocatalytic treatment (OER vs. HER), which dictates the overall performance and stability.

For the case of $\text{Ni}_{1.75}\text{Rh}_{0.25}\text{P}$ employed for OER at $\text{pH} = 14$, the enhancement in activity upon incorporation of 12.5 % Rh in Ni_2P relative to Ni_2P may be attributed to electronic effects and/or restructuring of the catalyst due to phase-segregation of Rh (Figure 4.17). The polarization curve provides strong evidence that the presence of Rh shifts the oxidation potential of Ni more negative, facilitating its oxidation. At the same time, the fact that the Rh, barely detectible and not quantifiable pre-catalysis, is in its reduced state after catalytic testing (Figure 4.18a) and also physically separated from Ni in the STEM/EDS mapping post-catalysis (Figure 4.17), is a strong indicator that the role of the Rh in promoting catalysis may be changing over time. The consequence of the Rh segregation is a decrease in the ECSA (0.7x vs. pre-catalysis), but at the same time, the ECSA normalized current density is increasing (1.5x vs. pre-catalysis, Figure 4.12, Table 4.5). The correlation of Rh phase segregation to decreased electrochemically active surface area, but enhanced catalytic activity, suggests the catalytic sites have become intrinsically more active over the course of catalytic testing. The activity trend dominates the surface area trend, such that a modest increase in geometric activity (ca 6%) is noted over the course of the 10 h study. We noted a similar trend in OER studies of $\text{Co}_{1.75}\text{Rh}_{0.25}\text{P}$ —the geometric activity is augmented over time and phase-segregation of Rh is evident.^{25, 182} This may be due to reconstruction of the base metal catalyst. Alternatively (or, in addition), the segregation of Rh might be a consequence of low—but not zero—solubility of Rh in the reconstructed oxide/hydroxide; i.e., some Rh may remain dispersed and may continue to moderate the activity of the base metal.

For $\text{Ni}_{0.25}\text{Rh}_{1.75}\text{P}$ employed for HER at $\text{pH} = 14$, the case is quite different. Notably, the ECSA increases over time, both at short times (30 cycles, 1.1x, Table 4.4) and long times (10 h, 1.4x, Table 4.5). These data correlate to oxidation of Ni to $\text{Ni}^{2+/3+}$ and Rh to Rh^{3+} , according to XPS data. At the same time, the ECSA normalized current density at 0.85 V is decreasing (Figure

4.12), suggesting that the overall enhancement in number of electroactive sites actually results in an overall decrease in the per site activity, or that new sites that form *in situ* are not contributing to the overall catalysis. However, when combined with the fact that the geometrically normalized activity also decreases (Figure 4.12), it is clear that the catalyst is deactivating, i.e., either the number of active sites—or their potency, is diminished. This may be a consequence of Ni replacing Rh (so that Ni is 81% by XPS) on a surface that started out already Ni-rich relative to the bulk composition (66% Ni by XPS vs. 12.5% Ni by TEM/EDS). Given that Rh₂P is reported to be more active than Ni₂P for HER, a decrease in the Rh content would be consistent with a decrease in the number of active catalytic sites. What is not clear is why the addition of Ni leads to enhancement in activity relative to Rh₂P itself, especially given the disproportionately large amount of Ni on the surface relative to the bulk composition. On the other hand, as previously mentioned, the “enhanced” activity is not seen in the geometrically normalized data, only in the ECSA-normalized data. Thus, the Ni may enhance the number of electrochemically active surface sites without playing a proportionate role in the catalytic reaction—or possibly any role. It is also possible that Ni may aid in initial restructuring, which leads to a higher ECSA-normalized current density than for Rh₂P itself (at least initially) or that Rh and Ni work synergistically, with activity loss over time a consequence of the changing surface ratio. However, it is clear that while addition of Ni seems to “goose” the initial activity of Rh₂P, this is achieved by sacrificing long-term stability.

Whereas the behavior of Rh-incorporation on base metal phosphides seems to be similar under alkaline OER conditions for Ni₂P vs. Co₂P, this is not the case for HER catalysis involving incorporation of base metals into Rh₂P; the behavior of Ni_{0.25}Rh_{1.75}P is distinct from that of the Co analog (Co_{0.25}Rh_{1.75}P). When normalized to geometric surface area, Ni_{0.25}Rh_{1.75}P demonstrates a larger overpotential—by 20 mV—relative to Rh₂P or Co_{0.25}Rh_{1.75}P. This may be due to differences

in the electronic structure of the bulk; however, XPS data suggest that surface effects may be responsible. Notably, the surface of $\text{Ni}_{0.25}\text{Rh}_{1.75}\text{P}$ has twice as much Ni as Rh, whereas for $\text{Co}_{0.25}\text{Rh}_{1.75}\text{P}$, the Co is barely evident in the XPS—indeed it is of too low a concentration to obtain a reliable fit.¹⁸² The excess Ni at the surface may reflect solubility challenges of Ni incorporation into Rh_2P , as reflected in the lack of solid solution formation across intermediate values of x . Thus, the surfaces of $\text{Ni}_{0.25}\text{Rh}_{1.75}\text{P}$ and $\text{Co}_{0.25}\text{Rh}_{1.75}\text{P}$ differ considerably in their base metal-to-Rh composition, making an apples-to-apples comparison of the two phases questionable. Additionally, in $\text{Co}_{0.25}\text{Rh}_{1.75}\text{P}$ the Rh remains metallic,¹⁸² even as surface phosphide is oxidized and dissolved as phosphate, whereas in $\text{Ni}_{0.25}\text{Rh}_{1.75}\text{P}$ the Rh is largely oxidized, despite the fact that HER is conducted at a more negative potential (by 25mV) for the Ni analog relative to the Co analog. The differences in the behavior of Ni and Co analogs are much greater than would be anticipated based on their atomic properties, underscoring the importance of experimental validation.

4.4. Conclusions

Phase pure $\text{Ni}_{2-x}\text{Rh}_x\text{P}$ colloidal nanoparticles ($x=0.25, 0.5, \text{ and } 1.75$) can be prepared with low polydispersity by solution-phase arrested precipitation reactions. Although the synthetic method incorporates an early Ni-Rh alloying step, and the bulk compositions mirror the targeted compositions, the surface compositions of the prepared nanocrystals have a superabundance of Ni relative to Rh and P. When employed as pre-catalysts in alkaline media for water oxidation and reduction, the most active phases (current density normalized to ECSA) are $x = 0.25$ and $x = 1.75$, respectively. However, the origin of the activity and the effect of restructuring on the stability is different. OER reactions ($x = 0.25$) demonstrate an augmented activity over time at 1.505 V, whether normalized to geometric surface area or ECSA, and this correlates to phase segregation

of metallic Rh. In contrast, HER reactions ($x = 1.75$) undergo a decrease in ECSA-normalized and geometrically normalized current densities at 0.85 V over time. In comparing to prior work from our lab on the related $\text{Co}_{2-x}\text{Rh}_x\text{P}$ nanoparticles, we find that the role of Rh as an “activator” for the base metal oxide is the same in both cases (likely driven by phase-segregation), whereas Co is distinct from Ni when incorporated into Rh_2P at similar bulk concentrations, in that the Co does not preferentially segregate to the surface (or does so on a much smaller scale), leaving the more active (and stable) Rh component to dominate despite being diluted by a base metal.

CHAPTER 5. Ni_{2-x}Rh_xP AS A STABLE ELECTROCATALYST FOR OVERALL WATER SPLITTING IN ACIDIC MEDIA

Abstract

In acidic media, transition metal phosphides (TMPs) are found to be stable catalysts for the hydrogen evolution reaction (HER), but typically exhibit poor stability towards the corresponding oxygen evolution reaction (OER). A notable exception appears to be Rh₂P/C nanoparticles, which were reported to be active and stable towards both HER and OER in acidic media. In our previous work we investigated base-metal substituted Rh₂P, specifically Co_{2-x}Rh_xP and Ni_{2-x}Rh_xP, for HER and OER as a means to reduce the noble metal content in catalytic materials. For both Co- and Ni-substituted systems in alkaline media, the Rh-rich phases were found to be best for HER, while base-metal-rich phases were found to be better for OER. However, Co_{2-x}Rh_xP, was not stable in acidic media for either HER or OER due to dissolution of Co. In the present contribution, the activity and the stability of our previously synthesized Ni_{2-x}Rh_xP nanoparticle catalysts ($x = 0.25, 0.50, 1.75$) toward HER and OER in acidic (0.5 M H₂SO₄) electrolyte, and relative to Rh₂P and commercial catalysts, is probed. The Ni_{0.25}Rh_{1.75}P phase was found to have comparable geometric activity (overpotential values at 10 mA/cm²_{geo}) and stability over 10 h to Rh₂P. In contrast, for OER, all of the tested Ni_{2-x}Rh_xP phases tested had similar overpotential values at 10 mA/cm²_{geo}, but these were > 2x the initial value for Rh₂P. However, the activity of Rh₂P fades rapidly (76% over 1 h), as does Ni₂P and Ni-rich Ni_{2-x}Rh_xP phases, whereas Ni_{0.25}Rh_{1.75}P shows only modest declines over the same time period. Overall water splitting (OWS) conducted using Ni_{0.25}Rh_{1.75}P as a catalyst (Ni_{0.25}Rh_{1.75}P || Ni_{0.25}Rh_{1.75}P) relative the state-of-the-art (RuO₂ || 20% Pt/C) couple revealed comparable stabilities over time, with the Ni_{0.25}Rh_{1.75}P system demanding an additional 200 mV overpotential to achieve the same current density (10 mA/cm²_{geo}). Whereas a Rh₂P || Rh₂P

OWS cell had a similar overpotential to RuO₂ || 20% Pt/C, but is unstable. These data suggest that Rh₂P is not a stable anode for OER, but can be stabilized, albeit with a loss of activity, by incorporation of nominally modest amounts of Ni.

5.1. Introduction

The development of inexpensive and efficient water electrolyzers for acidic media is challenging due to the instability of the anodic catalysts, which perform the oxygen evolution reaction (OER), generating electrons for hydrogen production at the cathode via the hydrogen evolution reaction (HER), and a lack of clear understanding of the OER mechanism and the nature of the catalytic sites under acidic conditions.^{182, 214-218} However, acidic water splitting is worth pursuing for several reasons: (1) due to the high mobility of H⁺ ions relative to OH⁻ ions, acidic media has a higher ionic conductivity than base, hence enabling a high current density; (2) acidic media dissolves CO₂, thereby enabling long electrolyzer lifetimes relative to alkaline electrolyzers, where metal carbonates precipitate and poison active catalytic sites.^{25, 181, 182, 214, 218-220}

With respect to metal phosphides, work done by Duan *et al.* showed that Rh₂P nanocube catalysts had higher activity and stability relative to Pt for HER and OER in acidic media.¹⁷⁷ However, the HER and OER stability of Rh₂P was reported for only 2000 s (33.3 min) and 1000 s (16.7 min), respectively.¹⁷⁷ Our previous studies on Co_{2-x}Rh_xP (x=1.75 for HER and x=0.25 for OER) and Ni_{2-x}Rh_xP (x=0.25 for OER) in basic media showed higher electrocatalytic activities compared to their monometallic end members, with Ni_{0.25}Rh_{1.75}P exhibiting a higher overpotential for HER relative to Rh₂P when compared on geometrical surface area, but a lower overpotential when normalized against the electrochemical surface area (ECSA).^{25, 182, 218} In acidic media, we found that adding 37.5% Co into the Rh₂P cubic antiferroite structure retained the crystal structure and high HER activity of Rh₂P while diluting the expensive noble metal with a base metal.¹⁸¹

However, the $\text{Co}_{2-x}\text{Rh}_x\text{P}$ system was not stable in acid at the positive potentials required for OER, and Co dissolution under HER conditions led to a loss in activity of ca 50% before leveling off.^{181, 221} Since Ni_2P is known to be more stable than Co_2P in acidic media, we hypothesized that the $\text{Ni}_{2-x}\text{Rh}_x\text{P}$ system will be more stable than the $\text{Co}_{2-x}\text{Rh}_x\text{P}$ system in acidic HER and OER, and may enable comparable activity to Rh_2P .^{169, 222}

In this chapter, the performance evaluation of our previously synthesized $\text{Ni}_{2-x}\text{Rh}_x\text{P}$ ($x = 0.25, 0.5, \text{ and } 1.75$) nanomaterial catalyst toward OER, HER and overall water splitting (OWS) in acidic media with respect to activity and stability is assessed and compared to Rh_2P and Ni_2P endmembers.

5.2. Experimental section

All materials used in this project are reported in Chapter 2.

5.2.1. Synthesis of $\text{Ni}_{2-x}\text{Rh}_x\text{P}$, Ni_2P , and Rh_2P nanoparticles

Nanoparticle preparation followed the protocols described in Chapter 4.2.1 – 4.2.3.

5.2.2. Characterization

Powder X-ray diffraction (PXRD), Transmission electron microscopy (TEM) equipped with energy dispersive X-ray spectroscopy (EDS, EDAX, inc.), and X-ray photoelectron spectrometry (XPS) were employed as described in Chapter 2.

5.2.3. Electrochemical measurements

Catalytic inks were prepared using $\text{Ni}_{2-x}\text{Rh}_x\text{P}$ nanoparticles for compositions that can be achieved as single phase ($x = 0, 0.25, 0.5, 1.75, 2.0$; see Chapter 4), and electrocatalytic activity, stability, and overall water splitting tests were performed following protocols described in Chapter 2.4.1-2.4.2. 0.5 M H_2SO_4 was used as the electrolyte; a carbon rod counter electrode was used for HER and a Pt counter electrode was used for OER.

5.3. Results

5.3.1. Electrocatalytic studies

Our previous work showed that the crystal structure of $\text{Ni}_{2-x}\text{Rh}_x\text{P}$ nanoparticles varies with composition, where Rh-rich and Ni-rich end-members adopt the cubic antiferroite- and hexagonal Fe_2P -type structures, respectively, and phase segregation/impurity formation occurs for $x = 0.75$ -1.5 compositions (Chapter 4).²¹⁸ Accordingly, three different compositions of $\text{Ni}_{2-x}\text{Rh}_x\text{P}$ ($x=0.25$, 0.5, and 1.75) nanoparticles, and their end members Ni_2P and Rh_2P , all determined to be phase-pure within the limitations of powder X-ray diffraction, were prepared by the solution-phase arrested precipitation method according to our established protocol (see Chapter 4.2.1-4.2.3).²¹⁸ These were used to make nanoparticle inks, $\text{Ni}_{2-x}\text{Rh}_x\text{P}/\text{C}$, by our standard method (see Chapter 2.4.1).²¹⁸ For comparison studies, commercial catalysts (RuO_2 and 20%Pt/C) were used to prepare inks with the same catalytic material concentration (RuO_2 and Pt: 2 mg/mL). For RuO_2/C ink preparation, a similar protocol as for $\text{Ni}_{2-x}\text{Rh}_x\text{P}/\text{C}$ was followed using RuO_2 as nanoparticles, while for 20%Pt/C ink, no additional C was added as the Pt was already supported by C in the commercial catalyst.

5.3.1.1 Hydrogen evolution reaction in acid

Figure 5.1 shows HER activity and stability studies in acidic media for the different compositions that were examined. Polarization curves clearly reveal that the HER performance of $\text{Ni}_{2-x}\text{Rh}_x\text{P}$ nanoparticles in acidic media are composition-dependent (Figure 5.1a), with the Rh-rich cubic antiferroite $\text{Ni}_{0.25}\text{Rh}_{1.75}\text{P}$ phase being the most active, and comparable to Rh_2P (ca 85 mV @ $10\text{mA}/\text{cm}^2_{\text{geo}}$), Figure 5.1b. In contrast, Ni-rich samples adopting the hexagonal Fe_2P structure have overpotentials that are above 150 mV.¹⁸¹ Interestingly, when going to higher current densities, both $\text{Rh}_2\text{P}/\text{C}$ and $\text{Ni}_{0.25}\text{Rh}_{1.75}\text{P}/\text{C}$ catalytic materials outperform 20% Pt/C activity. As shown in Figure 5.1c, the Tafel slopes of Rh_2P (35 mV/dec) and 20% Pt/C (36 mV/dec) are close

to the value for a rate-limiting chemical step preceded by the Volmer-Tafel mechanism (~ 30 mV/dec),¹⁹⁴ whereas the slopes for $\text{Ni}_{2-x}\text{Rh}_x\text{P}$ phases are considerably higher, ranging from 59-204 mV/dec.²²³ The trend in Tafel slopes is generally in agreement with the observed HER activity, with the most active group of samples (Rh-rich) having the smallest slope while the least active samples (Rh-poor) have the highest slope.

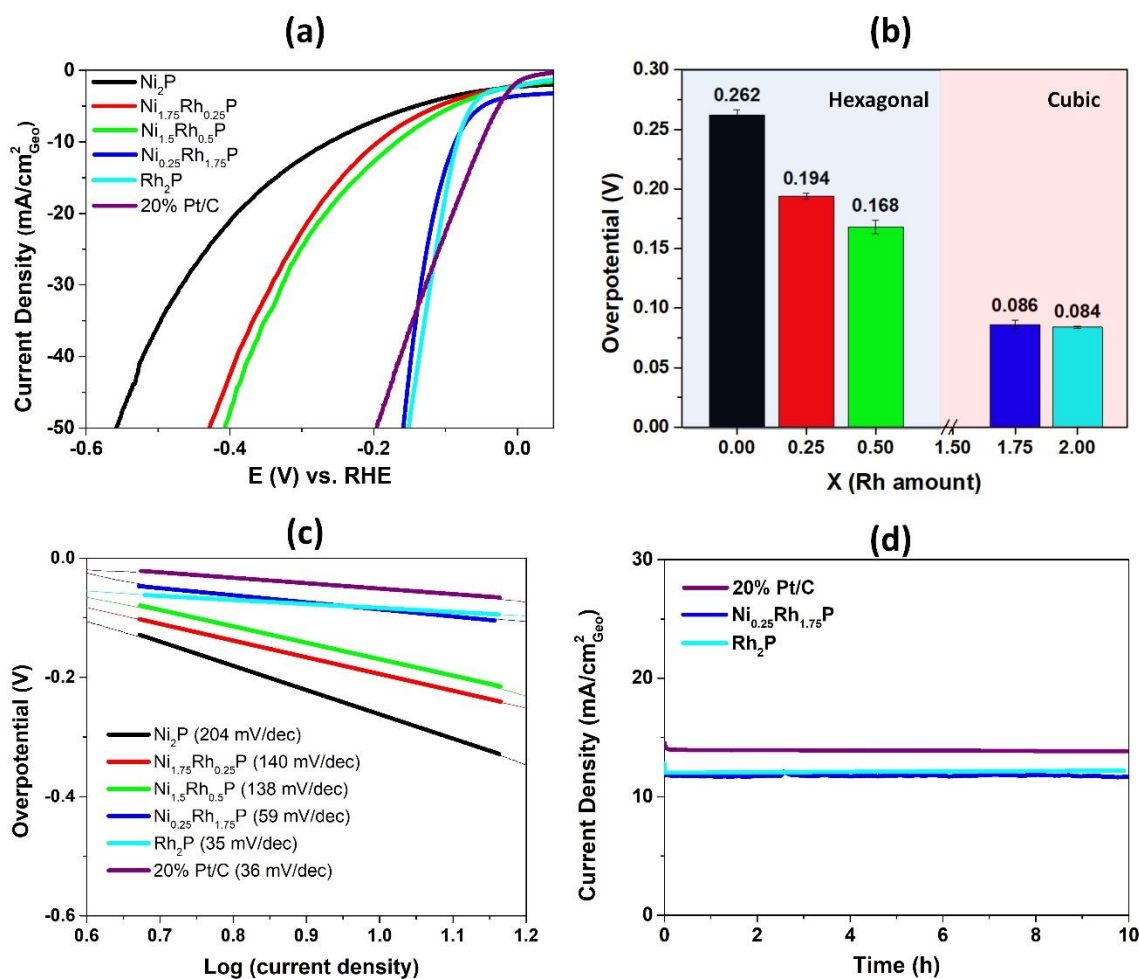


Figure 5.1. (a) HER polarization curves for $\text{Ni}_{2-x}\text{Rh}_x\text{P}$ nanoparticles compared to those for Rh_2P and Ni_2P endmembers and 20% Pt/C (b) Overpotential values at $10 \text{ mA}/\text{cm}^2_{\text{geo}}$ (geometrical surface area) (c) corresponding Tafel slopes (d) Long-term stability tests (carried out on C-cloth substrate with a surface area of 1 cm^2 , mass loading $0.285 \text{ mg}/\text{cm}^2$) at an applied potential of 0.08 V vs. RHE for $\text{Ni}_{0.25}\text{Rh}_{1.75}\text{P}$ nanoparticles compared to Rh_2P and 20% Pt/C in $0.5 \text{ M H}_2\text{SO}_4$

5.3.1.2. Oxygen evolution reaction in acid

OER data were collected on the same samples (Figure 5.2a). When comparing potential values required to obtain $10\text{mA}/\text{cm}^2_{\text{geo}}$ current density, Rh_2P activity is shown to be comparable to RuO_2 with an overpotential of 0.403 V and the performance of the Ni-containing phases is comparatively poor (ca 1V overpotential, Figure 5.2b). However, it is clear that to achieve higher current densities, the applied voltage for Rh_2P must be increased, whereas this is not the case for RuO_2 and the $\text{Ni}_{2-x}\text{Rh}_x\text{P}$. Indeed, at $50\text{mA}/\text{cm}^2_{\text{geo}}$, the voltage required by Rh_2P is not that much less than for the $\text{Ni}_{2-x}\text{Rh}_x\text{P}$ phases. This is also evident in the Tafel slopes (Figure 5.2c), where Rh_2P exhibits the largest slope (ca 450 mV/decade), RuO_2 the smallest (ca 120 mV/decade), and the $\text{Ni}_{2-x}\text{Rh}_x\text{P}$ samples fall in between (190-280 mV/decade).

Although the initial activity of Rh_2P far outperforms any of the $\text{Ni}_{2-x}\text{Rh}_x\text{P}$ samples, Rh_2P rapidly deactivates (Figure 5.2d), in contrast to claims made in the literature. Similar instabilities are observed for the Ni-rich compositions, including Ni_2P , but $\text{Ni}_{0.25}\text{Rh}_{1.75}\text{P}$ is demonstrated to be quite stable, as is RuO_2 , although $\text{Ni}_{0.25}\text{Rh}_{1.75}\text{P}$ is considerably less active. According to the original report on Rh_2P OER, Rh_2P activity drops by 18% over 16.7 min (1000 s), which is in line with what we observe (Rh_2P activity drops by 76% after 1 h).¹⁷⁷ However, with Ni addition the deactivation decreased from 76% to 21% for the $\text{Ni}_{0.25}\text{Rh}_{1.75}\text{P}$ sample while the commercial catalyst only showed 9% deactivation over a 1 h period. The stability tests were repeated twice and the same trend was observed.

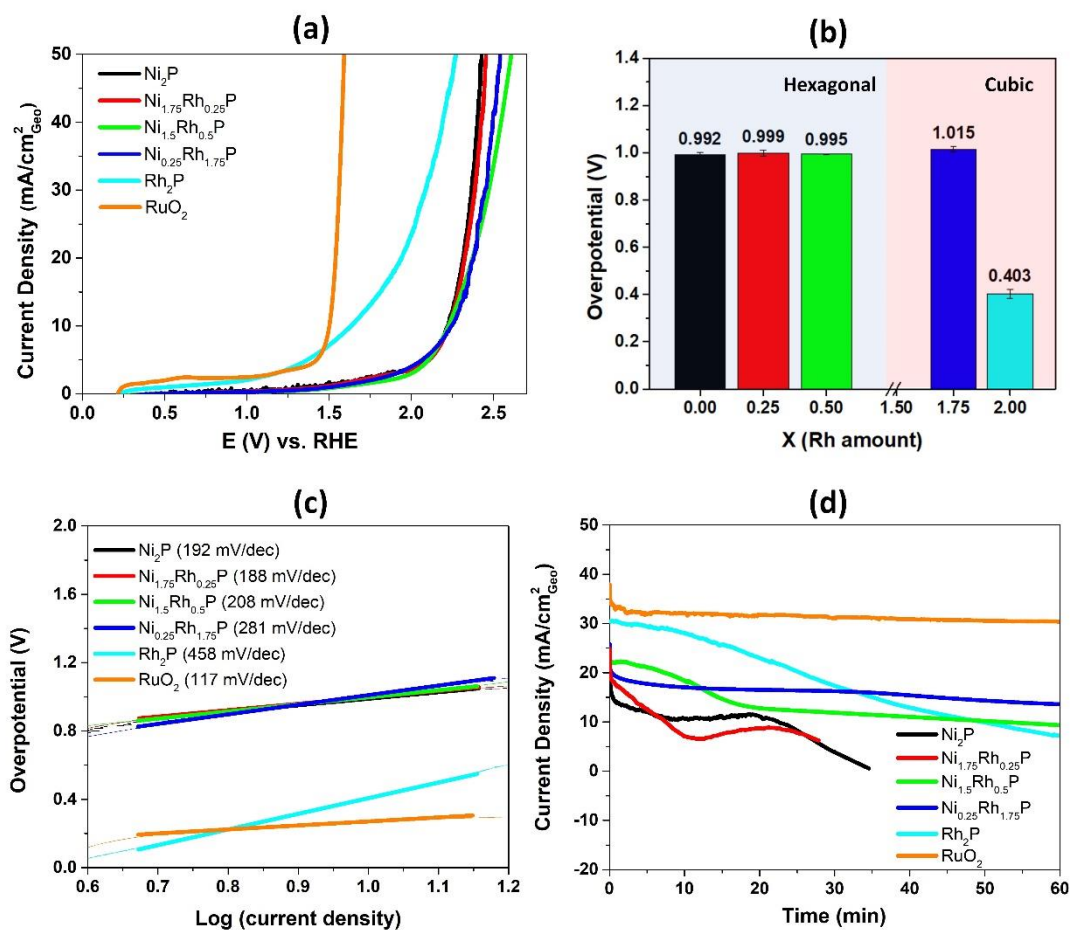


Figure 5.2 (a) OER polarization curves for Ni_{2-x}Rh_xP nanoparticles compared to those for Rh₂P and Ni₂P endpoints and RuO₂ (b) Overpotentials at 10 mA/cm²_{geo}. (c) Tafel slopes (d) Long-term stability tests (carried out on a C-cloth substrate with a surface area of 1 cm², mass loading 0.285 mg/cm²) at 2.0 V vs. RHE applied potential for Ni_{2-x}Rh_xP/C, Rh₂P/C, Ni₂P/C and RuO₂/C towards OER in 0.5 M H₂SO₄

5.3.1.3. Overall water splitting in acid

The Ni_{0.25}Rh_{1.75}P/C composite was evaluated as a catalyst for overall water splitting. For comparison, overall water splitting electrolyzers were also prepared using Rh₂P/C (Rh₂P/C || Rh₂P/C) and commercial catalysts (RuO₂/C || 20%Pt/C). The overall water electrolyzers were prepared in a two-electrode configuration (see Figure 4.14 in Chapter 4). The electrolytic activities of the three constructed overall cells were evaluated by collecting a cyclic voltammogram (Figure 5.3a). For the Ni_{0.25}Rh_{1.75}P/C composite, the overall cell potential to deliver 10 mA/cm²_{geometric} was

1.76 V (without IR correction). This value is ~ 200 mV higher than the voltage required by the Rh₂P/C (1.59 V to achieve 10 mA/cm²_{geometric}) and the commercial catalyst (1.55 V to achieve 10 mA/cm²_{geometric}).

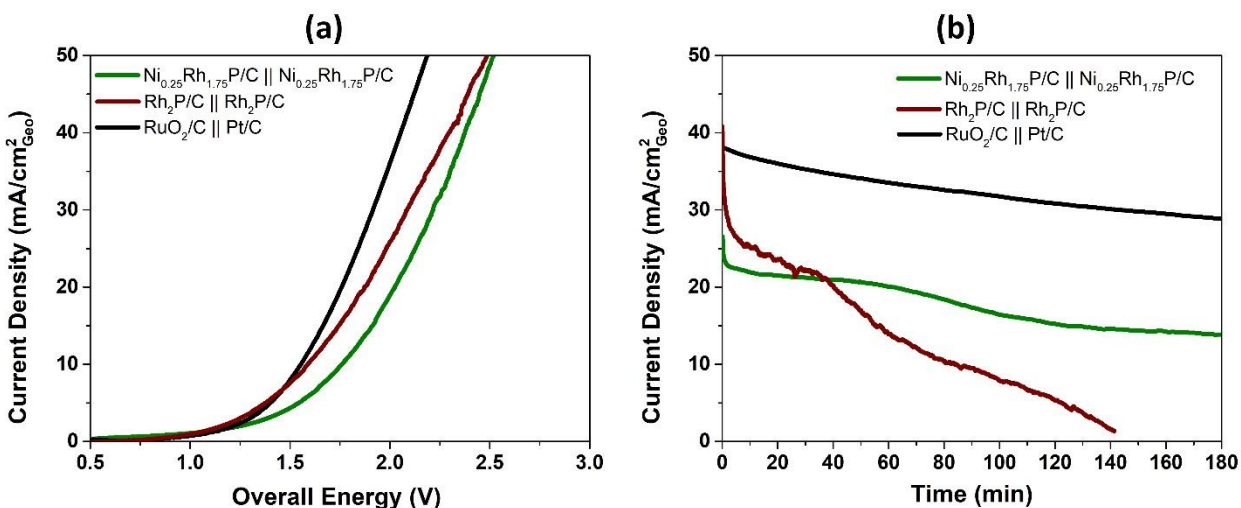


Figure 5.3. Overall water splitting of the cell Ni_{0.25}Rh_{1.75}P/C || Ni_{0.25}Rh_{1.75}P/C, Rh₂P/C || Rh₂P/C and RuO₂/C || 20% Pt/C (a) activity and (b) stability data

The electrochemical stability of the overall cells was also evaluated at a constant potential of 2.0 V for 180 min (Figure 5.3b). For the commercial catalysts, the observed current density was much higher than our catalysts, but in both cases, the current density was found to decrease over time (deactivation is 26% for RuO₂ and 47% for Ni_{0.25}Rh_{1.75}P). However, the Rh₂P/C catalyst rapidly lost its high initial activity, becoming completely deactivated after 140 min.

5.3.2. Structural elucidation: STEM-EDS mapping and XPS

STEM-EDS and XPS analysis were performed on Ni_{0.25}Rh_{1.75}P before and after the long-term stability tests to better understand the structural, compositional, and morphological changes in the catalyst as a consequence of use. According to STEM-EDS mapping images Ni, Rh, and P were uniformly distributed in the structure of the nanoparticles before catalysis (Figure 5.4).

After 10 h of HER, the elemental components in the $\text{Ni}_{0.25}\text{Rh}_{1.75}\text{P}$ sample were still uniformly distributed with no apparent changes. Also, the average EDS compositions collected from different areas of the TEM grid sample before and after catalytic testing were found to have no significant difference for both targeted compositions $\text{Ni}_{0.25}\text{Rh}_{1.75}\text{P}$ and Rh_2P (Table 5.1). However, post-OER catalytic activity, O is co-localized on the nanoparticles reflecting *in-situ* oxide/hydroxide formation, which is commonly found in OER activity studies of transition metal phosphide materials.^{179, 192, 224}

Table 5.1. EDS elemental compositions before and after catalytic testing (P was normalized assuming the metals sum to 2.0)

Targeted composition	Before catalysis	After 10 h HER	After 1 h OER
$\text{Ni}_{0.25}\text{Rh}_{1.75}\text{P}_{1.00}$	$\text{Ni}_{0.28(4)}\text{Rh}_{1.72(4)}\text{P}_{1.03(16)}$	$\text{Ni}_{0.24(2)}\text{Rh}_{1.76(2)}\text{P}_{0.98(10)}$	$\text{Ni}_{0.29(2)}\text{Rh}_{1.71(2)}\text{P}_{1.01(21)}$
$\text{Rh}_{2.00}\text{P}_{1.00}$	$\text{Rh}_{2.00(10)}\text{P}_{1.01(6)}$	$\text{Rh}_{2.00(9)}\text{P}_{1.04(9)}$	$\text{Rh}_{2.00(8)}\text{P}_{0.97(18)}$

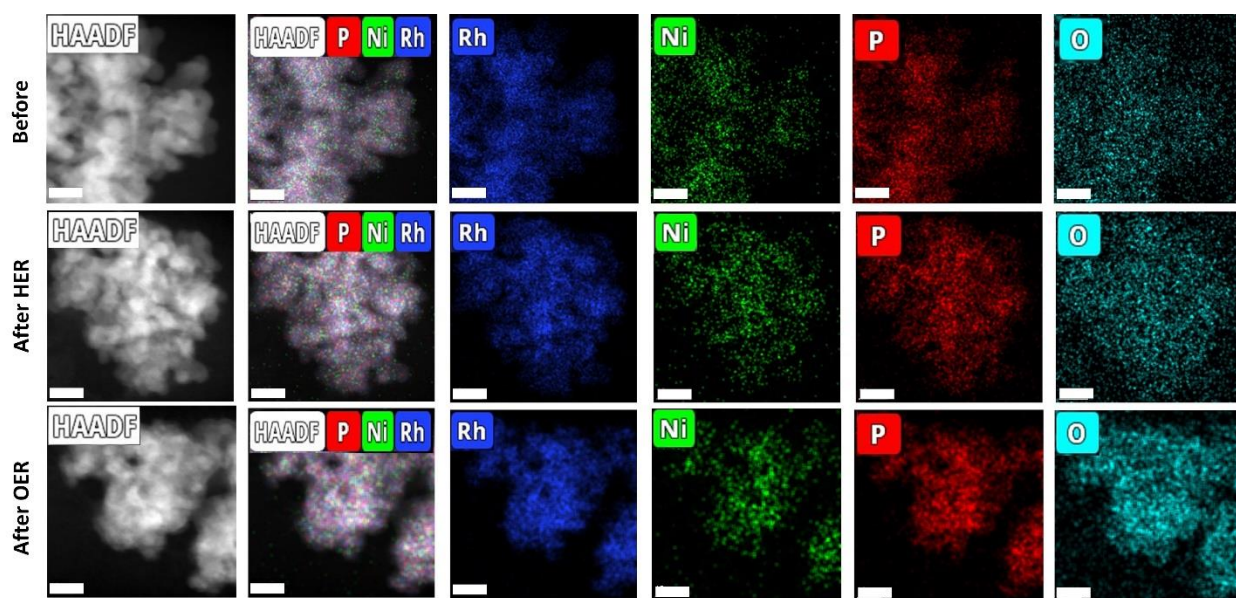


Figure 5.4. EDS mapping analysis of $\text{Ni}_{0.25}\text{Rh}_{1.75}\text{P}/\text{C}$ before, after 10h HER activity, and after 1 h OER activity. (Scale bar is 10 nm)

Detailed XPS analyses were carried out before and after stability tests with both $\text{Ni}_{0.25}\text{Rh}_{1.75}\text{P}/\text{C}$ and $\text{Rh}_2\text{P}/\text{C}$ materials to figure out the surface changes associated with the catalytic activity/stability similarities/differences between these materials. Figure 5.5 summarizes the XPS spectra of Ni 2p, Rh 3d, and P 2p before and after the 10 h HER and 1 h OER catalytic activities of $\text{Ni}_{0.25}\text{Rh}_{1.75}\text{P}$. According to the quantification analysis of $\text{Ni}_{0.25}\text{Rh}_{1.75}\text{P}$ before catalysis (see Table 5.2), the sample surface was found to be rich in Ni and deficient in P, with a composition of $\text{Ni}_{1.3}\text{Rh}_{0.7}\text{P}_{0.2}$.²¹⁸ In terms of speciation, the Ni 2p_{3/2} peaks at 853.8 eV, 856.5 eV, and 858.7 eV are attributed to Ni-P, Ni^{2+} , and Ni^{3+} , respectively.^{197, 218} The corresponding Rh 3d_{5/2} spectrum has peaks at 307.6 eV and 309.4 eV attributed to phosphorus bound Rh (Rh^0) and Rh^{3+} (Rh_2O_3), respectively. Finally, the P 2p_{1/2} spectrum has peaks at 129.5 eV and 133.3 eV for reduced phosphorus (M-P) and phosphate (PO_4^{3-}), respectively.

Figure 5.6 summarizes the XPS data for Rh_2P . In Rh_2P also, the surface is metal-rich/phosphorus poor as in $\text{Ni}_{0.25}\text{Rh}_{1.75}\text{P}$, with a composition of $\text{Rh}_2\text{P}_{0.2}$. The Rh 3d_{5/2} spectrum has peaks at 307.5 eV and 309.6 eV attributed to Rh^0 and Rh^{3+} , respectively. The P 2p_{1/2} spectrum has peaks at 129.6 eV and 133.2 eV for reduced P and PO_4^{3-} , respectively. Rh_2P is also found to have a larger proportion of reduced P compared to $\text{Ni}_{0.25}\text{Rh}_{1.75}\text{P}$.

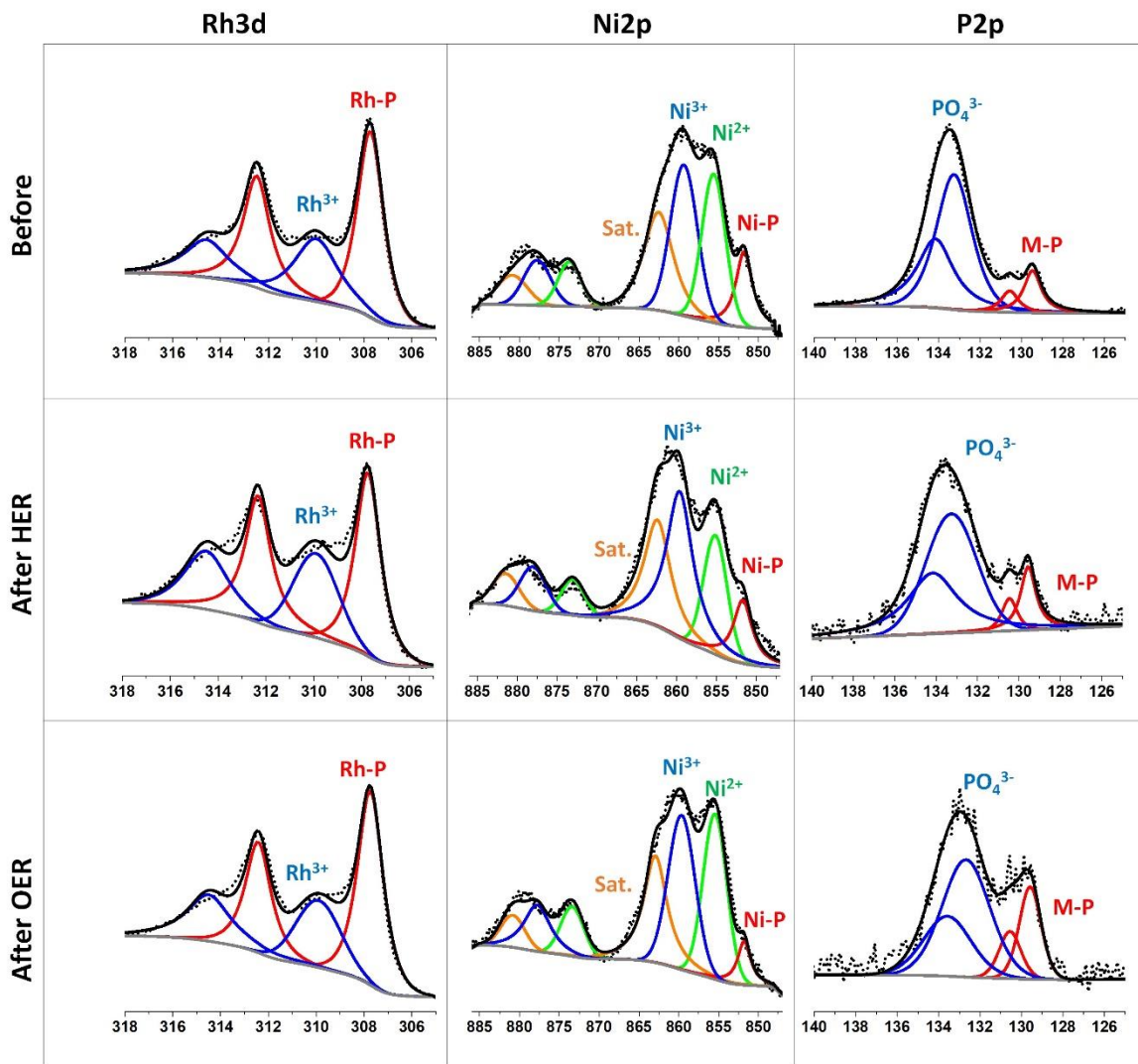


Figure 5.5. XPS spectra of N_{0.25}Rh_{1.75}P/C before and after 10 h HER and 1 h OER stability testing

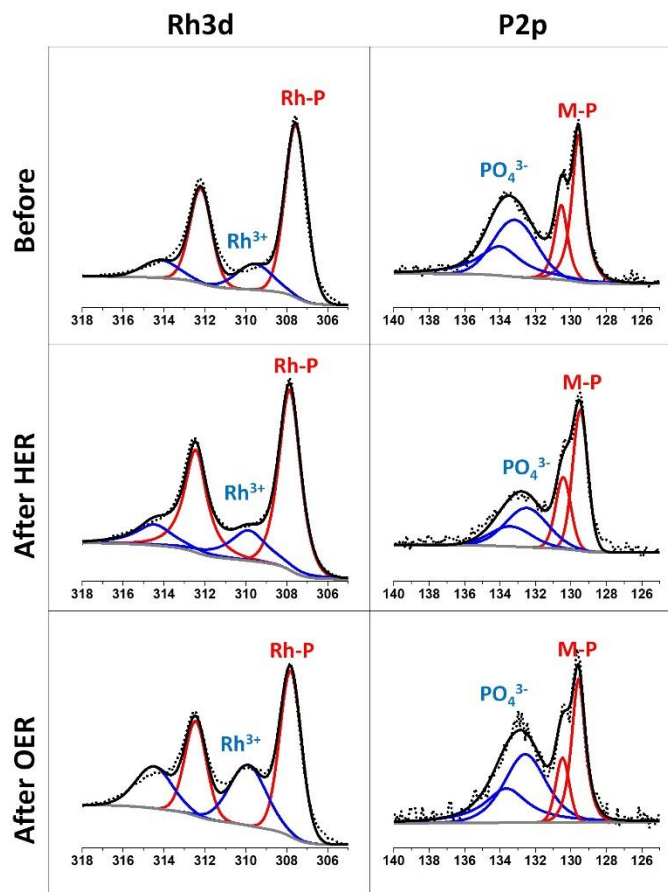


Figure 5.6. XPS spectra of Rh₂P/C before and after 10 h HER and 1 h OER stability testing

After HER catalysis in the acidic media, with both Ni_{0.25}Rh_{1.75}P/C and Rh₂P/C, a minimal change in the metallic components was observed in the overall surface composition, but the loss of P was significant (70% with Ni_{0.25}Rh_{1.75}P and 38% with Rh₂P/C, Table 5.2). However, for the OER study, we observed a significant difference between Ni_{0.25}Rh_{1.75}P vs. Rh₂P. In Ni_{0.25}Rh_{1.75}P, 50% of the metallic Ni on the surface has been oxidized after OER, with only 5% of Rh oxidation, whereas 23% of Rh on Rh₂P showed oxidation (Table 5.2). In the case of post-OER, again, we observed a decrease in P amount with both compositions (80% with Ni_{0.25}Rh_{1.75}P and 25% with Rh₂P/C, Table 5.2).

Table 5.2. XPS elemental ratios and oxidation state ratios before and after catalytic stability tests with $\text{Ni}_{0.25}\text{Rh}_{1.75}\text{P}/\text{C}$ and $\text{Rh}_2\text{P}/\text{C}$.

	$\text{Ni}_{0.25}\text{Rh}_{1.75}\text{P}$				Rh_2P		
	Rh: Ni: P	Rh	Ni	P	Rh: P	Rh	P
		(Rh-P): Rh³⁺	(Ni-P): Ni²⁺: Ni³⁺	(P-M): PO₄³⁻		(Rh-P): Rh³⁺	(P-M): PO₄³⁻
Before	31:59:10	63:37	18:38:44	16:84	92:8	80:20	48:52
After HER	25:72:3	59:41	17:30:53	19:81	95:5	75:25	56:44
After OER	30:68:2	65:35	9:45:46	27:73	94:6	62:38	42:58

5.4 Discussion

Similar to our observations in the previous work within an alkaline medium (Chapter 4), even before catalysis, the $\text{Ni}_{0.25}\text{Rh}_{1.75}\text{P}$ surface is found to be rich in Ni and poor in P, deviating from the bulk composition.²¹⁸ The initial surface metal-to-phosphorus ratio in Rh_2P is comparable to $\text{Ni}_{0.25}\text{Rh}_{1.75}\text{P}$, with a ratio of 2.0-to-0.2 M-to-P, but more reduced phosphorous was found on the Rh_2P surface compared to $\text{Ni}_{0.25}\text{Rh}_{1.75}\text{P}$ both pre- and post-catalysis, and the loss of P post-catalysis for the latter is more significant. These data suggest that Rh may stabilize reduced P on the surface, whereas oxidized P on Ni is more susceptible to dissolution as phosphate.

Most of the metal phosphide materials are found as stable catalysts for HER under acidic condition.¹⁶ In this study, with the post-activity analysis, no significant changes on the surface were found after HER. Unlike in the $\text{Co}_{2-x}\text{Rh}_x\text{P}$ system (Chapter 3) where we lose the acidic HER stability due to Co dissolution, with $\text{Ni}_{2-x}\text{Rh}_x\text{P}$ system the Ni metal was stable under the negative applied potentials and acidic conditions.¹⁸¹

On the other hand, considerable effort has been devoted to identifying why poor stability is observed in some high-activity catalysts for OER.²¹⁵ It has been proposed that with most noble

metal oxides, when catalysts undergo an intermediate species sharing mechanism, the overoxidation of the active material and lattice oxygen participation in the mechanism can induce instability.²¹⁵ The intermediate species sharing mechanism was first reported by Stucki *et al.* for Ru and RuO₂ electrodes. In the mechanism, RuO₄ serves as the reaction intermediate and the OER takes place by a cyclic transition between Ru⁸⁺ and Ru⁶⁺.²²⁵ A similar result was found for iridium-based electrodes;²²⁶ Stucki *et al.* suggested that IrO₃ serves as the intermediate species for the OER reaction and Ir dissolution happens due to IrO₃ formation. However, recent studies carried out with the help of scanning flow cells and inline electrochemical mass spectrometry revealed that both Ir³⁺ species and IrO₃ are formed as intermediates, and both are possible dissolution species for Ir during the OER.²²⁷ Thus, the low stability of phosphides might be due to the intermediate species sharing mechanism forming metal oxides and/or metal ions, and dissolution of those species resulting in low stability.

In keeping with this analysis, in the case of OER in both Ni_{0.25}Rh_{1.75}P and Rh₂P *in-situ* metal oxide/hydroxide formation was observed. Since metal oxides are not stable under acidic conditions (even noble metal oxides, as discussed above) a decrease in the OER activity over time was expected with both materials. Intriguingly, the noble metal phosphide Rh₂P, with comparable initial activity to RuO₂, was found to be far less stable than Ni_{0.25}Rh_{1.75}P to OER (Figure 5.2). The OWS activity and stability data show the rapid deactivation of the Rh₂P/C || Rh₂P/C electrolyzer, whereas Ni_{0.25}Rh_{1.75}P/C || Ni_{0.25}Rh_{1.75}P/C shows a much slower deactivation, comparable to RuO₂/C || 20%Pt/C, although considerably less active (Figure 5.3). Since XPS data shows that the Ni_{0.25}Rh_{1.75}P surface is Ni-rich, we could suggest that the surface Ni might be playing a major role as catalytic sites in Ni_{0.25}Rh_{1.75}P towards OER. In this analysis, the stability of the Ni catalyst towards OER may be associated with the underlying Rh. The fact that the percentage of oxidized

Rh is considerably larger than reduced Rh in Rh₂P vs. Ni_{0.25}Rh_{1.75}P suggests that the more favorable nickel oxidation may assist in preserving reduced Rh, with the reduced Rh in part facilitating the turn over of the Ni catalyst.

5.5 Conclusions

In this work, we have shown that in acidic media, Rh₂P-like activity and stability can be obtained for Ni_{0.25}Rh_{1.75}P as a water reduction electrocatalyst. In contrast, Ni_{0.25}Rh_{1.75}P is far less active than Rh₂P for OER, and yet it is the combination base-metal/noble-metal phosphide that is the most stable. Overall water splitting can be achieved at driving potentials of 1.76 V with Ni_{0.25}Rh_{1.75}P/C catalyst, about 200 mV higher than RuO₂/C || 20%Pt/C, but with a comparable stability. Although the exact OER mechanism of our catalyst is yet to be explored, we surmise that Rh catalytic sites in Rh₂P are subject to rapid deactivation, as are Ni sites in Ni₂P, but the combination of Ni + Rh, which yields Ni-rich surfaces (even at nominally low Ni loadings) with protected Rh underlayers, results in Ni catalytic sites that can “turn over” due to electronic effects of the Rh.

CHAPTER 6. ON THE FEASIBILITY OF Cu-BASED TERNARY TRANSITION METAL PHOSPHIDE NANOPARTICLE SYNTHESIS BY CATION EXCHANGE

Abstract

Inspired by the recently discovered ability of Cu_{3-x}P to undergo cation exchange (CEX) with In^{3+} under mild reaction conditions while retaining the hexagonal anion framework, we explored such reactions on Cu_{3-x}P with Ni^{2+} , Fe^{3+} , and Co^{2+} for the purpose of preparing Cu-M-P nanoparticles (M=Ni, Fe, Co). We hypothesized that Cu-M-P (M= Ni, Co, Fe) can be realized as nanoparticles despite the fact that the corresponding phases are not known as bulk crystalline phases, since metastable phases can be kinetically trapped as nanoparticles because of the low synthesis temperatures and high surface energies. Successful CEX is expected to be achievable because Cu vacancies that are endemic to Cu_{3-x}P will enable high mobility of Cu^+ . To test this hypothesis, nanoparticles of Cu_{3-x}P were prepared according to a literature-reported synthesis method with some modifications. Protocols for CEX of Cu^+ with Fe^{3+} using air-free conditions were evaluated as a function of different synthetic parameters (temperature, time, and ionic concentration). Preliminary studies of Cu_{3-x}P CEX with Ni^{2+} and Co^{2+} were also conducted. The resultant nanoparticles are characterized by PXRD and TEM/EDS to assess the structural and morphological changes associated with the CEX process. The potential for targeting new metastable bimetallic copper phosphide phases by this approach will be discussed in the context of these preliminary results.

6.1. Introduction

According to the Sabatier principle for heterogeneous electrocatalysis, the best catalytic activity can be achieved at the optimum binding energy of intermediates on the catalytic surface. The activity of catalytic materials can be plotted versus reactivity, and the resultant peak-shaped curve is known as the Sabatier or volcano plot.²²⁸ This plot illustrates the difference between the reactivity of various catalysts. The binding energy of the key intermediate indicates how strongly/weakly the catalyst interacts with the reactants.²²⁸ If the binding is too weak, it is difficult for the surface to activate them. If it is too strong, they will poison the reaction by occupying available surface sites.²²⁸ For HER, the optimum binding energy should be around $\Delta G_H = 0$ eV, while for OER, it should be around $\Delta G_O - \Delta G_{OH} = 1.6$ eV.^{229, 230} By combining two metals from extremes of the volcano plot to make a new catalytic surface for HER and by analyzing the stability and activity toward HER by using DFT calculations, Norskov and coworkers showed that some metal alloys can show high HER catalytic activity ($\Delta G_H = 0-0.1$ eV at 1 bar and 298 K).²²⁹ Among these alloys, our interest was piqued by Cu-Ni, Cu-Co, and Cu-Fe because binary transition metal phosphides (Cu₃P, Ni₂P, CoP, and Fe₂P) have shown considerable electrocatalytic activity toward water splitting reactions,^{21, 131, 224} and there are no previous studies done on discrete, single-phase ternary transition metal phosphide materials with these metal combinations.

When considering Cu_{3-x}P, the homogeneity range lies between Cu_{2.867}P and Cu_{2.755}P.^{231, 232} This deviation from the 3:1 Cu:P stoichiometry is due to Cu vacancies in the cell.²³¹ These Cu vacancies, and the high mobility of Cu⁺ ions, is expected to facilitate cation exchange reactions. Indeed, Cu_{3-x}P is reported to undergo cation exchange (CEX) with In³⁺ under mild reaction conditions while retaining the hexagonal anionic framework, leading to Cu-In-P phases, and eventually, a metastable wurtzite form of InP. The dissertation research seeks to explore CEX

reactions of Cu_{3-x}P with Fe^{3+} , Ni^{2+} and Co^{2+} in order to prepare Cu-M-P (M=Fe, Ni and Co) nanoparticles, with potential applicability as catalysts in the sector of hydrogen production via electrochemical water splitting.

6.2. Experimental section

All materials used in the synthesis of Cu_{3-x}P nanoparticles and in cation exchange (CEX) are reported in Chapter 2. A 100 mL two-neck Schlenk line flask with an attached 6-inch-long condenser and internal temperature controller was utilized for nanoparticle synthesis and CEX procedures. All reactions were carried out under an argon atmosphere using standard Schlenk line techniques.

6.2.1. Cu_{3-x}P nanoparticles synthesis

Cu_{3-x}P nanoparticle synthesis was carried out according to the procedure developed by Bertoni *et al.* with minor differences.²³² The metal precursor copper(I) chloride (CuCl , 1.0 mmol) was dissolved in a mixture of 5 mL of oleylamine (OAm) and 0.9 mL trioctylphosphine (TOP). The mixture was degassed at 110 °C for 20 min, then purged with Ar. The temperature was then increased to 250 °C, and a mixture of 0.16 mL of tris(diethylamino)phosphine (TDAP) and 1.0 mL of octadecene (ODE) was quickly injected, and the system was maintained at 250 °C for 30 min. After natural cooling, the product was then purified by sequential dispersion in toluene and precipitation with ethanol.

6.2.2. Cation exchange of Cu_{3-x}P nanoparticles with In^{3+}

6.2.2.1. Cation exchange of Cu_{3-x}P nanoparticles with In^{3+} protocol 1

This procedure was carried out according to a literature reported method by Trizio *et al.*¹²⁶ Here, 0.2 mmol of indium(III) bromide (InBr_3) was combined with 1.5 mL of TOP and 3.5 mL of ODE. The mixture was degassed at room temperature for 45 min, then purged with Ar at 110 °C

for 15 min. The temperature was then increased to 200 °C, and 0.2 mmol of synthesized Cu_{3-x}P nanoparticles dissolved in 1.0 mL of ODE under air-free conditions was quickly injected into the system, which was maintained at 200 °C for 15 min. After natural cooling, the product was purified by sequential chloroform dispersion and precipitation with ethanol.

6.2.2.2. Cation exchange of Cu_{3-x}P nanoparticles with In³⁺ protocol 2

A second In³⁺ CEx procedure was developed based on work done by Akkerman *et al* and Shan *et al.*^{233, 234} Here, a stock solution of In³⁺ was employed. In order to prepare the stock solution, 1.3 mg of indium(III) bromide (InBr₃) was combined with 11.8 mL of TOP and 13.2 mL of ODE in a Schlenk line flask. The mixture was degassed at room temperature for 20 min., and Ar was purged at 110 °C for another 15 min. Then the mixture was heated at 250 °C for 2 h. After natural cooling of the system, the setup was opened under air-free conditions (inside the glove box), and the stock solution was stored in a sealed glass container inside the glove box. To carry out the CEx, 4.8 mL (0.7 mmol of In³⁺) of In³⁺ stock solution, 0.3 mmol of synthesized Cu_{3-x}P nanoparticles, and 4.0 mL of ODE were mixed in a Schlenk line flask under an inert atmosphere. The mixture was then degassed at room temperature for 20 min, then purged with Ar at 110 °C for 20 min. The temperature was then increased to 250 °C and maintained for 30 min. After natural cooling, the product was purified with toluene and ethanol.

6.2.3. Cation exchange of Cu_{3-x}P nanoparticles with Fe³⁺

Based on In³⁺ cation exchange methods, two procedures were utilized to obtain low and high amounts of Fe³⁺ exchanged nanoparticles.^{126, 233, 234} In a typical low-end exchange reaction, 0.2 mmol of iron(III) chloride (FeCl₃) was combined with 1.5 mL of TOP and 3.5 mL of ODE. The mixture was degassed at room temperature for 45 min, then purged with Ar at 110 °C for 15 min. The temperature was then increased to T °C (T=200 or 250), and 0.2 mmol of synthesized

Cu_{3-x}P nanoparticles dissolved in 1.0 mL of ODE under air-free conditions was quickly injected into the system, which was maintained at T °C for t min (t=15 vs. 30 for both T = 200 or 250). After natural cooling, the product was purified by sequential chloroform dispersion and precipitation with ethanol.

To obtain a high degree of CEx, a stock solution of Fe³⁺ was employed. In order to prepare the stock solution, 1.0 mg of iron(III) chloride (FeCl₃) was used and the protocol described in section 6.2.2.2 was followed. To carry out the CEx, 4.8 mL (1.1 mmol of Fe³⁺) of Fe³⁺ stock solution, 0.2 mmol of synthesized Cu_{3-x}P nanoparticles, and 4.0 mL of ODE were mixed in a Schlenk line flask under an inert atmosphere. The mixture was then degassed at room temperature for 20 min, then purged with Ar at 110 °C for 15 min. The temperature was then increased to T °C (T=200 or 250) for 30 min. After natural cooling, the product was purified with chloroform and ethanol.

6.2.4. Cation exchange of Cu_{3-x}P nanoparticles with Ni²⁺ and Co²⁺

In a typical cation Ni²⁺ CEx reaction, 1.2 mmol of nickel(II) chloride hexahydrate (NiCl₂·6H₂O) was combined with 2.0 mL of OAm and 7.5 mL of benzyl ether. The mixture was degassed at 110 °C for 45 min, then purged with Ar at 110 °C for another 15 min. The temperature was then increased to 180 °C, and 0.3 mmol of synthesized Cu₃P nanoparticles dissolved in 2.0 mL of TOP under air-free conditions were quickly injected into the system while maintaining at 180 °C for t min (t=30 or 60). After natural cooling, the product was then purified by sequential dispersion in chloroform and precipitation with ethanol. For Co²⁺ CEx NiCl₂·6H₂O was replaced by 1.2 mmol of cobalt(II) chloride (CoCl₂) and using the same procedure, the CEx was carried out at 180 °C for 60 min, followed by purification as for Ni²⁺ CEx.

6.2.5. Characterization

Powder X-ray diffraction (PXRD) and Transmission electron microscopy (TEM) equipped with energy-dispersive X-ray spectroscopy (EDS, EDAX, inc.) were employed as described in Chapter 2.

6.3. Results and discussion

6.3.1. Cu_{3-x}P cation exchange with In^{3+}

Cu_{3-x}P nanoparticles were synthesized according to a literature procedure²³², and the PXRD pattern, TEM image, and an illustration of the structure are shown in Figure 6.1. The synthesized Cu_{3-x}P nanoparticles adopted the characteristic hexagonal structure of Cu_{3-x}P (from PXRD, Figure 6.1a) with low polydisperse hexagonal-shaped plate-like crystalline particles (from TEM, Figure 6.1b) with a diameter of 29.9 ± 4.2 nm. The EDS analysis of the as-synthesized Cu_{3-x}P NCs shows the presence of Cu and P species, with a Cu deficient average composition of $\text{Cu}_{2.8}\text{P}$.

Detailed calculations done by Trizio and coworkers suggest that Cu_{3-x}P has at least one Cu vacancy in the structure, most likely to be on the Cu1 site (see Figure 6.1c). Crystallographic refinement data presented by Olofsson also indicated that Cu1 and Cu2 are below full occupancy, suggesting that there are most likely one or two vacancies present per cell in Cu_{3-x}P .²³⁵ Because of these possible Cu vacant sites in Cu_3P , configurational entropy favors the increase of vacancies in the system with increasing temperatures.¹²⁶ Combining this tendency with the partial ionic character of Cu_{3-x}P should enable the exchange of Cu^+ ions with other cations.^{126, 127} However, so far the only reported CEx on pure Cu_{3-x}P has been carried out with In^{3+} .^{126, 127} In these studies, after complete CEx they obtained crystalline InP nanoparticles in the wurtzite (WZ) phase instead of the thermodynamically stable cubic zinc blende (ZB) phase.²³⁶ Interestingly, due to the close

match in the crystal structures of these two materials (hexagonal for Cu_{3-x}P and InP), the anionic lattice was mostly preserved in the CEx process, with only a little distortion.

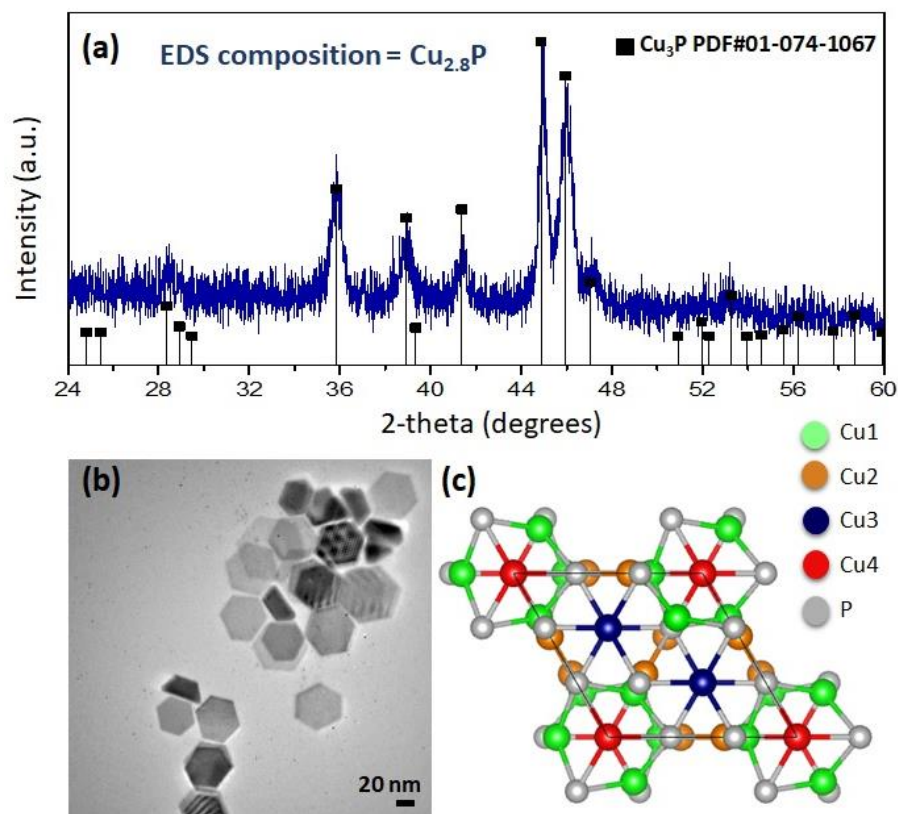


Figure 6.1. (a) PXRD patterns (b) TEM image (c) crystal structure of Cu_{3-x}P

First, we attempted to reproduce the In^{3+} cation exchange (CEx) procedure to obtain WZ InP nanoparticles as reported in the literature. The protocol (section 6.2.2.1) involved injection of Cu_{3-x}P nanoparticles into a solution of an In^{3+} salt at 200 °C. The procedure is purported to yield WZ “ InP ” with only 1% of Cu remaining along with 57% In and 42% P .¹²⁶ However, in our hands, the CEx protocol was unsuccessful. As shown in Figure 6.2, the product retains the hexagonal morphology, but is not very crystalline. The PXRD does not match any phase definitively, although there appears to be residual Cu_{3-x}P and a peak that may be due to ZB InP . Moreover, only 8.7% of In was incorporated.

Moving forward, we carried out a different procedure based on Cu_2S to Cu-In-S , and Cu_{3-x}P to $\text{In}_{1-x}\text{Ga}_x\text{P}$ CEx with our synthesized Cu_{3-x}P samples (see section 6.2.2.2).^{233, 234} This reaction involves heating of a mixture of the Cu_{3-x}P and an In^{3+} salt to 200 °C. The resultant PXRD, TEM, and EDS composition after In^{3+} CEx, along with the WZ InP crystal structure, is shown in Figure 6.3. The PXRD shows that the InP adopts the WZ phase, for which the predicted PDF pattern has been computed via DFT calculations.¹²⁶ The resultant nanoparticles retain their hexagonal plate-like morphology. However, we still had nearly 10% of Cu present in the sample, and the sample is P-rich.

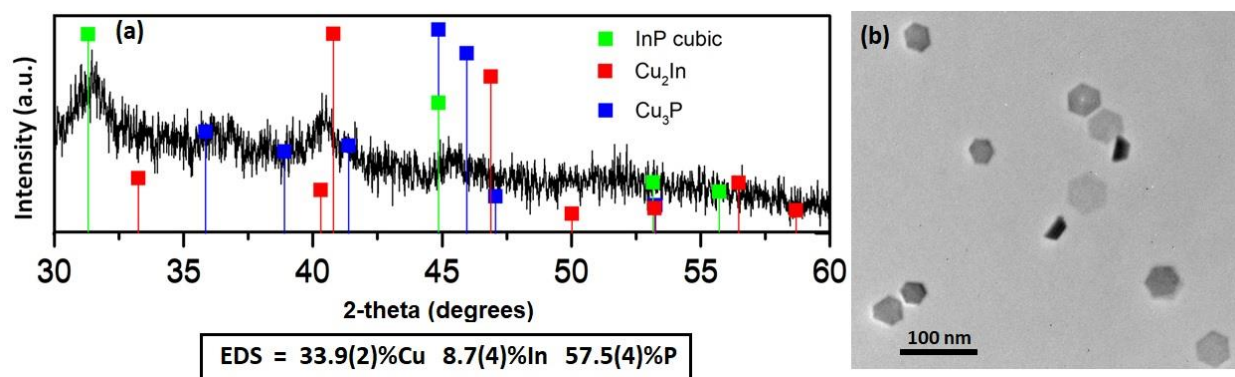


Figure 6.2. (a) PXRD pattern/ EDS composition and (b) TEM image of the product of Cu_{3-x}P CEx with In^{3+} via the protocol in section 6.2.2.1.

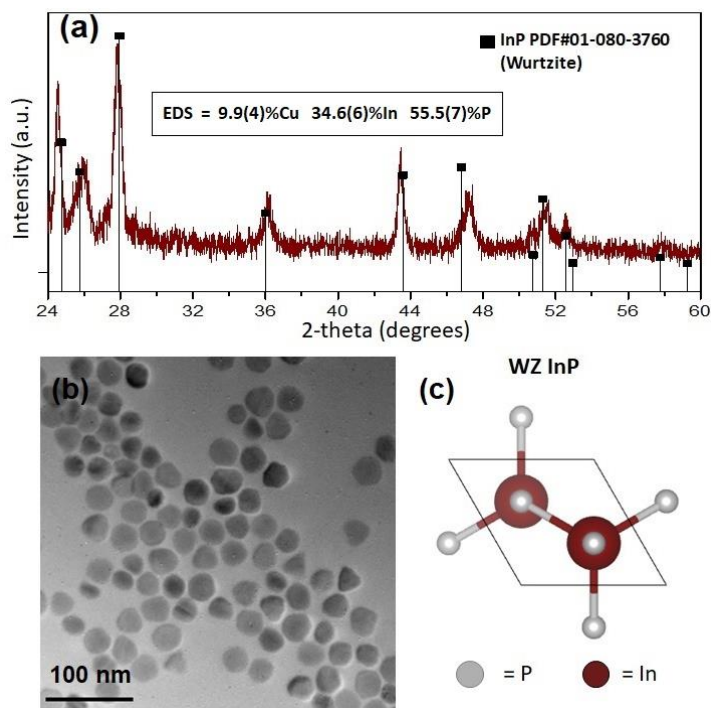


Figure 6.3. (a) PXRD pattern/ EDS composition and (b) TEM image of the product of Cu_{3-x}P CEx with In^{3+} via the protocol in section 6.2.2.2 and (c) crystal structure of WZ InP

6.3.2. Cu_{3-x}P cation exchange with Fe^{3+}

After demonstrating partial In^{3+} cation exchange (CEX) we turned our attention to CEx of Cu^+ in Cu_{3-x}P with Fe^{3+} by adapting literature reported work on CEx of In^{3+} into Cu_{3-x}P , Cu_2S and GaP .^{126, 233, 237} In our approach, the synthesized Cu_{3-x}P nanoparticles dispersed in ODE were hot injected into a $\text{Fe}^{3+}/\text{TOP}/\text{ODE}$ mixture. Two different $\text{Fe}^{3+}/\text{Cu}_{3-x}\text{P}$ ratios were investigated ($\text{Fe}^{3+}/\text{Cu}_{3-x}\text{P}$ 1:1 and $\text{Fe}^{3+}/\text{Cu}_{3-x}\text{P}$ 5.5:1) and CEx was carried out at T °C ($T=200$ or 250) for t min ($t=15$ vs. 30). The PXRDs of the isolated products are shown in Figure 6.4. The product collected from reactions at the higher temperature (250 °C) and at higher $\text{Fe}^{3+}/\text{Cu}_{3-x}\text{P}$ ratios ($\text{Fe}^{3+}/\text{Cu}_{3-x}\text{P} = 5.5:1$) displayed no Bragg peaks characteristics of a crystalline material. However, the product from the 200 °C reaction conducted with a 1:1 $\text{Fe}^{3+}/\text{Cu}_{3-x}\text{P}$ ratio retains the crystallinity and characteristic pattern of Cu_{3-x}P , but a peak shift to higher 2-theta is apparent with the introduction

of Fe^{3+} , suggesting partial incorporation of Fe may be occurring and leading to a compression in the unit cell. No crystalline peaks for other phases (e.g., Fe-P phases) were evident under any of these conditions.

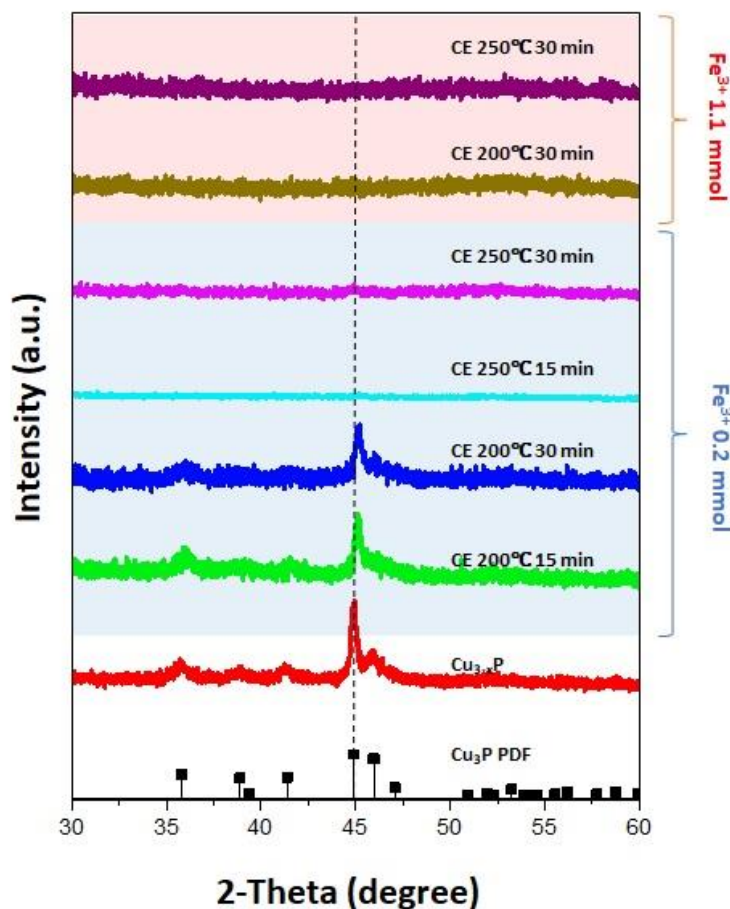


Figure 6.4. PXRD patterns for Cu_{3-x}P before and after CEx with Fe^{3+} for different Fe^{3+} amounts, CEx temperatures, and times (Cu_3P PDF #01-074-1067)

TEM images of the products of the exchange reactions are shown in Figure 6.5. Evidently, the morphology of the Cu_{3-x}P nanoparticles is largely retained under mild CEx conditions (200°C for 15 or 30 min) with a targeted ratio $\text{Fe}^{3+}/\text{Cu}_{3-x}\text{P}$ of 1. At 250 °C and with $\text{Fe}^{3+}/\text{Cu}_{3-x}\text{P}$ of 5.5, the particles undergo cracking, which might be due to the Kirkendall effect. In CEx, due to mobility

differences of the host and guest atoms, diffusion rate differences arise. Due to Cu^+ being a highly mobile atom, it tends to leave the structure faster at high temperatures, and this phenomenon leads to cracked particles.^{127, 237}

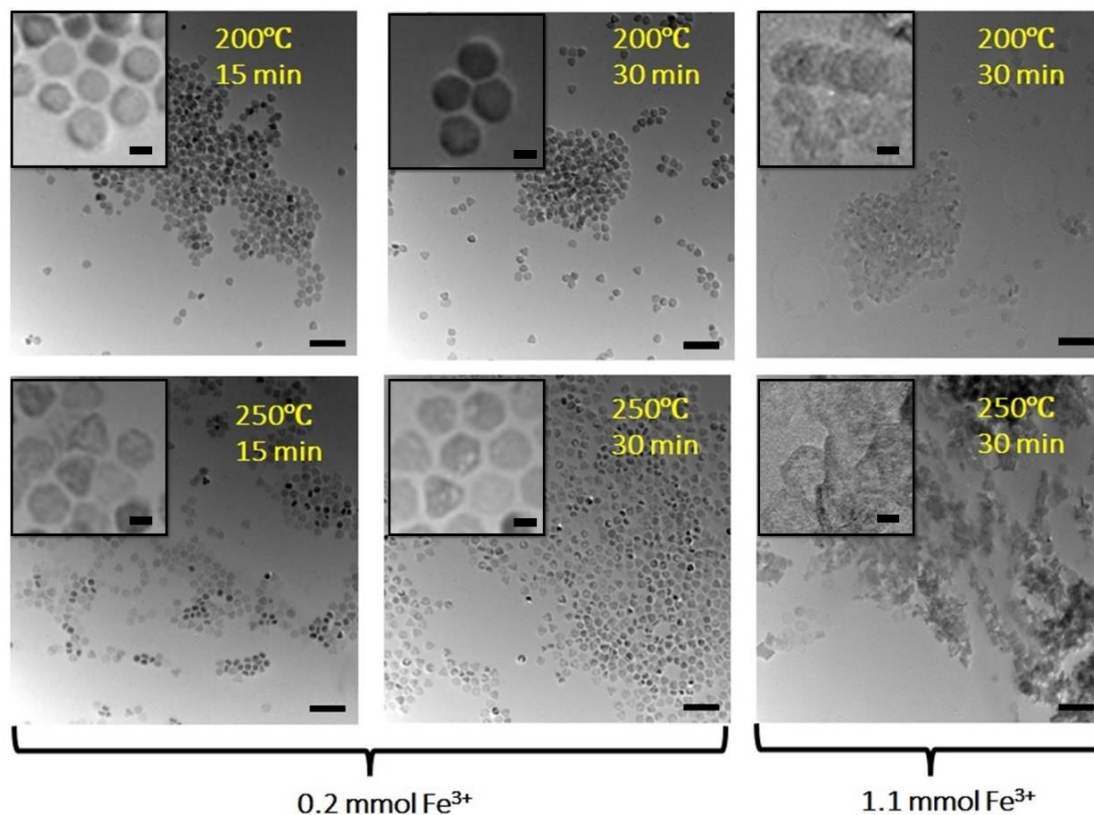


Figure 6.5. TEM images of Cu_{3-x}P after CEx with Fe^{3+} using different amounts of Fe^{3+} , CEx temperatures, and times (image scale bar is 100 nm, inset scale bar is 20 nm)

EDS data for the various CEx reactions are compiled in Table 6.1. For the crystalline samples produced under low Fe^{3+} concentrations at 200 °C, the percentage of P is marginally higher than the starting material, and the final Fe:Cu ratio is 4:1 after 15 min, corresponding to a composition of $\text{Cu}_2\text{Fe}_{0.5}\text{P}$, and 1.9:1 after 30 min, corresponding to $\text{Cu}_{1.6}\text{Fe}_{0.8}\text{P}$. These compositions are more in line with a formal Fe oxidation state of 2+ rather than 3+, assuming the formal oxidation state of P is unchanged at ~ -3 (Cu_3P , Cu^{1+}) composition. Mechanistically, this may reflect oxidation of departing Cu^{1+} to Cu^{2+} by Fe^{3+} , which is subsequently incorporated as

Fe^{2+} ($\text{Fe}^{3+} + \text{Cu}^{1+} \rightarrow \text{Fe}^{2+} + \text{Cu}^{2+}$; $E^{\circ} = +0.53$ V). Intriguingly, Fe incorporation is actually reduced at higher temperature (250 °C), leading to increases in the Cu:Fe ratio and, at the same time, the metal-to-phosphorus ratio is decreased. Interpretation of these data are complicated by the fact that the material is not crystalline. Under forcing conditions ($\text{Fe}^{3+}/\text{Cu}_{3-x}\text{P}$ molar ratio of 5.5) at either 200 or 250 °C, the products remain amorphous but with more Fe than Cu, and the M:P ratio decreases even further. Clearly, at high Fe concentrations and temperatures, the crystalline lattice is amorphized, although the particle morphology—at least the outline—is retained. The amorphization may be a consequence of the oxidizing nature of Fe^{3+} ($\text{Fe}^{3+} + e^{-} \rightarrow \text{Fe}^{2+}$; $E^{\circ} = +0.37$ V). Obviously, this is not a consideration for In^{3+} , which is quite stable in the 3+ oxidation state ($\text{In}^{3+} + e^{-} \rightarrow \text{In}^{2+}$; $E^{\circ} = -0.49$ V).

Table 6.1. TEM-EDS atomic percentages of Cu_{3-x}P before and after cation CEx with Fe^{3+} using different Fe^{3+} concentrations, CEx temperatures and times

Fe^{3+} (mmol)	Time (min)	Temp. (°C)	Cu%	Fe%	P%	Cu:Fe	M:P
Cu_{3-x}P before CEx			73.7±0.7	-	26.3±0.5	-	2.8:1.0
0.2	15	200	57.3±0.5	14.3±0.3	28.4±0.4	4.0:1.0	2.5:1.0
0.2	30	200	46.7±0.4	24.1±0.3	29.2±0.5	1.9:1.0	2.4:1.0
0.2	15	250	49.6±0.9	10.8±0.5	39.6±0.8	4.6:1.0	1.5:1.0
0.2	30	250	44.3±1.0	12.8±0.7	42.9±1.0	3.5:1.0	1.3:1.0
1.1	30	200	11.1±0.4	21.3±0.4	67.6±0.8	0.5:1.0	0.5:1.0
1.1	30	250	8.6±0.5	31.7±0.6	59.7±0.8	0.3:1.0	0.7:1.0

According to our data, the maximum Fe^{3+} cation incorporation without particle cracking was observed with 0.2 mmol of Fe^{3+} , CEx at 200 °C for 30 min. To see the atom distribution before and after CEx, we carried out STEM/EDS mapping analysis with the sample before and after CEx under the above conditions. As shown in Figure 6.6a, the $\text{Cu}_{2.8}\text{P}$ sample has homogeneously

distributed Cu and P, while after CEx (Figure 6.6b), we observe co-localization of Cu, Fe and P within the crystallites. However, the distribution of Fe and Cu do not appear to be uniform (areas where Cu is high seem to have low Fe, and vice-versa), suggesting the possibility of phase-segregation. However, after the CEx, the sample was more susceptible to the beam, making it challenging to collect higher quality data that might be more definitive. STEM/EDS data were not acquired on non-crystalline samples (high temperature and/or high Fe^{3+}/Cu ratio).

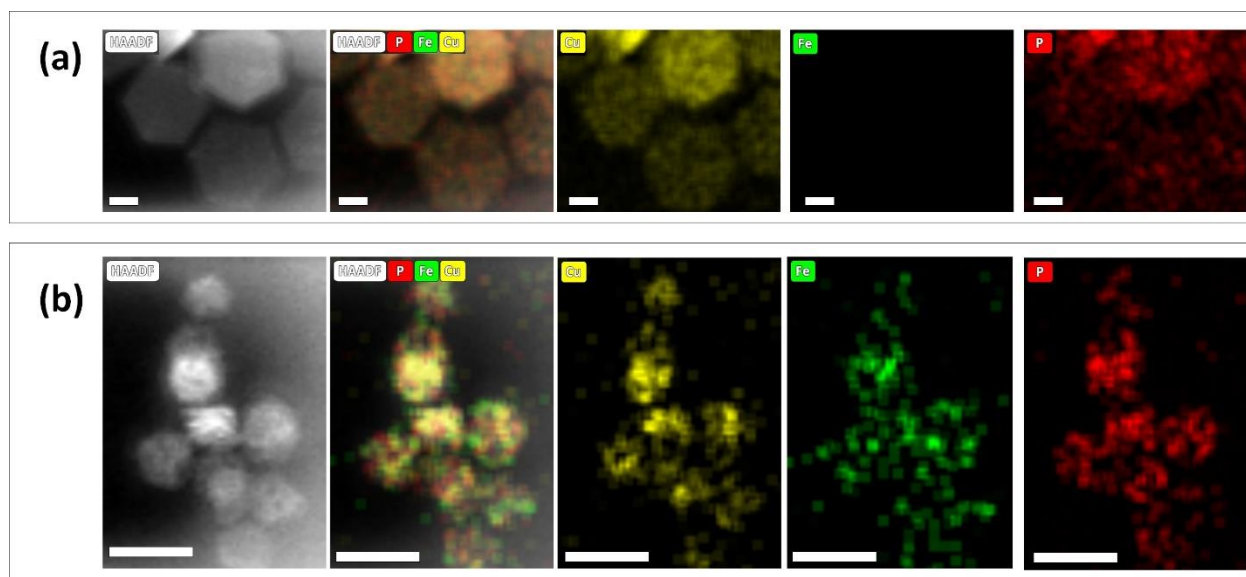


Figure 6.6. STEM/EDS mapping images of Cu_{3-x}P (a) before (scale bar is 20 nm) and (b) after (scale bar is 50 nm) CEx with 0.2 mmol of Fe^{3+} at 200 °C for 30 min

6.3.3. Cu_{3-x}P cation exchange with Ni^{2+} and Co^{2+}

Recently Hong and coworkers reported that Cu_2S can undergo anion exchange with P resulting in $\text{Cu}_3\text{P}_{1-x}\text{S}_x$, and this mixed anion complex can easily undergo CEx with Ni^{2+} and Co^{2+} replacing Cu^+ .²³⁷ Based on this study, we carried out preliminary experiments for CEx Cu^+ in Cu_{3-x}P with Ni^{2+} and Co^{2+} by adapting the work done by Hong *et al.*²³⁷ We first prepared a Ni-OAm or Co-OAm complex in benzyl ether followed by hot injection (at 180 °C) of Cu_{3-x}P nanoparticles dispersed in TOP.

In Ni^{2+} CEx, two different CEx times were utilized. According to the PXRD (Figure 6.7a), after 30 min and 60 min of CEx, the Cu_{3-x}P crystallinity is lost, and a very tiny peak, which could be a Ni-P phase can be observed. Due to the low intensity and broadening of the peak, it is hard to identify the exact phase of the material. However, the TEM images (Figure 6.7b) after 30 min CEx show the presence of different morphologies, whereas after 60 min CEx, the morphology seems less polydisperse and more like hexagonal plate-like particles. In Co^{2+} CEx, after 60 min (Figure 6.8a) again, the crystallinity was lost, and the TEM (Figure 6.8b) clearly shows hexagonal plate-like particles with lots of cracking, which presumably arises from the Kirkendall effect. According to EDS there is clear evidence for Ni and Co incorporation, and Cu loss, but it is not clear whether solid solutions are formed, or phase segregation is occurring.

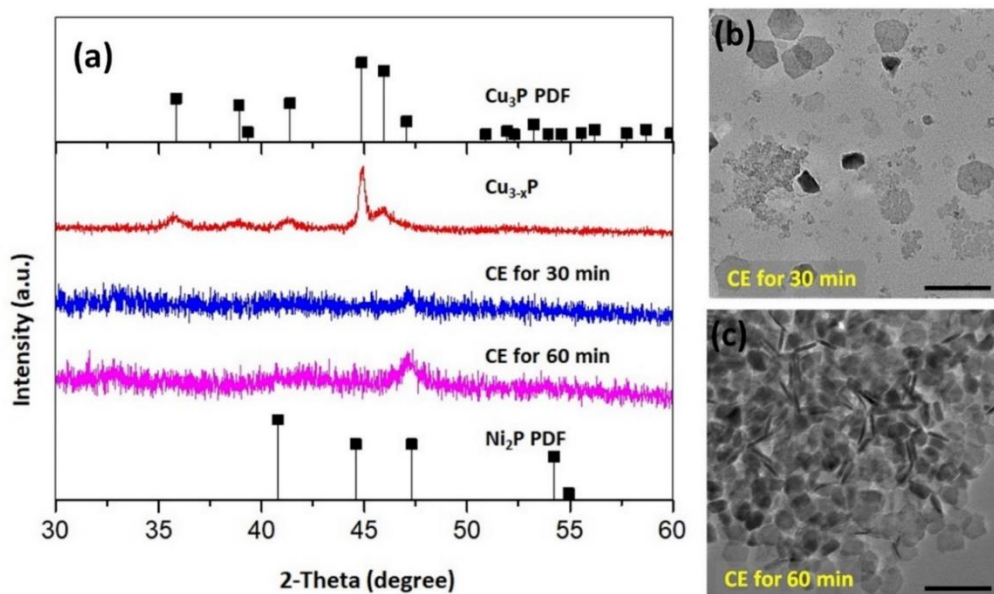


Figure 6.7. (a) PXRD patterns for Cu_{3-x}P before and after CEx with 1.2 mmol of Ni^{2+} ($\text{Ni}^{2+}/\text{Cu}_{3-x}\text{P}$: 4) at 180 °C for 30 min or 60 min (Cu_3P PDF #01-074-1067 and Ni_2P PDF #03-003-0953) (b) TEM images of Cu_{3-x}P after CEx with Ni^{2+} with different CEx times (scale bar is 100 nm)

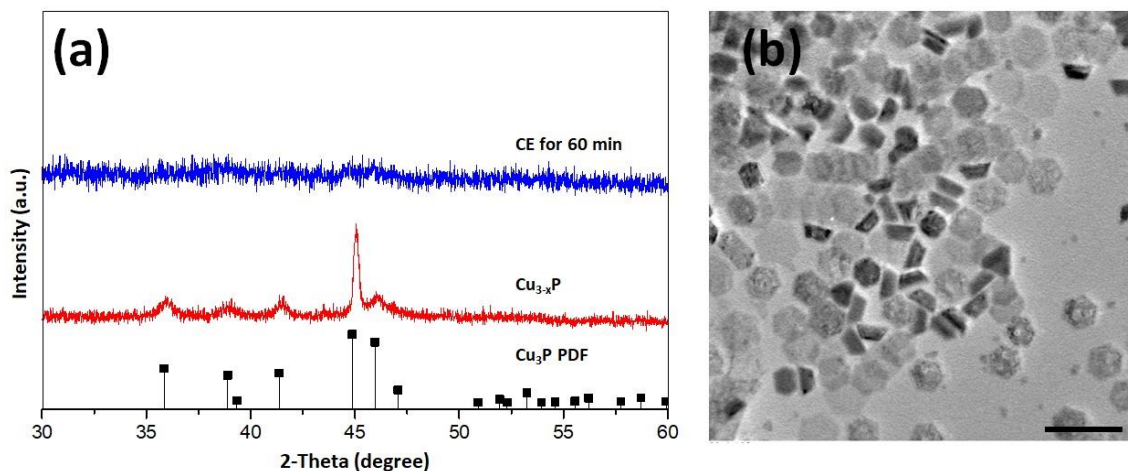


Figure 6.8. (a) PXRD patterns for Cu_{3-x}P before and after CEx with Co^{2+} at $180\text{ }^\circ\text{C}$ for 60 min (Cu_3P PDF #01-074-1067) (b) TEM images of Cu_{3-x}P after CEx with Co^{2+} at $180\text{ }^\circ\text{C}$ for 60 min (scale bar is 100 nm)

Table 6.2. TEM-EDS elemental percentages of Cu_{3-x}P before and after CEx with 1.2 mmol of Ni^{2+} at $180\text{ }^\circ\text{C}$ for 30 min and 60 min and after CEx with Co^{2+} at $180\text{ }^\circ\text{C}$ for 60 min

Guest metal Cation	CEx temp. ($^\circ\text{C}$)	CEx time (min)	Cu%	Ni%	Co%	P%
Cu_{3-x}P before CEx			73.8 ± 0.7	-	-	26.2 ± 0.5
Ni^{2+}	180	30	35.2 ± 0.8	47.6 ± 1.1	-	17.2 ± 0.8
Ni^{2+}	180	60	8.9 ± 0.8	66.7 ± 1.5	-	24.4 ± 1.1
Co^{2+}	180	60	36.7 ± 0.6	-	41.2 ± 0.6	22.1 ± 0.4

6.4. Conclusions

In order to make new bimetallic catalytic materials that could be utilized in electrochemical water splitting hydrogen production applications in the future, we report a preliminary study exploring the abilities of Cu_{3-x}P nanoparticles to undergo cation exchange (CEx) with different transition metal cations (Fe^{3+} , Co^{2+} , Ni^{2+}). Since we could not reproduce the literature that reported complete CEx with In^{3+} we suggest further optimizing the In^{3+} CEx process to identify the errors associated with our approach and improve the CEx processes with Fe, Ni, and Co. Further analysis

of possible redox reactions between Fe, Co, Ni and Cu, will also be important to identify what oxidation states are compatible with the CEx process.

CHAPTER 7. CONCLUSION AND PROSPECTUS

7.1. Conclusions

Modern energy management is balancing efforts to preserve natural resources, mitigate climate change, and satisfy increasing demands for inexpensive power. Electrochemical water splitting, when driven by renewable energy sources, provides a mechanism for the generation of highly pure hydrogen, which can be used to produce electrical energy "on-demand" by the use of fuel cells. However, a major limiting factor in the widespread adoption of water electrolysis is the absence of inexpensive, highly efficient catalysts for the hydrogen evolution reaction (HER) and oxygen evolution reaction (OER) that are stable under these extreme pH conditions. This need provides a driving force for discovering new catalytic materials, and transition metal phosphides (TMP) have emerged as a promising class of materials in this regard. Recently ternary TMP nanoparticles have shown higher catalytic activity than binary phosphides due to the synergism of the two metals. Combining two earth-abundant transition metals or diluting a noble metal with a base-metal makes it possible to achieve highly active, low-cost TPMs for catalytic applications. In this dissertation work, novel phase-pure ternary TMP materials were synthesized, and their structure-property relationships and electrocatalytic water-splitting hydrogen production applications were studied.

From literature reported studies, it is known that higher applied potentials which are enough to oxidize Pt (>1.2 eV vs RHE) have an effect on overestimating the non-Pt cathodic working electrodes activity when Pt is utilized as the anodic counter electrode. In Chapter 3, we evaluate whether Pt counter electrodes used under low applied potentials (<0.6 eV vs RHE) can affect the electrocatalytic HER activities and stabilities of $\text{Co}_{2-x}\text{Rh}_x\text{P}$ nanoparticles. In previous studies by the Brock lab, $\text{Co}_{2-x}\text{Rh}_x\text{P}$ has been found to exhibit higher catalytic activity compared

to Co_2P and Rh_2P end members for OER in basic media.²⁵ In the dissertation research, the HER catalytic performance of $\text{Co}_{2-x}\text{Rh}_x\text{P}$ nanoparticles in acidic and basic media is evaluated and found to be composition-dependent, with the Rh-rich phases being the most active as compared to the Co-rich ones.^{181, 182} Samples in which $x \geq 1.25$ have a more or less comparable HER performance to that of Rh_2P nanoparticles. Thus, one can dilute rhodium sites with cobalt up to a composition of $\text{Co}_{0.75}\text{Rh}_{1.25}\text{P}$ while still retaining the catalytic activity of pure Rh_2P . However, in long-term stability measurements, when C is the counter electrode, the initially high activity of $\text{Co}_{2-x}\text{Rh}_x\text{P}$ ($x \geq 1.25$) nanoparticles falls over 50% in the first half-hour. Surface XPS data reveal a significant loss of surface Co is occurring under catalytic conditions. Using a Pt counter electrode masks this activity/composition relationship, as the Pt deposits on the working electrode, compensating for Co loss, and possibly even be displacing Rh as the active catalyst. In distinct contrast to our observations in acid, the HER activity of $\text{Co}_{2-x}\text{Rh}_x\text{P}$ ($x \geq 1.25$) nanoparticles in basic media is quite robust, behaving similarly to Rh_2P , which maintained HER activity through a 10 h stability test. XPS data of $\text{Co}_{0.25}\text{Rh}_{1.75}\text{P}/\text{C}$ after HER catalysis in basic media reveal that the metal phosphide serves as a pre-catalyst, with the phosphide converting to phosphate under electrochemical conditions (solubilized in the aqueous media), and the active catalyst is a surface oxide/hydroxide species.

Since the $\text{Co}_{2-x}\text{Rh}_x\text{P}$ system suffered from stability issues, our second approach was diluting Rh_2P with a more stable base metal (Ni) than Co in order to improve the activity and stable towards electrocatalytic OER and HER. The novel $\text{Ni}_{2-x}\text{Rh}_x\text{P}$ nanomaterial synthesis and its electrocatalytic water splitting performances in basic media is reported in Chapter 4. A series of phases were targeted, $\text{Ni}_{2-x}\text{Rh}_x\text{P}$, using the solution-phase arrested precipitation method. Intriguingly, phase-pure $\text{Ni}_{2-x}\text{Rh}_x\text{P}$ particles were obtained only for $x = 0, 0.25, 0.50, 1.75$ and

2.00. $\text{Ni}_{2-x}\text{Rh}_x\text{P}$ particles with $x = 0, 0.25$ and 0.50 adopt the Fe_2P hexagonal structure-type and have a spherical morphology with hollow voids. Rh-rich $\text{Ni}_{2-x}\text{Rh}_x\text{P}$ ($x = 1.75, 2.00$) nanoparticles adopt a cubic antiferite structure with quasi-spherical morphology. Intermediate phases ($x = 0.75-1.5$) were found to be phase segregated due to inhibition of miscibility between Ni_2P and Rh_2P . When investigating the catalytic activities of $\text{Ni}_{2-x}\text{Rh}_x\text{P}/\text{C}$ in basic media, the geometric surface area normalized OER activity of $\text{Ni}_{1.75}\text{Rh}_{0.25}\text{P}$ is the best among the investigated electrocatalysts. $\text{Ni}_{1.75}\text{Rh}_{0.25}\text{P}$ is also the most active when normalized to the electrochemical surface area (ECSA). The enhancement in activity may be attributed to electronic effects and/or restructuring of the catalyst due to phase segregation of Rh. Rh phase segregation was observed to decrease the electrochemically active surface area and yet, the catalytic activity actually increases, suggesting that catalytic sites have become intrinsically more active during catalytic testing. With respect to the HER studies in basic media, the Rh-rich phases are more active, with Rh_2P exhibiting the lowest overpotential when normalized to geometry. However, when normalized to ECSA, the $\text{Ni}_{0.25}\text{Rh}_{1.75}\text{P}$ phase exhibits twice the activity of Rh_2P , possibly due to the lowering of the energy barrier in the water dissociation step. Additionally, the combined STEM/EDS and XPS data suggest that the surface composition of $\text{Ni}_{2-x}\text{Rh}_x\text{P}$ is quite different from the bulk composition with a Ni-rich composition on the surface. Also, we found that $\text{Ni}_{2-x}\text{Rh}_x\text{P}$ undergoes dramatic *in-situ* chemical modifications during both HER and OER processes. In both cases, the initial phosphide/phosphate on the pre-catalytic surface readily oxidizes and then dissolves in the basic electrolyte solution as metal oxides/hydroxide species are formed.

Since Ni_2P is known as a more stable metal phosphide compared to Co_2P in acidic media, we considered whether the $\text{Ni}_{2-x}\text{Rh}_x\text{P}$ system would be more stable than $\text{Co}_{2-x}\text{Rh}_x\text{P}$ for water splitting under acidic conditions.^{169, 222} With that motivation, the water splitting electrocatalytic

activities of $\text{Ni}_{2-x}\text{Rh}_x\text{P}/\text{C}$ in acidic media were investigated and are reported in Chapter 5.²¹⁸ The HER performance in acidic media of $\text{Ni}_{2-x}\text{Rh}_x\text{P}$ nanoparticles was similar to the $\text{Co}_{2-x}\text{Rh}_x\text{P}$ system.¹⁸¹ The activity is composition-dependent, with the Rh-rich cubic antiferromagnetic $\text{Ni}_{0.25}\text{Rh}_{1.75}\text{P}$ phase being the most active and stable, comparable to Rh_2P . Pre- and post-catalytic surface analysis data showed a minimal change in metallic components was found, suggesting that the metals present are stable under the negative applied potentials needed to drive HER. However, the initial OER activity of $\text{Ni}_{2-x}\text{Rh}_x\text{P}$, when normalized to the geometric area, is comparatively poor relative to Rh_2P , which exhibits an overpotential value that is $< 50\%$ of any of the phase-pure $\text{Ni}_{2-x}\text{Rh}_x\text{P}$ nanoparticles studied. Nevertheless, Ni incorporation into Rh_2P ($\text{Ni}_{0.25}\text{Rh}_{1.75}\text{P}$) resulted in increased stability towards OER in acidic media when compared to pure Rh_2P . According to EDS and XPS data, *in-situ* surface oxidation is evident post-catalysis. However, the fraction of oxidized Rh in Rh_2P is greater than in $\text{Ni}_{0.25}\text{Rh}_{1.75}\text{P}$, and the surface of the ternary phosphide is quite Ni rich, suggesting that the unique stability associated with this ternary phase may be a consequence of Ni serving as putative catalytic site, stabilized by a Rh phosphide underlayer.

Cu_{3-x}P is an earth-abundant metal phosphide that has demonstrated promising activities and stabilities towards HER in acidic media.^{136, 141, 238} Recent DFT calculations demonstrated a trend in enhanced HER activity with mixed metal alloys, and Cu based alloys including Cu-Co, Cu-Ni and Cu-Fe were in the optimum activity range.⁴³ Accordingly, the dissertation research sought to synthesize the corresponding phosphides as potential electrocatalysts for water splitting. Since, Cu_{3-x}P has been demonstrated to undergo cation exchange with In^{3+} under mild reaction conditions while retaining the hexagonal anion framework, in Chapter 6 the cation exchange of Cu_{3-x}P with Fe^{3+} , Ni^{2+} and Co^{2+} was investigated. As a starting point, the In^{3+} cation exchange was re-investigated. The literature procedure was not successful in our hands, but a modified procedure

led to partial cation exchange and apparent incorporation of In. Based on this limited success, exchange with Fe^{3+} , Ni^{2+} and Co^{2+} was investigated. With Fe^{3+} , exchange was conducted with two different concentrations of the metal and two different temperatures (200 and 250 °C). At low Fe^{3+} concentration (1:1 Fe: Cu_{3-x}P) and 200 °C, crystalline product was obtained. The pattern resembled Cu_3P with a slight peak shift to higher 2θ suggesting a compression of lattice parameters. Fe: Cu ratios of 1:4 (15 min) and 1:1.9 (30 min) were obtained in the product according to EDS, suggesting formulae of $\text{Cu}_2\text{Fe}_{0.5}\text{P}$ and $\text{Cu}_{1.6}\text{Fe}_{0.8}\text{P}$, respectively, when accounting for the observed phosphorus ratio. When considering charge balance, these formulas likely represent incorporation of Fe^{2+} , rather than Fe^{3+} . According to standard reduction potentials, Fe^{3+} will oxidize Cu^{1+} to Cu^{2+} ; accordingly, we hypothesize that Fe^{3+} oxidizes the Cu^{1+} leaving the lattice and intercalates as Fe^{2+} . Notably, STEM/EDS mapping suggests that Fe is not incorporated homogeneously, rather there appear to be islands within the hexagonal plates that are Fe-rich or Cu-rich. Fe^{3+} cation exchange reactions conducted at higher temperature (250 °C) and/or at higher $\text{Fe}^{3+}/\text{Cu}_{3-x}\text{P}$ ratios (5.5) produced products that were X-ray amorphous. In preliminary Ni^{2+} and Co^{2+} cation exchange reactions, the Ni and Co uptake and Cu loss was observed, but the PXRD pattern suggests the Cu_{3-x}P phase is no longer present. Peaks possibly corresponding to binary Ni or Co phosphides are observed instead.

7.2. Future research directions

Based on the insights gained from the above dissertation work, several exciting research paths could be studied in future work. Two such pathways are described below.

7.2.1. Studying the intrinsic catalytic activity dependency on material structure

In this dissertation, the OER and HER activity variation in $\text{M}_{2-x}\text{Rh}_x\text{P}$ ($\text{M} = \text{Co}, \text{Ni}$) was explored and found to be strongly dependent on the material composition. Studies were also

extended to understand the electrochemical surface area changes related to the material composition with $\text{Ni}_{2-x}\text{Rh}_x\text{P}$ in basic media using a non-faradaic technique (double-layer capacitance method). However, identifying the catalytically active surface area under applied potential and studying how the potency and the surface area depends on factors such as crystal structure, morphology, composition etc., is crucial. Underpotential deposition methods (UPD) are voltametric methods where the charge involved in electrochemically adsorbing/desorbing a layer of a selected chemical species (typically H or Cu) is measured by integration of the area under the voltage-current curve in the UPD region. Then using a conversion factor and the voltage-current area data we can calculate the electrochemically active surface area (ECSA).²³⁹

In future studies, UPD methods should be assayed, to identify the ECSA under faradaic conditions, instead of the double-layer capacitance methods that are conducted in the non-faradaic region. Furthermore, by combining this experimental data with theoretical DFT calculation data (studied in a collaborative approach), on compositional and structural dependency on catalytic activity, we will be able to better interpret the activity differences arising from different compositions and structures of these materials. Through these types of studies, we hope to reveal the potential applicability of different elemental combinations, crystal structure types and optimum compositions towards electrocatalytic water splitting applications.

7.2.2. Investigating electrochemical water splitting catalytic activities of Cu-based ternary phosphides

The work we started on Cu-based ternary phases synthesis via cation exchange described in Chapter 6 will continue in terms of method optimization and catalytic activity evaluation of resultant Cu-M-P (M = Fe, Co, Ni) materials. In addition, the synthesized In-Cu-P phase should be considered for photocatalysis or photoelectrochemical catalysis for water splitting. Bulk InP in

its cubic phase is a well-known semiconducting material with a direct band gap of 1.35 eV.²⁴⁰ The new wurtzite nanoparticles of InP have a bigger band gap of 1.55 eV.¹²⁶ We hypothesize that the combination of semiconducting InP with metallic and electrocatalytically active Cu₃P will facilitate solar-driven fuels production. This hypothesis can be tested by optimizing the cation exchange procedure to obtain targeted phase-separated InP-Cu₃P nanoparticles, and evaluating their structure-property-activity relationships.

APPENDIX A: SCAN DETAILS FOR XPS

XPS Core Line	Scan window (eV)	Pass-energy (eV)	Step-size (eV)	Dwell time (ms/step)	Number of sweeps
C1s	279-298	50	0.1	100	1
Rh3p	305-320	50	0.1	100	5
P2p	125-140	50	0.1	100	5
Ni2p	850-885	50	0.1	100	5
Co2p	775-810	50	0.1	100	5
O1s	525-540	50	0.1	100	5

APPENDIX B: BINDING ENERGIES FOR XPS ANALYSIS

Peak BE (eV)	Oxidation state	Ref.
Rh 3d		
307.0 ± 0.4	Rh ^{δ+}	241
311.7 ± 0.4		
308.9 ± 0.4	Rh ³⁺	
313.6 ± 0.4		
P 2p		
133.2 ± 0.7	P ⁵⁺ (PO ₄ ³⁻)	197, 241
134.1 ± 0.7		
130.2 ± 0.3	P ⁰	
131.4 ± 0.3		
Co 2p		
779.2 ± 0.3	Co ²⁺	242, 243
794.1 ± 0.3		
781.7 ± 0.2	Co ₃ O ₄	
797.2 ± 0.2		
784.3 ± 0.4	Co ₃ O ₄	
800.1 ± 0.4		
Ni 2p		
853.8 ± 0.2	Ni-P	197
870.8 ± 0.2		
856.5 ± 0.3	Ni ²⁺	
874.5 ± 0.3		

858.7±0.3	Ni ³⁺	
877.9±0.3		
Pt 4f		
81.3	Overlap	
71.1	Zero Valent Pt	244
74.3		
72.2	Pt ²⁺	
75.4		
68.7		
83.9		
O 1s		
531.1-532.0	Transition metal oxides	245
533.0	-F ₂ C-O-CF ₂ - in Nafion	246
535.7	Sulfonic acid oxygen in Nafion	

APPENDIX C: PERMISSION/LICENSE AGREEMENT FOR COPYRIGHT MATERIALS



[Home](#)
[Help](#)
[Email Support](#)
[Sign in](#)
[Create Account](#)



Rh2P Activity at a Fraction of the Cost? Co₂-xRh_xP Nanoparticles as Electrocatalysts for the Hydrogen Evolution Reaction in Acidic Media

Author: Samuel I. Mutinda, Tharanga N. Batugedara, Benjamin Brown, et al

Publication: ACS Applied Energy Materials

Publisher: American Chemical Society

Date: Jan 1, 2021

Copyright © 2021, American Chemical Society

PERMISSION/LICENSE IS GRANTED FOR YOUR ORDER AT NO CHARGE

This type of permission/license, instead of the standard Terms and Conditions, is sent to you because no fee is being charged for your order. Please note the following:

- Permission is granted for your request in both print and electronic formats, and translations.
- If figures and/or tables were requested, they may be adapted or used in part.
- Please print this page for your records and send a copy of it to your publisher/graduate school.
- Appropriate credit for the requested material should be given as follows: "Reprinted (adapted) with permission from {COMPLETE REFERENCE CITATION}. Copyright {YEAR} American Chemical Society." Insert appropriate information in place of the capitalized words.
- One-time permission is granted only for the use specified in your RightsLink request. No additional uses are granted (such as derivative works or other editions). For any uses, please submit a new request.

If credit is given to another source for the material you requested from RightsLink, permission must be obtained from that source.

[BACK](#)

[CLOSE WINDOW](#)



Co₂-xRh_xP Nanoparticles for Overall Water Splitting in Basic Media: Activation by Phase-Segregation-Assisted Nanostructuring at the Anode

Author: Stephanie L. Brock, Benjamin Brown, Tharanga N. Batugedara, et al

Publication: ChemCatChem

Publisher: John Wiley and Sons

Date: Aug 18, 2021

© 2021 Wiley-VCH GmbH

Order Completed

Thank you for your order.

This Agreement between Wayne State University -- Tharanga Batugedara ("You") and John Wiley and Sons ("John Wiley and Sons") consists of your license details and the terms and conditions provided by John Wiley and Sons and Copyright Clearance Center.

Your confirmation email will contain your order number for future reference.

License Number 5332860218647

 [Printable Details](#)

License date Jun 20, 2022

Role of Noble- and Base-Metal Speciation and Surface Segregation in Ni₂-xRh_xP Nanocrystals on Electrocatalytic Water Splitting Reactions in Alkaline Media



Author: Tharanga N. Batugedara, Stephanie L. Brock

Publication: Chemistry of Materials

Publisher: American Chemical Society

Date: May 1, 2022

Copyright © 2022, American Chemical Society

PERMISSION/LICENSE IS GRANTED FOR YOUR ORDER AT NO CHARGE

This type of permission/license, instead of the standard Terms and Conditions, is sent to you because no fee is being charged for your order. Please note the following:

- Permission is granted for your request in both print and electronic formats, and translations.
- If figures and/or tables were requested, they may be adapted or used in part.
- Please print this page for your records and send a copy of it to your publisher/graduate school.
- Appropriate credit for the requested material should be given as follows: "Reprinted (adapted) with permission from {COMPLETE REFERENCE CITATION}. Copyright {YEAR} American Chemical Society." Insert appropriate information in place of the capitalized words.
- One-time permission is granted only for the use specified in your RightsLink request. No additional uses are granted (such as derivative works or other editions). For any uses, please submit a new request.

If credit is given to another source for the material you requested from RightsLink, permission must be obtained from that source.

[BACK](#)

[CLOSE WINDOW](#)

REFERENCES

1. <Road+Map+to+a+US+Hydrogen+Economy+Full+Report.pdf>.
2. <BNEF-Hydrogen-Economy-Outlook-Key-Messages-30-Mar-2020.pdf>.
3. <https://www.scienceabc.com/nature/universe/how-does-the-iss-get-breathable-oxygen.html>.
4. https://www.freepik.com/premium-vector/energy-sources-icons_2701852.htm#page=2&query=geothermal%20icon&position=43&from_view=keyword.
5. <https://www.interos.ai/wp-content/uploads/2020/10/Hydrogen-Fuel-Cells.jpg>.
6. Winter, M.; Brodd, R. J., What Are Batteries, Fuel Cells, and Supercapacitors? *Chemical Reviews* **2004**, *104* (10), 4245-4270.
7. Lin, R.-H.; Xi, X.-N.; Wang, P.-N.; Wu, B.-D.; Tian, S.-M., Review on hydrogen fuel cell condition monitoring and prediction methods. *International Journal of Hydrogen Energy* **2019**, *44* (11), 5488-5498.
8. Hisatomi, T.; Kubota, J.; Domen, K., Recent advances in semiconductors for photocatalytic and photoelectrochemical water splitting. *Chemical Society Reviews* **2014**, *43* (22), 7520-7535.
9. Fountaine, K. T.; Lewerenz, H. J.; Atwater, H. A., Efficiency limits for photoelectrochemical water-splitting. *Nat Commun* **2016**, *7*, 13706-13706.
10. Simpson, A. P.; Lutz, A. E., Exergy analysis of hydrogen production via steam methane reforming. *International Journal of Hydrogen Energy* **2007**, *32* (18), 4811-4820.
11. *Fuel Cell Engineering*. Elsevier Science: 2012.
12. Xu, S.; Liu, J., Metal-based direct hydrogen generation as unconventional high density energy. *Frontiers in Energy* **2018**, *1*.

13. Lee, Y.; Suntivich, J.; May, K. J.; Perry, E. E.; Shao-Horn, Y., Synthesis and Activities of Rutile IrO₂ and RuO₂ Nanoparticles for Oxygen Evolution in Acid and Alkaline Solutions. *The Journal of Physical Chemistry Letters* **2012**, *3* (3), 399-404.
14. Marshall, A. T.; Haverkamp, R. G., Electrocatalytic activity of IrO₂-RuO₂ supported on Sb-doped SnO₂ nanoparticles. *Electrochimica Acta* **2010**, *55* (6), 1978-1984.
15. Cheng, J.; Zhang, H.; Chen, G.; Zhang, Y., Study of Ir_xRu_{1-x}O₂ oxides as anodic electrocatalysts for solid polymer electrolyte water electrolysis. *Electrochimica Acta* **2009**, *54* (26), 6250-6256.
16. Shi, Y.; Zhang, B., Recent advances in transition metal phosphide nanomaterials: synthesis and applications in hydrogen evolution reaction. *Chemical Society Reviews* **2016**, *45* (6), 1529-1541.
17. Anantharaj, S.; Ede, S. R.; Sakthikumar, K.; Karthick, K.; Mishra, S.; Kundu, S., Recent Trends and Perspectives in Electrochemical Water Splitting with an Emphasis on Sulfide, Selenide, and Phosphide Catalysts of Fe, Co, and Ni: A Review. *ACS Catalysis* **2016**, *6* (12), 8069-8097.
18. Callejas, J. F.; McEnaney, J. M.; Read, C. G.; Crompton, J. C.; Biacchi, A. J.; Popczun, E. J.; Gordon, T. R.; Lewis, N. S.; Schaak, R. E., Electrocatalytic and Photocatalytic Hydrogen Production from Acidic and Neutral-pH Aqueous Solutions Using Iron Phosphide Nanoparticles. *ACS Nano* **2014**, *8* (11), 11101-11107.
19. Chang, J.; Xiao, Y.; Xiao, M.; Ge, J.; Liu, C.; Xing, W., Surface Oxidized Cobalt-Phosphide Nanorods As an Advanced Oxygen Evolution Catalyst in Alkaline Solution. *ACS Catalysis* **2015**, *5* (11), 6874-6878.

20. Yu, J.; Li, Q.; Li, Y.; Xu, C.-Y.; Zhen, L.; Dravid, V. P.; Wu, J., Ternary Metal Phosphide with Triple-Layered Structure as a Low-Cost and Efficient Electrocatalyst for Bifunctional Water Splitting. *Advanced Functional Materials* **2016**, *26* (42), 7644-7651.
21. Stern, L.-A.; Feng, L.; Song, F.; Hu, X., Ni₂P as a Janus catalyst for water splitting: the oxygen evolution activity of Ni₂P nanoparticles. *Energy & Environmental Science* **2015**, *8* (8), 2347-2351.
22. Li, D.; Baydoun, H.; Verani, C. N.; Brock, S. L., Efficient Water Oxidation Using CoMnP Nanoparticles. *Journal of the American Chemical Society* **2016**, *138* (12), 4006-4009.
23. Li, D.; Baydoun, H.; Kulikowski, B.; Brock, S. L., Boosting the Catalytic Performance of Iron Phosphide Nanorods for the Oxygen Evolution Reaction by Incorporation of Manganese. *Chemistry of Materials* **2017**, *29* (7), 3048-3054.
24. Liyanage, D. R.; Li, D.; Cheek, Q. B.; Baydoun, H.; Brock, S. L., Synthesis and oxygen evolution reaction (OER) catalytic performance of Ni_{2-x}Ru_xP nanocrystals: enhancing activity by dilution of the noble metal. *Journal of Materials Chemistry A* **2017**, *5* (33), 17609-17618.
25. Mutinda, S. I.; Li, D.; Kay, J.; Brock, S. L., Synthesis and characterization of Co_{2-x}Rh_xP nanoparticles and their catalytic activity towards the oxygen evolution reaction. *Journal of Materials Chemistry A* **2018**, *6* (25), 12142-12152.
26. Cook, T. R.; Dogutan, D. K.; Reece, S. Y.; Surendranath, Y.; Teets, T. S.; Nocera, D. G., Solar Energy Supply and Storage for the Legacy and Nonlegacy Worlds. *Chemical Reviews* **2010**, *110* (11), 6474-6502.
27. Hashimoto, K.; Irie, H.; Fujishima, A., TiO₂ Photocatalysis: A Historical Overview and Future Prospects. *Japanese Journal of Applied Physics* **2005**, *44* (12), 8269-8285.

28. Kojima, Y.; Suzuki, K.-i.; Fukumoto, K.; Sasaki, M.; Yamamoto, T.; Kawai, Y.; Hayashi, H., Hydrogen generation using sodium borohydride solution and metal catalyst coated on metal oxide. *International Journal of Hydrogen Energy* **2002**, *27* (10), 1029-1034.
29. Zafeiratos, S., *2D Nanomaterials for Energy Applications: Graphene and Beyond*. Elsevier Science: 2019.
30. You, B.; Sun, Y., Innovative Strategies for Electrocatalytic Water Splitting. *Accounts of Chemical Research* **2018**, *51* (7), 1571-1580.
31. Zou, X.; Zhang, Y., Noble metal-free hydrogen evolution catalysts for water splitting. *Chemical Society Reviews* **2015**, *44* (15), 5148-5180.
32. Pei, Y.; Cheng, Y.; Chen, J.; Smith, W.; Dong, P.; Ajayan, P. M.; Ye, M.; Shen, J., Recent developments of transition metal phosphides as catalysts in the energy conversion field. *Journal of Materials Chemistry A* **2018**, *6* (46), 23220-23243.
33. Liu, P.; Rodriguez, J. A., Catalytic Properties of Molybdenum Carbide, Nitride and Phosphide: A Theoretical Study. *Catalysis Letters* **2003**, *91* (3), 247-252.
34. Chianelli, R. R.; Berhault, G.; Raybaud, P.; Kasztelan, S.; Hafner, J.; Toulhoat, H., Periodic trends in hydrodesulfurization: in support of the Sabatier principle. *Applied Catalysis A: General* **2002**, *227* (1), 83-96.
35. Nørskov, J. K.; Bligaard, T.; Logadottir, A.; Kitchin, J. R.; Chen, J. G.; Pandelov, S.; Stimming, U., Trends in the Exchange Current for Hydrogen Evolution. *Journal of The Electrochemical Society* **2005**, *152* (3), J23.
36. Nørskov, J. K.; Bligaard, T.; Logadottir, A.; Kitchin, J. R.; Chen, J. G.; Pandelov, S.; Stimming, U., Response to “Comment on ‘Trends in the Exchange Current for Hydrogen

Evolution' [J. Electrochem. Soc., 152, J23 (2005)]". *Journal of The Electrochemical Society* **2006**, *153* (12), L33.

37. Wei, J.; Zhou, M.; Long, A.; Xue, Y.; Liao, H.; Wei, C.; Xu, Z. J., Heterostructured Electrocatalysts for Hydrogen Evolution Reaction Under Alkaline Conditions. *Nano-Micro Letters* **2018**, *10* (4), 75.

38. Conway, B. E.; Bai, L., Determination of adsorption of OPD H species in the cathodic hydrogen evolution reaction at Pt in relation to electrocatalysis. *Journal of Electroanalytical Chemistry and Interfacial Electrochemistry* **1986**, *198* (1), 149-175.

39. Conway, B. E.; Jerkiewicz, G., Relation of energies and coverages of underpotential and overpotential deposited H at Pt and other metals to the 'volcano curve' for cathodic H₂ evolution kinetics. *Electrochimica Acta* **2000**, *45* (25), 4075-4083.

40. Subbaraman, R.; Tripkovic, D.; Chang, K.-C.; Strmcnik, D.; Paulikas, A. P.; Hirunsit, P.; Chan, M.; Greeley, J.; Stamenkovic, V.; Markovic, N. M., Trends in activity for the water electrolyser reactions on 3d M(Ni,Co,Fe,Mn) hydr(oxy)oxide catalysts. *Nature Materials* **2012**, *11* (6), 550-557.

41. Bligaard, T.; Nørskov, J. K.; Dahl, S.; Matthiesen, J.; Christensen, C. H.; Sehested, J., The Brønsted–Evans–Polanyi relation and the volcano curve in heterogeneous catalysis. *Journal of Catalysis* **2004**, *224* (1), 206-217.

42. Karlberg, G. S., Adsorption trends for water, hydroxyl, oxygen, and hydrogen on transition-metal and platinum-skin surfaces. *Physical Review B* **2006**, *74* (15), 153414.

43. Greeley, J.; Jaramillo, T. F.; Bonde, J.; Chorkendorff, I.; Nørskov, J. K., Computational high-throughput screening of electrocatalytic materials for hydrogen evolution. *Nature Materials* **2006**, *5* (11), 909-913.

44. Suen, N.-T.; Hung, S.-F.; Quan, Q.; Zhang, N.; Xu, Y.-J.; Chen, H. M., Electrocatalysis for the oxygen evolution reaction: recent development and future perspectives. *Chemical Society Reviews* **2017**, *46* (2), 337-365.
45. Sapountzi, F. M.; Gracia, J. M.; Weststrate, C. J.; Fredriksson, H. O. A.; Niemantsverdriet, J. W., Electrocatalysts for the generation of hydrogen, oxygen and synthesis gas. *Progress in Energy and Combustion Science* **2017**, *58*, 1-35.
46. Li, X.; Hao, X.; Abudula, A.; Guan, G., Nanostructured catalysts for electrochemical water splitting: current state and prospects. *Journal of Materials Chemistry A* **2016**, *4* (31), 11973-12000.
47. Wei, C.; Sun, S.; Mandler, D.; Wang, X.; Qiao, S. Z.; Xu, Z. J., Approaches for measuring the surface areas of metal oxide electrocatalysts for determining their intrinsic electrocatalytic activity. *Chemical Society Reviews* **2019**, *48* (9), 2518-2534.
48. Jung, S.; McCrory, C. C. L.; Ferrer, I. M.; Peters, J. C.; Jaramillo, T. F., Benchmarking nanoparticulate metal oxide electrocatalysts for the alkaline water oxidation reaction. *Journal of Materials Chemistry A* **2016**, *4* (8), 3068-3076.
49. Wei, C.; Xu, Z. J., The Comprehensive Understanding of as an Evaluation Parameter for Electrochemical Water Splitting. *Small Methods* **2018**, *2* (11), 1800168.
50. Mohamed, R.; Cheng, X.; Fabbri, E.; Levecque, P.; Kötz, R.; Conrad, O.; Schmidt, T. J., Electrocatalysis of Perovskites: The Influence of Carbon on the Oxygen Evolution Activity. *Journal of The Electrochemical Society* **2015**, *162* (6), F579-F586.
51. Stoerzinger, K. A.; Risch, M.; Han, B.; Shao-Horn, Y., Recent Insights into Manganese Oxides in Catalyzing Oxygen Reduction Kinetics. *ACS Catalysis* **2015**, *5* (10), 6021-6031.

52. Zheng, J.; Sheng, W.; Zhuang, Z.; Xu, B.; Yan, Y., Universal dependence of hydrogen oxidation and evolution reaction activity of platinum-group metals on pH and hydrogen binding energy. *Science Advances* **2016**, *2* (3), e1501602.
53. Stephens, I. E. L.; Bondarenko, A. S.; Grønbjerg, U.; Rossmeisl, J.; Chorkendorff, I., Understanding the electrocatalysis of oxygen reduction on platinum and its alloys. *Energy & Environmental Science* **2012**, *5* (5), 6744-6762.
54. Green, C. L.; Kucernak, A., Determination of the Platinum and Ruthenium Surface Areas in Platinum–Ruthenium Electrocatalysts by Underpotential Deposition of Copper. 2. Effect of Surface Composition on Activity. *The Journal of Physical Chemistry B* **2002**, *106* (44), 11446-11456.
55. Herrero, E.; Buller, L. J.; Abruña, H. D., Underpotential Deposition at Single Crystal Surfaces of Au, Pt, Ag and Other Materials. *Chemical Reviews* **2001**, *101* (7), 1897-1930.
56. Stevens, M. B.; Enman, L. J.; Batchellor, A. S.; Cosby, M. R.; Vise, A. E.; Trang, C. D. M.; Boettcher, S. W., Measurement Techniques for the Study of Thin Film Heterogeneous Water Oxidation Electrocatalysts. *Chemistry of Materials* **2017**, *29* (1), 120-140.
57. Trotochaud, L.; Young, S. L.; Ranney, J. K.; Boettcher, S. W., Nickel–Iron Oxyhydroxide Oxygen-Evolution Electrocatalysts: The Role of Intentional and Incidental Iron Incorporation. *Journal of the American Chemical Society* **2014**, *136* (18), 6744-6753.
58. Sheng, W.; Myint, M.; Chen, J. G.; Yan, Y., Correlating the hydrogen evolution reaction activity in alkaline electrolytes with the hydrogen binding energy on monometallic surfaces. *Energy & Environmental Science* **2013**, *6* (5), 1509-1512.

59. Scholz, J.; Risch, M.; Stoerzinger, K. A.; Wartner, G.; Shao-Horn, Y.; Jooss, C., Rotating Ring–Disk Electrode Study of Oxygen Evolution at a Perovskite Surface: Correlating Activity to Manganese Concentration. *The Journal of Physical Chemistry C* **2016**, *120* (49), 27746-27756.
60. McCrory, C. C. L.; Jung, S.; Peters, J. C.; Jaramillo, T. F., Benchmarking Heterogeneous Electrocatalysts for the Oxygen Evolution Reaction. *Journal of the American Chemical Society* **2013**, *135* (45), 16977-16987.
61. Chen, J. Y. C.; Miller, J. T.; Gerken, J. B.; Stahl, S. S., Inverse spinel NiFeAlO₄ as a highly active oxygen evolution electrocatalyst: promotion of activity by a redox-inert metal ion. *Energy & Environmental Science* **2014**, *7* (4), 1382-1386.
62. Stoerzinger, K. A.; Qiao, L.; Biegalski, M. D.; Shao-Horn, Y., Orientation-Dependent Oxygen Evolution Activities of Rutile IrO₂ and RuO₂. *The Journal of Physical Chemistry Letters* **2014**, *5* (10), 1636-1641.
63. Gorlin, Y.; Jaramillo, T. F., A Bifunctional Nonprecious Metal Catalyst for Oxygen Reduction and Water Oxidation. *Journal of the American Chemical Society* **2010**, *132* (39), 13612-13614.
64. Poux, T.; Napolskiy, F. S.; Dintzer, T.; Kéranguéven, G.; Istomin, S. Y.; Tsirlina, G. A.; Antipov, E. V.; Savinova, E. R., Dual role of carbon in the catalytic layers of perovskite/carbon composites for the electrocatalytic oxygen reduction reaction. *Catalysis Today* **2012**, *189* (1), 83-92.
65. Fabbri, E.; Mohamed, R.; Levecque, P.; Conrad, O.; Kötz, R.; Schmidt, T. J., Composite Electrode Boosts the Activity of Ba_{0.5}Sr_{0.5}Co_{0.8}Fe_{0.2}O_{3-δ} Perovskite and Carbon toward Oxygen Reduction in Alkaline Media. *ACS Catalysis* **2014**, *4* (4), 1061-1070.

66. Yoon, Y.; Yan, B.; Surendranath, Y., Suppressing Ion Transfer Enables Versatile Measurements of Electrochemical Surface Area for Intrinsic Activity Comparisons. *Journal of the American Chemical Society* **2018**, *140* (7), 2397-2400.
67. Callejas, J. F.; Read, C. G.; Roske, C. W.; Lewis, N. S.; Schaak, R. E., Synthesis, Characterization, and Properties of Metal Phosphide Catalysts for the Hydrogen-Evolution Reaction. *Chemistry of Materials* **2016**, *28* (17), 6017-6044.
68. Chen, J.-H.; Whitmire, K. H., A structural survey of the binary transition metal phosphides and arsenides of the d-block elements. *Coordination Chemistry Reviews* **2018**, *355*, 271-327.
69. Carencio, S.; Portehault, D.; Boissière, C.; Mézailles, N.; Sanchez, C., Nanoscaled Metal Borides and Phosphides: Recent Developments and Perspectives. *Chem. Rev.* **2013**, *113*, 7981–8065.
70. Blanchard, P. E. R.; Grosvenor, A. P.; Cavell, R. G.; Mar, A., X-ray Photoelectron and Absorption Spectroscopy of Metal-Rich Phosphides M₂P and M₃P (M = Cr–Ni). *Chemistry of Materials* **2008**, *20* (22), 7081-7088.
71. Tegus, O.; Brück, E.; Buschow, K. H. J.; de Boer, F. R., Transition-metal-based magnetic refrigerants for room-temperature applications. *Nature* **2002**, *415* (6868), 150-152.
72. Oyama, S. T., Novel Catalysts for Advanced Hydroprocessing: Transition Metal Phosphides. *J. Catal.* **2003**, *216*, 343-352.
73. Brock, S. L.; Perera, S. C.; Stamm, K. L., Chemical Routes for Production of Transition Metal Phosphides on the Nanoscale: Implications for Advanced Magnetic and Catalytic Materials. *Chem. Eur. J.* **2004**, *10*, 3364-3371.
74. Sudha, P. N.; Sangeetha, K.; Vijayalakshmi, K.; Barhoum, A., Chapter 12 - Nanomaterials history, classification, unique properties, production and market. In *Emerging Applications of*

Nanoparticles and Architecture Nanostructures, Barhoum, A.; Makhoulf, A. S. H., Eds. Elsevier: 2018; pp 341-384.

75. Taniguchi, N., On the Basic concept of Nanotechnology. *Proceeding of the ICPE* **1974**.
76. Drexler, K. E., *Engines of Creation*. Anchor Press/Doubleday: 1986.
77. Bayda, S.; Adeel, M.; Tuccinardi, T.; Cordani, M.; Rizzolio, F., The History of Nanoscience and Nanotechnology: From Chemical-Physical Applications to Nanomedicine. *Molecules* **2019**, *25* (1), 112.
78. Alivisatos, A. P., Perspectives on the Physical Chemistry of Semiconductor Nanoparticles. *J. Phys. Chem. B* **1996**, *100*, 13226-13239.
79. Alivisatos, A. P., Semiconductor Clusters, Nanocrystals, and Quantum Dots. *Science* **1996**, *271* (5251), 933.
80. Leslie-Pelecky, D. L.; Rieke, R. D., Magnetic Properties of Nanostructured Materials. *Chem. Mater.* **1996**, *8*, 1770-1783.
81. Eustis, S.; El-Sayed, M. A., Why gold nanoparticles are more precious than pretty gold: Noble metal surface plasmon resonance and its enhancement of the radiative and nonradiative properties of nanocrystals of different shapes. *Chemical Society Reviews* **2006**, *35* (3), 209-217.
82. Ng, C. K.; Sivakumar, K.; Liu, X.; Madhaiyan, M.; Ji, L.; Yang, L.; Tang, C.; Song, H.; Kjelleberg, S.; Cao, B., Influence of outer membrane c-type cytochromes on particle size and activity of extracellular nanoparticles produced by *Shewanella oneidensis*. *Biotechnology and Bioengineering* **2013**, *110* (7), 1831-1837.
83. Boisseau, P.; Loubaton, B., Nanomedicine, nanotechnology in medicine. *Comptes Rendus Physique* **2011**, *12* (7), 620-636.

84. Huynh, W. U.; Dittmer, J. J.; Alivisatos, A. P., Hybrid Nanorod-Polymer Solar Cells. *Science* **2002**, *295* (5564), 2425.
85. Michalet, X.; Pinaud, F. F.; Bentolila, L. A.; Tsay, J. M.; Doose, S.; Li, J. J.; Sundaresan, G.; Wu, A. M.; Gambhir, S. S.; Weiss, S., *Science* **2005**, *307*, 538.
86. Talapin, D. V.; Lee, J. S.; Kovalenko, M. V.; Shevchenko, E. V., *Chem. Rev.* **2010**, *110*, 389.
87. Wang, M.-F.; Raghunathan, N.; Ziaie, B., A Nonlithographic Top-Down Electrochemical Approach for Creating Hierarchical (Micro–Nano) Superhydrophobic Silicon Surfaces. *Langmuir* **2007**, *23* (5), 2300-2303.
88. Wang, Y.; Xia, Y., Bottom-Up and Top-Down Approaches to the Synthesis of Monodispersed Spherical Colloids of Low Melting-Point Metals. *Nano Letters* **2004**, *4* (10), 2047-2050.
89. Hoepfener, S.; Maoz, R.; Cohen, S. R.; Chi, L. F.; Fuchs, H.; Sagiv, J., Metal Nanoparticles, Nanowires, and Contact Electrodes Self-Assembled on Patterned Monolayer Templates—A Bottom-up Chemical Approach. *Advanced Materials* **2002**, *14* (15), 1036-1041.
90. Mijatovic, D.; Eijkel, J. C. T.; van den Berg, A., Technologies for nanofluidic systems: top-down vs. bottom-up—a review. *Lab on a Chip* **2005**, *5* (5), 492-500.
91. Lee, D. C.; Smith, D. K.; Heitsch, A. T.; Korgel, B. A., Colloidal magnetic nanocrystals: synthesis, properties and applications. *Annual Reports Section "C" (Physical Chemistry)* **2007**, *103* (0), 351-402.
92. Burda, C.; Chen, X.; Narayanan, R.; El-Sayed, M. A., Chemistry and Properties of Nanocrystals of Different Shapes. *Chemical Reviews* **2005**, *105* (4), 1025-1102.

93. Rodriguez, A.; Amiens, C.; Chaudret, B.; Casanove, M.-J.; Lecante, P.; Bradley, J. S., Synthesis and Isolation of Cuboctahedral and Icosahedral Platinum Nanoparticles. Ligand-Dependent Structures. *Chemistry of Materials* **1996**, *8* (8), 1978-1986.
94. Sau, T. K.; Murphy, C. J., Room Temperature High-Yield Synthesis of Semiconducting Metal Sulfide Nanocrystals. *J. Am. Chem. Soc.* **2004**, *126*, 8648-8649.
95. LaMer, V. K.; Dinegar, R. H., Theory, Production and Mechanism of Formation of Monodispersed Hydrosols. *Journal of the American Chemical Society* **1950**, *72* (11), 4847-4854.
96. Klimov, V., Semiconductor and Metal Nanocrystals: Synthesis, Electronic, and Optical Properties. Vol. 87 Vol. 87. **2003**.
97. Beberwyck, B. J.; Surendranath, Y.; Alivisatos, A. P., Cation Exchange: A Versatile Tool for Nanomaterials Synthesis. *The Journal of Physical Chemistry C* **2013**, *117* (39), 19759-19770.
98. Cho, G.; Park, Y.; Hong, Y.-K.; Ha, D.-H., Ion exchange: an advanced synthetic method for complex nanoparticles. *Nano Convergence* **2019**, *6*, NA.
99. Son, D. H.; Hughes, S. M.; Yin, Y.; Paul Alivisatos, A., Cation Exchange Reactions in Ionic Nanocrystals. *Science* **2004**, *306* (5698), 1009-1012.
100. Moon, G. D.; Ko, S.; Xia, Y.; Jeong, U., Chemical Transformations in Ultrathin Chalcogenide Nanowires. *ACS Nano* **2010**, *4* (4), 2307-2319.
101. Casavola, M.; van Huis, M. A.; Bals, S.; Lambert, K.; Hens, Z.; Vanmaekelbergh, D., Anisotropic Cation Exchange in PbSe/CdSe Core/Shell Nanocrystals of Different Geometry. *Chemistry of Materials* **2012**, *24* (2), 294-302.
102. Lesnyak, V.; Brescia, R.; Messina, G. C.; Manna, L., Cu Vacancies Boost Cation Exchange Reactions in Copper Selenide Nanocrystals. *Journal of the American Chemical Society* **2015**, *137* (29), 9315-9323.

103. Barman, D.; Ghosh, S.; Paul, S.; Dalal, B.; De, S. K., Cation Exchange-Mediated Synthesis of Library of Plasmomagnetic Nanoheterostructures: Transformation of 2-Dimensional-Shaped Fe₇S₈ Nanoplates to Cu–Fe–S-Based Ternary Compound. *Chemistry of Materials* **2018**, *30* (16), 5550-5560.
104. Fan, Z.; Lin, L. C.; Buijs, W.; Vlugt, T. J. H.; van Huis, M. A., Atomistic understanding of cation exchange in PbS nanocrystals using simulations with pseudoligands. *Nat Commun* **2016**, *7*, 11503.
105. Rivest, J. B.; Jain, P. K., Cation exchange on the nanoscale: an emerging technique for new material synthesis, device fabrication, and chemical sensing. *Chemical Society Reviews* **2013**, *42* (1), 89-96.
106. Wark, S. E.; Hsia, C.-H.; Son, D. H., Effects of Ion Solvation and Volume Change of Reaction on the Equilibrium and Morphology in Cation-Exchange Reaction of Nanocrystals. *Journal of the American Chemical Society* **2008**, *130* (29), 9550-9555.
107. Parr, R. G.; Pearson, R. G., Absolute hardness: companion parameter to absolute electronegativity. *Journal of the American Chemical Society* **1983**, *105* (26), 7512-7516.
108. Pearson, R. G., Hard and Soft Acids and Bases. *Journal of the American Chemical Society* **1963**, *85* (22), 3533-3539.
109. Li, H.; Zanella, M.; Genovese, A.; Povia, M.; Falqui, A.; Giannini, C.; Manna, L., Sequential Cation Exchange in Nanocrystals: Preservation of Crystal Phase and Formation of Metastable Phases. *Nano Letters* **2011**, *11* (11), 4964-4970.
110. Zhang, D.; Wong, A. B.; Yu, Y.; Brittman, S.; Sun, J.; Fu, A.; Beberwyck, B.; Alivisatos, A. P.; Yang, P., Phase-Selective Cation-Exchange Chemistry in Sulfide Nanowire Systems. *Journal of the American Chemical Society* **2014**, *136* (50), 17430-17433.

111. Ha, D.-H.; Caldwell, A. H.; Ward, M. J.; Honrao, S.; Mathew, K.; Hovden, R.; Koker, M. K. A.; Muller, D. A.; Hennig, R. G.; Robinson, R. D., Solid–Solid Phase Transformations Induced through Cation Exchange and Strain in 2D Heterostructured Copper Sulfide Nanocrystals. *Nano Letters* **2014**, *14* (12), 7090-7099.
112. Robinson, R. D.; Sadtler, B.; Demchenko, D. O.; Erdonmez, C. K.; Wang, L.-W.; Alivisatos, A. P., Spontaneous Superlattice Formation in Nanorods Through Partial Cation Exchange. *Science* **2007**, *317* (5836), 355.
113. Sadtler, B.; Demchenko, D. O.; Zheng, H.; Hughes, S. M.; Merkle, M. G.; Dahmen, U.; Wang, L.-W.; Alivisatos, A. P., Selective Facet Reactivity during Cation Exchange in Cadmium Sulfide Nanorods. *Journal of the American Chemical Society* **2009**, *131* (14), 5285-5293.
114. Zhang, C.; Fu, X.; Peng, Z.; Gao, J.; Xia, Y.; Zhang, J.; Luo, W.; Li, H.; Wang, Y.; Zhang, D., Phosphine-free synthesis and optical stabilities of composition-tuneable monodisperse ternary PbSe_{1-x}S_x alloyed nanocrystals via cation exchange. *CrystEngComm* **2018**, *20* (18), 2519-2527.
115. Wang, W.; Winkler, M. T.; Gunawan, O.; Gokmen, T.; Todorov, T. K.; Zhu, Y.; Mitzi, D. B., Device Characteristics of CZTSSe Thin-Film Solar Cells with 12.6% Efficiency. *Advanced Energy Materials* **2014**, *4* (7), 1301465.
116. Zhang, J.; Chernomordik, B. D.; Crisp, R. W.; Kroupa, D. M.; Luther, J. M.; Miller, E. M.; Gao, J.; Beard, M. C., Preparation of Cd/Pb Chalcogenide Heterostructured Janus Particles via Controllable Cation Exchange. *ACS Nano* **2015**, *9* (7), 7151-7163.
117. Justo, Y.; Goris, B.; Kamal, J. S.; Geiregat, P.; Bals, S.; Hens, Z., Multiple Dot-in-Rod PbS/CdS Heterostructures with High Photoluminescence Quantum Yield in the Near-Infrared. *Journal of the American Chemical Society* **2012**, *134* (12), 5484-5487.

118. Fruchart, R.; Roger, A.; Senateur, J. P., Crystallographic and Magnetic Properties of Solid Solutions of the Phosphides M_2P , $M = Cr, Mn, Fe, Co,$ and Ni . *J. Appl. Phys.* **1969**, *40*, 1250-1257.
119. Yoon, K. Y.; Jang, Y.; Park, J.; Hwang, Y.; Koo, B.; Park, J.-G.; Hyeon, T., Synthesis of Uniform-Sized Bimetallic Iron-Nickel Phosphide Nanorods. *J. Solid State Chem.* **2008**, *181*, 1609-1613.
120. Hitihami-Mudiyanselage, A.; Arachchige, M. P.; Seda, T.; Lawes, G.; Brock, S. L., Synthesis and Characterization of Discrete $Fe_xNi_{2-x}P$ Nanocrystals ($0 < x < 2$): Nanocompositional Effects on Magnetic Properties. *Chemistry of Materials* **2015**, *27*, 6592-6600.
121. Liyanage, D. R.; Danforth, S. J.; Liu, Y.; Bussell, M. E.; Brock, S. L., Simultaneous Control of Composition, Size and Morphology in Discrete $Ni_{2-x}Co_xP$ Nanoparticles. *Chemistry of Materials* **2015**, *27*, 4349-4357.
122. Ye, E.; Zhang, S.-Y.; Lim, S. H.; Bosman, M.; Zhang, Z.; Win, K. Y.; Han, M.-Y., Ternary Cobalt–Iron Phosphide Nanocrystals with Controlled Compositions, Properties, and Morphologies from Nanorods and Nanorice to Split Nanostructures. *Chem. Eur. J.* **2011**, *17* (21), 5982-5988.
123. Mendoza-Garcia, A.; Zhu, H.; Yu, Y.; Li, Q.; Zhou, L.; Su, D.; Kramer, M. J.; Sun, S., Controlled Anisotropic Growth of Co-Fe-P from Co-Fe-O Nanoparticles. *Angewandte Chemie International Edition* **2015**, *54* (33), 9642-9645.
124. Li, D.; Arachchige, M. P.; Kulikowski, B.; Lawes, G.; Seda, T.; Brock, S. L., Control of Composition and Size in Discrete $Co_xFe_{2-x}P$ Nanoparticles: Consequences for Magnetic Properties. *Chemistry of Materials* **2016**, *28* (11), 3920-3927.
125. Colson, A. C.; Whitmire, K. H., Synthesis of $Fe_{2-x}Mn_xP$ Nanoparticles from Single-Source Molecular Precursors. *Chem. Mater.* **2011**, *23* (16), 3731-3739.

126. De Trizio, L.; Gaspari, R.; Bertoni, G.; Kriegel, I.; Moretti, L.; Scotognella, F.; Maserati, L.; Zhang, Y.; Messina, G. C.; Prato, M.; Marras, S.; Cavalli, A.; Manna, L., Cu₃-xP Nanocrystals as a Material Platform for Near-Infrared Plasmonics and Cation Exchange Reactions. *Chemistry of Materials* **2015**, *27* (3), 1120-1128.
127. Koh, S.; Kim, W. D.; Bae, W. K.; Lee, Y. K.; Lee, D. C., Controlling Ion-Exchange Balance and Morphology in Cation Exchange from Cu₃-xP Nanoplatelets into InP Crystals. *Chemistry of Materials* **2019**, *31* (6), 1990-2001.
128. Liu, P.; Rodriguez, J. A., Catalysts for Hydrogen Evolution from the [NiFe] Hydrogenase to the Ni₂P(001) Surface: The Importance of Ensemble Effect. *Journal of the American Chemical Society* **2005**, *127* (42), 14871-14878.
129. Popczun, E. J.; McKone, J. R.; Read, C. G.; Biacchi, A. J.; Wiltrout, A. M.; Lewis, N. S.; Schaak, R. E., Nanostructured Nickel Phosphide as an Electrocatalyst for the Hydrogen Evolution Reaction. *Journal of the American Chemical Society* **2013**, *135* (25), 9267-9270.
130. Popczun, E. J.; Read, C. G.; Roske, C. W.; Lewis, N. S.; Schaak, R. E., Highly Active Electrocatalysis of the Hydrogen Evolution Reaction by Cobalt Phosphide Nanoparticles. *Angewandte Chemie International Edition* **2014**, *53* (21), 5427-5430.
131. Read, C. G.; Callejas, J. F.; Holder, C. F.; Schaak, R. E., General Strategy for the Synthesis of Transition Metal Phosphide Films for Electrocatalytic Hydrogen and Oxygen Evolution. *ACS Applied Materials & Interfaces* **2016**, *8* (20), 12798-12803.
132. Yang, Y.; Fei, H.; Ruan, G.; Tour, J. M., Porous cobalt-based thin film as a bifunctional catalyst for hydrogen generation and oxygen generation. *Advanced materials (Deerfield Beach, Fla.)* **2015**, *27* (20), 3175-80.

133. Li, W.; Xiong, D.; Gao, X.; Liu, L., The oxygen evolution reaction enabled by transition metal phosphide and chalcogenide pre-catalysts with dynamic changes. *Chemical Communications* **2019**, *55* (60), 8744-8763.
134. Han, A.; Chen, H.; Sun, Z.; Xu, J.; Du, P., High catalytic activity for water oxidation based on nanostructured nickel phosphide precursors. *Chemical Communications* **2015**, *51* (58), 11626-11629.
135. Xu, J.; Li, J.; Xiong, D.; Zhang, B.; Liu, Y.; Wu, K.-H.; Amorim, I.; Li, W.; Liu, L., Trends in activity for the oxygen evolution reaction on transition metal (M = Fe, Co, Ni) phosphide pre-catalysts. *Chemical Science* **2018**, *9* (14), 3470-3476.
136. Tian, J.; Liu, Q.; Cheng, N.; Asiri, A. M.; Sun, X., Self-Supported Cu₃P Nanowire Arrays as an Integrated High-Performance Three-Dimensional Cathode for Generating Hydrogen from Water. *Angewandte Chemie International Edition* **2014**, *53* (36), 9577-9581.
137. Son, C. Y.; Kwak, I. H.; Lim, Y. R.; Park, J., FeP and FeP₂ nanowires for efficient electrocatalytic hydrogen evolution reaction. *Chemical Communications* **2016**, *52* (13), 2819-2822.
138. Du, H.; Kong, R.-M.; Guo, X.; Qu, F.; Li, J., Recent progress in transition metal phosphides with enhanced electrocatalysis for hydrogen evolution. *Nanoscale* **2018**, *10* (46), 21617-21624.
139. Tang, C.; Zhang, R.; Lu, W.; He, L.; Jiang, X.; Asiri, A. M.; Sun, X., Fe-Doped CoP Nanoarray: A Monolithic Multifunctional Catalyst for Highly Efficient Hydrogen Generation. *Advanced Materials* **2017**, *29* (2), 1602441.

140. Wang, P.; Pu, Z.; Li, Y.; Wu, L.; Tu, Z.; Jiang, M.; Kou, Z.; Amiin, I. S.; Mu, S., Iron-Doped Nickel Phosphide Nanosheet Arrays: An Efficient Bifunctional Electrocatalyst for Water Splitting. *ACS Applied Materials & Interfaces* **2017**, *9* (31), 26001-26007.
141. Du, H.; Zhang, X.; Tan, Q.; Kong, R.; Qu, F., A Cu₃P–CoP hybrid nanowire array: a superior electrocatalyst for acidic hydrogen evolution reactions. *Chemical Communications* **2017**, *53* (88), 12012-12015.
142. Chung, Y.-H.; Jang, I.; Jang, J.-H.; Park, H. S.; Ham, H. C.; Jang, J. H.; Lee, Y.-K.; Yoo, S. J., Anomalous in situ Activation of Carbon-Supported Ni₂P Nanoparticles for Oxygen Evolving Electrocatalysis in Alkaline Media. *Scientific Reports* **2017**, *7* (1), 8236.
143. Zhou, M.; Sun, Q.; Shen, Y.; Ma, Y.; Wang, Z.; Zhao, C., Fabrication of 3D microporous amorphous metallic phosphides for high-efficiency hydrogen evolution reaction. *Electrochimica Acta* **2019**, *306*, 651-659.
144. He, R.; Li, J.; Feng, L., NiCoP selenization for enhanced oxygen evolution reaction in alkaline electrolyte. *Catalysis Communications* **2022**, *163*, 106407.
145. Kasiviswanathan, K. V., Hot Cells, Glove Boxes, and Shielded Facilities. In *Encyclopedia of Materials: Science and Technology*, Buschow, K. H. J.; Cahn, R. W.; Flemings, M. C.; Ilshner, B.; Kramer, E. J.; Mahajan, S.; Veyssi re, P., Eds. Elsevier: Oxford, 2001; pp 3830-3833.
146. Errington, R. J., *Advanced Practical Inorganic and Metalorganic Chemistry*. Taylor & Francis: 1997.
147. Millar, S. Tips and Tricks for the Lab: Air-Sensitive Techniques (1). https://www.chemistryviews.org/details/education/3728881/Tips_and_Tricks_for_the_Lab_Air-Sensitive_Techniques_1.html.

148. Rao, C. N. R., Chemical synthesis of solid inorganic materials. *Materials Science and Engineering: B* **1993**, *18* (1), 1-21.
149. Cullity, B. D., *Elements of X-ray Diffraction*. 2nd ed.; Addison-Wesley: Reading, Massachusetts, 1978.
150. Parkin, I. P., Basic Solid State Chemistry Anthony R. West 2nd edn. John Wiley & Sons, Chichester, 1999 xvi + 480 pages. £24.95 ISBN 0-471-98756-5 (pbk). *Applied Organometallic Chemistry* **2000**, *14* (4), 227-228.
151. Williams, D. B.; Carter, C. B., *Transmission Electron Microscopy: A Textbook for Materials Science*. Springer US: 2009.
152. Fultz, B.; Howe, J. M., *Transmission Electron Microscopy and Diffractometry of Materials*. Springer Berlin Heidelberg: 2012.
153. Sardela, M., *Practical Materials Characterization*. Springer New York: 2014.
154. Li, J.-S.; Wang, Y.; Liu, C.-H.; Li, S.-L.; Wang, Y.-G.; Dong, L.-Z.; Dai, Z.-H.; Li, Y.-F.; Lan, Y.-Q., Coupled molybdenum carbide and reduced graphene oxide electrocatalysts for efficient hydrogen evolution. *Nat Commun* **2016**, *7* (1), 11204.
155. Fan, L.; Liu, P. F.; Yan, X.; Gu, L.; Yang, Z. Z.; Yang, H. G.; Qiu, S.; Yao, X., Atomically isolated nickel species anchored on graphitized carbon for efficient hydrogen evolution electrocatalysis. *Nat Commun* **2016**, *7* (1), 10667.
156. Chen, R.; Yang, C.; Cai, W.; Wang, H.-Y.; Miao, J.; Zhang, L.; Chen, S.; Liu, B., Use of Platinum as the Counter Electrode to Study the Activity of Nonprecious Metal Catalysts for the Hydrogen Evolution Reaction. *ACS Energy Letters* **2017**, *2* (5), 1070-1075.
157. Yadav, A. P.; Nishikata, A.; Tsuru, T., Effect of halogen ions on platinum dissolution under potential cycling in 0.5M H₂SO₄ solution. *Electrochimica Acta* **2007**, *52* (26), 7444-7452.

158. Wang, Z.; Tada, E.; Nishikata, A., In Situ Analysis of Chloride Effect on Platinum Dissolution by a Channel-Flow Multi-Electrode System. *Journal of The Electrochemical Society* **2014**, *161* (9), F845-F849.
159. Ji, S. G.; Kim, H.; Choi, H.; Lee, S.; Choi, C. H., Overestimation of Photoelectrochemical Hydrogen Evolution Reactivity Induced by Noble Metal Impurities Dissolved from Counter/Reference Electrodes. *ACS Catalysis* **2020**, *10* (5), 3381-3389.
160. Ha, D.-H.; Moreau, L. M.; Bealing, C. R.; Zhang, H.; Hennig, R. G.; Robinson, R. D., The Structural Evolution and Diffusion During the Chemical Transformation from Cobalt to Cobalt Phosphide Nanoparticles. *J. Mater. Chem.* **2011**, *21* (31), 11498-11510.
161. Henkes, A. E.; Schaak, R. E., Template-Assisted Synthesis of Shape-Controlled Rh₂P Nanocrystals. *Inorg. Chem.* **2008**, *47*, 671-677.
162. Yang, F.; Zhao, Y.; Du, Y.; Chen, Y.; Cheng, G.; Chen, S.; Luo, W., A Monodisperse Rh₂P-Based Electrocatalyst for Highly Efficient and pH-Universal Hydrogen Evolution Reaction. *Advanced Energy Materials* **2018**, *8* (18), 1703489.
163. Yang, J.; Shao, Q.; Huang, B.; Sun, M.; Huang, X., pH-Universal Water Splitting Catalyst: Ru-Ni Nanosheet Assemblies. *iScience* **2019**, *11*, 492-504.
164. Kundu, M. K.; Mishra, R.; Bhowmik, T.; Barman, S., Rhodium metal–rhodium oxide (Rh–Rh₂O₃) nanostructures with Pt-like or better activity towards hydrogen evolution and oxidation reactions (HER, HOR) in acid and base: correlating its HOR/HER activity with hydrogen binding energy and oxophilicity of the catalyst. *Journal of Materials Chemistry A* **2018**, *6* (46), 23531-23541.

165. Wang, K.; Huang, B.; Lin, F.; Lv, F.; Luo, M.; Zhou, P.; Liu, Q.; Zhang, W.; Yang, C.; Tang, Y., Wrinkled Rh₂P Nanosheets as Superior pH-Universal Electrocatalysts for Hydrogen Evolution Catalysis. *Advanced Energy Materials* **2018**, *8* (27), 1801891.
166. Duan, H.; Li, D.; Tang, Y.; He, Y.; Ji, S.; Wang, R.; Lv, H.; Lopes, P. P.; Paulikas, A. P.; Li, H., High-performance Rh₂P electrocatalyst for efficient water splitting. *Journal of the American Chemical Society* **2017**, *139* (15), 5494-5502.
167. Yang, F.; Zhao, Y.; Du, Y.; Chen, Y.; Cheng, G.; Chen, S.; Luo, W., A Monodisperse Rh₂P-Based Electrocatalyst for Highly Efficient and pH-Universal Hydrogen Evolution Reaction. *Advanced Energy Materials* **2018**, 1703489.
168. Liu, S.; Chen, Y.; Yu, L.; Lin, Y.; Liu, Z.; Wang, M.; Chen, Y.; Zhang, C.; Pan, Y.; Liu, Y.; Liu, C., A supramolecular-confinement pyrolysis route to ultrasmall rhodium phosphide nanoparticles as a robust electrocatalyst for hydrogen evolution in the entire pH range and seawater electrolysis. *J. Mater. Chem. A* **2020**, *8* (48), 25768-25779.
169. Zhang, Y.; Gao, L.; Hensen, E. J. M.; Hofmann, J. P., Evaluating the Stability of Co₂P Electrocatalysts in the Hydrogen Evolution Reaction for Both Acidic and Alkaline Electrolytes. *ACS Energy Letters* **2018**, *3* (6), 1360-1365.
170. Popczun, E. J.; McKone, J. R.; Read, C. G.; Biacchi, A. J.; Wiltrout, A. M.; Lewis, N. S.; Schaak, R. E., Nanostructured Nickel Phosphide as an Electrocatalyst for the Hydrogen Evolution Reaction. *J. Am. Chem. Soc.* **2013**, *135* (25), 9267-9270.
171. Pu, Z.; Liu, T.; Amiin, I. S.; Cheng, R.; Wang, P.; Zhang, C.; Ji, P.; Hu, W.; Liu, J.; Mu, S., Transition-Metal Phosphides: Activity Origin, Energy-Related Electrocatalysis Applications, and Synthetic Strategies. *Advanced Functional Materials* **2020**, *30* (45), 2004009.

172. Ying, J.; Wang, H., Strategies for Developing Transition Metal Phosphides in Electrochemical Water Splitting. *Front Chem* **2021**, *9*, 700020-700020.
173. Habas, S. E.; Baddour, F. G.; Ruddy, D. A.; Nash, C. P.; Wang, J.; Pan, M.; Hensley, J. E.; Schaidle, J. A., A Facile Molecular Precursor Route to Metal Phosphide Nanoparticles and Their Evaluation as Hydrodeoxygenation Catalysts. *Chem. Mater.* **2015**, *27* (22), 7580-7592.
174. Mendoza-Garcia, A.; Su, D.; Sun, S., Sea urchin-like cobalt–iron phosphide as an active catalyst for oxygen evolution reaction. *Nanoscale* **2016**, *8* (6), 3244-3247.
175. Zhang, Y.; Li, N.; Zhang, Z.; Li, S.; Cui, M.; Ma, L.; Zhou, H.; Su, D.; Zhang, S., Programmable Synthesis of Multimetallic Phosphide Nanorods Mediated by Core/Shell Structure Formation and Conversion. *Journal of the American Chemical Society* **2020**, *142* (18), 8490-8497.
176. El-Refaei, S. M.; Russo, P. A.; Pinna, N., Recent Advances in Multimetal and Doped Transition-Metal Phosphides for the Hydrogen Evolution Reaction at Different pH values. *ACS Applied Materials & Interfaces* **2021**, *13* (19), 22077-22097.
177. Duan, H.; Li, D.; Tang, Y.; He, Y.; Ji, S.; Wang, R.; Lv, H.; Lopes, P. P.; Paulikas, A. P.; Li, H.; Mao, S. X.; Wang, C.; Markovic, N. M.; Li, J.; Stamenkovic, V. R.; Li, Y., High-Performance Rh₂P Electrocatalyst for Efficient Water Splitting. *Journal of the American Chemical Society* **2017**, *139* (15), 5494-5502.
178. Yang, F.; Zhao, Y.; Du, Y.; Chen, Y.; Cheng, G.; Chen, S.; Luo, W., A Monodisperse Rh₂P-Based Electrocatalyst for Highly Efficient and pH-Universal Hydrogen Evolution Reaction. *Advanced Energy Materials* **2018**, *8* (18), 1703489.
179. Parra-Puerto, A.; Ng, K. L.; Fahy, K.; Goode, A. E.; Ryan, M. P.; Kucernak, A., Supported Transition Metal Phosphides: Activity Survey for HER, ORR, OER, and Corrosion Resistance in Acid and Alkaline Electrolytes. *ACS Catalysis* **2019**, *9* (12), 11515-11529.

180. Wu, X.; Wang, R.; Li, W.; Feng, B.; Hu, W., Rh₂P Nanoparticles Partially Embedded in N/P-Doped Carbon Scaffold at Ultralow Metal Loading for High Current Density Water Electrolysis. *ACS Applied Nano Materials* **2021**, *4* (4), 3369-3376.
181. Mutinda, S. I.; Batugedara, T. N.; Brown, B.; Adeniran, O.; Liu, Z.-F.; Brock, S. L., Rh₂P Activity at a Fraction of the Cost? Co_{2-x}Rh_xP Nanoparticles as Electrocatalysts for the Hydrogen Evolution Reaction in Acidic Media. *ACS Applied Energy Materials* **2021**, *4* (1), 946-955.
182. Mutinda, S. I.; Batugedara, T. N.; Brown, B.; Brock, S. L., Co_{2-x}Rh_xP Nanoparticles for Overall Water Splitting in Basic Media: Activation by Phase-Segregation-Assisted Nanostructuring at the Anode. *ChemCatChem* **2021**, *13* (19), 4111-4119.
183. Du, X.; Tan, S.; Cai, P.; Luo, W.; Cheng, G., A RhNiP/rGO hybrid for efficient catalytic hydrogen generation from an alkaline solution of hydrazine. *Journal of Materials Chemistry A* **2016**, *4* (38), 14572-14576.
184. Muthuswamy, E.; Savithra, G. H. L.; Brock, S. L., Synthetic Levers Enabling Independent Control of Phase, Size, and Morphology in Nickel Phosphide Nanoparticles. *ACS Nano* **2011**, *5* (3), 2402-2411.
185. Jain, A. a. O., Shyue Ping and Hautier, Geoffroy and Chen, Wei and Richards, William Davidson and Dacek, Stephen and Cholia, Shreyas and Gunter, Dan and Skinner, David and Ceder, Gerbrand and Persson, Kristin a., The Materials Project: A materials genome approach to accelerating materials innovation. *APL Materials* **2013**, *1*, 011002.
186. Hettiarachchi, M. A.; Su'a, T.; Abdelhamid, E.; Pokhrel, S.; Nadgorny, B.; Brock, S. L., Synthesis of colloidal MnAs_xSb_{1-x} nanoparticles: compositional inhomogeneity and magnetic consequences. *Journal of Materials Chemistry C* **2021**, *9* (38), 13292-13303.

187. Henkes, A. E.; Vasquez, Y.; Schaak, R. E., Converting Metals into Phosphides: A General Strategy for the Synthesis of Metal Phosphide Nanocrystals. *J. Am. Chem. Soc.* **2007**, *129*, 1896-1897.
188. Su, L.; Cui, X.; He, T.; Zeng, L.; Tian, H.; Song, Y.; Qi, K.; Xia, B. Y., Surface reconstruction of cobalt phosphide nanosheets by electrochemical activation for enhanced hydrogen evolution in alkaline solution. *Chemical Science* **2019**, *10* (7), 2019-2024.
189. Xu, K.; Ding, H.; Zhang, M.; Chen, M.; Hao, Z.; Zhang, L.; Wu, C.; Xie, Y., Regulating Water-Reduction Kinetics in Cobalt Phosphide for Enhancing HER Catalytic Activity in Alkaline Solution. *Advanced Materials* **2017**, *29* (28), 1606980.
190. Shifa, T. A.; Yusupov, K.; Solomon, G.; Gradone, A.; Mazzaro, R.; Cattaruzza, E.; Vomiero, A., In Situ-Generated Oxide in Sn-Doped Nickel Phosphide Enables Ultrafast Oxygen Evolution. *ACS Catalysis* **2021**, *11* (8), 4520-4529.
191. Kim, D.; Park, S.; Yan, B.; Hong, H.; Cho, Y.; Kang, J.; Qin, X.; Yoo, T.; Piao, Y., Synthesis of Remarkably Thin Co-Fe Phosphide/Carbon Nanosheet for Enhanced Oxygen Evolution Reaction Electrocatalysis Driven by Readily Generated Active Oxyhydroxide. *ACS Applied Energy Materials* **2022**, *5* (2), 2400-2411.
192. Dutta, A.; Pradhan, N., Developments of Metal Phosphides as Efficient OER Precatalysts. *The Journal of Physical Chemistry Letters* **2017**, *8* (1), 144-152.
193. Liu, G.; Li, P.; Zhao, G.; Wang, X.; Kong, J.; Liu, H.; Zhang, H.; Chang, K.; Meng, X.; Kako, T.; Ye, J., Promoting Active Species Generation by Plasmon-Induced Hot-Electron Excitation for Efficient Electrocatalytic Oxygen Evolution. *Journal of the American Chemical Society* **2016**, *138* (29), 9128-9136.

194. Surendranath, Y.; Kanan, M. W.; Nocera, D. G., Mechanistic Studies of the Oxygen Evolution Reaction by a Cobalt-Phosphate Catalyst at Neutral pH. *Journal of the American Chemical Society* **2010**, *132* (46), 16501-16509.
195. Danilovic, N.; Subbaraman, R.; Strmcnik, D.; Chang, K. C.; Paulikas, A. P.; Stamenkovic, V. R.; Markovic, N. M., Enhancing the alkaline hydrogen evolution reaction activity through the bifunctionality of Ni(OH)₂/metal catalysts. *Angewandte Chemie (International ed. in English)* **2012**, *51* (50), 12495-8.
196. Malaman, B.; Le Caër, G.; Delcroix, P.; Fruchart, D.; Bacmann, M.; Fruchart, R., Magneto-elastic Transition and Magnetic Couplings: A ⁵⁷Mossbauer Spectroscopy Study of the MnFeP_{1-x}As_x System. *J. Phys.: Cond. Matter* **1996**, *8*, 8653-8667.
197. NIST X-ray Photoelectron Spectroscopy Database, NIST Standard Reference Database Number 20, National Institute of Standards and Technology, Gaithersburg MD, 20899 (2000), doi:10.18434/T4T88K, (retrieved [date of access]).
198. Zhang, F.-S.; Wang, J.-W.; Luo, J.; Liu, R.-R.; Zhang, Z.-M.; He, C.-T.; Lu, T.-B., Extraction of nickel from NiFe-LDH into Ni₂P@NiFe hydroxide as a bifunctional electrocatalyst for efficient overall water splitting. *Chemical Science* **2018**, *9* (5), 1375-1384.
199. Liu, H.; Zhu, S.; Cui, Z.; Li, Z.; Wu, S.; Liang, Y., Ni₂P nanoflakes for the high-performing urea oxidation reaction: linking active sites to a UOR mechanism. *Nanoscale* **2021**, *13* (3), 1759-1769.
200. Liyanage, D. R.; Danforth, S. J.; Liu, Y.; Bussell, M. E.; Brock, S. L., Simultaneous Control of Composition, Size, and Morphology in Discrete Ni_{2-x}CoxP Nanoparticles. *Chemistry of Materials* **2015**, *27* (12), 4349-4357.

201. Pu, Z.; Xue, Y.; Li, W.; Amiin, I. S.; Mu, S., Efficient water splitting catalyzed by flexible NiP₂ nanosheet array electrodes under both neutral and alkaline solutions. *New Journal of Chemistry* **2017**, *41* (5), 2154-2159.
202. Milliron, D. J.; Hughes, S. M.; Cui, Y.; Manna, L.; Li, J.; Wang, L.-W.; Alivisatos, A. P., Colloidal Nanocrystal Heterostructures with Linear and Branched Topology. *Nature Mater.* **2004**, *430*, 190-195.
203. Benkoula, S.; Sublemontier, O.; Patanen, M.; Nicolas, C.; Sirotti, F.; Naitabdi, A.; Gaielevrel, F.; Antonsson, E.; Aureau, D.; Ouf, F.-X.; Wada, S.-I.; Etcheberry, A.; Ueda, K.; Miron, C., Water adsorption on TiO₂ surfaces probed by soft X-ray spectroscopies: bulk materials vs. isolated nanoparticles. *Scientific Reports* **2015**, *5* (1), 15088.
204. Ganesan, P.; Sivanantham, A.; Shanmugam, S., Inexpensive electrochemical synthesis of nickel iron sulphides on nickel foam: super active and ultra-durable electrocatalysts for alkaline electrolyte membrane water electrolysis. *Journal of Materials Chemistry A* **2016**, *4* (42), 16394-16402.
205. Liu, S.-Q.; Wen, H.-R.; Ying, G.; Zhu, Y.-W.; Fu, X.-Z.; Sun, R.; Wong, C.-P., Amorphous Ni(OH)₂ encounter with crystalline CuS in hollow spheres: A mesoporous nano-shelled heterostructure for hydrogen evolution electrocatalysis. *Nano Energy* **2018**, *44*, 7-14.
206. Machida, M.; Yoshida, H.; Hamada, T.; Tsushida, M.; Hinokuma, S.; Nagao, Y.; Endo, Y., Metal-Support Interactions in Rhodium Catalysts Supported on Tetravalent Metal Pyrophosphates (MP₂O₇; M = Si, Ti, and Zr). *The Journal of Physical Chemistry C* **2021**, *125* (45), 24920-24929.

207. Samira, S.; Camayang, J. C. A.; Patel, K.; Gu, X.-K.; Nikolla, E., Modulating Catalytic Properties of Targeted Metal Cationic Centers in Nonstoichiometric Mixed Metal Oxides for Electrochemical Oxygen Reduction. *ACS Energy Letters* **2021**, *6* (3), 1065-1072.
208. Zhang, Y.; Liao, Y.; Shi, G.; Wang, W.; Su, B., Preparation, characterization, and catalytic performance of Pd–Ni/AC bimetallic nano-catalysts. *Green Processing and Synthesis* **2020**, *9* (1), 760-769.
209. Kibis, L. S.; Stadnichenko, A. I.; Koscheev, S. V.; Zaikovskii, V. I.; Boronin, A. I., XPS Study of Nanostructured Rhodium Oxide Film Comprising Rh⁴⁺ Species. *The Journal of Physical Chemistry C* **2016**, *120* (34), 19142-19150.
210. van der Walt, C.; Terblans, J. J.; Swart, H. C., A study of diffusion, atom migration and segregation in Cu and Ag alloy bulk- and nanocrystals. *AIP Advances* **2017**, *7* (5), 055102.
211. Costa, J. D.; Lado, J. L.; Carbó-Argibay, E.; Paz, E.; Gallo, J.; Cerqueira, M. F.; Rodríguez-Abreu, C.; Kovnir, K.; Kolen'ko, Y. V., Electrocatalytic Performance and Stability of Nanostructured Fe–Ni Pyrite-Type Diphosphide Catalyst Supported on Carbon Paper. *The Journal of Physical Chemistry C* **2016**, *120* (30), 16537-16544.
212. Liang, B.; Hu, X.; Sun, D.; Yang, Q.; Tang, H.; Zuo, X.; Lin, Y.; Li, G., Facile fabrication of bimetallic Fe₂P–Ni₂P heterostructure for boosted oxygen evolution. *Journal of Materials Science: Materials in Electronics* **2021**, *32* (18), 23420-23428.
213. Fu, Q.; Wang, X.; Han, J.; Zhong, J.; Zhang, T.; Yao, T.; Xu, C.; Gao, T.; Xi, S.; Liang, C.; Xu, L.; Xu, P.; Song, B., Phase-Junction Electrocatalysts towards Enhanced Hydrogen Evolution Reaction in Alkaline Media. *Angewandte Chemie International Edition* **2021**, *60* (1), 259-267.

214. Jin, H.; Joo, J.; Chaudhari, N. K.; Choi, S.-I.; Lee, K., Recent Progress in Bifunctional Electrocatalysts for Overall Water Splitting under Acidic Conditions. *ChemElectroChem* **2019**, *6* (13), 3244-3253.
215. Shi, Z.; Wang, X.; Ge, J.; Liu, C.; Xing, W., Fundamental understanding of the acidic oxygen evolution reaction: mechanism study and state-of-the-art catalysts. *Nanoscale* **2020**, *12* (25), 13249-13275.
216. Lian, Y.; Sun, H.; Wang, X.; Qi, P.; Mu, Q.; Chen, Y.; Ye, J.; Zhao, X.; Deng, Z.; Peng, Y., Carved nanoframes of cobalt–iron bimetal phosphide as a bifunctional electrocatalyst for efficient overall water splitting. *Chemical Science* **2019**, *10* (2), 464-474.
217. Zhang, H.; Maijenburg, A. W.; Li, X.; Schweizer, S. L.; Wehrspohn, R. B., Bifunctional Heterostructured Transition Metal Phosphides for Efficient Electrochemical Water Splitting. *Advanced Functional Materials* **2020**, *30* (34), 2003261.
218. Batugedara, T. N.; Brock, S. L., Role of Noble- and Base-Metal Speciation and Surface Segregation in Ni₂-xRh_xP Nanocrystals on Electrocatalytic Water Splitting Reactions in Alkaline Media. *Chemistry of Materials* **2022**, *34* (10), 4414-4427.
219. Tong, Y.; Chen, P., Cobalt phosphide nanowires with adjustable iridium, realizing excellent bifunctional activity for acidic water splitting. *Dalton Transactions* **2021**, *50* (21), 7364-7371.
220. Baeumer, C.; Liang, A. Y.-L.; Trstenjak, U.; Lu, Q.; Waser, R.; Mefford, J. T.; Gunkel, F.; Nemšák, S.; Chueh, W. C., Carbonate formation lowers the electrocatalytic activity of perovskite oxides for water electrolysis. *Journal of Materials Chemistry A* **2021**, *9* (35), 19940-19948.

221. Mutinda, S. I., *Synthesis and Characterization of the Ternary Phase Co₂-Xr_hxp Nanoparticles and Their Composition-dependent Electrocatalytic Activity Towards the Oxygen Evolution and Hydrogen Evolution Reactions, and Their Performance in Overall Water Splitting*. Wayne State University: 2019.
222. Feng, L.; Vrabel, H.; Bensimon, M.; Hu, X., Easily-prepared dinickel phosphide (Ni₂P) nanoparticles as an efficient and robust electrocatalyst for hydrogen evolution. *Physical Chemistry Chemical Physics* **2014**, *16* (13), 5917-5921.
223. Wang, S.; Lu, A.; Zhong, C.-J., Hydrogen production from water electrolysis: role of catalysts. *Nano Convergence* **2021**, *8* (1), 4.
224. Li, J.; Li, J.; Zhou, X.; Xia, Z.; Gao, W.; Ma, Y.; Qu, Y., Highly Efficient and Robust Nickel Phosphides as Bifunctional Electrocatalysts for Overall Water-Splitting. *ACS Applied Materials & Interfaces* **2016**, *8* (17), 10826-10834.
225. Kötzt, R.; Lewerenz, H. J.; Stucki, S., XPS Studies of Oxygen Evolution on Ru and RuO₂ Anodes. *Journal of The Electrochemical Society* **1983**, *130* (4), 825-829.
226. Kötzt, R.; Neff, H.; Stucki, S., Anodic Iridium Oxide Films: XPS-Studies of Oxidation State Changes and. *Journal of The Electrochemical Society* **1984**, *131* (1), 72-77.
227. Kasian, O.; Grote, J. P.; Geiger, S.; Cherevko, S.; Mayrhofer, K. J. J., The Common Intermediates of Oxygen Evolution and Dissolution Reactions during Water Electrolysis on Iridium. *Angewandte Chemie (International ed. in English)* **2018**, *57* (9), 2488-2491.
228. Laursen, A. B.; Varela, A. S.; Dionigi, F.; Fanchiu, H.; Miller, C.; Trinhammer, O. L.; Rossmeisl, J.; Dahl, S., Electrochemical Hydrogen Evolution: Sabatier's Principle and the Volcano Plot. *Journal of Chemical Education* **2012**, *89* (12), 1595-1599.

229. Greeley, J.; Jaramillo, T. F.; Bonde, J.; Chorkendorff, I. B.; Nørskov, J. K., Computational high-throughput screening of electrocatalytic materials for hydrogen evolution. *Nat Mater* **2006**, *5* (11), 909-13.
230. Prins, R.; Bussell, M. E., Metal Phosphides: Preparation, Characterization and Catalytic Reactivity. *Catal. Lett.* **2012**, *142* (12), 1413-1436.
231. De Trizio, L.; Figuerola, A.; Manna, L.; Genovese, A.; George, C.; Brescia, R.; Saghi, Z.; Simonutti, R.; Van Huis, M.; Falqui, A., Size-Tunable, Hexagonal Plate-like Cu₃P and Janus-like Cu–Cu₃P Nanocrystals. *ACS Nano* **2011**, *6* (1), 32-41.
232. Bertoni, G.; Ramasse, Q.; Brescia, R.; De Trizio, L.; De Donato, F.; Manna, L., Direct Quantification of Cu Vacancies and Spatial Localization of Surface Plasmon Resonances in Copper Phosphide Nanocrystals. *ACS Materials Letters* **2019**, *1* (6), 665-670.
233. Akkerman, Q. A.; Genovese, A.; George, C.; Prato, M.; Moreels, I.; Casu, A.; Marras, S.; Curcio, A.; Scarpellini, A.; Pellegrino, T.; Manna, L.; Lesnyak, V., From Binary Cu₂S to Ternary Cu–In–S and Quaternary Cu–In–Zn–S Nanocrystals with Tunable Composition via Partial Cation Exchange. *ACS Nano* **2015**, *9* (1), 521-531.
234. Shan, X.; Li, B.; Ji, B., Synthesis of Wurtzite In and Ga Phosphide Quantum Dots Through Cation Exchange Reactions. *Chemistry of Materials* **2021**, *33* (13), 5223-5232.
235. OLOFSSON, O. J. A. C. S., The crystal structure of Cu₃P. **1972**, *26* (7), 2777-2787.
236. Hitihami-Mudiyanselage, A.; Senevirathne, K.; Brock, S. L., Assembly of Phosphide Nanocrystals into Porous Networks: Formation of InP Gels and Aerogels. *ACS Nano* **2013**, *7* (2), 1163-1170.

237. Hong, Y.; Kim, T.; Jo, J.; Kim, B.; Jin, H.; Baik, H.; Lee, K., Highly Crystalline Hollow Toroidal Copper Phosphosulfide via Anion Exchange: A Versatile Cation Exchange Nanoplatfrom. *ACS Nano* **2020**, *14* (9), 11205-11214.
238. Ma, L.; Shen, X.; Zhou, H.; Zhu, J.; Xi, C.; Ji, Z.; Kong, L., Synthesis of Cu₃P nanocubes and their excellent electrocatalytic efficiency for the hydrogen evolution reaction in acidic solution. *RSC Advances* **2016**, *6* (12), 9672-9677.
239. Dix, S. T.; Lu, S.; Linic, S., Critical Practices in Rigorously Assessing the Inherent Activity of Nanoparticle Electrocatalysts. *ACS Catalysis* **2020**, *10* (18), 10735-10741.
240. Toufanian, R.; Piryatinski, A.; Mahler, A. H.; Iyer, R.; Hollingsworth, J. A.; Dennis, A. M., Bandgap Engineering of Indium Phosphide-Based Core/Shell Heterostructures Through Shell Composition and Thickness. **2018**, *6*.
241. <http://www.xpsfitting.com/>.
242. Cabrera-German, D.; Gomez-Sosa, G.; Herrera-Gomez, A., Accurate peak fitting and subsequent quantitative composition analysis of the spectrum of Co 2p obtained with Al K α radiation: I: cobalt spinel. *Surface and Interface Analysis* **2016**, *48* (5), 252-256.
243. Biesinger, M. C.; Payne, B. P.; Grosvenor, A. P.; Lau, L. W. M.; Gerson, A. R.; Smart, R. S. C., Resolving surface chemical states in XPS analysis of first row transition metals, oxides and hydroxides: Cr, Mn, Fe, Co and Ni. *Applied Surface Science* **2011**, *257* (7), 2717-2730.
244. Bancroft, G. M.; Adams, I.; Coatsworth, L. L.; Bennewitz, C. D.; Brown, J. D.; Westwood, W. D., ESCA study of sputtered platinum films. *Analytical Chemistry* **1975**, *47* (3), 586-588.
245. Dupin, J.-C.; Gonbeau, D.; Vinatier, P.; Levasseur, A., Systematic XPS studies of metal oxides, hydroxides and peroxides. *Physical Chemistry Chemical Physics* **2000**, *2* (6), 1319-1324.

246. Friedman, A. K.; Shi, W.; Losovyj, Y.; Siedle, A. R.; Baker, L. A., Mapping Microscale Chemical Heterogeneity in Nafion Membranes with X-ray Photoelectron Spectroscopy. *Journal of The Electrochemical Society* **2018**, *165* (11), H733-H741.

ABSTRACT**SYNTHESIS AND INVESTIGATION OF PROPERTIES IN TERNARY TRANSITION METAL PHOSPHIDE NANOMATERIALS FOR ELECTROCHEMICAL WATER SPLITTING**

By

THARANGA NISANSALA BATUGEDARA**August 2022****Advisor:** Dr. Stephanie L. Brock**Major:** Chemistry (Inorganic)**Degree:** Doctor of Philosophy

Nanoscale transition metal phosphides are emerging as efficient catalysts for hydrogen production via electrochemical water splitting. Although monometallic phases have been extensively studied, enhanced catalytic activities and stabilities can be gained by the synergism of two metals in bimetallic ternary transition metal phosphides. In this dissertation, we report (1) the effect of the counter electrode and electrolyte on stabilities of $\text{Co}_{2-x}\text{Rh}_x\text{P}$ nanoparticles for water reduction (hydrogen evolution reaction, HER), (2) novel synthetic protocol development and electrocatalytic water splitting activity and stability study on $\text{Ni}_{2-x}\text{Rh}_x\text{P}$ nanoparticles, and (3) a preliminary investigation employing cation exchange methods to synthesize Cu-M-P (M= Fe, Co, and Ni) nanoparticles.

$\text{Co}_{2-x}\text{Rh}_x\text{P}$ nanoparticles show promising electrocatalytic activity toward HER in acidic and basic media. However, Co is not stable in acidic media under electrocatalytic conditions due to Co dissolution, and the activity was found to deplete 50% with Co loss. Studies on the use of Pt counter electrode and its interference on the working electrode at lower potentials (<0.6 V vs. RHE) revealed that the deactivation of $\text{Co}_{2-x}\text{Rh}_x\text{P}/\text{C}$ due to Co dissolution was masked by Pt

dissolution and redeposition on the working electrode. However, in basic media, no Co dissolution, activity deactivation, or Pt redeposition was observed. At high pH, the increased activity and stability are attributed to *in-situ* formed metal oxide/hydroxides on the catalytic surface.

In order to create a more stable catalyst, we replaced Co in $\text{Co}_{2-x}\text{Rh}_x\text{P}$ nanoparticles with Ni to produce $\text{Ni}_{2-x}\text{Rh}_x\text{P}$ ($x=0.25, 0.5, \text{ and } 1.75$) nanoparticles with low polydispersity. Intermediate compositions were not phase pure. Ni-rich compositions ($x=0.25$ and 0.5) were hollow spherical nanoparticles with hexagonal structures, while the Rh-rich composition ($x=1.75$) adopted a quasi-spherical shape with a cubic antiferroite structure. $X=0.25$ showed the highest OER intrinsic and geometric catalytic activities in basic media with overpotentials of 261.8 mV and 273.8 mV to achieve $2.0 \mu\text{A}/\text{cm}^2_{\text{ECSA}}$ and $10 \text{ mA}/\text{cm}^2_{\text{Geo}}$, respectively. $X=1.75$ showed the highest HER intrinsic catalytic activity in basic media with an overpotential of 44.5 mV to get producing $-2.0 \mu\text{A}/\text{cm}^2_{\text{ECSA}}$. The $x=1.75$ composition also had competitive geometric HER activity with an overpotential of 82.1 mV to obtain $10 \text{ mA}/\text{cm}^2_{\text{Geo}}$. The XPS and EDS mapping data revealed that for both HER and OER, *in-situ* formed oxide/hydroxide species play a role in the catalytic activity, and Rh phase segregation is found post-OER. The use of $\text{Ni}_{0.25}\text{Rh}_{1.75}\text{P}$ as a cathode and $\text{Ni}_{1.75}\text{Rh}_{0.25}\text{P}$ as an anodic in an overall water splitting electrolyzer resulted in an overpotential of 554 mV to obtain a current density of $20 \text{ mA}/\text{cm}^2$. In acidic media, the $x=1.75$ phase showed comparable HER activity and stability relative to Rh_2P . For OER, the $x=1.75$ phase is unique in terms of its stability. While it is initially less active than Rh_2P , the latter phase rapidly deactivates, whereas $\text{Ni}_{1.75}\text{Rh}_{0.25}\text{P}$ has a stability profile similar to the state-of-the-art RuO_2 catalyst. The enhanced stability is attributed to a nickel-rich surface with a Rh underlayer, in which the active nickel catalyst is moderated by the Rh, enabling turnover.

Finally, the synthesis of bimetallic phosphides of Cu-Fe, Cu-Ni and Cu-Co was explored by cation-exchange reactions of Cu_{3-x}P . Preliminary data suggest that treatment of Cu_{3-x}P with equimolar Fe^{3+} at 200 °C produces a crystalline product with the Cu_{3-x}P structure but a slightly compressed lattice. STEM/EDS mapping suggests the hexagonal plates of the starting Cu_{3-x}P are retained, with Cu and Fe forming separate domains. We hypothesize a redox-mediated uptake in which Fe^{3+} oxidizes Cu^{1+} departing the lattice, with Fe^{2+} then incorporated. Attempted exchanges with Ni^{2+} and Co^{2+} were not successful. Optimization of protocols is expected to lead to make new bimetallic catalytic materials that could be utilized in electrochemical water splitting applications.

AUTOBIOGRAPHICAL STATEMENT

THARANGA NISANSALA BATUGEDARA

EDUCATION

- **2017-2022: Ph.D. Wayne State University, Detroit, MI, USA**
Dissertation: Synthesis and investigation of properties in ternary transition metal phosphide nanomaterials for electrocatalytic water splitting applications
Advisor: Prof. S.L. Brock, Major: Inorganic Chemistry, GPA: 3.77
- **2011-2016: B.Sc. University of Kelaniya, Sri Lanka**
Dissertation: Removal of cadmium from wastewater using chitosan beads as a low-cost adsorbent
Advisor: Prof. C.S.K. Rajapakse, Major: Chemistry, GPA: 3.75

PUBLICATIONS

- **Batugedara, T. N.**; Brock, S. L., Role of Noble- and Base-Metal Speciation and Surface Segregation in Ni_{2-x}Rh_xP Nanocrystals on Electrocatalytic Water Splitting Reactions in Alkaline Media. *Chemistry of Materials* **2022**, *34* (10), 4414-4427.
- Mutinda, S. I.; **Batugedara, T. N.**; Brown, B.; Brock, S. L., Co_{2-x}Rh_xP Nanoparticles for Overall Water Splitting in Basic Media: Activation by Phase-Segregation-Assisted Nanostructuring at the Anode. *ChemCatChem* **2021**, *13* (19), 4111-4119.
- Mutinda, S. I.; **Batugedara, T. N.**; Brown, B.; Adeniran, O.; Liu, Z.-F.; Brock, S. L., Rh₂P Activity at a Fraction of the Cost? Co_{2-x}Rh_xP Nanoparticles as Electrocatalysts for the Hydrogen Evolution Reaction in Acidic Media. *ACS Applied Energy Materials* **2021**, *4* (1), 946-955.
- Kirinda, V.C., Hettiarachchi, H.P., **Batugedara, T.N.**, Rajapakse, C.S.K., Use of Chitosan Films for Removal of Cd (II) from Aqueous Solutions by Adsorption and an Electrochemically Assisted Method. *Chemistry Research Journal*, 2019, *4* (2), 160-169.
- **Batugedara, T.N.**, Rajapakse, C.S.K., Chitosan Beads as a Natural Adsorbent for the Removal of Cd(II) from Aqueous Solutions. *International Journal of Science Environment and Technology* 2017, *6*, 606-619.

FELLOWSHIPS AND AWARDS

- **Summer 2022 Dissertation Award**, Wayne State University, 2022
- **Best Oral Presentation Award**, 42nd Annual Michigan Catalysis Society (MCS) Symposium, 2021
- **Materials Science and Nanoscience Division Graduate Poster Presentation Award**, National Organization for the Professional Advancement of Black Chemists and Chemical Engineers (NOBCChE), 2021
- **Thomas C. Rumble University Graduate Fellowship**, Wayne State University, 2021-2022
- **A. Paul and Carole C. Schaap Endowed Distinguished Graduate Award in Chemistry**, Department of Chemistry, Wayne State University, 2021